Metal Dusting of Heat-Resistant Alloys

Abdulaziz I. Al-Meshari
Hughes Hall, Cambridge

University of Cambridge
Department of Materials Science and Metallurgy

A dissertation submitted to the University of Cambridge for
the degree of Doctor of Philosophy
October, 2008

PREFACE

This dissertation reports research that was carried out in the Department of Materials Science and Metallurgy under the supervision of Dr. John A. Little.

Unless otherwise stated, the work described in this dissertation is that of the author and has not been previously submitted in support of an application for another degree or qualification at this or other universities. This dissertation does not exceed word limit of 60,000 words. Attached to this dissertation is a CD with appendices A, B, and C containing supplementary data.

Part of this work has been published as follows:

1. Al-Meshari, Abdulaziz and John Little, *Oxidation of Heat-Resistant Alloys*, Oxidation of Metals (2008)69:109-118.
2. Al-Meshari, Abdulaziz and John Little, *Oxidation of Commercial Heat-Resistant Alloys*, Materials Performance, June 2008:68-72.
3. Al-Meshari, Abdulaziz and John Little, *Oxidation of Centrifugally Cast Superalloys*, The 7th International Conference on Microscopy of Oxidation, 15-17 September 2008, Chester, UK

Abdulaziz Al-Meshari
October 2008

ACKNOWLEDGMENTS

I would like to thank my supervisor Dr. John Little for his support, motivation, and valuable advice.

I also thank all the people in the Department of Materials Science and Metallurgy who contributed by any mean to produce this work.

I would like to express my thanks to my employer, Saudi Basic Industries Corporation (SABIC), for giving me the opportunity to carry out this study. I am also grateful to SABIC Technology Centre-Jubail (STC-J), particularly Mr Mosaed Al-Garni, for allowing part of the analyses to be carried out in STC-J analytical labs.

I wish to thank Kubota Corporation, Japan for providing the alloys used throughout this research.

Table of Contents

ABSTRACT

Metal dusting leads to disintegration of such alloys as iron and nickel-based into a "dust" of particulate metal, metal carbide, carbon, and/or oxide. It occurs in strongly carburising environments at 400-900°C. Literature survey has shown that alloys behave differently in metal dusting conditions based on their composition and the environment. Metal dusting mechanisms for iron and nickel-based alloys have been proposed but, nevertheless, have not been agreed upon and numerous modifications to them have been suggested. Further adding to the complexity, the mechanisms were found to have differed due to operating condition alterations. In view of that, this research was carried out to gain a better understanding of metal dusting process(s) by evaluating the performance of heat-resistant alloys, namely KHR35C HiSi© (HP), KHR45A LC© (35Cr-45Ni), and UCX©, in metal dusting conditions. HP, which is an iron-based alloy, was modified by adding more silicon in order to improve its resistance through the development of SiO_2 at the surface. The carbon content in the nickel-based alloy, 35Cr-45Ni, was lowered to delay the attack onset by accommodating more diffused carbon. UCX©, however, has the highest nickel and chromium levels. The alloys were exposed to a gas containing 80 vol% CO+20 vol% H_2 at 650, 750, and 850ºC for 100, 500, and 1000h. Analyses including visual inspection, XRD, and SEM/EDX revealed that the alloys suffered localised attacks at the three temperatures but to varying degrees and in different shapes. In general, the attack initiated at the matrix rather than the primary carbides and also progressed through the matrix. Increasing the exposure temperature caused less carbon deposition and more oxides formation on the alloy surfaces leading to a reduction in the attack aggressiveness. UCX© exhibited the highest resistance to metal dusting whilst HP suffered the severest attack. The presence of high concentrations of chromium at the surface catalysed a quick formation of Cr_2O_3 scale that reduced the extent of metal dusting. Also, the increase in nickel content might have slowed down the carbon diffusion into the alloy. In addition, the presence of other oxide and carbide-forming elements such as silicon and tungsten might well have enhanced the alloy performance. Diffused carbon binds with free tungsten, niobium, and chromium to form carbides prolonging the incubation period prior to the attack initiation.

1 LITERATURE REVIEW

1.1 Introduction

Metal dusting can be defined as a high temperature phenomenon that causes materials, such as iron, nickel, and cobalt-based alloys, to lose their desirable properties as they disintegrate into powder (or dust). The powder is generally composed of metal, metal carbide, carbon, and oxide particles. Metal dusting can alternatively be described as a catastrophic carburisation that occurs in environments with high carbon activities (i.e. more than unity) and low oxygen partial pressures [1][2]. Carburisation plays an important role in the metal dusting process and unstable carbides (in steels) are apparently a major factor in the reaction [3].

Metal dusting usually takes place in temperatures within the range 450-800°C [1][2]. However, the temperature range has not been well identified as it has also been reported to be 400-800°C [4] or 450-900°C [5][6]. Conversely, in heat-treating industry, metal dusting has been reported to have occasionally occurred in the temperature range 900-930°C [7]. Additionally, it is documented that metal dusting has happened at temperatures as high as 1100°C in strongly reducing environments [8]. Theoretically, metal dusting should be possible at any temperature as long as the carbon activity is greater than one [9][10].

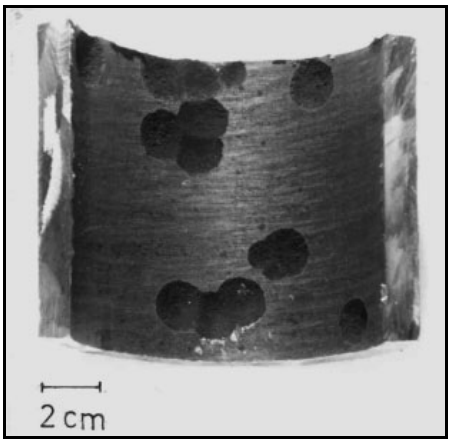

Figure 1.1 **Metal dusting in heater tube of direct reduction plant. The attack occurred at about 600°C. The tube alloy is HK 40 [11].**

Metal dusting is a chronic problem that is responsible for many premature failures in a wide variety of industrial sectors. It has been encountered in CO, methane, methane plus hydrogen, ethane, propane, and butane plus CO, hydrogen, and other mixtures of similar gases [3]. In petrochemical plants, for example, metal dusting has been experienced in steam reforming furnaces used to manufacture synthesis gases (e.g. H_2, CO, and CO_2). The frequency of such failures has recently increased as plant operators tend to boost the process efficiency by introducing less steam to the system, thereby increasing the carbon monoxide content and consequently raising the probability of metal dusting [12]. Iron, nickel, cobalt and their alloys are susceptible to metal dusting which can be localised and/or uniform [13]. Metal dusting has also been encountered in the heat-treating industry, especially in atmospheres used to carburise steels [7]. Petroleum refineries also suffer metal dusting in processes involving hydro-dealkylation and catalyst regeneration systems. Metal dusting can also be a serious problem in other industrial sectors including nuclear plants, coal gasification units, ethylene plants, fuel cells, chemical reactors, steam generators, acetic acid cracking furnaces, and waste heat boilers [14][15][16]. Steel making plants are also vulnerable to metal dusting. In fact, blast furnaces and reformers using direct reduction of iron ore are readily susceptible to metal dusting [1].

(a)

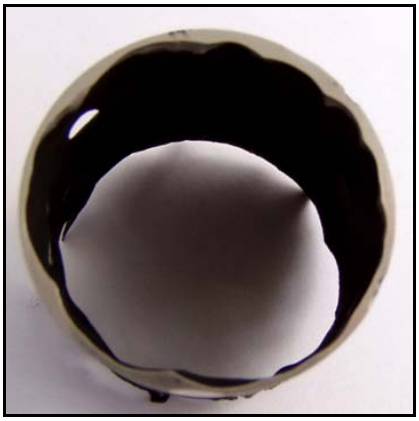

(b)

Figure 1.2 Metal dusting in an inlet tube of heat exchanger unit. The material is alloy 800 [8].

Historically, "metal wastage" phenomenon has actually been recognised for a long time. In 1876, Pattinson [1] *as referenced in* [17] observed metal wastage of iron in carbon monoxide-containing environment. The term "metal dusting" was probably first used in the late 1950s or early 1960s [6]. More specifically, it was firstly reported as a concept by Camp and co workers in 1945 [2] *as referenced in* [17].

Metal dusting mechanisms have recently been proposed and elucidated for both iron and nickel (and cobalt) based alloys [10][18]. The mechanisms are generally accepted to some degree but, nevertheless, the influence of individual parameters has not yet been studied in great detail [19]. It is true to state that there is a still no universal agreement on the mechanisms of metal dusting [6][17][20]. It is known that there are several gaps in

knowledge, which need to be bridged in order to gain a better understanding of the mechanisms [17].

Figure 1.3 Metal dusting in alloy RA330 tube used in heat-treating environments at about 930ºC [7].

Although the phenomenon of metal dusting has been much investigated since the 1950s (Camp *et al*. 1945; Hoyt *et al.* 1959), its occurrence is still unpredictable. There does not appear to be a sound criterion and/or method that can be adopted to predict the metal dusting onset. In fact, it has been stated that it is almost impossible to identify the exact environment and conditions in which metal dusting will occur [6].

According to Grabke *et al.* [11], it is true that metal dusting may start immediately and sometimes unexpectedly but, in most cases, it initiates due to condition changes such as:

- Changes in operating conditions,
- Equipment repairs and bad workmanship,
- Changes in the material of construction, and
- Sudden contamination by impurities (e.g. chlorine or mineral salts) which may act to damage the protective oxide scale [11].

In general, metal dusting is insidious and can occur suddenly and unpredictably leading to plant emergency shutdowns and, therefore, huge production losses. Indeed, metal dusting failures cost many millions of dollars globally [7][9]. Interestingly, the US Department of Energy has estimated a financial impact of about $220-290 million that could be saved annually in hydrogen production plants alone, if the limitations caused by metal dusting could be circumvented [17].

Unfortunately, no method is currently available that can completely mitigate metal dusting [10]. There are, however, some effective measures that have been widely proven to control metal dusting. For example, control of operating conditions, addition of sulphur-containing compounds, change of alloy, and application of surface coatings [10].

The purpose of this research is to gain a better understanding of metal dusting process through evaluating and comparing the performance of three, commercially available, heat-resistant alloys, namely KHR35C HiSi© (HP), KHR45A LC© (35Cr-45Ni), and UCX©, in metal dusting conditions. A literature review covering the aspects of metal dusting is given in Chapter 1. Thermodynamic and kinetic considerations as well as the suggested metal dusting mechanisms are elucidated. Chapter 2 reports the experimental apparatus, procedures, and characterisation techniques used thorough the research. Metallographic examination of the alloys is shown in Chapter 3. The microstructural changes due to different exposures are also reported. Chapter 4 describes findings concerning the oxidation study carried out to assess the alloys ability to form protective oxide scale at 650, 750, and 850ºC for 100 and 1000h. Chapters 5, 6, and 7 report and discuss the findings concerning the behaviour of alloys, HP, 35Cr-45Ni, and UCX respectively that had been exposed to the gas mixture at 650, 750, and 850ºC for periods of 100, 500, and 1000 hours. Chapter 8 is to discuss the results illustrated in Chapters, 5, 6, and 7 and to evaluate and compare the alloys performance in the gas mixture. The conclusions that have been reached are shown in Capter 9. The chapter also includes the future work suggested in order to continue investigating the metal dusting process and gain a better understanding concerning the roles of different parameters on the alloys performance.

1.2 Thermodynamic Considerations

Metal dusting occurrence may be predicted by studying the conditions in which graphite forms. For carbon steel, carbon activity can be estimated by assuming that it is in equilibrium with cementite (Fe_3C):

$$3Fe + C \leftrightarrow Fe_3C \tag{1.1}$$

The Gibbs free energy change of the reaction can be written as:

$$\Delta G = \Delta G^o + RT \ln \left(\frac{a_{Fe_3C}}{a^3_{Fe}.a_C} \right) \tag{1.2}$$

where ΔG^o is the standard Gibbs free energy change, R is the ideal gas constant (R = 8.314 J mol^{-1} K^{-1}), and T is the absolute temperature. The symbols a_{Fe_3C}, a_{Fe}, and a_C denote the activities of cementite, iron, and carbon respectively. In equilibrium state, $\Delta G = 0$, hence:

$$\Delta G^o = - RT \ln K = - RT \ln \left(\frac{a_{Fe_3C}}{a^3_{Fe}.a_C} \right) \tag{1.3}$$

where K is the equilibrium constant.

If the activity of pure solids is assumed unity, then the standard Gibbs free energy change for the process can be expressed as:

$$\Delta G^{o} = -RT \ln \left(\frac{1}{a_{\mathrm{C}}} \right) \tag{1.4}$$

Thus, ΔG^{o} is equal to zero at equilibrium with graphite where the carbon activity is unity, see Figure 1.4 [6][21].

Negative values of the free energy change indicate that the reaction is spontaneous and the formation of cementite is thermodynamically favourable. If the value of ΔG^{o} is positive, however, then the reverse reaction is favoured. Accordingly, cementite is no longer thermodynamically stable and, consequently, tends to decompose into iron and carbon particles.

Interestingly, Figure 1.4 shows that the formation of cobalt and nickel carbides in metal dusting environment is unlikely owing to their positive standard free energy changes. This supports the currently proposed metal dusting mechanism for nickel and cobalt-based alloys (1.4.2). Other carbides such as those of chromium, niobium, and titanium are deemed stable and readily form in carburising environments.

The hydrogen reforming process is reckoned to be an “ideal” environment for metal dusting to occur. In such process, natural gas is mixed with steam and then passed through catalyst filled tubes at elevated temperatures (e.g. 800°C) to produce a gas mixture containing carbon monoxide, carbon dioxide, hydrogen, and water vapour (i.e. typical metal dusting environment) [12].

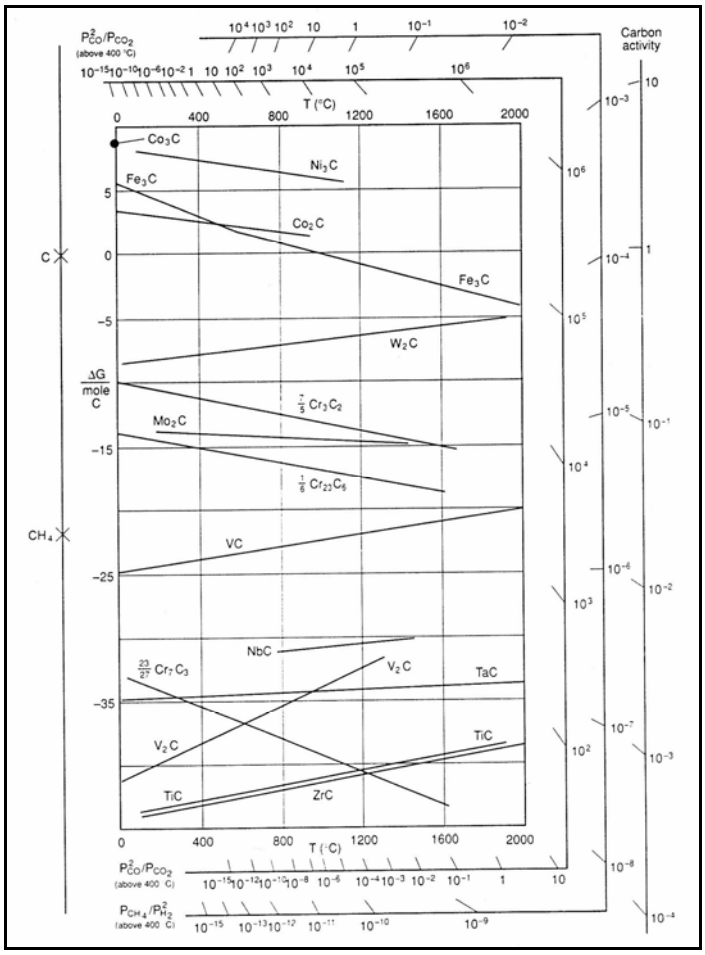

Figure 1.4 Standard free energies of formation for carbides [6].

The metal dusting tendency is evaluated by considering the carbon activity (a_c) and oxygen partial pressure (pO_2) of the gas mixture [22]. In metal dusting environments, the two main reactions, by which carbon transfer from the atmosphere can occur, are carbon monoxide reduction and the Boudouard reaction. Carbon monoxide reduction can be written as [21][23]:

$$CO + H_2 \leftrightarrow H_2O + C \tag{1.5}$$

Hence, the standard free energy change:

$$\Delta G^o = -RT \ln \left(\frac{a_{c1.5}.pH_2O}{pCO.pH_2} \right) = -RT \ln K_{1.5} \tag{1.6}$$

Therefore, the carbon activity ($a_{c1.5}$) can be written as:

$$a_{c1.5} = K_{1.5}\left(\frac{p\mathrm{CO}.p\mathrm{H_2}}{p\mathrm{H_2O}}\right) \tag{1.7}$$

where p is the partial pressure for the given gaseous compounds. Partial pressures can be obtained at atmospheric pressure from the volume percentage divided by a hundred.

The chart in Figure 1.5 displays the variation of carbon activity as a function of CO/CO_2 and H_2O/H_2 ratios for reaction (1.5) at 627ºC. In general, it can be interpreted that high carbon activities of the gas mixture are associated with low H_2O/H_2 ratio and vice versa.

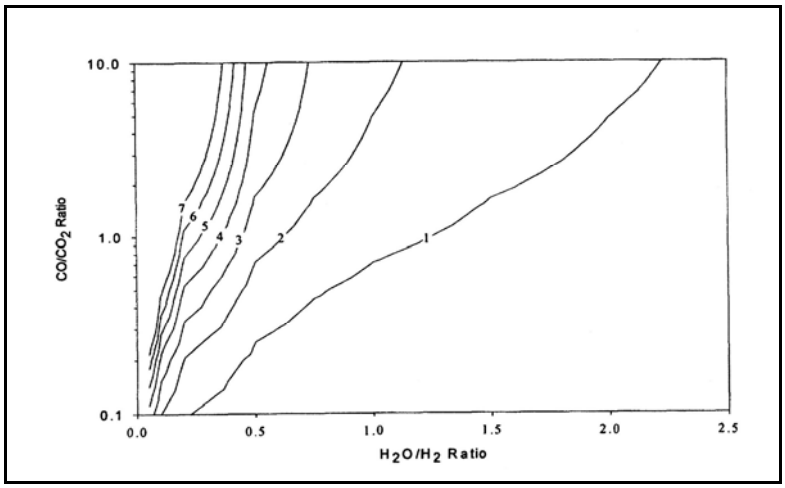

Figure 1.5 **Carbon activity as a function of CO/CO_2 and H_2O/H_2 for the reduction of CO by H_2 at 627ºC with 1% H_2O [24].**

Indeed, the equilibrium constant can also be expressed as a function of temperature. This can be derived by considering the relationship between the standard free energy change and both standard enthalpy and entropy changes:

$$\Delta G^o = \Delta H^o - T\,\Delta S^o = -RT\ln K \tag{1.8}$$

Solving for K:

$$\ln K = -\frac{\Delta H^o}{RT} + \frac{\Delta S^o}{R} \tag{1.9}$$

Since the standard enthalpy and standard entropy changes do not vary with temperature and are assumed constants, then the equilibrium constant can be written as a function of temperature only. According to Ref. [21], $K_{1.5}$ (reaction (1.5)) can be obtained by:

$$\log K_{1.5} = \frac{7100}{T} - 7.496 \tag{1.10}$$

The second main reaction that plays a significant role in metal dusting initiation is the Boudouard reaction:

$$2CO \leftrightarrow CO_2 + C \tag{1.11}$$

ΔG^o for this reaction is:

$$\Delta G^o = -RT \ln \left(\frac{a_{c1.11} . pCO_2}{p^2 CO} \right) = -RT \ln K_{1.11} \tag{1.12}$$

And the carbon activity is given by:

$$a_{c1.11} = K_{1.11} \left(\frac{p^2 CO}{pCO_2} \right) \tag{1.13}$$

Where the equilibrium constant is given by:

$$\log K_{1.11} = \frac{8817}{T} - 9.071 \text{ [21][23]} \tag{1.14}$$

In addition to these two reactions, some other reactions are known to take place in metal dusting environments. The dissociation of hydrocarbons, e.g.: [1]

$$CH_4 \leftrightarrow 2H_2 + C \tag{1.15}$$

The ΔG^o of this reaction:

$$\Delta G^o = -RT \ln \left(\frac{a_{c1.15}.p^2H_2}{pCH_4} \right) = -RT \ln K_{1.15} \tag{1.16}$$

Therefore, the carbon activity is given by:

$$a_{c1.15} = K_{1.15} \left(\frac{pCH_4}{p^2H_2} \right) \tag{1.17}$$

The production of carbon in this reaction is slow in the metal dusting temperature range. Thus, it is unlikely to be responsible for the metal dusting and its effect is usually ignored [4][22][25].

The following reactions also take place in metal dusting environments, i.e. the water gas/shift reaction [1]:

$$H_2O + CO \leftrightarrow CO_2 + H_2 \qquad (1.18)$$

And the steam/methane-reforming process:

$$H_2O + CH_4 \leftrightarrow CO + 3H_2 \qquad (1.19)$$

However, in metal dusting conditions, the gases are at high temperatures and are not in the equilibrium state suggesting that the carbon activities may be appreciably high. As seen in the two main reactions above (i.e. (1.5) and (1.11)), carbon activity increases as the temperature is decreased [1][21]. For example, if the temperature is decreased from 850 to 600°C, then $K_{1.5}$ (equation (1.10)) will increase from 0.07 to 4.33. This results in a significant increase in the carbon activity $a_{c1.5}$ (equation (1.7)). The equilibrium constants of reactions (1.5), (1.11), and (1.15) are plotted as functions of temperature, Figure 1.6.

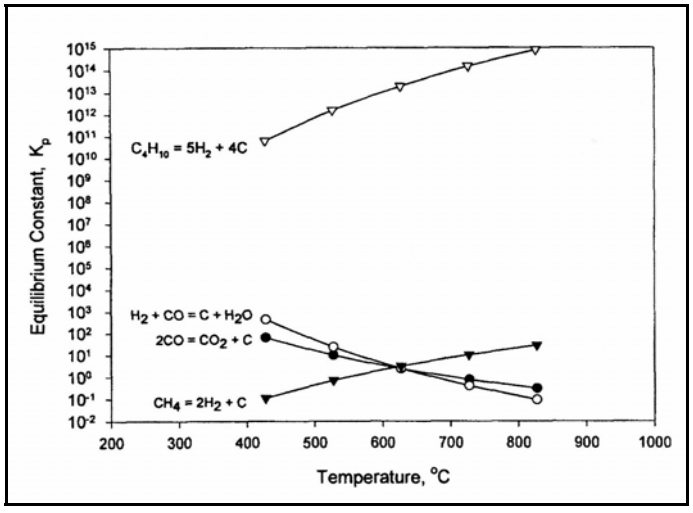

Figure 1.6 **Equilibrium constants for carbon-producing reactions in metal dusting environments [24].**

It has also been proposed that the extent of metal dusting is strongly related to the CO/CO_2 and H_2O/H_2 ratios. Parks *et al.* [19] *as referenced in* [22] has suggested these two ratios to predict the likelihood that the gas mixture might cause metal dusting (Figure 1.7). However, it is not clear whether these ratios are reliable and they might need to be validated by making thermodynamic and kinetics correlations [22].

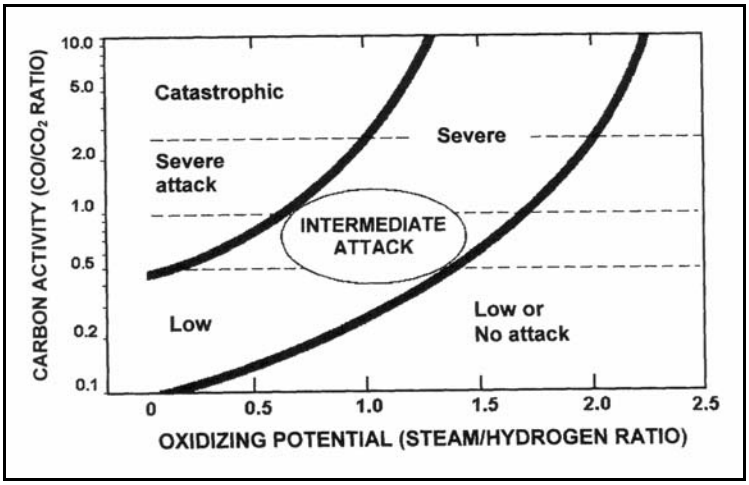

Figure 1.7 **Graph published by Parks *et al.* [3] *as referenced in* [24] relating the severity of metal dusting attack of alloys 800 and 304 to CO/CO_2 and H_2O/H_2 within critical zones of ammonia plant waste heat boiler.**

Oxygen partial pressure is also an important parameter in metal dusting environment as the presence of oxygen is necessary for the formation of oxides. Schueler [26] suggested that metal dusting might not occur if oxygen is completely absent. The role of oxidation in metal dusting is discussed in (1.6) in more details. Oxygen can be released in metal dusting environments by the following two reactions [12]:

Water dissociation reaction:

$$2H_2O \leftrightarrow 2H_2 + O_2 \qquad (1.20)$$

The oxygen partial pressure can be obtained:

$$\Delta G^o = -RT \ln K_{1.20} = -RT \ln \left(\frac{p^2\mathrm{H_2}.p\mathrm{O_2}}{p^2\mathrm{H_2O}} \right) \tag{1.21}$$

So;

$$p\mathrm{O_2} = K_{1.20} \left(\frac{p^2\mathrm{H_2O}}{p^2\mathrm{H_2}} \right) \tag{1.22}$$

And carbon dioxide dissociation: [12]

$$2\mathrm{CO_2} \leftrightarrow 2\mathrm{CO} + \mathrm{O_2} \tag{1.23}$$

The oxygen partial pressure is given by:

$$\Delta G^o = -RT \ln K_{1.23} = -RT \ln \left(\frac{p^2\mathrm{CO}.p\mathrm{O_2}}{p^2\mathrm{CO_2}} \right) \tag{1.24}$$

Hence;

$$p\mathrm{O_2} = K_{1.23} \left(\frac{p^2\mathrm{CO_2}}{p^2\mathrm{CO}} \right) \tag{1.25}$$

In Figure 1.8, the equilibrium constants of reactions (1.20) and (1.23) are plotted as functions of temperature. Reaction (1.20) appears to have higher equilibrium constant at metal dusting temperature range and, therefore, is anticipated to be dominant. Figure 1.9 discloses the values of partial pressure of oxygen as a function of the CO/CO_2 and H_2O/H_2 ratios in synthesis gas environment. It is obvious that oxygen partial pressure increases with H_2O/H_2 ratio.

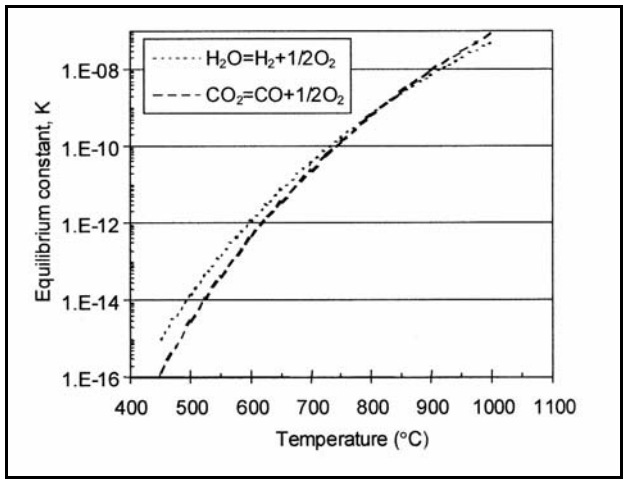

Figure 1.8 **Equilibrium constants of reactions (1.20) and (1.23) [22].**

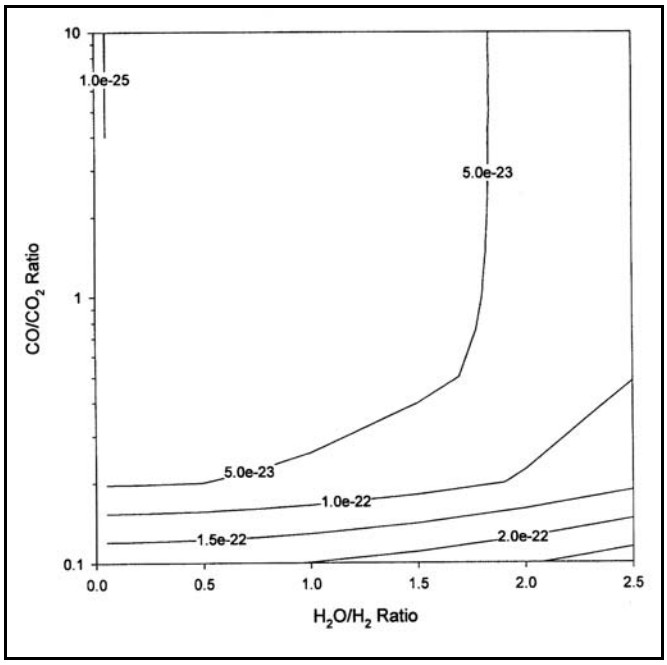

Figure 1.9 **Partial pressure of oxygen as a function of the CO/CO_2 and H_2O/H_2 ratios in synthesis gas environment with 1% H_2O [24].**

The thermodynamic considerations can only predict the tendency of metal dusting using the gas carbon activity and oxygen partial pressure. However, the occurrence of metal dusting cannot be totally predicted based on these considerations given the different behaviours of alloys nominally in the same gas atmospheres.

Thermodynamics of a gas mixture may indicate the likelihood of metal dusting while it is not evident in practical situations [6][20]. In fact, different alloys have different incubation periods before the onset of metal dusting, and these periods seem to be controlled by many

factors such as alloy composition, oxide scale stability, operating pressure, and operating temperature [1][8]. For nickel-based alloys, metal dusting reaction has a long period of incubation, especially when the iron content is low [8][14]. Figure 1.10 discloses that the addition of high amounts of nickel drastically improves the performance of Fe-Ni alloys in metal dusting conditions. It has also been noticed that low gas velocity areas over an alloy tend to favour metal dusting [5]. The effects of hydrogen, water vapour, oxygen, impurities, gas flow rate, temperature, and pressure on metal dusting initiation have not yet been clearly defined [26].

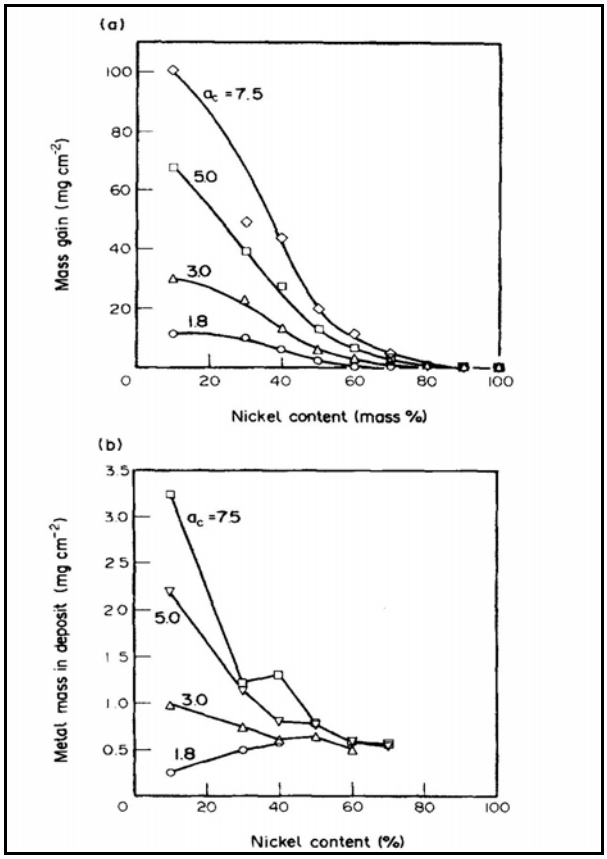

Figure 1.10 **Deposits on Fe-Ni alloys after 24h in CO-H_2-H_2O at 0.1bar and 650°C vs. nickel content in the alloy: (a) total mass gain; (b) metal content in the deposit [27].**

1.3 Kinetics Considerations

Metal dusting attack can be categorised as either uniform or localised depending on alloy chemistry and exposure conditions. Iron, nickel, and low-alloyed steels are usually subject to general thinning. However, as the chromium concentration is increased in an alloy, the

overall corrosion rate decreases considerably and the attack becomes more localised [28]. Accordingly, high chromium iron and nickel-based alloys are usually susceptible to metal dusting by pitting [21]. Therefore, the kinetics of metal dusting is expected to vary from an alloy to the other based on their chemical composition. As seen in Figure 1.11, metal dusting kinetics is also significantly influenced by the change in exposure temperature [19].

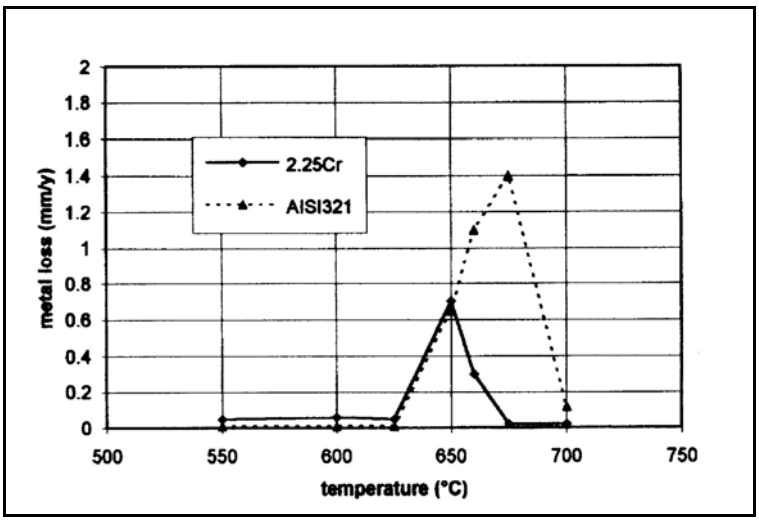

Figure 1.11 **Metal loss rate as a function of temperature [19]. This Figure is based on short butane/hydrogen test carried without sulphur addition.**

According to Grabke [21], a steady state carbon activity is established on the free metal surface of iron during exposure to a metal dusting environment. The carbon activity has a value close to $a_{c1.5}$ since the reaction (1.5) has a faster kinetics compared to the reaction (1.11). In fact, the Boudouard reaction (i.e. (1.11)), which is much slower than reaction (1.5), plays a minor role in the kinetics and thermodynamics of non-equilibrium gas mixtures. Therefore, reaction (1.5) is considered to be the dominant for the establishment of the steady state carbon activity on the free iron surface. Additionally, in non-equilibrium conditions, reaction (1.20) (i.e. the water dissociation reaction) is generally dominant in the establishment of the oxygen partial pressure due to its rapid kinetics.

The kinetics of carburisation of an iron foil at 650°C and three different carbon activities is shown in Figure 1.12. In a carbon activity of 1.3, the material experienced metal dusting [27].

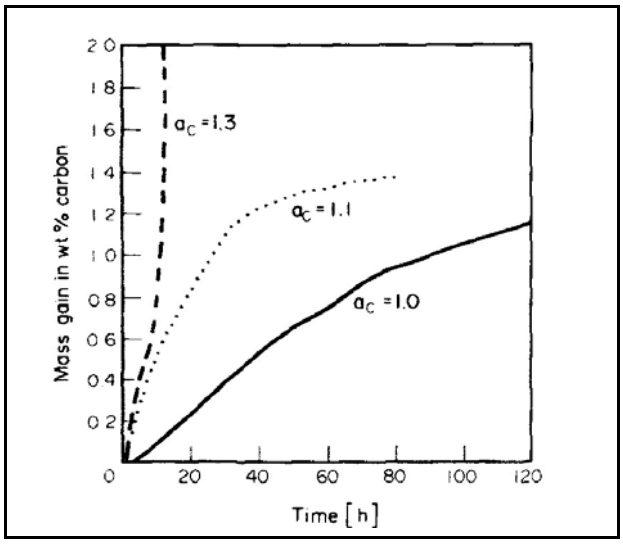

Figure 1.12 Kinetics of carburisation of an iron foil at 650°C at different carbon activities [27].

Olsson *et al.* [13] *as referenced in* [17] have also measured the kinetics of reactions (1.5) and (1.11) on pure iron as a function of both CO/H_2 ratio and temperature. It was found that reaction (1.5) was dominant generally at higher H_2 concentrations whereas reaction (1.11) was dominant at higher CO concentrations. Interestingly, with a 50% CO-50% H_2 mixture at 600°C, the kinetics of the two reactions was found to be equal.

According to Szakalos [17], experiments showed that reactions (1.5) and (1.11) seem to be somewhat suppressed in highly alloyed materials (i.e. those that form stable oxides), especially reaction (1.5), as no water was detected at the cooled gas outlet. However, the influence of the oxide layer integrity (e.g. size and distribution of defects in the oxide layer) on the metal dusting kinetics has not yet been fully understood [29].

Nishiyama *et al.* [22] calculated the reaction rates of reactions (1.5), (1.11), and (1.15) in different gas compositions and the results were plotted as functions of temperature; Figure 1.13. The following equations were used to plot the reaction rates (k_p): [30]

$$k_{p1.5} = \{4.75\times10^{5}\left(\frac{p\mathrm{H_2O}}{p^{1/2}\mathrm{H_2}}\right)\exp\left(\frac{-27150}{T}\right)\}\ \{1+5.6\times10^{6}\left(\frac{p\mathrm{H_2O}}{p\mathrm{H_2}}\right)\exp\left(\frac{-12900}{T}\right)\}^{-1} \quad (1.26)$$

$$k_{p1.11} = 184\left(\frac{p\mathrm{CO_2}}{p\mathrm{CO}}\right)^{-0.3} p\mathrm{CO_2}\exp\left(\frac{-22400}{T}\right) \text{ [30][31]} \quad (1.27)$$

$$k_{p1.15} = 1.96\times10^{-2}\, p^{3/2}\mathrm{H_2}\exp\left(\frac{-17600}{T}\right) \text{ [30][32]} \quad (1.28)$$

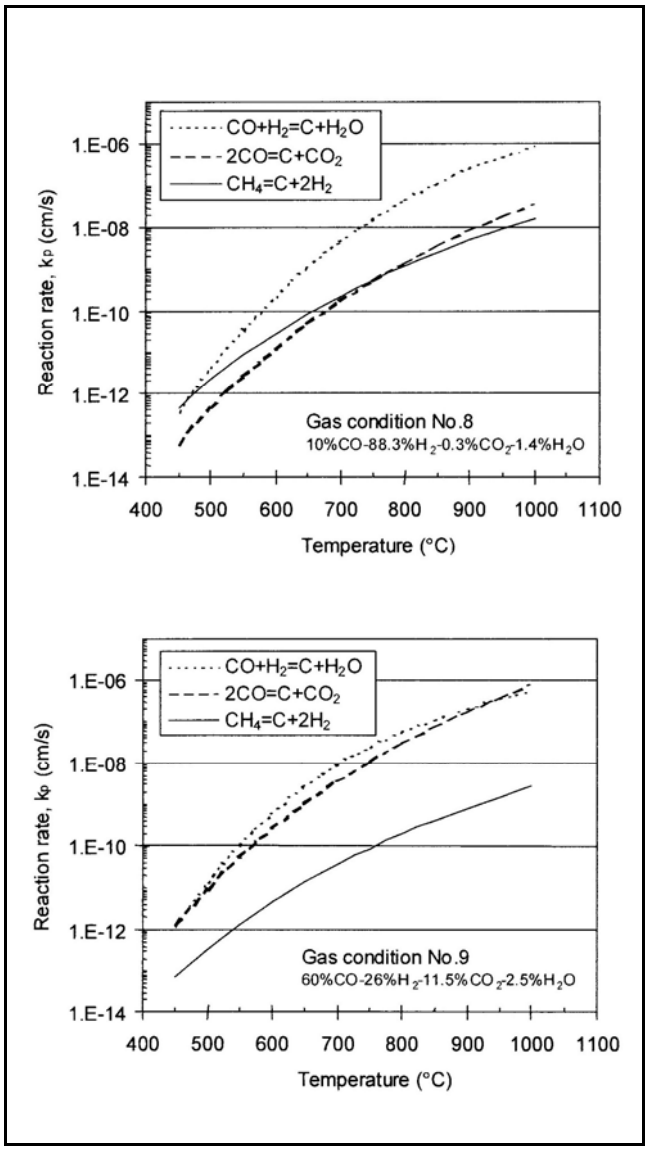

Figure 1.13 Rate of reactions (1.5), (1.11), and (1.15) for different gas compositions [22].

Carbon deposition is catalytically accelerated by contact with iron, nickel, and cobalt. For example, coking which is a chronic problem in ethylene furnaces was thought to be caused by the reduction of a porous (Fe, Ni, Cr) spinel oxide layer at the metal surface into catalytically active (Fe, Ni) particles [33][34]. Coke formation generally indicates the start or continuation of metal dusting as it is catalysed by the metal particles at the alloy surface [35].

Turkdogan *et al.* [36] studied the catalytic effect of iron on decomposition of carbon monoxide in H_2-CO mixtures. In 100% CO, the amount of carbon accumulated at a given time was proportional to the amount of iron catalyst present in the system. In H_2-CO mixtures, carbon deposition increased to a lesser extent with an increasing amount of the catalyst. As the reaction progressed, most iron was converted to cementite and no further carbon deposition occurred. It was concluded that graphite, iron carbides, oxides, and sulphides had no catalytic effect on the decomposition of carbon monoxide.

Olsson *et al.* [37] studied the catalytic effect of iron on decomposition of carbon and the effect of additions of H_2, H_2O, CO_2, SO_2, and H_2S. The Boudouard reaction was catalysed by hydrogen adsorbed on the iron surface. The contribution of the reaction, $CO + H_2 \leftrightarrow C + H_2O$, to the total rate was minor up to 50% hydrogen. In CO-H_2-H_2O mixtures with H_2/CO greater than 0.1, the rate of carbon deposition decreased with increasing the concentration of water vapour due to the reverse reaction of $CO + H_2 \leftrightarrow C + H_2O$. In the absence of hydrogen, the rate of Boudouard reaction at 400 to 600ºC increased with increasing the water content, at least up to 6% H_2O.

Maximum wastage rates of iron, cobalt, and ferritic stainless steels are reported to have occurred within the temperature range 400-700°C in CO and CO-H_2 gases. Austenitic stainless steels, however, showed maximum wastage rates at 650-800°C. Nickel-based alloys exhibited maximum dusting at 675-850°C [1].

The metal dusting rate could be minimised by adding elements such as nickel, molybdenum, silicon, aluminium, and titanium (Figure 1.14). Incorporating such elements imparts better metal dusting resistance as they act to reduce the solubility and diffusivity of carbon through alloys [21][24][38][39].

Although the nickel addition helps to minimise the metal dusting rate, it has been reported that the resistance of stainless steels was reduced as the nickel content was increased whilst the chromium concentration remained constant [26].

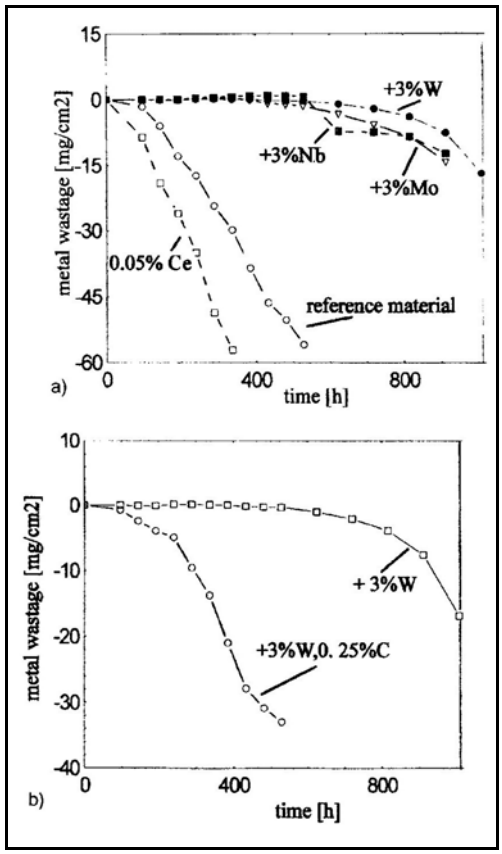

Figure 1.14 Behaviour of Alloy 800 in metal dusting environment. The influence of the addition of alloying elements is shown [21].

Maier *et al.* [14, 15] *as referenced in* [9] studied the influence of pressure (0.1 to 0.5MPa) on metal dusting kinetics. It was concluded that metal dusting rates tended to increase as the pressure was increased [9]. Figure 1.15 shows the influence of temperature and pressure on carbon activity. The carbon activity was increased with pressure, especially at temperatures below 900°C [40].

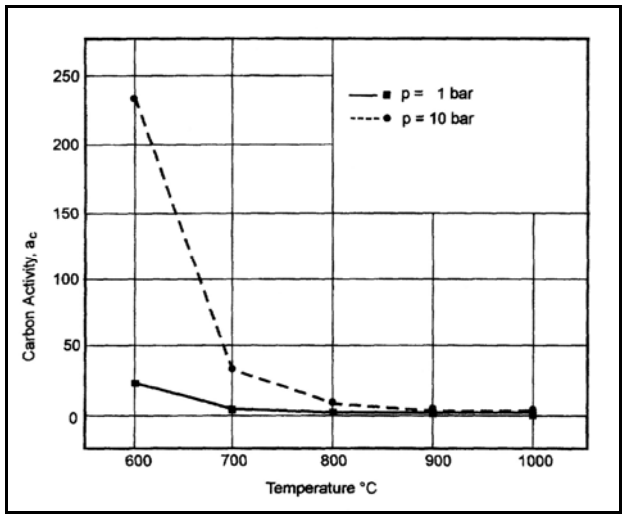

Figure 1.15 Carbon activity vs. temperature and pressure (Perez) [40].

Almost all alloys show different kinetics (or behaviours) in metal dusting environments (Figures 1.16 and 1.17). In these Figures, all the alloys were tested in the same environment (CO-20% H_2 at 621°C). It was obvious that metal wastage rates were governed by gas and gas-alloy kinetics [15].

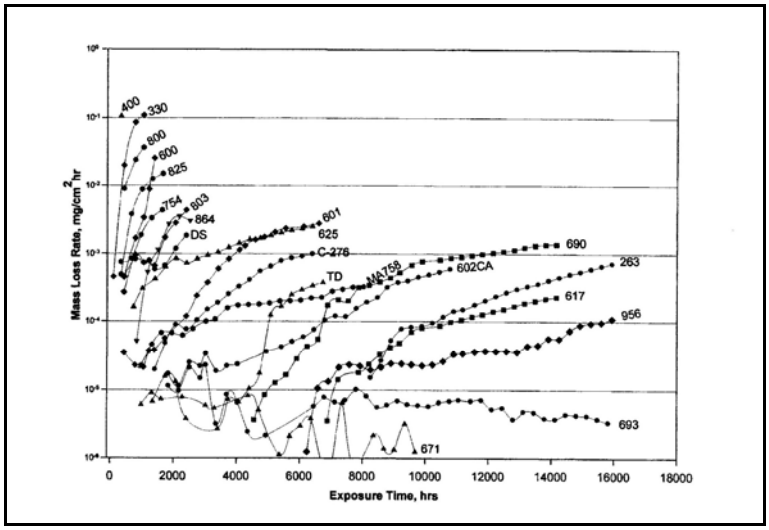

Figure 1.16 Mass loss rate vs. time for different alloys exposed to CO-20% H_2 at 621°C [15].

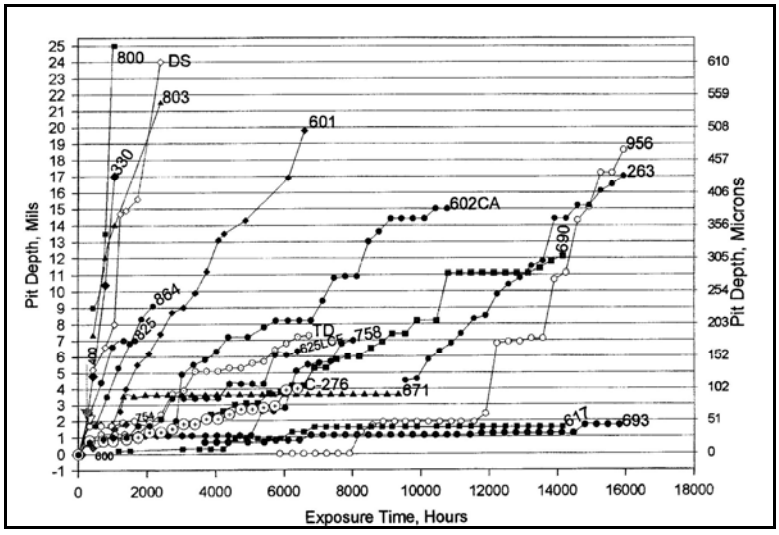

Figure 1.17 Maximum pit depth for different alloys exposed to CO-20% H_2 at 621°C [15].

1.4 Metal Dusting Mechanisms

Metal dusting mechanisms have been extensively studied since the 1950s. Prange [3] *as referenced in* [17] carried out some studies concerning the metal dusting mechanisms of alloys exposed to carbon-containing environments in petrochemical plants.

Further investigations were conducted in the 1950s and 1960s by several researchers (e.g. Prange [3] *as referenced in* [17], Eberle *et al.* [4] *as referenced in* [17], Hoyt *et al.* [5] *as referenced in* [17], and Hopkins *et al.* [6] *as referenced in* [17]). Most of these works concentrated on the behaviour of some alloys in metal dusting conditions and suggested possible mechanisms.

Indeed, it is interesting to note that the currently proposed metal dusting mechanism of binary Fe-Ni alloys was firstly described during the 1950s by Hultgren *et al.* [7] *as referenced in* [17]. Subsequently, Peppel *et al* [16, 17] *as references to* [17] investigated this mechanism in more detail.

1.4.1 Metal Dusting Mechanism for Iron and Low Alloy Steels

The process of metal dusting for iron and low alloy steels was originally investigated by Hochman [4] *as referenced in* [27]. It has also been thoroughly studied and modified by different researchers, especially Grabke and co-workers [27][41].

The steps suggested to be involved in the metal dusting process for iron and low alloy steels are as follows (Figure 1.18) [27][42][43][44]:

a. Carbon transfers from a strongly reducing gas, with $a_c > 1$, and supersaturates the metal surface.
b. Carbon adsorbed by the metal reacts to form carbides (such as cementite) at the metal surface and grain boundaries.

c. The formation of a cementite layer consequently hinders the carbon diffusion into the metal.

d. The cementite becomes supersaturated as the carbon keeps diffusing through the alloy, and hence graphite starts to nucleate and deposit on the surface leading to a significant reduction in the carbon activity at the graphite/metal interface.

e. The graphite accumulation eventually results in the carbon activity approaching unity where cementite becomes thermodynamically instable and hence decomposes into pure metal particles and graphite (according to the reaction $Fe_3C \rightarrow 3Fe + C$).

f. The decomposed metal particles diffuse through the graphite lattice structure and agglomerate into nanometre size particles that serve as catalysts for more carbon deposition.

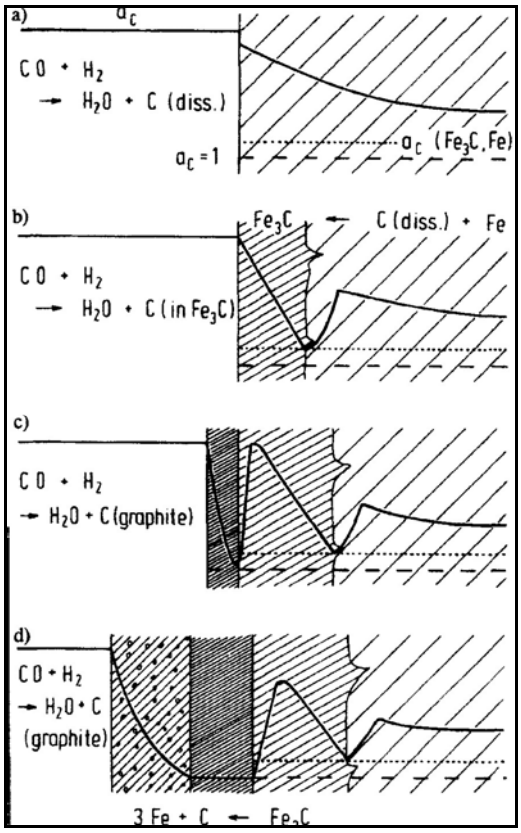

(a)

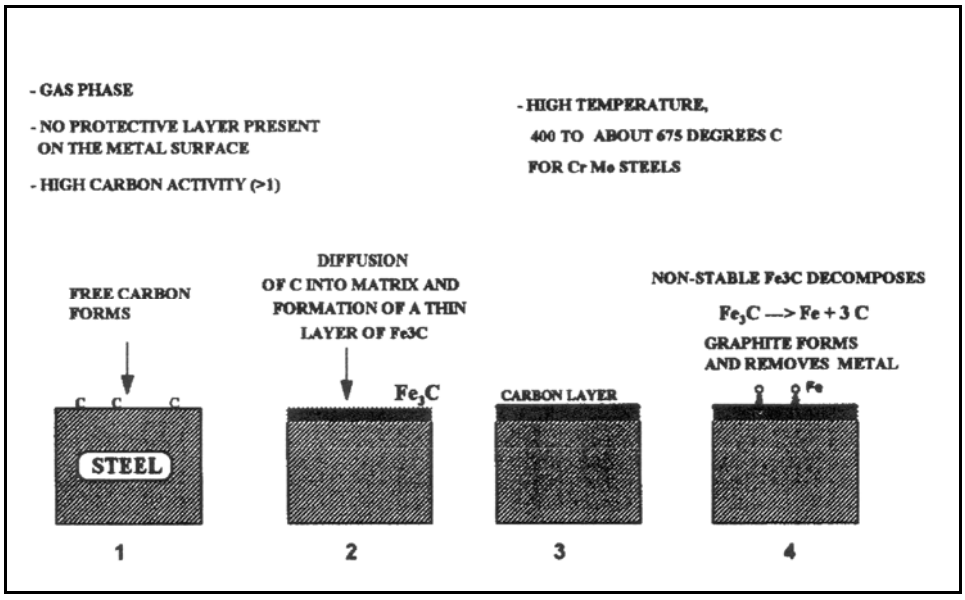

(b)

Figure 1.18 **(a) Schematic of the proposed mechanism of metal dusting on iron and low alloy steels [45] and (b) another schematic of the same mechanism [19]**

According to Grabke [21], the suggested metal dusting mechanism for iron and low alloy steels was observed at 400-650°C in H_2-CO-H_2O mixtures.

At higher temperatures (T > 700°C), however, the iron atoms produced by the cementite decomposition agglomerated to form an iron layer that reduced the carbon diffusion rate. Accordingly, the metal dusting process was slowed down as it became controlled by carbon diffusion through ferrite. At even higher temperatures, 900-1000°C in CH_4-H_2 mixtures with a_c > 1, the cementite did not form.

Schneider [46] reported that the iron layer produced by cementite decomposition, at 700ºC in CO-H_2-H_2O gas mixture with a_C = 15.9 and 20, had a thickness of 1-3μm.

The metal dusting mechanism suggested for iron and low alloy steels is more or less accepted by most researchers. Nevertheless, many related questions are still uncertain, especially regarding the steady state situation and driving force of this mechanism. It is very difficult to explain thermodynamically the carbon diffusion in opposite direction to the carbon activity gradient.

In view of that, some modifications to the original mechanism have been suggested to overcome these points, Figure 1.19. It has been proposed that the cementite layer forms only during the initiation stage of the metal dusting process and that stage may last for more than twenty hours and can last for 100h at 650-700°C. Metal dusting then proceeds but with a different mechanism involving internal graphitisation (i.e. similar mechanism to that proposed for nickel and cobalt).

The coke formed during this process showed steady state situation of the corrosion end products with small catalytic cementite particles producing carbon nanotubes. These different steps were summarised with thermodynamically consistent carbon activity curves, Figure 1.19 (b) [17]

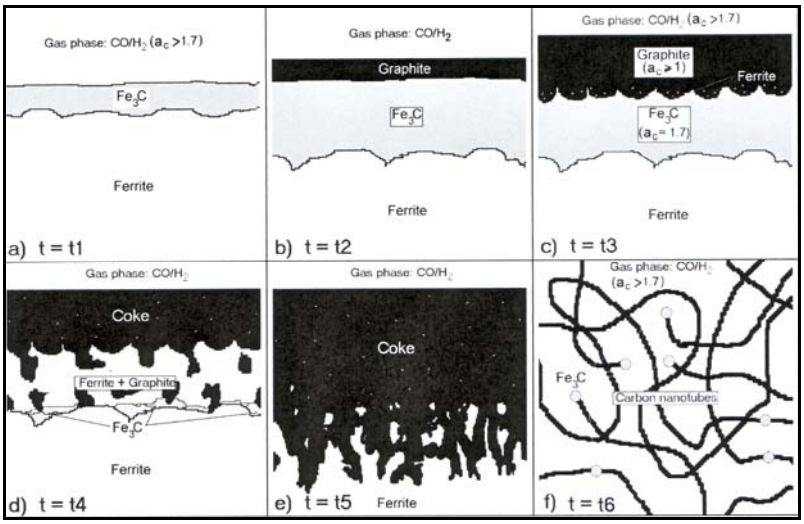

(a)

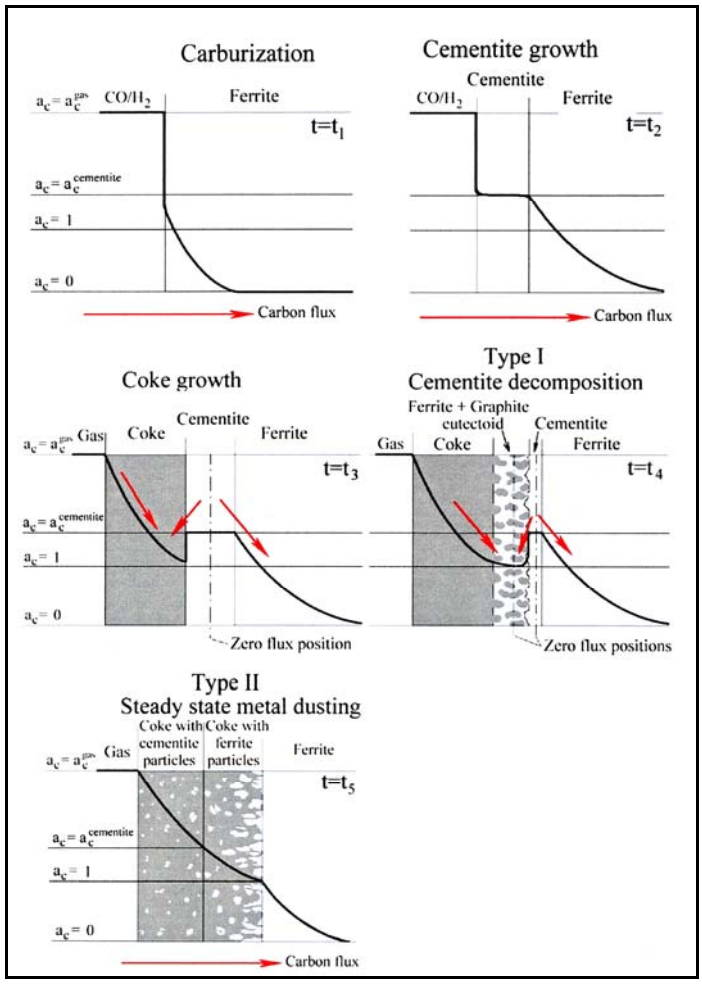

(b)

Figure 1.19 **(a) Proposed modification of metal dusting mechanism on pure iron and low alloy steels and (b) carbon activity profile and flux for that mechanism, Szakalos [17]**

Many researches have suggested other modifications to the original mechanism proposed for iron and low alloy steels [43]:

a. **Unreleased Stresses** were believed to play a role in metal dusting. Koszman [16] *as referenced in* [43] observed that metal dusting could proceed due to the presence of surface localised stresses. However, no conclusive study concerning the effect of stress has been published.

b. **Deposition of Carbon** on a catalytically active metal surface was thought to be a possible cause of metal dusting. Several studies concluded that carbon monoxide dissociation involved the removal of metal particles from the surface after the growth of graphite [43]. It was suggested that carbon monoxide is adsorbed and dissociates on the steel surface and that the dissociation is enhanced by surface defects and steps [47]. According to Hochman [48], metal dusting process starts with adsorption, then catalytic decomposition of CO (Boudouard reaction), followed by absorption of released carbon into the surface. This hypothesis could be supported by that it is difficult for graphite to nucleate directly from the gas phase even in high carbon activities. It is also well known that iron, nickel, and cobalt are very efficient catalysts that promote graphite nucleation and growth [17].

c. **Oxidation** role on the metal dusting process has not been fully understood. Many studies, however, have strongly suggested that metal dusting was significantly influenced by oxidation. Eberle *et al.* [19] *as referenced in* [43] reported that metallic particles and coke formation could be produced through exposing alloys to cyclic carburisation and oxidation. Interestingly, it was also observed that simultaneous carburisation and oxidation exposure would lead to damage that appeared similar to metal dusting. Perkins *et al.* [21] *as referenced in* [43] suggested that the metal dusting process is controlled by the simultaneous reaction of carbon and oxygen with chromium. Szakalos [17] proposed a mechanism that applies to high alloy steels and nickel-based alloys and it involves selective oxidation of alloyed carbides i.e. not pure cementite [49][50].

d. **Coke Structure:** Chun *et al.* [28] suggested that metal dusting aggressiveness on low chromium steels could be assessed based on the nature of the carbon formed. For example, the formation of crystallised carbon on steel provided diffusion paths

for iron atoms produced by cementite decomposition where the iron atoms diffused through the carbon to the gas environment and then acted to catalyse filamentous carbon deposition. However, if the carbon layer was amorphous, then the iron atoms would not be able to diffuse, except when the layer suffered cracking.

e. **Cementite Role:** Toh *et al.* [51] studied metal dusting of Fe-Cr and Fe-Cr-Ni alloys under cyclic exposures and observed that the cementite layer formed at the alloy surfaces has catalysed the carbon deposition. Carbon deposition was observed to have started only after the formation of a surface layer of cementite on pure iron exposed to carbon-containing gas.

f. **Driving Forces:** According to Zeng *et al.* [52], the suggested metal dusting mechanisms are not fully clear. Although Hochman [4] *as referenced in* [27], suggested that the final products of the metal dusting process are graphite and iron, cementite is usually detected. It is not clear what drives the cementite formation and decomposition under the same conditions of temperature, pressure, and gas composition. Zhang *et al*.[53] studied the influence of the gas composition on the final product of metal dusting of pure iron. Cementite and iron were detected in the coke when the iron was exposed to a gas mixture bearing low concentrations of carbon monoxide (e.g. 5%). Introducing more carbon monoxide (e.g. 30% or more), however, resulted in the presence of only cementite particles in the dust.

g. **Carbon Activity Level:** The metal dusting mechanisms for moderate carbon activities and high carbon activities were shown to be slightly different [42].

These modifications and comments have a strong potential to improve the current mechanisms. The effect of the oxygen partial pressure on the metal dusting mechanisms needs to be investigated in more details. Currently, the oxygen partial pressure is only considered to predict the establishment of stable oxide scales [43].

LeFrancois *et al.* (1963) [54] proposed a metal dusting mechanism of stainless steel in which reduced nickel, iron, or exposed metal activates the carbon-producing reactions leading to carbon diffusion into the steel matrix and causing $Cr_{23}C_6$ precipitation, initially at grain boundaries. It was also proposed that direct reaction of chromium in the steel with carbon monoxide could produce chromium carbides:

$$23/6\ Cr + C \leftrightarrow 1/6\ Cr_{23}C_6 \quad (1.29)$$

$$23/6\ Cr + 2CO \leftrightarrow 1/6\ Cr_{23}C_6 + CO_2 \quad (1.30)$$

As the grain boundaries become saturated with carbides, the carbon reacts with the chromium remaining in the grain leading to an appreciable change in the volume and as a consequence the grain is disintegrated from the steel at the grain boundary.

Figure 1.20 illustrates the metal dusting process of low chromium steel proposed by Chun *et al.* [28]. Carbon transfers from the gas and diffuses through the defects of the spinel oxide layer leading to localised metal wastage.

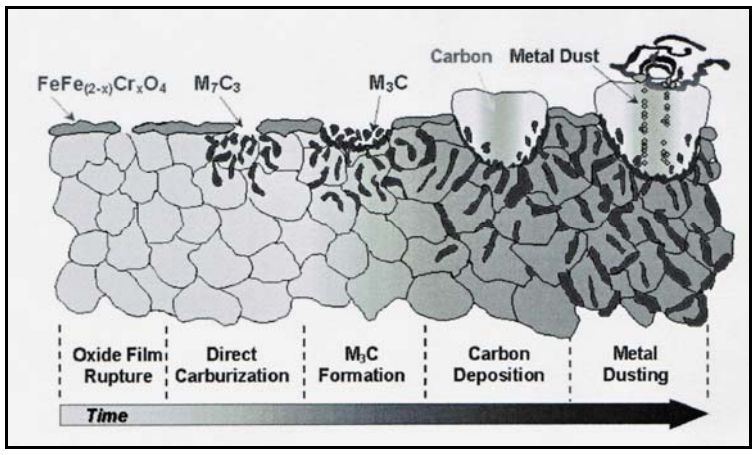

Figure 1.20 Schematic of the progression of metal dusting of low-chromium steel [28].

1.4.2 Metal Dusting Mechanism for Nickel and Nickel-Based Alloys

Nickel and cobalt are believed to exhibit similar behaviour in typical metal dusting environments but they behave differently from iron and low alloy steels.

The metal dusting mechanism of nickel and cobalt was first described by Hultgren *et al.* in the 1950s [17]. Hochman [6,7] *as referenced in* [43] also proposed a mechanism, for metal dusting of nickel and cobalt, similar to the one he proposed for iron. He suggested the presence of metastable carbide although its existence has never been proven. He stated that " …at some point in the reaction sequence, there may be highly metastable or activated

complexes of the carbides of these metals, but they must deteriorate rapidly, since carbides cannot be identified in the corrosion products in the work performed to date…" [55].

As seen in the Ellingham–Richardson diagram (Figure 1.21), the shaded area represents the typical metal dusting environment. The oxides within or below the marked area are thermodynamically stable in metal dusting conditions. According to this diagram, nickel and cobalt do not form protective oxide layers in metal dusting conditions. Furthermore, they do not form carbides (Figure 1.4) because of a highly positive free energy of formation throughout the metal dusting temperature range. However, they dissolve carbon and stabilise graphite and they also have strong catalytic properties on carbon monoxide dissociation. Iron or low alloy steels, however, form metastable cementite having slightly positive free energy [17].

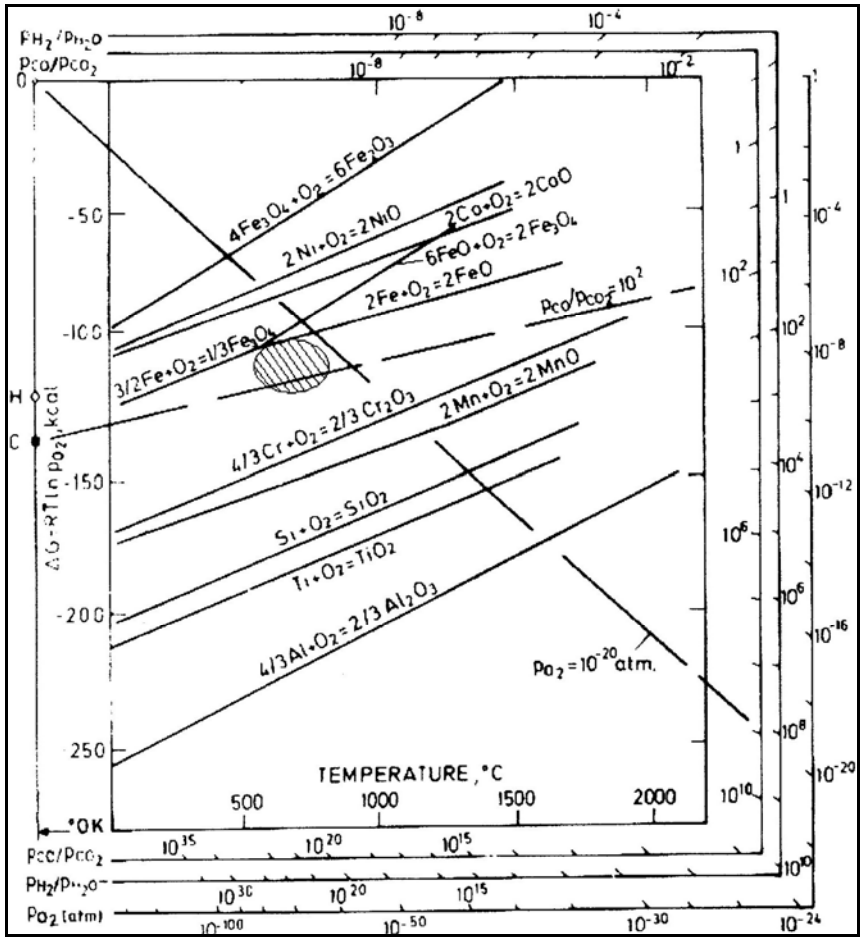

Figure 1.21 **Ellingham–Richardson diagram for some oxides. The shaded area represents a typical metal dusting environment [17].**

Unlike iron and low alloy steels, the metal dusting process in nickel and nickel-based alloys does not involve the formation of metastable carbides. Instead, the alloy disintegrates by direct inward growth of graphite into the supersaturated structure.

Grabke [21] has described the metal dusting mechanism for nickel-based alloys [17][40][43]. Carbon atoms transfer from the gas and diffuse through defects in the oxide layer. The diffusion of carbon atoms into the alloy leads to the formation of a carbon-supersaturated solution in the nickel matrix. Next, graphite deposits, in different orientations, on the alloy surface and starts to grow inward. The graphite growth is caused by carbon atoms from the solid solution attached to the graphite planes growing vertical to the alloy surface. This initiates degradation of the alloy and, as a result, metallic particles are released. The metallic particles, which are relatively large (~100nm), transfer into the coke layer. These particles are less active catalysts for coke formation than the iron particles and, accordingly, the coking rate on nickel is much lower. Finally, graphite continues to deposit from the gas mixture on the catalytically active surfaces [17][40][43][44]. Figure 1.22 shows the two proposed mechanisms for high chromium steels and Fe-Cr-Ni alloys [17][21]. It is thought the inward growth of graphite "roots" or "tongues" into the metal during the metal dusting lead to compressive stresses and metal particles are pressed outward [56].

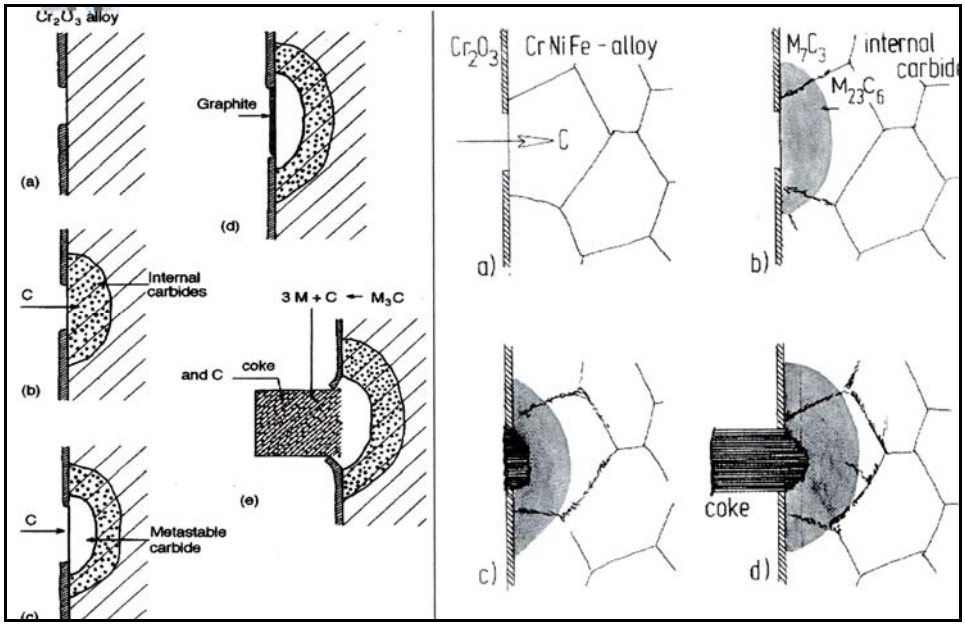

Figure 1.22 Schematic of the metal dusting mechanisms proposed on high chromium steels (left) and Fe-Cr-Ni alloys (right),Grabke [17].

The metal dusting mechanism for nickel and nickel-based alloys is generally accepted by most researchers. However, there is another mechanism that was proposed by Pippel *et al.* [16,17] *as referenced in* [17] for iron and nickel. This mechanism involves metal dissolution and diffusion into the graphite. It was further discussed by Chun *et al.* for iron and cobalt [17][57][58][59].

The addition of nickel to iron leads to a change from one mechanism to the other and, as a certain amount of nickel is added to iron, the formation of the metastable cementite is inhibited. The mechanism change is experienced when the nickel content in the alloy reaches 40%. At that level, it was observed that cementite did not form after exposure to metal dusting environment at 650°C. However, Transmission Electron Microscope analyses indicated that the mechanism had already changed at Ni > 10% [21]. Interestingly, Pippel *et al.* [44] also observed that the mechanism change in Fe-Ni system occurred even at a lower nickel concentration (Ni ~ 5%). Moreover, Pippel *et al.* [2] studied the micro-mechanisms of metal dusting of iron (HK 40) and nickel (Inconel 600) based alloys (Figure 1.23) [2].

Motin *et al*. [60] showed that cementite layer would not form if 10 wt % germanium is added to iron. The Fe-10 wt %Ge alloy exposed at 680ºC to the gas, CO-H_2-H_2O (a_c = 2.9), formed no cementite and the carbon deposited directly on the metal surface. The alloy was attacked by inward growth of graphite, in the same manner as nickel-based alloys. Metal consumption and graphite growth were, however, more rapid than pure iron case.

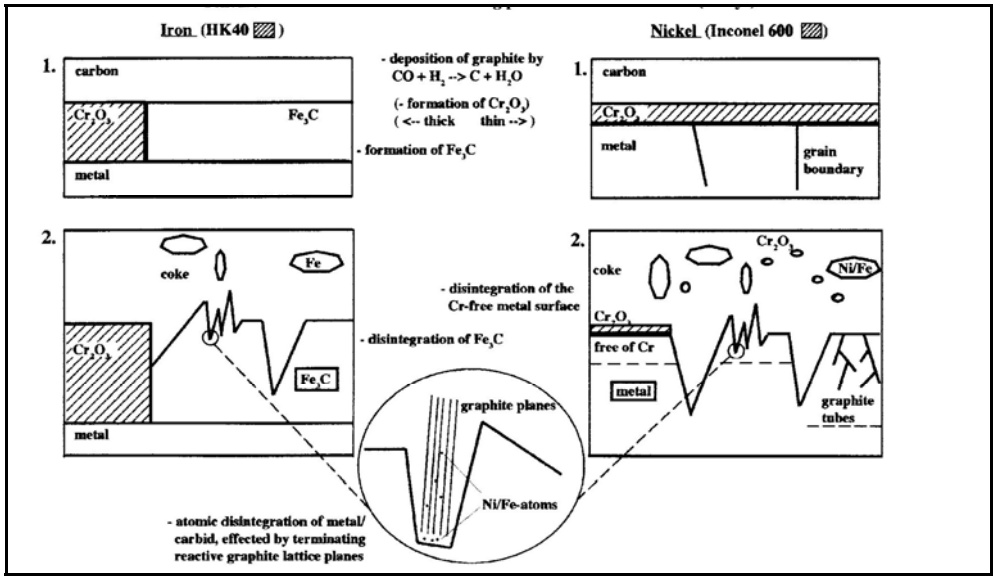

Figure 1.23 Schematic of the metal dusting mechanisms of iron and nickel-based alloys [2]

Different mechanisms of metal dusting were proposed by Zeng *et al.* [52] for both iron and nickel-based alloys, see Figure 1.24. It was suggested that metal dusting mechanism of iron involves carbon transfer from the gas and deposition on the iron surface. The carbon then dissolves into the alloy to form a cementite layer which causes a volume increase of about 10% leading to defects in the cementite layer. Next, the carbon diffuses through the cementite and precipitates at the defects causing the cementite to crack and separate. Consequently, the gas penetrates into the cracked areas and the resultant carbon deposition leads to the formation of more cementite and accordingly further metal dusting. Finally, the carbon continues to precipitate under the cementite particles and grows to carbon filaments [52][61].

On the other hand, in nickel-based alloys (Figure 1.24 (b)), it was proposed that carbon deposits on the surface of nickel and then dissolves and diffuses to precipitate and accumulate at defects causing the nickel particles to separate. The gas, in turn, penetrates the cracked areas and deposits carbon leading to more metal dusting. The carbon continues to precipitate under the nickel and becomes a carbon filament. The decrease of free energy from highly disordered carbon to well-crystallized carbon was suggested to be the driving force for both catalytic growth of carbon filaments and metal dusting [52].

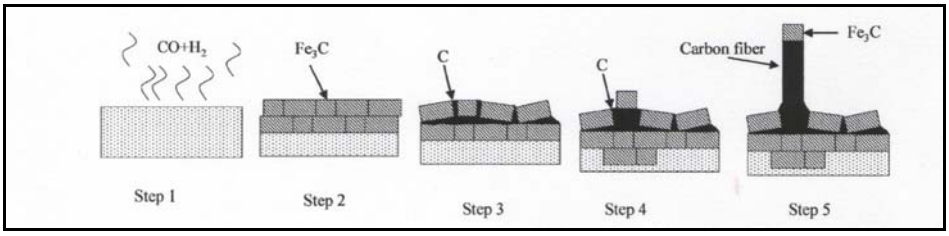

(a) Process of metal dusting in iron-based alloys

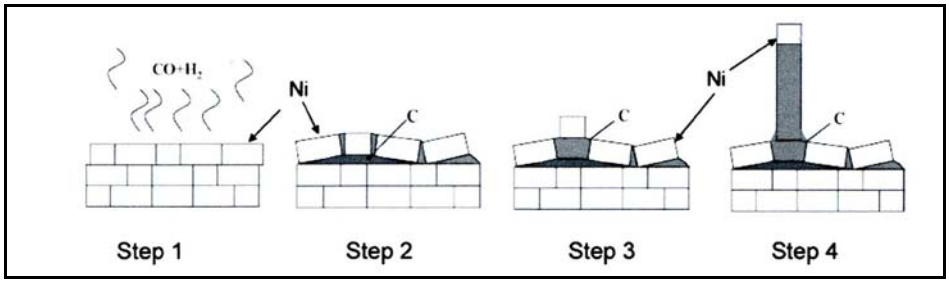

(b) Process of metal dusting in nickel-based alloys

Figure 1.24 A mechanism, proposed by Zeng *et al.*, for metal dusting of both iron and nickel-based alloys [52].

In conclusion, it is obvious that there is a still no universal agreement on metal dusting mechanisms [5]. Zeng *et al.* [9] *as referenced in* [17] concluded that the mechanisms of metal dusting are not fully understood although they have been studied for more than fifty years. Further researches are needed to gain a better understanding of the mechanisms, particularly in high alloy metals. Grabke [62] emphasised that the complex processes in the metal dusting of iron and steels are not completely recognised. Gabriele *et al.* [12] stated that understanding metal dusting of nickel-based alloys still lacks precision and reliability.

1.5 Alloys Performance in Metal Dusting

Many researches have been carried out to study the performance of various alloys in metal dusting conditions. The typical chemical compositions of the alloys are tabulated in Tables 1.1 and 1.2.

In 1945, Camp *et al.* [183] *as referenced in* [1] investigated the metal dusting behaviour of stainless steel type 304 at 704-870°C for 20h in petroleum naphtha in a simulated superheater environment. The metal wastage rate varied from zero at 704°C and 870°C to 53 mm/year at 760°C.

Eberle *et al.* [181] *as referenced in* [1] investigated the behaviour of sixteen nickel and iron-based alloys at different locations in a waste heat boiler for 14 and 41days respectively. The temperature in the system varied within the range 370-927°C and the total gas pressure was 2.17MPa. Metal dusting rate was generally the highest at 593-704°C with stainless steel type 446 showing a good resistance.

Prange [179] *as referenced in* [1] tested different alloys in a butane dehydrogenation process environment at 600°C. Some alloys showed good resistance to metal dusting, namely: 31Cr-9Ni, 30Cr-65Co-4W, 24Cr-15Ni, 20Cr-10Ni-3.6Mo, 18Cr-12Ni-2.5Si, and 27Cr alloy. However, alloys 20Cr-3Ni, 18Cr-11Ni, 17Cr-13Ni-2Mo, 12Cr, 9Cr-1.4Mo, Fe-Ni, and 14Si-Fe exhibited poor resistance and suffered severe metal dusting.

Wolfe [143] *as referenced in* [1] studied the performance of engineering alloys in H_2-CO-H_2O at 649-816°C and pressures 345-1,034KPa. The alloys were stainless steel types 202, 302, 316, 347, 16Cr, and 18-18-2, Cb-3, copper alloy 400, Nichrome, Chromal,

Alumel, Constantan, C-4, X, 601, 811E, and 702. All the tested alloys experienced localised metal dusting, except copper alloy 400 and alloy 702 which, however, exhibited good resistance to metal dusting.

Grabke *et al.* [103] *as referenced in* [1] tested 13 commercial alloys in H_2-CO-H_2O mixtures at 450,500,550, and 600°C for 3-28days. The best resistance to metal dusting was observed on the alloys 18Cr-1.3Si-1Al, X18CrN28, and 25Cr-7.2Mn-3Ni. Furthermore, the performance of high nickel alloys in metal dusting was suggested to have been improved by the addition of more chromium.

Grabke *et al.* [63] studied the behaviour of alloys including stainless steel type 304, 17Cr-10Mn, 153MA, and alloy 800 in metal dusting condition (H_2-24%CO-2%H_2O at 600°C). As a consequence, all the alloys suffered metal dusting but in different degrees. Interestingly, alloys possessed fine grain microstructure or deformed surface exhibited less metal dusting.

Gommans *et al.* [84] *as referenced in* [1] evaluated nine commercial alloys by placing them in a waste heat boiler and superheater of an ammonia plant for 19,000-25,000h. The alloys were DS, stainless steel type 310, stainless steel type 310Si, alloy AC66, Fe-18Cr-17Ni-5Si, Fe-18Cr-20Ni-5Si-Cu/Mo, 253MA, 353MA, and Pack aluminised TP 304 stainless steel. Metal dusting occurred on the all alloys but the Pack aluminised TP 304 stainless steel.

Stahl *et al.* [71] *as referenced in* [1] investigated the performance of alloys 617 and 601 in a mixed gas environment (a_c = 3.6) at 620 and 660°C and a pressure of 3.4MPa for an undisclosed time. Both alloys experienced localised metal dusting..

Shibasaki *et al.* [72] *as referenced in* [1] reported results on metal dusting behaviour of stainless steel types 304, 321, and 310S, Incoloy 800H, 32X, Inconel 600, Inconel 601, Inconel 625, HP-Nb & HP-Nb-Ti, 20Cr-32Ni-Nb, and Filler Metal 82. The alloys were evaluated at a transfer line of a reformed gas reheater in a direct iron ore reduction plant at 444-875°C and a pressure of 5atm. The environment was a gas mixture of 15%CO-9.2%CH_4-10%H_2O-1%CO_2. Exposing the alloys for several months resulted in metal dusting on stainless steels 304 and 321, and alloys 600 and 601

Maier *et al.* [64] tested P91, stainless steel type 410, stainless steel type 310, and a model alloy (12Cr-2.75Si) in an environment that contained a mixture of 73.2%H_2-24.4%CO-2.4%H_2O at 560°C and 1.5bar for 200h. P91 and stainless steel type 410 suffered metal

dusting before 25h whereas stainless steel type 310 and the model alloy did not show metal dusting after 200h.

Klower *et. al*. [18] exposed commercial alloys to metal dusting conditions at 650°C for up to 10,000h. The alloys were Incoloy 800H, HK40, HP40, DS, alloy 600, alloy 601, C-4, 214, HR-160, 45-TM, alloy 602CA, alloy 617, and alloy 690. In the first 5,000h, the gas composition was 24%CO-74%H_2-2%H_2O and in the second 5,000h, the composition was changed to 49%CO-2%H_2-49%H_2O. The least metal wastage rates were observed on the alloys 45-TM, 690, and 602CA (Figures 1.25-1.27).

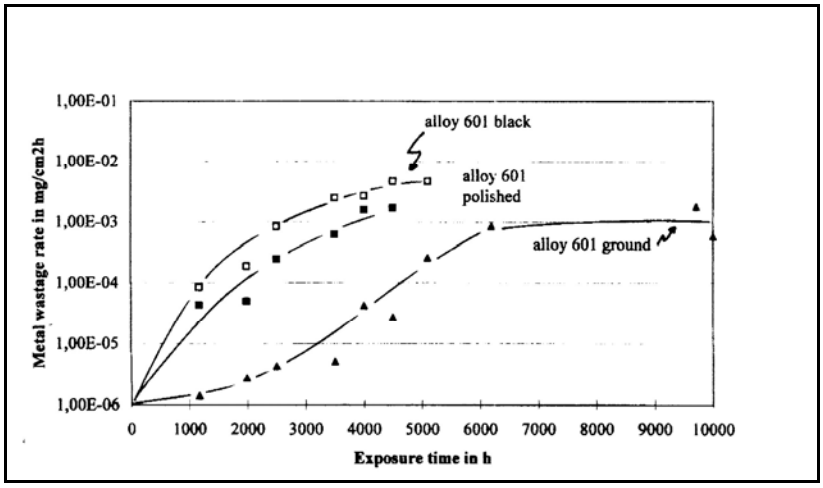

Figure 1.25 **Metal dusting of alloy 601, with different surface conditions, after exposure to CO-H_2-H_2O gas at 650°C [18].**

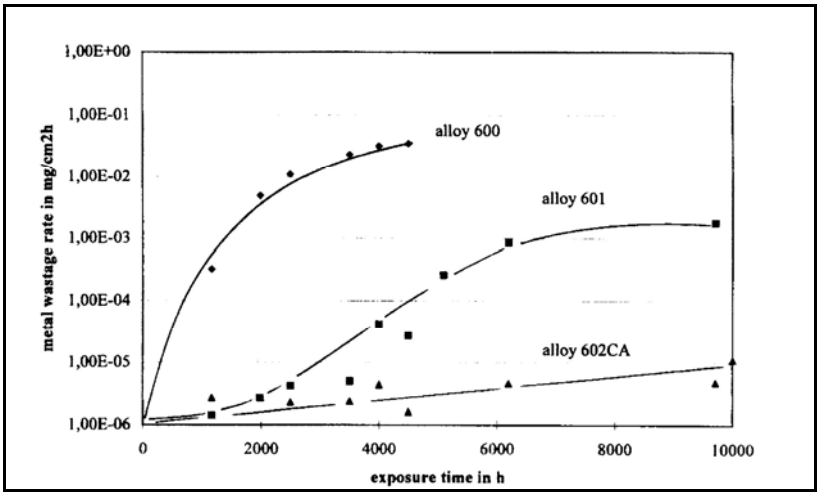

Figure 1.26 **Metal wastage rate for nickel-based alloys exposed to CO-H_2-H_2O gas at 650°C [18].**

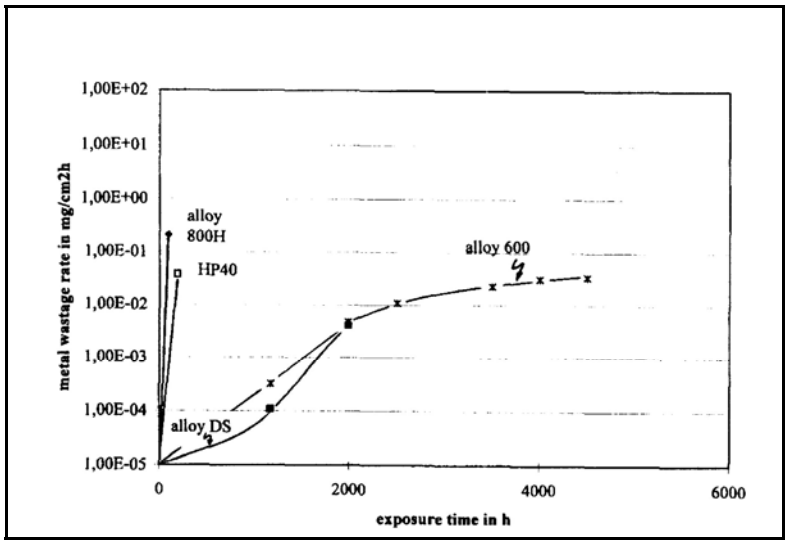

Figure 1.27 **Metal dusting of iron-based alloys in comparison to the nickel-based alloy 600H after exposure to CO-H_2-H_2O gas at 650°C[18].**

Levi *et al.* [9] investigated the behaviour of stainless steel type 316 by exposing it to 75%H_2–25%CO at 450-650°C in 1.0MPa and 2.0MPa. The metal dusting became more aggressive as the temperature or pressure or both were increased.

Baker *et al.* [24] evaluated several alloys at 621°C and 1atm for up to 8,600h in 70%CO-25.25%H_2-4%CO_2-0.75%H_2O. The alloys were 9Cr-1Mo, 690, 825, 800, 330, 803, 864, 600, 601, 263, MA956, K500, DS, and 617. Figure 1.28 shows the weight change for the alloys that experienced pitting. Alloys 690, 617, MA956, and 263, however, exhibited the best resistance to metal dusting [4][24].

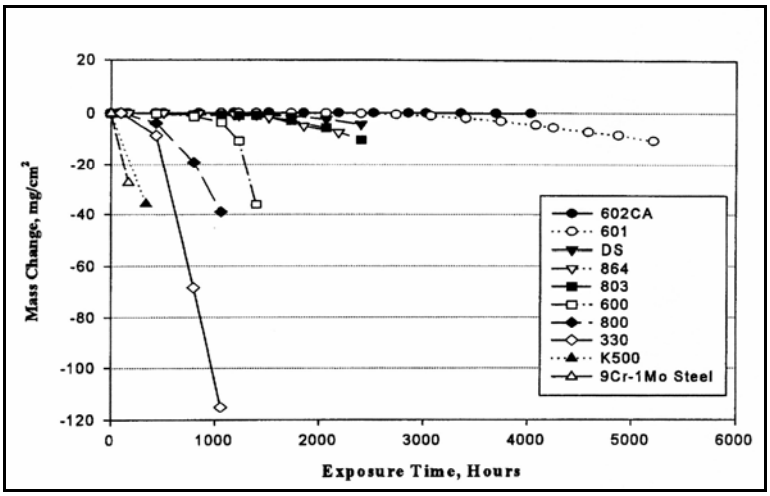

Figure 1.28 **Mass change due to exposure to H_2-80%CO at 621°C for alloys that formed pits during the experiment [4].**

The performance of alloys 754, TD, 600, 758, 400, 693, 602CA, 625LCF, 601, 690, 276, 671, 617, 263, 825, DS, 330, 803, 864, 800/800HT, and 956 in metal dusting conditions was evaluated by Baker *et al.* [15]. The experiment was carried out in CO-20%H_2 gas at 621°C for 16,000h. Alloy 693 exhibited the best performance; see Figures 1.10 and 1.11.

Fabiszewski *et. al.* [20] tested six commercial alloys in 99.99%CO and 90%CO-10% H_2 atmospheres for four weeks at 482, 566, 649, and 732°C and a pressure of 2.2atm. The alloys were stainless steel types 304 and 310, alloys RA85H, 800H, 601, and RA333. Metal dusting attack was generally more aggressive in 90%CO-10%H_2 although, in pure CO, pitting was observed on four of the alloys exposed at 482°C. In 90%CO-10% H_2, however, five alloys suffered pitting at 482°C. The exposure to this gas at the higher temperatures also led to metal dusting on stainless steels 304, 310, and alloy 800H and the aggressiveness of the attack increased with temperature. No metal dusting was observed on the alloys at 732°C in 90%CO-10%H_2.

Toh *et al.* [51][65] studied metal dusting of Fe-Cr and Fe-Cr-Ni systems under cyclic conditions. Model alloys used were Fe-25Cr, Fe-60Cr, Fe-25Cr-2.5Ni, Fe-25Cr-5Ni, Fe-25Cr-10Ni, and Fe-25Cr-25Ni. The alloys were exposed to a mixture of 68%CO-26%H_2-6%H_2O at 680°C and were under thermal cycling; heating for 60min and cooling for 15min. The thermal cycling led to spallation of Cr_2O_3 scale and depletion of chromium from the alloy substrate that aggravated metal dusting (Figures 1.29 and 1.30). The attack was localised on the low nickel alloys and more general on the high nickel alloys [51].

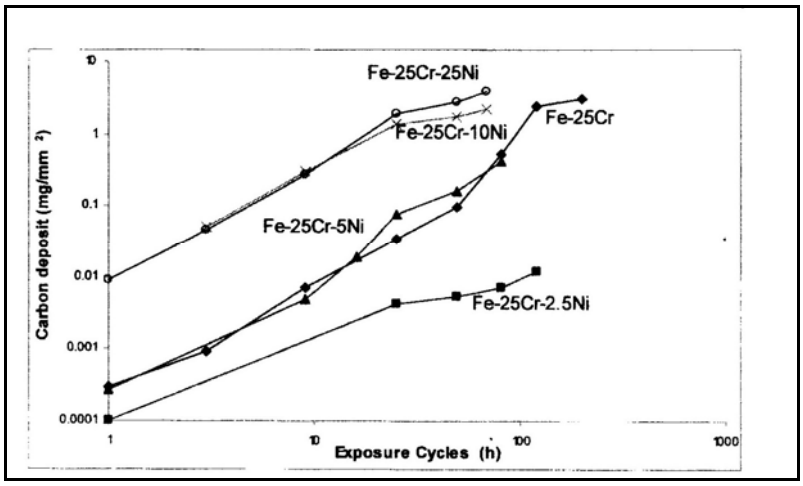

Figure 1.29 Carbon deposition rate of the model alloys [51].

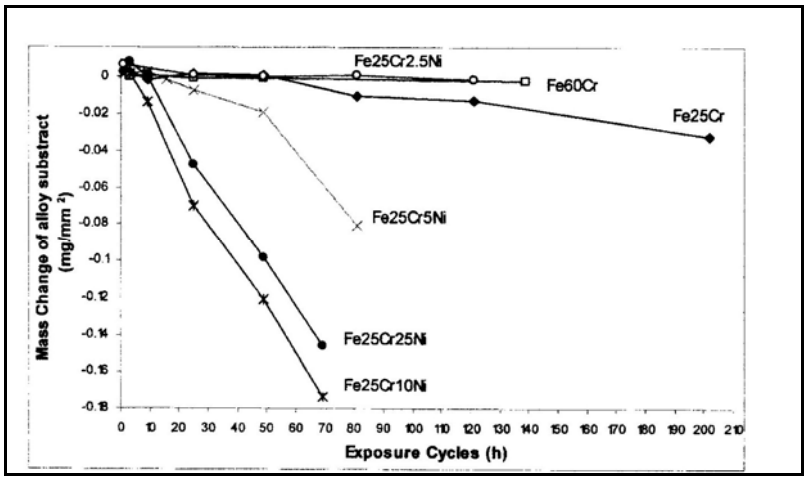

Figure 1.30 Mass change of the alloys due to the exposure to the metal dusting condition [51].

Muller *et al.* [35] explored the metal dusting resistance of welded alloys (i.e. 800, 600H, 601H, and 602CA). Samples with welds were exposed at 600°C and 650°C in a gas containing H_2-24%CO-2%H_2O for 1624.5h to 2604.5h. The iron-based alloy (i.e. alloy 800) experienced rapid carbon deposition and metal dusting and the experiment had to be interrupted after 24h. The Heat Affected Zones (HAZ) were severely attacked by metal dusting due to the re-crystallisation caused by welding process. Moreover, the weld materials of all samples were also attacked.

Bruyn *et al.* [66] evaluated alloys in a secondary reformer feed gas for six months. The alloys were 600, 810, stainless steel type 310, 601, 602CA, and 50Cr-50Ni. The environment was estimated to contain 7%CO_2-4.8%CO-34.5%H_2-22.9%CH_4-1.8 %N_2-26.3%H_2O. The operating temperature and pressure were 620°C and 2.6MPa respectively. The results showed that metal dusting resistance increased with chromium concentration in the alloys. The alloys were ranked as follows (increasing metal dusting resistance): 600, 810, stainless steel 310, 601, 602CA, 50Cr-50Ni.

The performance of several nickel-based alloys was evaluated by Klarstrom *et al.* [67]. The alloys, namely HAYNES 214, 230, HR-120, HR-160, Inconel 601, and Incoloy 800H were exposed to a mixture of 49%CO-49%H_2-2%H_2O at 650°C for periods up to 10,000h. Alloys HR-120 and 800H, which contain high iron levels, suffered severe metal dusting within the first 1,000 hours. However, the resistance to metal dusting improved with increasing the nickel concentration. Furthermore, the addition of 22-23% chromium at the expense of nickel was extremely effective because of its role in forming and, more importantly, maintaining a protective oxide scale. The presence of tungsten and

molybdenum in alloy 230 was thought to considerably have improved the alloy performance in metal dusting. HR-160 exhibited the best resistance to metal dusting due to its high contents of nickel, chromium, and silicon. The behaviour of some of the alloys is plotted in Figure 1.31.

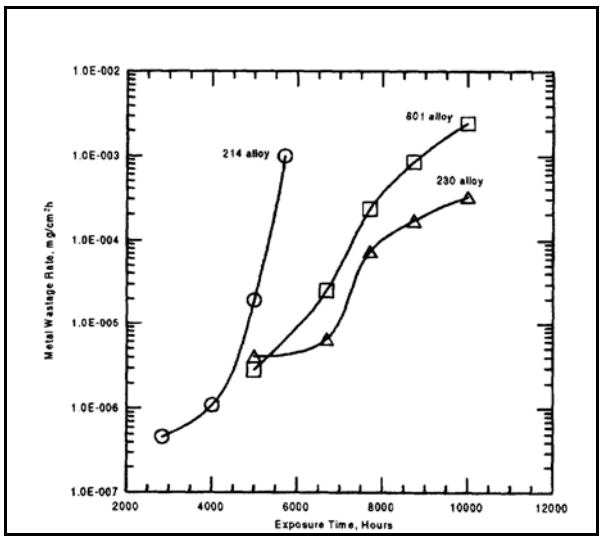

Figure 1.31 Metal wastage rate of three alloys in 49%CO-49%H_2-2%H_2O gas at 650°C [67].

Nishiyama *et al.* [22] evaluated alloys 600 and 690 in a gas composed of CO, CO_2, H_2O, and H_2 at 650°C for 200h. The findings showed that alloy 600 underwent metal wastage associated with carbon deposition. Alloy 690, on the other hand, exhibited no metal dusting at all.

Di Gabriele *et al.* [68] studied metal dusting of alloys 601, 603XL, 617, 671, 690, and 890 in a 20%H_2-80%CO mixture at 650°C for 100h. Specimens placed in ceramic crucibles, which contained impurities such as Fe_2O_3, suffered metal dusting whilst those suspended from a quartz hanger were almost intact. The presence of Fe_2O_3 impurities was thought to have catalyzed carbon deposition from the environment. For most alloys, it seemed that the formation rate of protective Cr_2O_3 scale was not fast enough to prevent carbon ingress into the alloys.

Schneider *et al.* [29] investigated metal dusting of binary Fe-Al systems in CO-H_2-H_2O at 500-700°C. The alloys were Fe-15 at.% Al, Fe-26 at.% Al, and Fe-40 at.% Al. Addition of aluminium was beneficial and led a reduction in metal dusting (Figures 1.32-1.34).

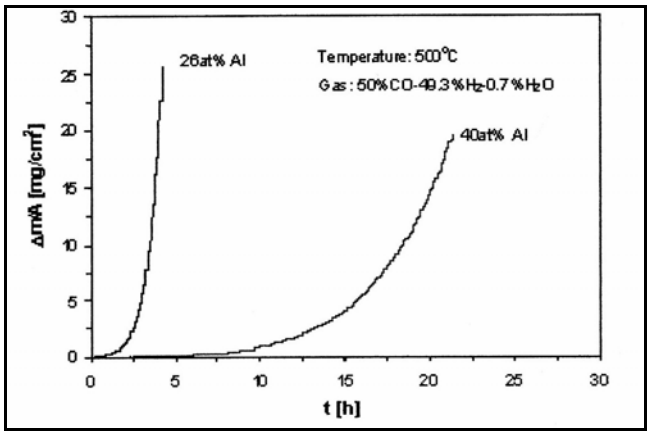

Figure 1.32 **The influence of aluminium content on alloy performance in metal dusting environment at 500°C [29]**

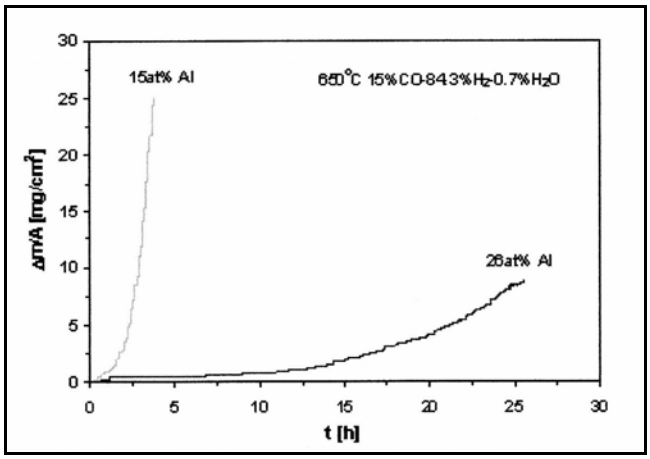

Figure 1.33 **The influence of aluminium content on alloy performance in metal dusting environment at 650°C [29]**

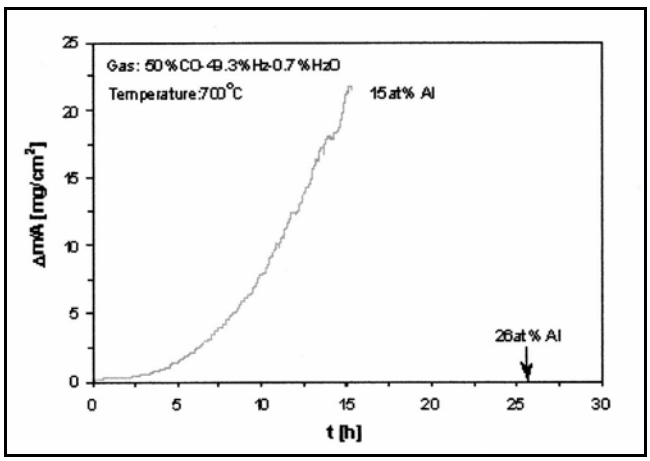

Figure 1.34 **The influence of aluminium content on alloy performance in metal dusting environment at 700°C [29]**

From the researches reported previously, it is obvious that there is a still no standardised testing protocol or procedure for metal dusting [1].

It should also be pointed out that most of the lab researches were carried out in controlled conditions where only one parameter was changed at a time. Accordingly, the results would not be expected to predict the simultaneous interaction between parameters such as those encountered in real plant life.

Furthermore, the experimental conditions selected for metal dusting research are intended to produce fast results within a certain time frame and relating such data to plant experience is extremely difficult. This gap might be bridged if a reliable simulation to plant conditions could be achieved in researches [43].

In labs, for example, the samples are usually unstressed unlike the case in plant where the alloys are under stress and the resulting strain may lead to damages in the protective oxide scale leading to the onset of metal dusting [69].

In some cases, the plant experience appears to contradict some of the research results. For instance, in plant metal dusting conditions, alloy 800 has been found to behave much better than the nickel-based alloy 600 (as reported by Holland *et al.*) [25]. This is clearly different to some of the research results.

Table 1.1 Chemical composition of wrought alloys, wt. %.

Alloy	C	Fe	Cr	Ni	Si	Mn	Ti	Others
Alloy Cb-3	0.06	36	20	33	1	2	….	1Ta, 2Mo, 3Cu, 1Nb
9Cr-1Mo steel	0.1	89	9	….	….	0.5	….	1Mo
P91 Steel	0.1	88	9	0.26	0.36	0.4	….	0.9Mo, 0.05N, 0.2V, 0.07Nb
12CrMoV lo steel	0.2	86.5	10.4	0.66	0.27	0.5	….	0.25V, 0.8Mo,0.02N, 0.01Nb
12CrMoV hi steel	0.19	86	11.2	0.66	0.32	0.5	….	0.25V, 0.9Mo
1 1/4Cr-1/2Mo steel	0.11	bal	1	….	0.72	0.4	….	0.5Mo
5Cr-1/2Mo steel	0.08	bal	4.8	….	0.38	0.4	….	0.5Mo
17Cr-10Mn	….	….	17	2.5	0.2	10.5	….	2Cu
153MA	0.05	….	18.5	9.5	1.4	0.06	….	0.2Mo,0.15N, 0.04Ce
Stainless steel 446	0.2	75	26	0.3	1	1.5	….	….
Stainless steel 202	0.15	68	18	5	1	10	….	0.25N
Stainless steel 347	0.08	68	17	11	1	2	….	0.8Nb+Ta
Stainless steel 321	0.08	68	18	11	1	2	0.15	….
Stainless steel 446 (X18CrN28)	0.2	bal	28	….	1	1	….	0.2N
Stainless steel 430 (X10CrA118)	0.12	bal	11	….	1	1	….	….
Stainless steel 304	0.08	70.3	18.8	8.3	0.6	1.8	….	….
Stainless steel 310	0.04	51.4	25.9	20.5	0.6	1.5	….	….
Stainless steel 410	0.1	85	12	….	0.2	0.5	….	1Mo, 0.1W,0.3V
Stainless steel 309	0.05	62	23	13	0.8	….	….	….
Stainless steel 310S	0.08	bal	25	21	1.5	2	….	….
Stainless steel 310Si	0.2	bal	25	21	2.50	2	….	0.1N
Stainless steel 302	0.1	72	18.5	8	0.5	….	….	0.05N
Incoloy 800/800HT	0.07	45	21	32	0.1	1	0.4	0.4Al
Incoloy 800H	0.1	46	20	32	0.5	….	0.4	0.4Al, Al+Ti < 0.7
Incoloy MA 956	0.05	75	20	….	….	….	0.5	4.5Al, 0.5Y_2O_3
Incoloy 825	0.01	29	22	42	0.1	0.4	1	0.1Al, 3Mo
Incoloy DS	0.08	41	16	37	2.3	1	….	….
Incoloy 330	0.07	44	19	35	1.3	1	….	….

Table 1.1, Cont.

Alloy	C	Fe	Cr	Ni	Si	Mn	Ti	Others
Incoloy 803	0.08	36	27	34	0.8	1	0.4	0.4Al
Incoloy 864	0.03	39	21	….	0.8	0.4	0.6	0.3Al, 4.2Mo
Incoloy 890	0.07	27.4	25	42.5	1.8	1	0.2	0.1Al, 1.5Mo, 0.4Nb
Incoloy 810	0.25	bal	21	32	0.8	0.9	….	0.5Cu
Inconel 693	0.02	4	29	62	….	….	0.3	3Al, Zr, 0.7Nb
Inconel 702	0.4	0.35	16	bal	0.2	0.05	0.7	0.1Cu,3.4Al
Inconel 601	0.05	13	23	60.5	0.2	1	0.4	1.4Al
Inconel 602 CA	0.2	9.5	25	60	0.1	…	0.1	0.1Y, 2Al
Inconel 690	0.02	9	29	59	0.1	1	0.3	0.3Al
Inconel 617	0.08	1	22	55	0.1	….	0.4	9.7Mo,1.2Al, 12.5Co
Inconel 600	0.08	8	15.5	72	0.3	0.3	0.3	0.3Al
Inconel 600H	0.1	9	16	72	….	….	….	….
Inconel MA 754	0.07	….	20	78	….	….	0.5	0.3Al, $0.5Y_2O_3$
Inconel MA 758	0.05	….	30	67	….	….	0.5	0.4Al, $0.5Y_2O_3$
Inconel 625	0.02	2.5	21.5	61	0.1	….	0.2	9Mo, 0.1Al, 3.6Nb
Inconel 671	0.03	….	46	53	….	….	0.3	0.3Al
Inconel 603 XL	0.01	0.1	22.1	74	1.4	….	….	3Mo
Filler metal 82	….	1	20	73	….	3	….	2.5Nb
Incotherm TD	0.01	….	22	73	1.4	….	….	3Mo
Alloy 214	0.04	4	16	75.5	….	….	….	4.5Al, Zr,Y
Alloy X	0.1	18	22	47	1	1	….	0.6W, 9Mo, 0.008B, 1.5Co
Nichrome	….	23	15	62	….	….	….	….
Alloy 811E	….	bal	21	33	0.5	….	….	1.7Al
Alloy AC66	0.06	bal	27	32	0.15	0.4	0.01	0.025Al, 0.08Co, 0.8Nb
Alloy K-500	0.15	0.8	0.1	64	0.1	0.7	0.6	2.7Al, 29.5Cu
Nimonic 263	0.06	39	20	51	0.1	0.3	2.2	0.5Al, 5.9Mo
Monel 400	0.15	1.6	0.1	64	0.1	0.7	0.4	32Cu
Alloy C-4	….	….	16	68	….	….	….	16Mo

Table 1.1, Cont.

Alloy	C	Fe	Cr	Ni	Si	Mn	Ti	Others
Alloy HR 160	0.05	2	28	37	2.8	….	0.5	30Co
Alloy 45TM	0.08	23	27	47	2.7	….	….	Rare Earth
Alloy RA85H	0.13	60	19	15	4.6	0.4	0.03	0.05Mo, 1.2Al, 0.1Co
Alloy RA333	0.03	17.8	25.5	44.6	1.4	….	….	3.2W, 2.8Mo, 3.4Co
Alloy H46M	0.4	15	35	45	1.8	1	….	1Nb
Alloy RA330	0.05	43	19	35	1.2	….	….	….
Alloy HR 120	0.05	35	25	37	0.6	….	….	0.2N, 0.1Al, 0.7Nb
Alloy RA253MA	0.08	65	21	11	1.7	….	….	0.17N, 0.04Ce
Alloy RA353MA	0.05	36	25	35	1.2	….	….	0.16N, 0.05Ce
Alloy 230	0.1	3	22	bal	0.4	0.5	….	0.3Al, 2Mo,14W,0.02La, 5Co
Chromal	….	….	10	90	….	….	….	….
Constantan	….	….	….	48	….	….	….	52Cu
Alumel	….	….	….	95	….	2	…	2Al

Table 1.2 Chemical composition of casting alloys, wt.%.

Alloy	C	Fe	Cr	Ni	Si	Mn	Nb	Ti	Others
HK 40	0.4	51	25	20	1.5	1.5	….	….	….
HP 40	0.45	37.5	25	35	1.5	0.7	….	….	….
HP Nb Mod.	0.4	35	25	35	1.5	1.5	1.5	….	….
HP Nb+Ti Micro.	0.45	35.5	25	35	1.5	1	0.8	0.16	0.08Zr, Rare earth
HP Si Micro.	0.45	34	25	35	2.6	1	0.8	0.12	0.02Mo, 0.04Zr, Rare earth
Alloy 45 Micro.	0.45	14	35	45	1.6	1	1.	<1	<1Zr, Rare earth
Alloy 45 LC	0.15	14.5	35	45	1.6	1	1	<1	<1Zr
Supertherm	0.5	13	26	35	1.5	….	….	….	5W, 15Co
HT	0.5	44	17	35	1.7	….	….	….	….
HU	0.5	40	18	38	1.7	….	….	….	….
NC-19,HOM-3	0.5	16	26	46	1.5	….	….	….	3Mo, 3W, 3Co
22H	0.5	16	28	48	1	….	….	….	5W

1.6 Control and Prevention of Metal Dusting

Although metal dusting cannot be completely prevented, it can be controlled by several means including the upgrade of the alloys, modification of the operating condition, application of coatings, addition of sulphur, and optimisation of metal processing. The metal dusting control methods described below are not the same for each case because of the inexactly defined conditions causing metal dusting and the different behaviour of almost each alloy in metal dusting conditions [26].

1.6.1 Materials Selection

Both iron and nickel-based alloys are susceptible to metal dusting, but from different mechanisms, kinetics, and to different extents. In general, nickel-based alloys (Ni ~50%) impart better resistance to metal dusting owing to the low carbon diffusivity and solubility in nickel. The addition of scale and carbide-forming elements such as Cr, Si, Al, Nb, Mo, W, and Ti improves the resistance of nickel-based alloys to metal dusting (Figure 1.14). But, nonetheless, the adverse effect of adding such elements on the alloy properties must be taken into account and they must be added carefully in specific amounts. The addition of relatively high concentrations of Ti, for instance, may lead to the formation of internal oxides that weaken the alloy. The presence of high amounts of W and Si in an alloy may degrade desirable properties such as ductility and toughness [70][71][72][73].

Zhang *et al*. [74] reported that the addition of copper in appropriate concentrations to stainless steel types 304 and 310 and incoloy 800H resulted in an improved metal dusting resistance. The addition of copper decreased the internal carburisation by lowering the carbon solubility in the austenite.

The formation of protective oxide scale (such as Cr_2O_3) slows down metal dusting by blocking carbon diffusion into the alloy. Aluminium addition is also desirable as it leads to the formation of a protective aluminium oxide scale or sub-scale. The carbide-forming elements such as Nb, Mo, and W work to immobilise carbon through the formation of

carbides and hence delay the onset of metal dusting by delaying the saturation of the alloy matrix [14][18][21][73].

Some investigation suggested that the presence of aluminium in the alloys helped in the formation of protective chromium-rich scales by immediate passivation of the surface by a thin Al_2O_3 film in the carburising environment [56]. In short, it is believed that carbon diffusion is not possible through perfect, dense oxide layers and it can only take place if the layers experience pores or fissures [75].

It has been reported that the oxide scale became less protective when the Ni/Fe < 2/3 [76]. It was also thought that metal dusting performance of heat-resistant alloys (e.g. HK 40) is adversely influenced by aging at high temperatures as the alloys experience more precipitation of chromium-rich carbides as well as brittle sigma phase (rich with chromium and iron) leading to chromium depletion in the surrounding matrix adjacent to such phases. The precipitation of carbides and sigma phases are functions of time and temperature [77].

It is well recognized that metal dusting resistance is drastically improved by adding sufficient amounts of chromium to the alloys. Indeed, nickel-based alloys with 25%Cr or higher experienced no severe metal dusting even after 10,000h at 650°C [18]. Interestingly, austenitic stainless steels having similar chromium levels as ferritic steels were found to be less resistant to metal dusting and that was most probably due to the lower chromium diffusivity in the austenitic matrix [21].

Higher nickel and chromium concentrations are needed to improve metal dusting resistance of cast alloys where the microstructure is relatively inhomogeneous and suffers phase segregation. It was recommended to keep the nickel and chromium levels well above 40% and 25-30% respectively. Addition of 1.5-2.5% silicon as well as aluminium and rare earth is also important [40][78].

A qualitative criterion to predict the tendency of occurrence of metal dusting was proposed by Schueler [159] *as referenced in* [1]. He suggested a value for a "chromium equivalent" above which the material is likely to exhibit resistance to metal dusting. The chromium equivalent was $Cr_{equiv} = \%Cr + 2 \times \%Si > 22$. It was further revised by Schillmoller [126] *as referenced in* [1] and modified to $Cr_{equiv} > 24$. It was also later modified by Schillmoller [65] *as referenced in* [1] to $Cr_{equiv} = \%Cr + 3 \times (\%Si + \%Al)$. It should be borne in mined that this equation was proposed to be utilised as a qualitative ranking indicator of resistance to metal dusting [76].

Unfortunately, the precipitation of carbides and nitrides is not always useful and it may significantly shorten the attack incubation period and quicken the metal dusting onset. It is very possible that such precipitates form at the alloy surface leading to destruction of the of protective oxide scale. Equally, the presence of cerium, which is usually desired at higher temperatures, was proven to have a negative influence on the metal dusting behaviour (Figure 1.14) [21][79][80]. It was thought that cerium disturbs the formation of a continuous protective oxide layer in metal dusting environment. Moreover, the oxide scales may also fail by creep strain, thermal cycling, or defects [40]. Oxides are also known to be instable in metal dusting environments and they can be reduced by gases in which the oxygen partial pressure is very low [1][14][81]. Additionally, the chromium oxides do not easily form in the metal dusting temperature range (about 600°C) because of the quite low chromium diffusivity [10][21][63]. According to Grabke *et al.* [11], at temperatures below 650°C, a protective chromium oxide scale did not form quickly because of the slow chromium diffusion.

Heat-treating and petrochemical conditions are appreciably different as a typical heat treatment medium contains 39%N_2-19.8%CO-0.1%CO_2-40.4%H_2-0.2%H_2O-0.5%CH_4. Therefore, it is not obvious if the experience in heat-treating industries is applicable for petrochemical plants. The common alloys used in heat-treating furnace components are RA330, RA333, 601, 600, NC-11/22H, HT, HU, HK, HP, HL, and NC-14/Supertherm where the alloys RA333 and NC-14/Supertherm are considered the best. High nickel alloys are usually very susceptible to metal dusting in heat-treating industries and the addition of high nickel and/or chromium amounts was not enough to improve the alloys resistance. Interestingly, alloying with aluminium up to 4.5% was not beneficial and the pre-oxidation of the alloy surface offered no improvement and might even be harmful [7][82]. However, alloys with high chromium and silicon exhibited reasonable resistance to metal dusting. Tungsten addition may be useful as well [7][82][83].

1.6.2 Influence of Surface Condition, Grain Size, and Metal Processing

The competition between oxide formation and carbon ingress decides the start of metal dusting on an alloy. Nickel-based alloys with high chromium content show low carbon solubility and diffusivity and a relatively fast chromium diffusion [84].

Easy and fast diffusion of chromium toward an alloy surface is required to form and maintain a protective chromium oxide scale which in turn inhibits metal dusting. Ways investigated to enhance the chromium diffusivity near the alloy surface included grinding, polishing, machining, grit blasting, and shot peening (Figures 1.35 and 1.36). Alloys with fine grain microstructures also offered improved chromium diffusion rate. Figures 1.37 and 1.38 show that only some alloys exhibited a better metal dusting resistance as a result of grain size reduction. In fact, the chromium diffusivity in ferritic steels (i.e. BCC structure) is double that in austenitic steels (i.e. FCC structure) [5][21][85].

Surface working induces high number of dislocations near the alloy surface accelerating the chromium diffusion through the substrate [85]. However, some studies suggested that the surface working also blocks the carbon diffusion paths through the alloy [86]. Pre-oxidation and grinding of alloy surfaces were also thought to improve the alloys resistance [66]. In contrast, solution annealed and electrochemically polished samples suffered aggressive attack [24].

Smith *et. al.*[87] reported that Fe-Cr-Ni and Cr-Ni alloys with electropolished surfaces formed non-uniform oxide layers with differences between grains and grain boundaries and at scratches and phases. Surface cold working, however, promoted the formation of more uniform and denser oxide layers.

It has also been reported that metal dusting resistance of alloy 800H could be improved by laser surface melting followed by quenching to attain a refined microstructure which possesses a higher density of chromium diffusion paths [88].

Chromium is a substitutional solute atom requiring the presence of vacancies for diffusion and hence the introduction of dislocations and grain boundaries creates areas with more vacancies as the lattice is more open. However, carbon is an interstitial solute atom but since there is already a high probability of empty neighbouring interstitial sites, negligible advantage is gained by inducing more diffusion paths which should enhance the outward diffusion of chromium with a negligible effect on the inward diffusion of carbon [88].

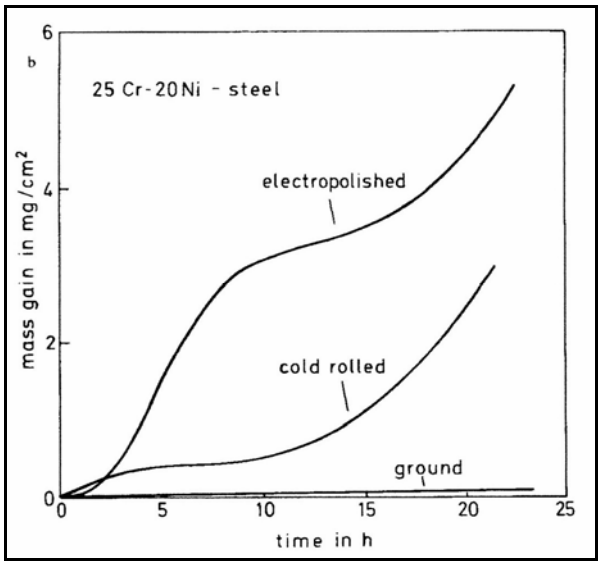

Figure 1.35 **Behaviour of stainless steel type 310 with different surface conditions. The alloy was exposed to CO-H_2-H_2O at 600°C [85].**

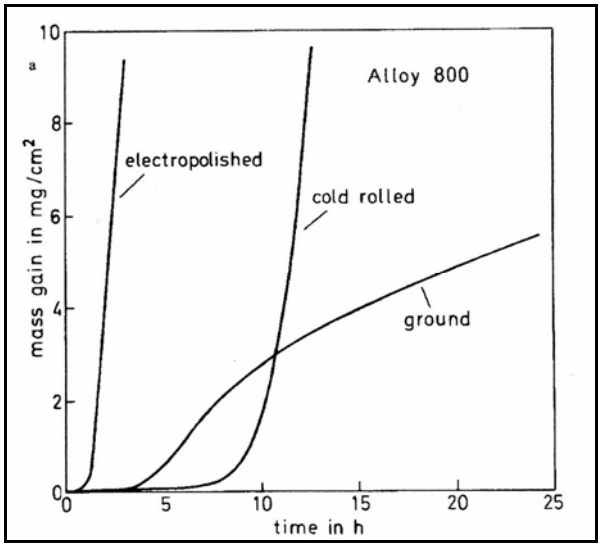

Figure 1.36 **Behaviour of incoloy 800 with different surface conditions. The alloy was exposed to CO-H_2-H_2O at 600°C [85].**

Some researchers suggested that surface working may only delay the onset of metal dusting and that it is unlikely to have a long-term effect [64]. It has also been reported that cold working of alloy 800 by 10% and 30% did not impart a considerable improvement on the metal dusting performance [89]. Schmid *et al.* [90] tested mild steel, with a surface ground to a 600 grit and the other in as-received condition with rusty appearance, in metal dusting environment (CO-H_2O-H_2 mixture at 650ºC) and reported no significant difference in metal dusting behaviour for prolonged exposure. Some other studies revealed that

etched samples exhibited almost the same behaviour as unetched ones. It has also been reported that electropolishing and pickling are deleterious and lead to immediate metal dusting for many alloys [9]. In short, further investigations are obviously required to study the role of surface working [40].

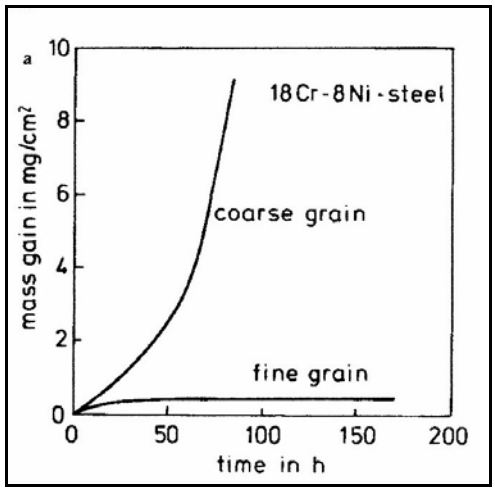

Figure 1.37 **The influence of grain size on metal dusting behaviour of stainless steel type 304 in CO-H_2-H_2O at 600°C [85].**

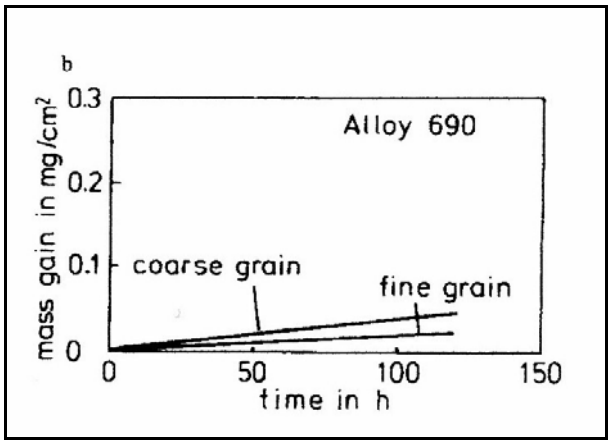

Figure 1.38 **The influence of grain size on metal dusting behaviour of the nickel-based alloy 690 in CO-H_2-H_2O at 600°C [85].**

1.6.3 Coating

Surface coating is another alternative that can be very effective in metal dusting conditions [5][91]. It is thought that coating leads to a significant reduction in gas phase reactions (and thus in carbon deposition) catalysed by free metal surfaces. In addition, coatings hinder carbon ingress into the alloy [92].

Coatings containing sufficient concentrations of oxide-forming elements are usually applied to facilitate the development of a protective oxide scale. Aluminium diffused coating is widely used since alumina, rather than chromium oxide, has a greater stability in high carbon activities and low oxygen partial pressures [25] [93][94]. However, the slow kinetics of aluminium oxide at metal dusting temperatures limits the effectiveness of aluminium-based coatings and, as such, chromium-based coatings are preferred [93].

New coatings to improve alloys performance against metal dusting were investigated using systems based on Si, Cr, Ti, and/or Al-containing phases. The coatings were applied on alloys 10Cr-9Mo, X10CrA118, X18CrN28, 800H, and P91 and exposed to a mixture of 25%CO-73%H_2-2%H_2O at 400 and 700°C. The aluminium diffusion coating was protective for all alloys at both temperatures. The silicon diffusion coating, however, showed good performance on two of the alloys, X10CrA118 and 800H. The titanium-aluminium diffusion coating performed well on alloy 800H [41].

Thermally sprayed and plasma sprayed coatings usually contain defects such as porosity, unmelted particles, and micro-cracks. Laser treatment could improve the coating integrity by remelting either a thin surface layer or the entire thickness of the coating in order to eliminate the porosity. Remelting the entire coating thickness could also improve the coating adhesion as the original interface is replaced by metallurgical bonding. It has been reported that the metal dusting resistance of various thermal sprayed coating (Ni31Cr11Al0.6Y) applied on alloys 600 and 800H was improved by laser treatment [93].

1.6.4 Process Modification

Slight alterations to process parameters may significantly delay or even prevent metal dusting [40][95]:

- Using additives such as S, As, Sb, and P-containing compounds;
- Increasing steam-to-carbon ratio;
- Reducing pressure and/or temperature;
- Upgrading the alloy; and
- Adding ammonia to the process stream [81].

However, it is not always easy to modify the process. Using additives is not practical in certain cases where the product purity is of high concern. It is also important to realise that plant operators always aim to increase production. Accordingly, recommendations to reduce temperature or pressure or increase steam-to-carbon ratio need to be strongly justified, as they will not be easily accepted.

It was thought that introducing steam would maintain a thermodynamically stable surface oxide given that the gas stream is not too abrasive [3].

Exposing iron-based alloys to steam-containing environment may lead to an increase in the iron concentration in the spinel, $Fe_{1+X}Cr_{2-X}O_4$, $0 \leq X \leq 1$, making it easier to be reduced by carbon in metal dusting conditions [96] [97].

The decoking procedure was believed to have an adverse affect on alloys metal dusting resistance [26].

Such a procedure is carried out in equipments like ethylene furnaces in order to restore the heat transfer efficiency. During decoking, steam at high pressure and temperature is introduced into the system where carbon particles, which have been deliberately removed from the alloy surface, are carried over by the steam in high velocities. This may lead to damages in the oxide scale and cause erosion [34][95][98][99].

The increase in steam-to-carbon ratio may reduce the likelihood of metal dusting but, once metal dusting occurs, the steam may aggravate the attack through the oxidation of matrix carbides [43]. Injecting a chloride-containing agent in reformers to activate the catalysts may also play a role in the initiation of metal dusting. They most probably weaken the protective sulphur layer at the alloy surface [19].

1.6.5 Sulphur Addition

The addition of sulphur is a well-known method to inhibit metal dusting [26][81][100]. For instance, the presence of sufficient amount of H_2S in the environment could protect the steel against metal dusting [11]. It should be pointed out, however, that the amounts of sulphur needed to achieve protection change with temperature (Figure 1.39) [101]. Although it is not entirely clear, the sulphur role could be related to the retardation of carbon transfer from carburising atmosphere to metals and the suppression of graphite nucleation and growth [102]. It has also been proposed that deposition of sulphur atoms blocks the adsorption and/or dissociation of carbon monoxide on alloy surfaces [47].

It was suggested that sulphur is chemisorbed on metal surfaces (especially iron) and blocks carbon diffusion [45]. As for iron, it was also proposed that sulphur diffuses into the surface and reacts with cementite to form the more stable $Fe_3(C,S)$ that slow the progression of metal dusting [3]. Sulphur is usually added as H_2S which in turn decomposes into hydrogen and sulphur:

$$H_2S \leftrightarrow H_2 + S\ (ad) \qquad (1.31)$$

Sufficient H_2S must always be ensured in the environment, otherwise the reaction (1.31) shifts to the left [102].

The positive influence of sulphur addition is clearly evident in Figure 1.40 which shows the behaviour of three alloys exposed to metal dusting environment with and without sulphur [21].

However, the addition of sulphur-containing compounds is not always possible especially in processes such as synthesis of methanol, hydrocarbons, as well as processes involving

presence of catalysts, since sulphur causes a drastic reduction in the catalysts efficiency [102].

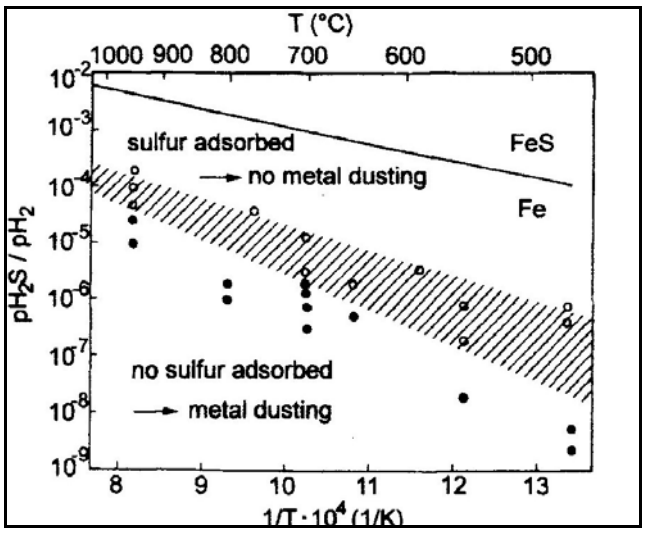

Figure 1.39 Thermodynamics of sulphur effect on metal dusting for iron [45].

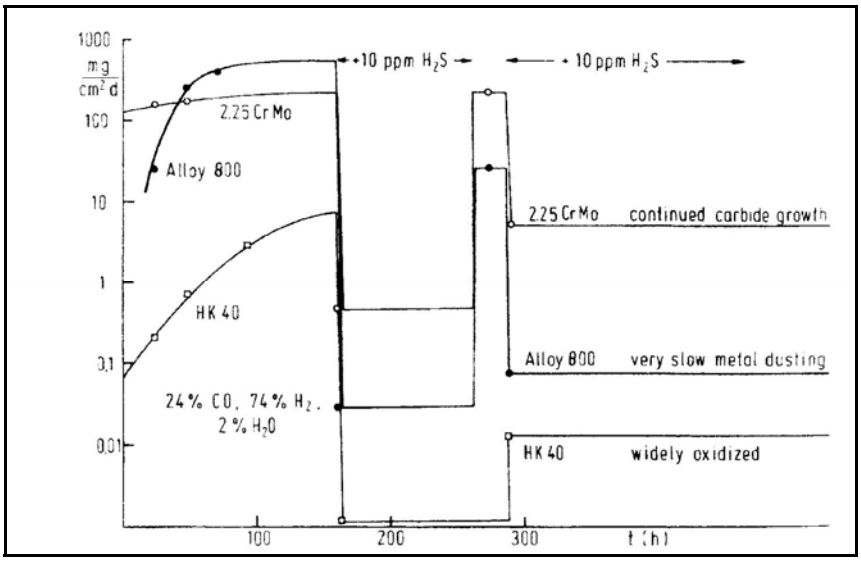

Figure 1.40 Change of metal dusting rate without and with H_2S addition for three different alloys in metal dusting conditions at 600°C [21].

2 EXPERIMENTAL PLAN AND METHODOLOGY

2.1 Research Target

The literature survey conducted in Chapter 1 has emphasised that several aspects of metal dusting are not well understood or agreed upon. Therefore, the main goal of this research is to gain a better understanding of the metal dusting process through evaluating and comparing the performance of three, commercially available, heat-resistant alloys in metal dusting conditions. The reason behind selecting commercial alloys, instead of models, was to make the project more relevant to plant experience and requirements. During the study, the alloys were subjected to a carbon-containing gas mixture (80 vol% CO + 20 vol% H_2) at 650, 750, and 850ºC for periods of 100, 500, and 1000 hours.

2.2 Test Alloys

Three heat-resistant alloys had been proposed for the study, namely KHR35C-Hi Si (HP), KHR45A LC (35Cr-45Ni), and UCX [103][104][105]. All were fabricated using centrifugal casting and have been provided, as tube portions, by the manufacturer; Kubota Corporation, Japan. The sample chemical compositions as well as dimensions are provided in Tables 2.1-2.3 below [106]. Microalloying elements had been added, in very small amounts, to modify the alloys 35Cr-45Ni and UCX but their names and quantities have been kept confidential by the manufacturer. However, the microstructural analyses reported in Chapters 3&4 revealed the presence of zirconium, titanium, aluminium, and nitrogen.

The alloys had been chosen based on their applications and chemical composition, as HP is an iron-based alloy and 35Cr-45Ni and UCX are nickel-based. Each alloy contains different concentrations of elements to enable the investigation of their influence on the alloys' behaviour in metal dusting conditions. These alloys are currently, widely used in elevated temperature applications including but not limited to ethylene furnaces, direct reduction furnaces, steam reformers, and superheater tubes.

As indicated in the literature review, there are presently two different metal dusting mechanisms that have been proposed for iron and nickel-based alloys. It has also been thought that incorporating adequate percentages of oxide-forming elements to the alloys could abruptly reduce metal wastage rate. For example, the addition of sufficient quantities of chromium and silicon would drastically lengthen the incubation period before metal dusting starts, as they tend to form protective oxide scale on the alloy surface hindering the carbon ingress into the alloy. Research has also suggested that the addition of carbide-forming elements, such as niobium and tungsten, enhances the resistance to metal dusting due to their ability to bind with the diffused carbon and hence delay the onset of the attack.

Table 2.1 Alloys composition (wt. %) as per their data sheet.

		C	Si	Mn	P	S	Ni	Cr	Nb	Others
HP	min	0.40	1.5	0.0	0.00	0.00	34.0	24.0	0.6	-
	max	0.50	2.0	1.5	0.03	0.03	37.0	28.0	1.5	-
35Cr-45Ni	min	0.10	0.0	0.0	0.00	0.00	40.0	30.0	0.5	Add.
	max	0.15	2.0	2.0	0.03	0.03	46.0	35.0	1.8	Add.
UCX	min	0.20	0.0	0.0	0.00	0.00	45.0	40.0	-	Add.
	max	0.50	2.5	1.5	0.03	0.03	50.0	43.0	-	Add.

Table 2.2 The composition (wt. %) of the three tube samples (as per mill sheet).

	C	Si	Mn	P	S	Ni	Cr	Nb	W	Others
HP	0.45	1.59	0.85	0.008	0.007	35.1	25.1	0.92	-	-
35Cr-45Ni	0.12	1.16	1.47	0.006	0.006	45.5	33.2	0.97	-	Add.
UCX	0.28	2.22	0.75	0.004	0.003	50.2	40.4	-	1.13	Add.

Table 2.3 Size and weight of the three samples.

	OD (mm)	T (mm)	L (mm)	W (Kg)
HP	129.9	7.15	301	6.4
35Cr-45Ni	129.4	6.75	300	6.2
UCX	129.9	7.2	301	6.5

2.3 Risk Assessment

It had been essential to carry out risk assessment before conducting the lab work in order to evaluate any potential hazards and hence make the proper precautions to ensure safe and smooth running of the experiments. Consequently, carbon monoxide and hydrogen detectors had to be installed near the furnace and good ventilation systems had also to be

provided to prevent the risk of asphyxia in case of gas leakage. The experimental setup and electrical connections were checked by a certified technician.

2.4 Experimental Apparatus

By surveying the current literature and considering high temperature testing guidelines [107], suitable apparatus were selected to carry out the experiments:

- **Furnace:** a horizontal tube furnace, made by Lenton Thermal Design with Eurotherm Controller type 815, equipped with an impervious mullite working tube (60% Al_2O_3 and 40% SiO_2 with zero porosity) was utilised throughout the metal dusting research.
- **Specimens:** nine samples from each alloy, with sizes 20 mm × 20 mm × 5 mm, were cut and prepared for the tests, Figure 2.1. Each sample dimension was measured using digital callipers and micrometer. The specimen surfaces were ground and finished to 120 grit SiC, and their edges were slightly rounded to minimise scale spallation.

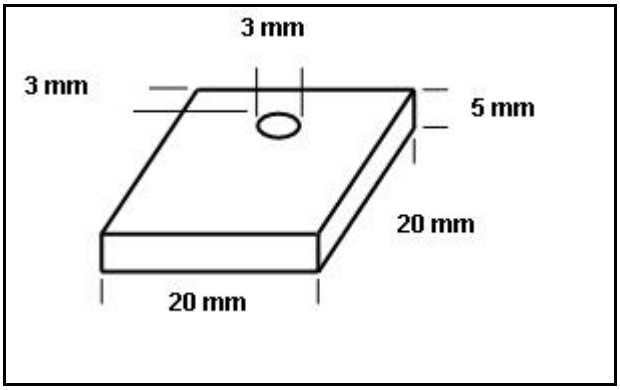

Figure 2.1 Geometry and dimensions of the test samples.

- **Specimen Holders:** an alumina tube was cut and reconstructed to build a rack that carried the wires, by which the samples were suspended, Figure 2.2. Joining the parts of the rack together was achieved by applying water-based ceramic adhesive (composed mainly of mullite and alumina). Platinum wires, with purity of 99.95% and diameter of 0.4 mm, were selected to hold the alloys, because of their superior

resistance to metal dusting. Suspending the samples ensured more uniform and even exposure to the gas mixture and eliminated the potential reaction with crucible impurities which, in turn, might catalyse the metal dusting process (see 1.5 for further details).

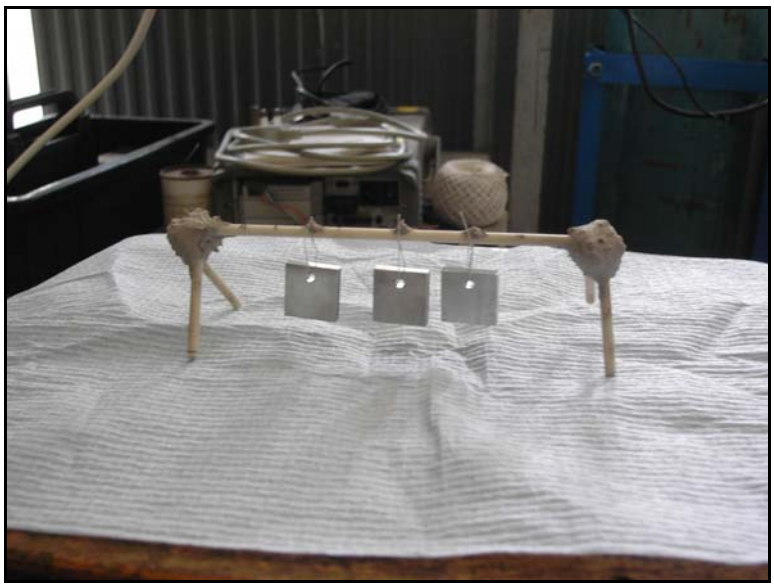

Figure 2.2 The samples were held by platinum wires suspended from alumina rack.

- **Thermocouple**: a thermocouple type K in combination with a temperature measuring instrument (testo 925) was used throughout the research, in order to determine the temperature profile and monitor the temperature at the rack. The thermocouple had been calibrated as new and was protected against the carburising environment by mean of an alumina shield.
- **Gas Source:** cylinders containing premixed 80 vol% CO+20 vol% H_2 were supplied to provide the experimental environment. Argon was also used for purging. The purity of argon was 99.997% with oxygen content of less than 0.0005%. The hydrogen and carbon monoxide specifications, as provided by their manufacturer; BOC Limited, are shown in Table 2.4 below.

Table 2.4 **Specifications for H_2 and CO used in the experiments. The maximum level of impurities is shown.**

Hydrogen (min. purity 99.995%)		**Carbon monoxide** (min. purity 99.9%)	
Oxygen	5 ppm	Oxygen	50 ppm
Nitrogen	20 ppm	Nitrogen	800 ppm
Total Hydrocarbons	5 ppm	Total Hydrocarbons	25 ppm
Carbon Dioxides	5 ppm	Carbon Dioxides	50 ppm
Water	5 ppm	Water	5 ppm
Carbon Monoxide	10 ppm	Hydrogen	200 ppm
		Carbonyl Sulphide	200 ppb

- **Others:** valves, fittings, flow meters, and connection (copper tubes with diameter of 4 mm) were installed.
- **Experiment Operating Conditions:**

  - Temperature: 650°C, 750°C, and 850°C;
  - Pressure: 1.0atm;
  - Gas Flow Rate: $100cm^3\ min^{-1}$;
  - Exposure Times: 100, 500, and 1,000hours.

2.5 Experimental Procedure

Bearing in mind the best practices stated in the literature [107], the experiments were conducted according to the following steps:

- Firstly, the temperature profiling was carried out in order to determine the hot zone within the tube, at temperatures set to 650, 750, and 850ºC. The maximum air temperatures measured were 656, 749, and 846 respectively, and the hot zone was eventually located 55cm from the tube inlet. Despite setting the furnace to heat in the rate 100ºC per minute, it took 30, 35, and 40 minutes to reach 650, 750, and 850ºC respectively. However, it needed much longer time to cool down. More details of the

temperature profiling and heating/cooling can be seen in Appendix C. Importantly, the heating and cooling periods were not included within the test times.

- An experimental setup was designed and assembled as shown in Figure 2.3. Steel clips were inserted to hold the silicone bungs in position and ensure better sealing of the system. A pressure relief valve was installed as a precautionary measure to handle any back pressure resulting from blockage in the tube that could occur due to carbon deposition and accumulation on the samples. A leak detection spray was also used to confirm that the system was perfectly sealed after each time that it was opened.

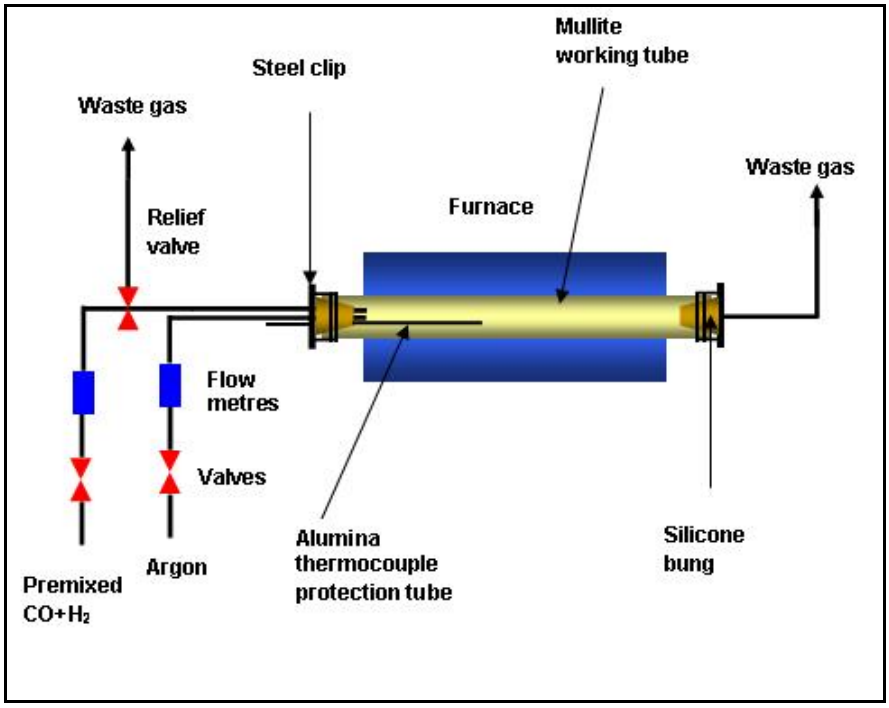

Figure 2.3 Schematic showing the experiment's setup.

- All specimens were washed in water and then ultrasonically cleaned in acetone, using an ultrasonic bath (Fisherbrand FB 11004) with ultrasound power set to 100%.
- The samples were weighed using a four decimal, digital balance (Mettler AT261 DeltaRange with 0.1 mg readability).
- The specimens were then loaded on individual platinum wires and checked so that they were to be vertical as shown in Figure 2.2. Next, they were carefully placed inside the furnace at location shown in Figure 2.4.

- More amounts of carbon, water vapour, and/or carbon dioxide, as a result of reactions such as 1.5 and 1.11 (stated in Chapter 1), were anticipated to have been produced as the gas mixture proceeded through the furnace tube. Accordingly, the gas composition, just before the rack, might have well been different from the gas composition at the other end of the rack, meaning that the alloy specimens most likely saw different gas mixture based on their location at the rack. For that reason, the sample order on the rack was inverted before the 500h experiments in order to study the effect, if any, of this composition change on the alloys behaviour, Figure 2.5.

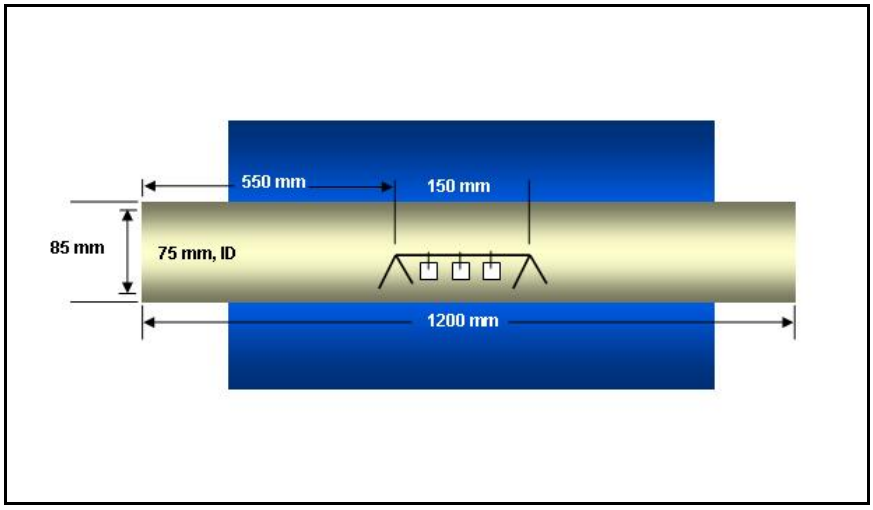

Figure 2.4 Schematic of the dimensions of the working tube and location of the rack.

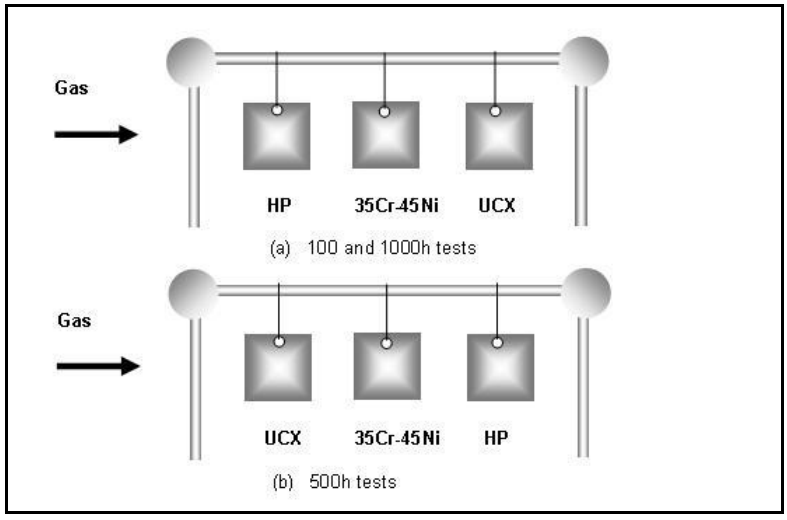

Figure 2.5 Sample arrangements during the metal dusting tests.

- The system was assembled, as seen in Figure 2.3, and was leak tested. Next, argon was introduced, at 100cm^3 min^{-1}, for one hour to displace air from the tube. The test gas was then switched on for an hour in order to establish the corrosion environment prior to turning the furnace on.
- The furnace controller had been programmed to heat up the system at the rate of 100°C min^{-1} to minimise the likelihood of corrosion during heating. However, in practice, the furnace took longer time to heat. The temperature at the rack was being monitored regularly during the experiment.
- On completion of the test, the samples were allowed to cool down in the gas mixture. Once the temperature had reached 200°C, the system was purged with argon, flowing in 100cm^3 min^{-1}, for a period of an hour, and finally left to cool down to room temperature.
- If the experiment had to be interrupted for such situations as gas cylinder replacement, the previous steps were repeated.
- After each exposure, the working tube was inspected and cleaned of any carbon depositions.

These procedures were adopted to conduct nine experiments, each one involving the testing of the three different alloys. The tests comprised three short-term (100h), three medium-term (500h), and three long-term (1000h) experiments, carried out at three different temperatures, i.e. 650, 750, and 850ºC.

2.6 Analyses and Characterisations

After being exposed to the carburising environment, the samples were inspected and evaluated according to the following steps [107]:

- The rack holding the samples was carefully removed from the furnace and a photo of the specimens was immediately taken.
- Each sample was then removed and visually inspected and then photo taken.

- Deposits on samples, if any, were mechanically removed by bristle brush and collected in containers for chemical analyses (SEM/EDX & XRD).
- The samples were thoroughly washed in water and ultrasonically cleaned in acetone, using an ultrasonic bath (Fisherbrand FB 11004) with ultrasound power set to 100%, for at least 40 minutes. Then the alloys were weighed using a four decimal, digital balance (Mettler AT261 DeltaRange).
- After cleaning the samples were visually inspected and photographed.
- Weight change was determined from the difference in the sample weight before and after the exposure, in mg/cm^2. Some small error in the sample surface area calculations had been anticipated due to the specimen edge rounding. Indeed, the actual surface area was expected to be smaller than that calculated.
- The alloys were then analysed by XRD to identify phases present on their surfaces. Additionally, deposits on samples, if any, were collected and analysed. All the analyses were carried out by a Philips vertical diffractometer, PW 1830/00, with Cu Kα radiation. For very small amounts of powder, however, the machine; Bruker D8 Advance with vertical diffractometer and position sensitive detector "LynxEye", was utilised because of its very high acquisition (count) rate. The data collection and peak searching and phase identification were achieved by the software Philips X'pert Data Collector and Philips X'pert Plus and HighScore Plus respectively. It is worth saying that interpreting the XRD peaks was indeed an uneasy task as many probable oxide compounds had been suggested by the software. Also, there were relatively wide peaks that could accommodate more than one phase. In view of that, we endeavoured to make the best judgment and select the most likely oxides based on the best fit within the patterns.
- The extent of corrosion was then assessed by scanning the sample surfaces firstly by optical microscope and secondly by SEM. Surface deposits and pit contents were chemically analysed by EDX. The investigation was carried out using the scanning electron microscope, FEI Quanta 200 SEM with Oxford INCA 250 EDX system attachment. Spot size number of all EDX analyses was set to 5.5. Table 2.5, below, reveals the EDX quantitative analysis accuracy for the elements. For example, if an element was detected to be present at 21.13 wt%, then the analysis accuracy is ± 2% of 21.13% which results in 21.13 wt% ± 0.42wt%.

Table 2.5 EDX quantitative analysis accuracy.

Results (in wt %)	Description	Relative %
100-20	Main element	2%
20-5	Major element	4%
5-1	Minor element	10% to 20%
1-0.2	Trace element	50% (up to 100%)

- Cross sections of the alloys were prepared for metallographic examination. The samples were mounted in either Multifast (manufactured by Struers) or Bakelite (made by Buehler) that were nonconductive, and therefore copper tapes were used to provide a conductive path from the samples to ground in order to avoid charging. The samples were ground and then polished to 9μm using diamond suspension and finally polished to 0.04μm by colloidal silica suspension.
- The sample substrates and reaction fronts were thoroughly examined for any type of attacks. Moreover, the layers formed on surfaces, if any, were investigated and analysed.

2.7 Oxidation Experiments

One method to mitigate metal dusting attack is based on isolating the alloy from the surrounding environment through the development of a protective scale composed of chromium, silicon, and/or manganese-bearing oxides. However, some oxides such as iron oxides, nickel oxides, and iron-containing spinels, are believed to be unstable in metal dusting conditions and hence would not be able to provide an adequate protection. Accordingly; it was proposed to carry out oxidation experiments in the metal dusting temperature range in order to explore the scale growth and identify the oxide phases formed at these temperatures. The alloys were tested in air at 650, 750, and 850ºC for 100 and 1000h. More details of the study are elucidated in Chapter 4.

3 MICROSTRUCTURAL ANALYSES

3.1 Microstructure of Heat-Resistant Alloys

Heat-resistant alloys are designed for the use at high temperatures (T > 540ºC). The physical metallurgy of these alloys is quite complex. In general, the microstructure of heat-resistant alloys consists of an austenitic matrix with precipitation of second phases such as metal carbides and/or nitrides [108][109]. Table 3.1 summarises the roles of alloying elements in heat-resistant alloys. It should be emphasised though that not all of these effects necessarily take place in a given alloy [109].

Table 3.1 Role of elements in heat-resistant alloys [109].

Effect	Iron Base Alloys	Nickel Base Alloys
Solid solution strengtheners	Cr, Mo	Co, Cr, Fe, Mo, W, Ta
Face centred cubic matrix stabilisers	C, Ni	….
Carbide formers:		
MC	Ti	W, Ta, Ti, Mo, Nb
M_7C_3	….	Cr
$M_{23}C_6$	Cr	Cr, Mo, W
M_6C	Mo	Mo, W
Oxidation resistance	Cr	Al, Cr
Improves hot corrosion resistance	La, Y	La, Th
Sulphidation resistance	Cr	Cr
Carbonitrides: M(CN)	C, N	C, N
Forms γ' Ni_3(Al, Ti)	Al, Ni, Ti	Al, Ti

Grain size is an important microstructural parameter that plays an essential role on the performance of heat-resistant alloys. Alloys with fine grains usually exhibit good toughness, strength, and fatigue resistance whereas alloys with coarse grains show a better creep strength. Grain size also influences the precipitation of carbides at the grain boundaries. For example, microstructure with coarse grains has less grain boundary surface area and, as a consequence, the carbide precipitation is more continuous and thicker and

that may lead to a significant degradation in the alloy properties. Hence, a uniform intermediate grain size is generally preferred [109].

Metal carbide might be regarded as the most important second phase precipitated in heat-resistant alloys. Carbides precipitated at the grain boundaries improve the alloys strength, prevent grain boundaries sliding, and permit stress relaxation. Moreover, the formation of fine carbides within the matrix results in alloy strengthening [109].

Carbides can be categorised as primary and secondary where the formers are precipitated during the solidification process and distributed at the dendrite and grain boundaries. The primary carbides are very effective in preventing grain boundaries sliding. The secondary carbides start to form once the alloy is introduced to elevated temperature service and they are precipitated heterogeneously within the dendrites and at the grain boundaries. Secondary carbides precipitation is also desired in order to hinder the motion of dislocations during high temperature exposures [110].

Carbide growth and morphology are time and temperature dependents. The carbides tend to coarsen and coalescence as a result of increasing temperature and time. In general, the useful life of heat-resistant alloys is significantly influenced by the carbide size and shape. The carbides growth with time results in a gradual degradation of the alloy properties until a stage where the alloy cannot function at the operating condition any longer. In other words, once the carbides reach a critical size, their interaction with dislocations becomes less effective and the alloy consequently loses its strength. The critical size of the carbides may vary from one alloy to another depending on the ductility of the alloy [111].

3.2 Objective

Metallographic examination was carried out in order to investigate the microstructure of virgin samples of alloys HP, 35Cr-45Ni, and UCX. Phases observed in the microstructures were also analysed by EDX. Additionally, the microstructural change of the alloys after exposures for 100, 500, and 1000h is reported in Appendix A. Sample preparation and characterisation procedures are given in Chapter 2.

3.3 Metallographic Examination

3.3.1 HP

Most of the phases present in the microstructure of heat-resistant alloys (e.g. carbides and nitrides) are readily observed without etching [109].

The microstructure of alloy HP is composed of an austenitic matrix containing a complex network of carbides that outlines the boundaries of the original dendrites (Figure 3.1). It is generally characterised by the equiaxed grain shape.

EDX of the phases observed on the microstructure is shown in Figure 3.2. Chromium was the main constituent of the dark grey precipitate (A1) confirming it to be chromium carbides. The whitish phase (A2), however, was found to be niobium-based carbide. The composition of the base metal was also confirmed (A3).

Going through all EDX analyses done on the alloy after different exposures (Appendix A), Y and N were detected in some of the niobium-based carbides in considerable concentrations (0.7 and 2.6 wt% respectively). Moreover, introducing the alloy to the high temperature environments resulted in the precipitation of secondary carbides across the matrix. More carbide precipitation was observed as the temperature and/or time were increased. Also, a transformation of niobium carbides into niobium, nickel, and silicon-rich phase appeared to have occurred on the samples exposed at 850ºC for 500 and 1000h. In the former, the weight percentages of Nb, Ni, and Si were 30.6, 48.4, and 10.4 respectively; whilst, in the latter, the amounts were 49.6, 31.3, and 6.7 respectively. Some transformation was also observed in the alloy exposed for 500h at 750ºC.

It seemed that the niobium carbides transformed partially into the intermetallic nickel-niobium silicide ($Ni_{16}Nb_6Si_7$), also known as G-phase. It has been reported that the formation of G-phase improved the high temperature performance of the alloys but, nonetheless, resulted in an extreme brittleness at ambient temperature not to mention the poor weldability [112][113].

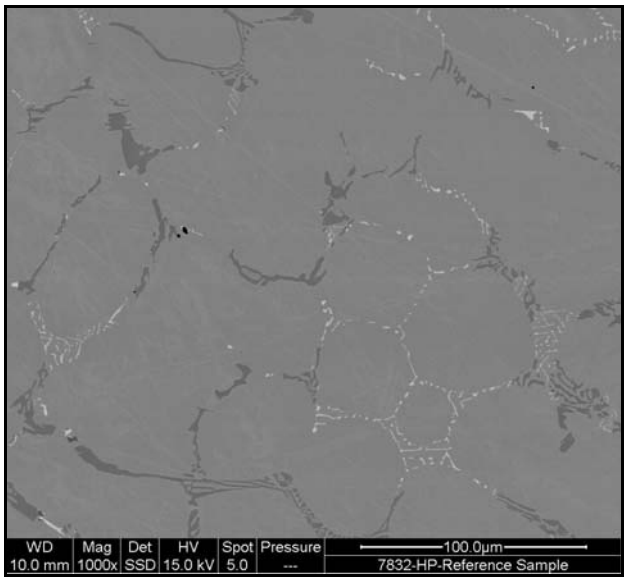

Figure 3.1 Alloy HP has an austenitic microstructure with a network of primary carbides.

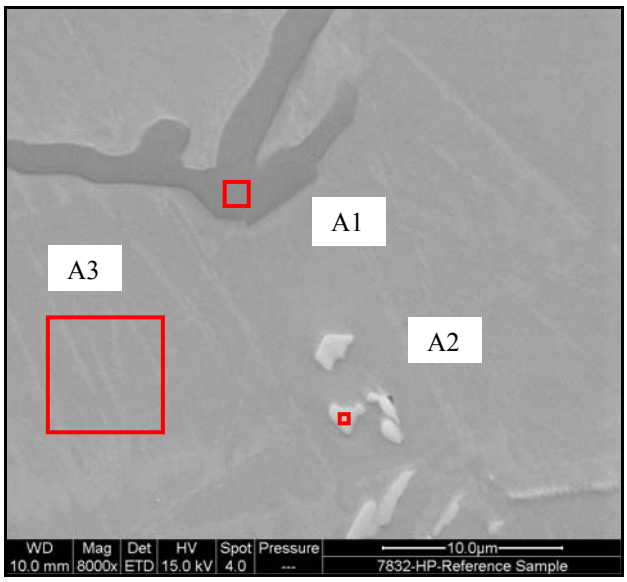

A1

Element	Weight%	Atomic%
C K	9.14	29.11
O K	2.81	6.71
Cr K	77.72	57.15
Mn K	0.68	0.47
Fe K	8.04	5.51
Ni K	1.61	1.05
Totals	100.00	

A2

Element	Weight%	Atomic%
C K	11.44	43.04
N K	2.34	7.54
O K	1.25	3.52
Si K	0.21	0.34
Cr K	5.04	4.38
Mn K	0.42	0.34
Fe K	3.89	3.14
Ni K	3.58	2.76
Nb L	71.83	34.93
Totals	100.00	

A3

Element	Weight%	Atomic%
C K	1.11	4.72
O K	1.46	4.64
Si K	1.81	3.28
Cr K	24.11	23.64
Mn K	1.24	1.15
Fe K	34.29	31.31
Ni K	35.98	31.24
Totals	100.00	

Figure 3.2 EDX of matrix and primary carbides.

3.3.2 35Cr-45Ni

The microstructure of alloy 35Cr-45Ni is austenite with a much lower concentration of primary carbides, see Figure 3.3. This is attributed to the lower carbon concentration in the alloy (0.12 wt% C). Discontinuous and discrete primary carbides are distributed throughout the grain boundaries. EDX confirmed that the grey (A1) and whitish (A2) phases are chromium and niobium-based carbides respectively (Figure 3.4). The alloy composition was also confirmed (A3). The microstructural and chemical analyses carried out on the samples after exposure (Appendix A) showed the presence of other phases and elements. "Diamond-like" titanium nitrides were observed across the alloy microstructure. Some of the nitrides contained considerable amounts of Ce (~ 6.9 wt%). Moreover, inclusions composed mainly of 41.3 wt% Mn, 22.5 wt% S, and 3.0 wt% Se were detected. Significant levels of Ti, N, and Y were found in some of the niobium-based carbides. Interestingly, partial transformation of niobium carbides to G-Phase was noticed on samples exposed at 750ºC for 1000h and at 850ºC for 500h. In the former, the whitish phase was confirmed to contain 44.7 wt% Nb, 30.7 wt% Ni, and 5.8 wt% Si. In the latter, however, 65.9 wt% Nb, 10.6 wt% Ni, and 1.0 wt% Si were detected suggesting only a little transformation of the carbides to G-phase.

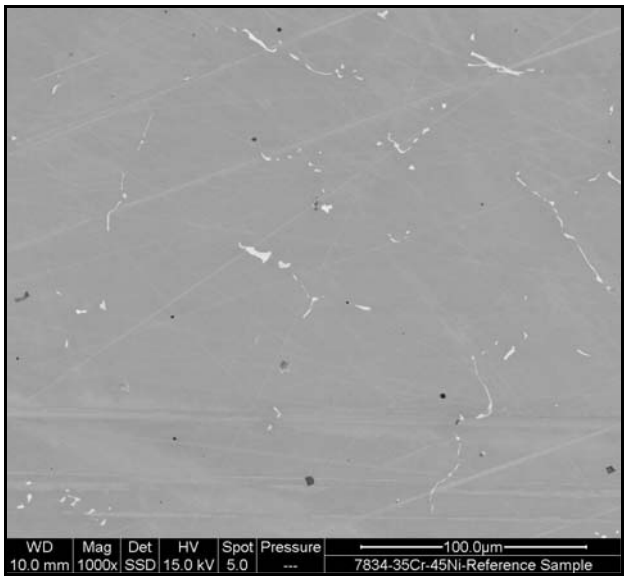

Figure 3.3 **Alloy KHR45ALC has an austenitic microstructure with discontinuous primary carbides.**

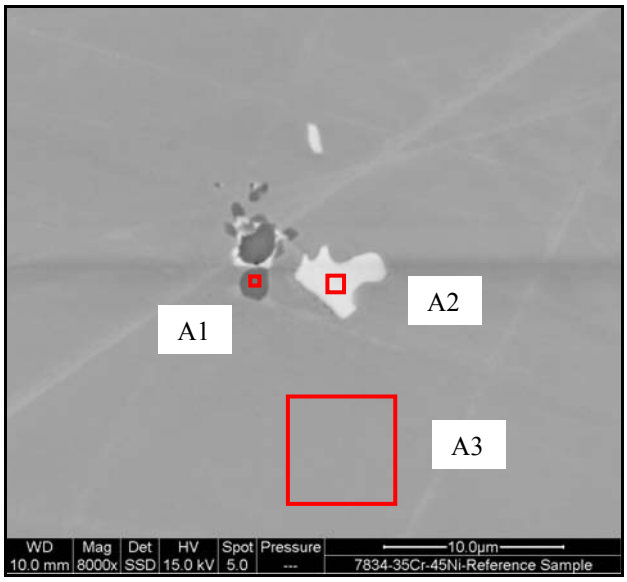

A1

Element	Weight%	Atomic%
C K	6.17	21.64
O K	2.65	6.99
Si K	0.76	1.13
Cr K	64.35	52.16
Mn K	1.25	0.96
Fe K	5.91	4.46
Ni K	15.41	11.06
Nb L	3.51	1.59
Totals	100.00	

A2

Element	Weight%	Atomic%
C K	10.73	44.36
O K	1.66	5.14
Cr K	5.51	5.26
Fe K	1.17	1.04
Ni K	3.06	2.58
Nb L	77.87	41.61
Totals	100.00	

A3

Element	Weight%	Atomic%
C K	1.17	4.91
O K	1.60	5.06
Si K	1.81	3.26
Cr K	35.38	34.43
Mn K	1.80	1.66
Fe K	15.28	13.85
Ni K	42.34	36.49
Nb L	0.62	0.34
Totals	100.00	

Figure 3.4 **Higher magnification photomicrograph showing the low carbide concentration within the microstructure.**

3.3.3 UCX

Alloy UCX has an austenitic microstructure enriched with a network of interdendritic precipitation of carbides, Figure 3.5. By comparison with the microstructure of alloy HP, UCX possesses coarser primary carbides as well as higher carbide concentration. The carbides in this alloy resemble almost pearlite in steels.

In addition to chromium carbides (A2 in Figure 3.6), titanium nitrides were observed throughout the alloy microstructure (A3). Zirconium rich particles were also detected within the nitrides (A1). Some of the nitrides (Appendix A) also contained considerable amounts of Ce (~ 3.34 wt%).

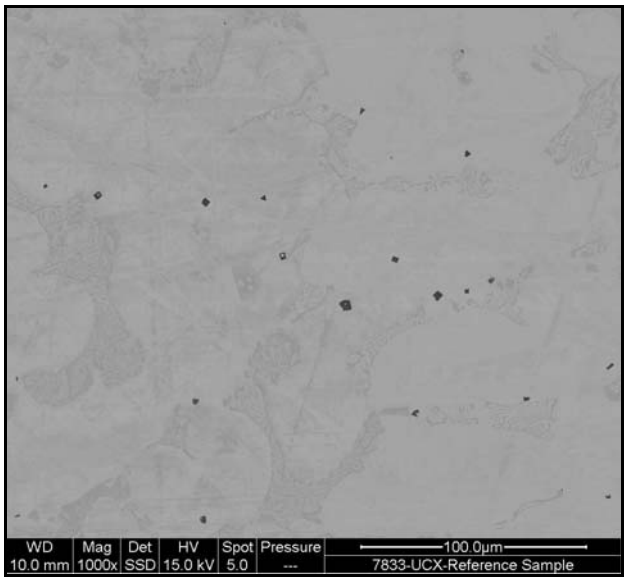

Figure 3.5 **UCX alloy has an austenitic microstructure enriched with primary carbides.**

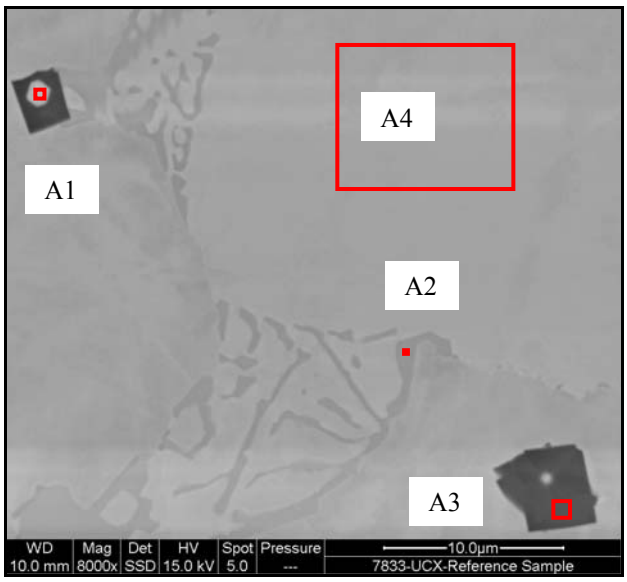

A1

	Wt%	At%
C K	1.73	4.78
N K	6.25	14.86
O K	24.89	51.81
Ti K	10.15	7.05
Cr K	1.76	1.13
Ni K	1.71	0.97
Zr L	52.76	19.26
W M	0.75	0.14
Totals	100.0	

A2

	Wt%	At%
C K	6.50	22.63
O K	3.05	7.96
Si K	0.22	0.32
Cr K	72.84	58.58
Fe K	2.08	1.55
Ni K	11.26	8.02
W M	4.06	0.92
Totals	100.0	

A3

	Wt%	At%
C K	0.64	1.64
N K	22.99	50.25
Ti K	68.27	43.63
Cr K	5.70	3.35
Ni K	1.79	0.93
Nb L	0.61	0.20
Totals	100.0	

A4

	Wt%	At%
C K	1.22	5.13
O K	1.75	5.54
Si K	1.85	3.33
Cr K	37.42	36.42
Mn K	0.79	0.73
Fe K	5.54	5.02
Ni K	50.58	43.60
W M	0.86	0.24
Totals	100.0	

Figure 3.6 **This photomicrograph reveals the lamellar structure of the primary carbides precipitated in alloy UCX.**

3.4 Conclusion

In general, carbides are deliberately precipitated in heat-resistant alloys to improve their high temperature strength. The microstructures of cast heat-resistant alloys are austenitic and characterised by the presence of interdendritc primary carbides in different concentration, shape, and distribution. Unlike wrought alloys, these alloys have coarser grains and contain alloy segregation (inhomogeneous microstructure). Furthermore, casting alloys have equal properties in all directions [114][115].

EDX confirmed that all alloys contained additives of rare earth elements (e.g. Y and Ce). Furthermore, nitrides of Ti and Zr were also detected on 35Cr-45Ni and UCX. It was also evident that introducing the alloys to the high temperature environments led to precipitation and growth of secondary carbides within the matrix and at the grain boundaries. Increasing the exposure temperature and/or time obviously caused more formation of carbides. Also, a transformation of the niobium-based carbides to G-phase in HP and 35Cr-45Ni was also observed. HP experienced that transformation after 500 and 1000h at 850ºC and after 500h at 750ºC whereas 35Cr-45Ni showed transformation after 1000h at 750ºC and after 500h at 850ºC.

4 OXIDATION OF HEAT-RESISTANT ALLOYS

Most alloys rely on the development of protective oxide scales to perform in a satisfactory manner at high temperatures. The scale acts as a barrier between the environment and the alloy in order to meet the requirements of the desired life time of the equipment. Not all oxide layers are protective and therefore alloys are carefully designed to form such protective scales as chromium, aluminium and/or silicon oxides. In addition to the scale composition and morphology, the protectiveness of the oxide scales depends strongly on several factors including pressure, temperature, environment, applied stresses, and component geometry.

4.1 Introduction to High Temperature Oxidation

The oxidation process involves the adsorption of oxygen on the metal surface followed by the formation of individual oxide nuclei which grows laterally to form a continuous oxide film. Then the oxide film grows normal to the metal surface. Nucleation of oxides usually occurs at high energy sites including surface defects, such as dislocations, grain boundaries, impurities, and surface precipitates. Once a continuous oxide film has developed the reaction can only proceed by solid state diffusion of one or both reactants through the film. The oxidation rate is controlled by the slowest step which, in many cases, is the transport of reactants across the scale [116].

4.1.1 Thermodynamic Considerations

Most metals are thermodynamically unstable in oxygen-containing environments and may consequently undergo oxidation through reactions of the type:

$$M + O_2 \leftrightarrow MO_2 \tag{4.1}$$

The oxidation process is thermodynamically favourable if the oxygen partial pressure in the environment exceeds the dissociation pressure of the oxide in equilibrium with the metal. The latter can be computed using the expression of the standard free energy change of formation of the oxide:

$$\Delta G^{o} = -RT \ln K = -RT \ln \left(\frac{a_{MO_2}}{a_M . pO_2} \right) \tag{4.2}$$

By assuming a unit activity for the solid species, the dissociation pressure can be written as:

$$pO_2 = \exp \left(\frac{\Delta G^{o}}{RT} \right) \tag{4.3}$$

The Ellingham/Richardson diagram (Figure 1.21) is a vital tool that can be effectively utilised to determine the oxygen partial pressure required for any metal to develop oxide at any temperature. In this diagram, the standard free energy of formation of oxides is plotted as a function of temperature. The values of dissociation pressure of the oxide can be obtained directly from that diagram by drawing a straight line from point O, through the appropriate free energy curve at the temperature of interest and reading the oxygen partial pressure value at its point of intersection with the right hand axis labelled (pO_2) [117] [118].

4.1.2 Kinetic Considerations

An accurate determination of the oxidation rate is of an extreme importance in order to produce a reliable estimation of the design life of an alloy subject to oxidising conditions. However, calculating the rate is not an easy task as parameters like temperature, oxygen pressure, and surface treatment have considerable influence on the oxidation kinetics. Also, oxidation of metals and alloys follows different rate laws including linear, parabolic,

logarithmic, and/or combinations of these. In fact, the oxidation behaviour of most engineering alloys obeys parabolic law at elevated temperatures at which the oxidation rate is controlled by diffusion of reactants across the scale. In these alloys, the oxide grows with a decreasing oxidation rate (Figure 4.1) according to the expression:

$$x^2 = 2\,k_p\,t + C \tag{4.4}$$

Where x is the oxide thickness, k_p is the parabolic rate constant, t is the time, and C is a constant.

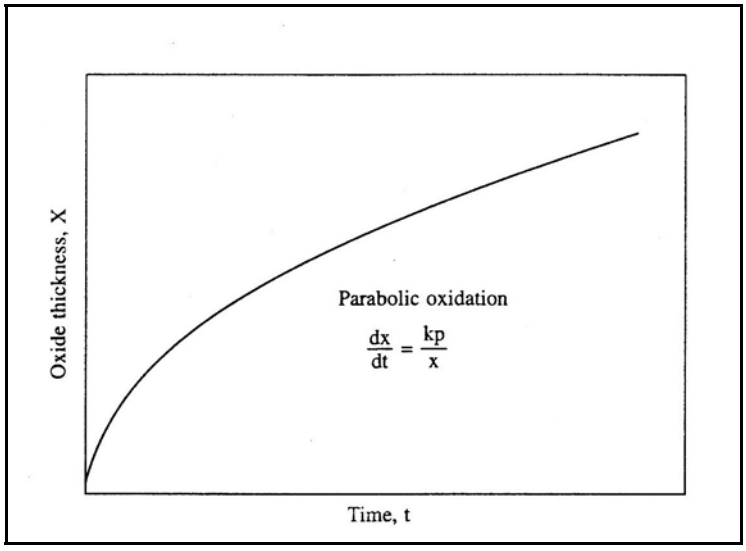

Figure 4.1 The kinetics of parabolic oxidation [117].

Another important rate law, combining the parabolic and linear laws, is usually observed at high temperatures (Figure 4.2) at which a protective oxide scale develops on the alloy for some time, which fails due to causes such as creep deformation, severe depletion of oxide forming elements, extremely high temperature, thermal expansion, and thermal shocks [117].

For example, alloys with high chromium content form oxide scales that can be protective at temperatures below 1000ºC. Exceeding that temperature may well catalyse the chromium oxide (Cr_2O_3) to further react with oxygen producing volatile chromium oxides (CrO_3) according to the reaction [119]:

$$0.5Cr_2O_3 + 0.75O_2 \rightarrow CrO_3\ (g) \qquad (4.5)$$

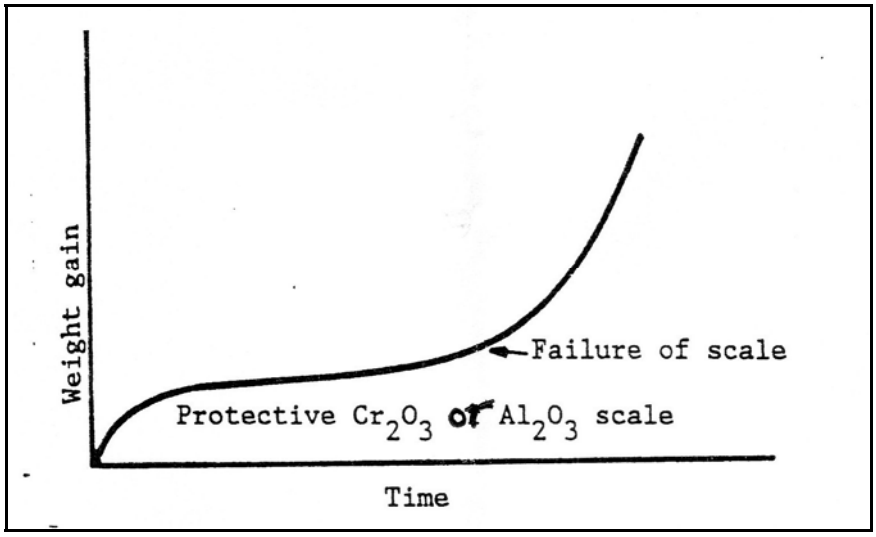

Figure 4.2 The combination of parabolic and linear kinetics [116].

4.1.3 Oxidation of Engineering Alloys

Corrosion and mechanical properties are often conflicting requirements and a compromise solution must be reached in order to design an optimum engineering alloy. Although high temperature alloys are primarily designed to possess adequate mechanical properties at high temperatures, they must also be able to resist high temperature corrosion through the development of protective, adherent, rehealing, and slow-growing oxide scales [118].

Incorporating sufficient amounts of oxide-forming elements (i.e. chromium, aluminium, and/or silicon) to an alloy is necessary in order to develop continuous oxide scales. Most commercial heat-resistant alloys, however, rely on the formation of protective chromium oxide scale. The addition of silicon is believed to be beneficial as amorphous silica layer tends to form at the alloy/oxide interface improving oxidation resistance by suppressing cation transport across the chromium oxide scale, leading to considerable reduction in the scale growth rate. However, the presence of relatively high levels of silicon may lead to

scale spallation. It has also been reported that addition of aluminium boosts the spallation resistance of chromium oxide scales [120] [121].

The effect of manganese on the oxidation performance of chromium-containing alloys has long been of debate. Douglass *et al.* [122] had studied the influence of manganese additions on the oxidation mechanism of Ni-20Cr alloy and concluded that "the presence of manganese is generally beneficial when it promotes the formation of an inner spinel layer (i.e. $MnCr_2O_4$). The outer spinel layer is generally lost by spallation and offers little protection, but the inner spinel is tightly adherent, and the slow rate of ion transport across this layer increases the oxidation resistance". It has also been reported that alloying Ni-Cr system with manganese had been proven effective in reducing chromium oxide evaporation at high temperatures in strongly oxidising environments. Indeed, incorporating manganese was found to have lowered the chromium activity in the oxides leading to a remarkable reduction in chromium oxide volatilisation by a factor of 35 at 800ºC and 55 at 700ºC [123]. Conversely, according to Caplan *et al.* [6] *as referenced in* [73] manganese has an adverse effect on the integrity of chromium oxide scales, in that it promotes scale blistering and cracking. Stott *et al.* [9] *as referenced in* [73] investigated the role of manganese on oxidation of the iron-based alloy, Fe-28Cr, and observed considerable deterioration of the alloy's oxidation resistance caused by the relatively rapid diffusion rate of manganese through the chromium oxide scale and formation of the less protective $MnCr_2O_4$ on its outer surface.

Rare earth elements have long been recognised for their role in enhancing oxidation resistance. Introducing very low amounts (~ 0.1%) of these elements to alloys has been proven to be very effective in improving the reliability of the oxide scale. The influence of their addition on oxidation of Fe-20Cr and Ni-20Cr alloys is demonstrated in Figures 4.3 and 4.4 respectively. Although the action(s) of rare earth elements is not fully understood, several mechanisms have been proposed, including but not limited to the following [124]:

1. Improving the scale adhesion through the development of oxide pegs into the alloy acting as mechanical keying.
2. Reducing the accumulation of voids at the alloy/scale interface leading to better adhesion.

3. Imparting higher spallation resistance by enhancing the scale plasticity through the modification the oxide structure.
4. Suppressing segregation of sulphur to the alloy/scale interface.

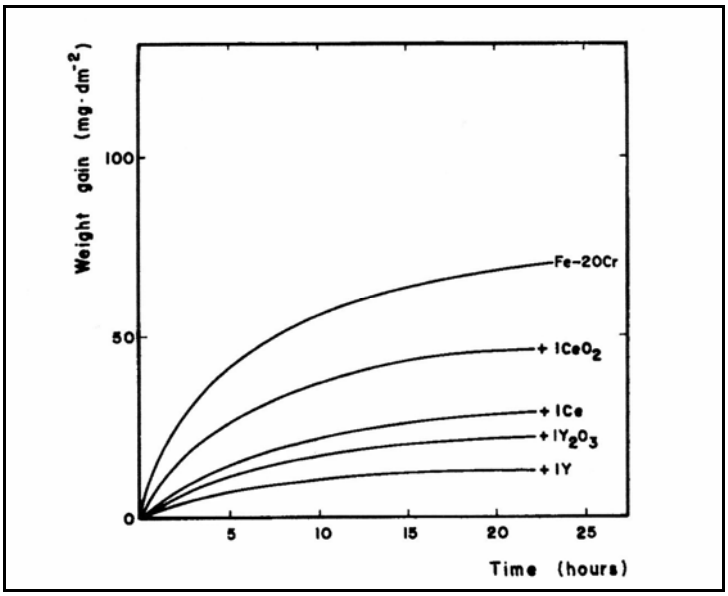

Figure 4.3 **Oxidation of Fe-20Cr at 1000ºC with and without addition of rare earth elements and oxides [124].**

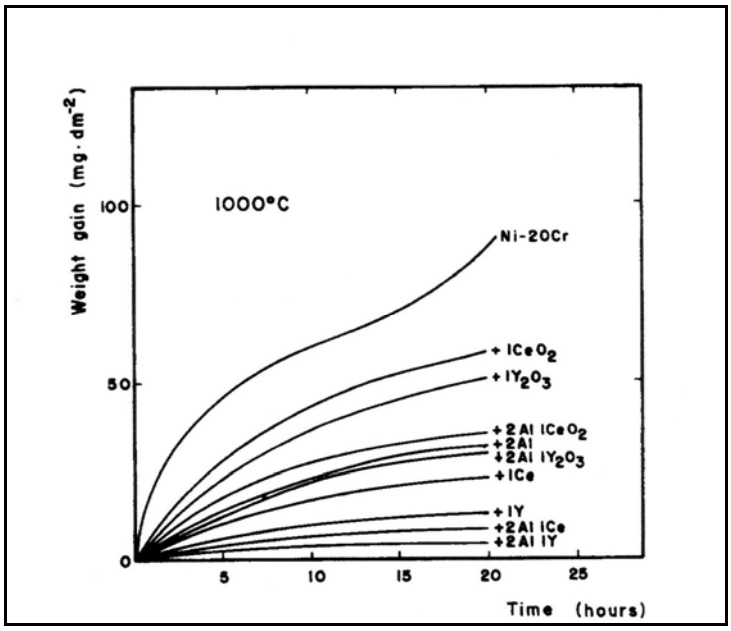

Figure 4.4 **Oxidation of Ni-20Cr at 1000ºC with and without addition of rare earth elements and oxides [124].**

An ideal protective oxide scale would completely isolate the alloy from the surrounding environment. Such scales need to be crack free, pore free, spallation resistant, stress free and slow growing which is, unfortunately, almost impossible to accomplish, as oxide scales are susceptible to cracking or spallation. Cracking of the scale is immediately followed by reformation of replacement scale provided that the alloy bears a sufficient amount of scale-forming elements. However, as the time goes on, the protective oxide-forming elements are consumed and depleted in the alloy allowing oxides of other elements such as iron, nickel, and cobalt to form giving rise to unprotective layers. Failure of the oxide scale may consequently lead to accelerated degradation of alloys particularly in environments containing species such as carbon, sulphur, and chlorine that, in turn, react with the alloy forming less protective layers [118].

Stresses are usually generated as an oxide scale grows until a point is reached where the scale fails to accommodate the increasing stresses (caused by increasing thickness) and starts to crack or spall (Figure 4.5) [117].

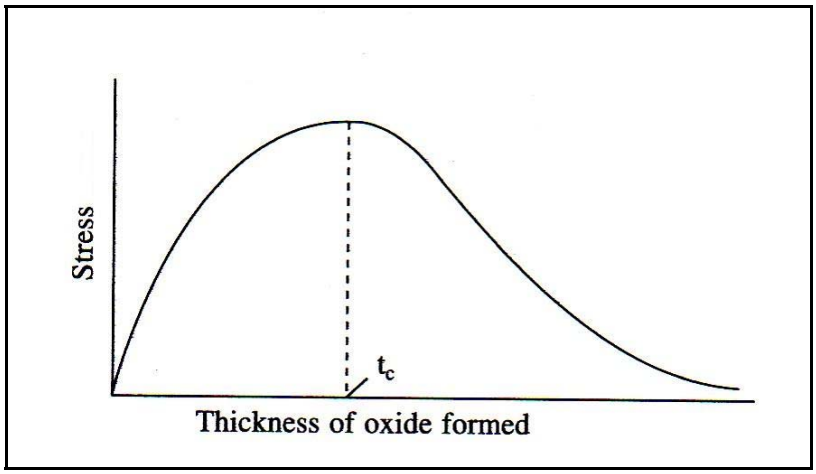

Figure 4.5 Stress accumulation in growing oxide layer [117].

Compositional changes in either alloy substrate or scale during oxidation can also induce internal stresses. Indeed, the depletion of the oxide-forming elements from the substrate may cause alteration in the lattice parameters that may, in turn, produce more stresses. Similarly, the change in the scale composition can also generate stresses as different oxides have different volumes [125]. High stresses are also induced as the scale grows on curvature surfaces or sharp corners. In general, the stress magnitude increases rapidly as the radius of curvature of the surface decreases [118].

The adhesion of the oxide scales in many metals is adversely affected by cation diffusion through the oxide film. This outward cationic diffusion, which has been observed in Fe-Cr alloys, generates vacancies that, upon accumulation, may lead to the formation of voids at the alloy/oxide interface (lack of adhesion) and eventually spallation. However, the formation of the voids could be prevented by the presence of dislocations or adding rare earth elements like Y or Sc, that are believed to act as a sink for the vacancies [117].

Thermally-induced stresses are generated as a consequence of the fluctuation in the exposure temperature, considering that the alloy and oxide possess different thermal expansion coefficients. In general, the resultant strain can be given by [118]:

$$\Delta\varepsilon = \Delta T(\alpha_O - \alpha_M) \tag{4.6}$$

where ΔT is the temperature drop; α_O and α_M are the thermal expansion coefficients of the oxide and metal respectively. The stresses are generated as a consequence of constraining the strain by the elasticity of the scale and substrate. Figure 4.6 shows the estimated oxide strains developed on some oxidised alloys as a result of the temperature change. The oxide strain generally increases as the temperature change increases [117].

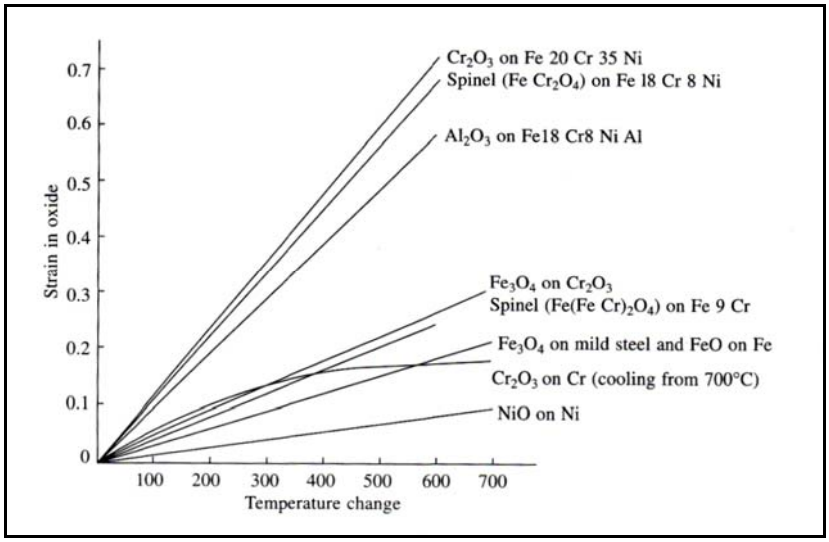

Figure 4.6 **Strains generated at the interface between various oxides and substrates by differential thermal expansion [117].**

The stress induced by temperature change is given by:

$$\sigma = \frac{E_O \Delta T(\alpha_O - \alpha_M)}{1 + 2(E_O / E_M)(t_O / t_M)} \tag{4.7}$$

where E_O and E_M are the Young's modulus of the oxide and metal respectively; α_O and α_M are the thermal expansion coefficients of the oxide and metal; t_O and t_M are the thicknesses of the oxide and metal; and ΔT is the temperature drop [117]. An equation has also been suggested to estimate the magnitude of the scale internal stresses. Considering the method of bending a metal strip of thickness d, clamped at one end and oxidised on one side, forming a thin oxide (of thickness t) with the radius of curvature due to bending r, the following formula has been obtained:

$$\sigma = \frac{E_O t(t+d)}{6rd} + \frac{(E_O - E_M)^3}{6rd(t+d)} \tag{4.8}$$

where E_O and E_M are the Young's modulus of the oxide and metal respectively [117].

4.1.4 Effect of Oxide Scale Composition on Metal Dusting

The composition of oxides depends mainly on alloy chemistry, oxygen partial pressure, and alloy pre-treatment. The establishment of Cr_2O_3, Al_2O_3, and SiO_2-containing scales has been proven to be an effective defence against metal dusting because of their reasonable stability under very low oxygen pressures. $MnCr_2O_4$ spinel has also been reported as stable and very impermeable to carbon, unlike MnO that was reported to have been less protective [63]. Indeed, spinel oxides become more stable in direct proportion to their chromium content. For instance, $Fe(Cr_{1-X}\ Fe_X)_2O_4$ is not as stable as chromium oxide, because of the presence of iron, which can be easily reduced in strongly carburising atmosphere. The composition of the iron-chromium spinel can vary from $FeCr_2O_4$ to Fe_3O_4 (magnetite) with $FeCr_2O_4$ as more stable than magnetite, though it was reported to have

been readily reduced by carbon at 600ºC [96]. In short, nickel and/or iron-bearing spinels could be reduced by carbon in metal dusting conditions and, also, their nickel and/or iron content may catalyse the carbon deposition on alloys, and hence increase the probability of metal dusting [63].

4.2 Investigation Objectives

Much metal dusting research has emphasised the role of oxidation in slowing down or even preventing metal dusting. However, it is not clear whether the oxide layers formed at the metal dusting temperature range (i.e. 400-800ºC) are sufficient to provide a reliable barrier between the metal and the environment. Therefore, oxidation of the heat-resistant alloys KHR35C HiSi (HP), KHR45A LC (35Cr-45Ni), and UCX was of extremely high interest in order to assess their performance and ability to form protective oxide scale at such temperatures. Accordingly, a study has been undertaken where the alloys were exposed to static air at temperatures of 650, 750, and 850ºC, for 100 and 1000 hours. The investigation was basically aimed at exploring the scale growth and identifying the oxide phases formed at these conditions. The alloys were characterised using visual examination, weight change measurements, scanning electron microscopy (SEM), energy dispersive x-ray spectroscopy (EDX), and x-ray diffraction (XRD) techniques.

The alloys performance in metal dusting may be predicted by considering their chromium equivalents (elucidated in Chapter 1; 1.6.1), i.e. Cr_{equiv} = %Cr + 3 × (%Si + %Al). Using Table 2.1, the chromium equivalents were calculated for the three alloys as follows:

Alloy HP,	Cr_{equiv} = 29.9
Alloy 35Cr-45Ni,	Cr_{equiv} = 36.8
Alloy UCX,	Cr_{equiv} = 47.0

Accordingly, alloy UCX possesses the maximum chromium equivalent and, hence, is anticipated to exhibit the optimum metal dusting resistance. However, this does not imply that any alloy is immune to metal dusting.

4.3 Experimental Apparatus and Procedure

4.3.1 Short-Term Tests

A ceramic tube furnace, designed by Lenton Furnaces, was used for the short-term tests. The experiment set up is shown in Figure 4.7. Apparatus used were:

- Tube furnace with dimension: 7.5cm ID & 65cm long.
- Alumina crucibles (99.8% Al_2O_3 and 0.05% max MgO) with dimension 74mm long, 53mm wide and 15mm deep.
- Samples from each alloy with dimension 20X20X5mm, ground to 120grit. The specimen edges were rounded to minimise oxide spallation. Each sample dimension was measured using digital callipers and micrometer. In total, eighteen samples were used in this study.
- Four decimal, digital balance (Mettler AT261 DeltaRange) was used for weight measurements.
- Thermocouple type K.
- Temperature measuring instrument (testo 925).
- Ceramic fibres at the tube ends, to reduce the air flow through the tube in order to avoid significant temperature fluctuations.

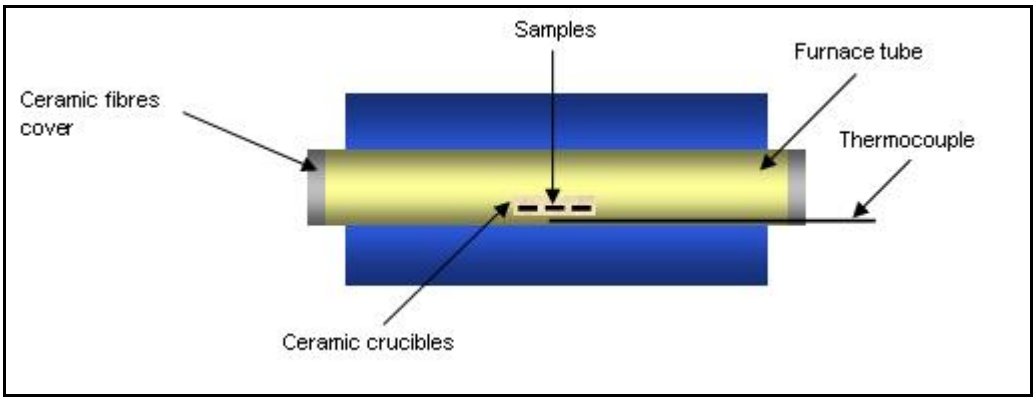

Figure 4.7 A schematic of the experiment's set up.

Temperature profiling measurements, at 650 and 750ºC were carried out in order to establish the temperature distribution along the tube and locate the hot zones. The measurements were attained by gradually inserting a marked thermocouple into the tube and recording the corresponding temperature. The temperature readings were obtained with and without the use of ceramic fibre sealing in order to understand the airflow effect on temperature. Details of temperature profiling are included in Appendix B.

The samples were thoroughly washed, firstly by water and secondly by acetone. They were then weighed and placed in the crucible as shown in Figure 4.8, and placed in the hottest region of the furnace.

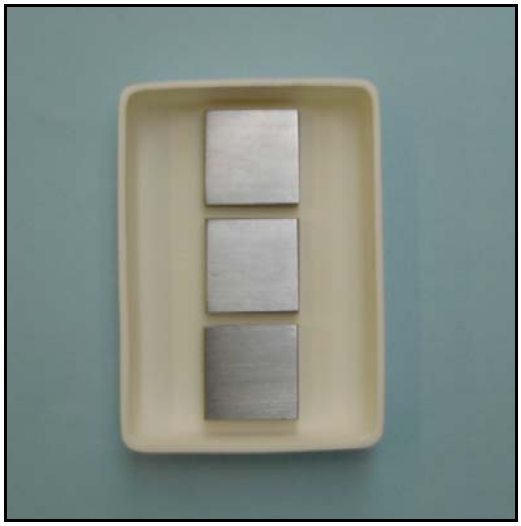

Figure 4.8 The samples were placed in alumina crucibles.

The heating and cooling rates were recorded and are shown in Appendix B. The furnace heated up to 650, 750, and 850ºC in 28, 30, and 38 minutes respectively. However, it took much longer time for the furnace to cool down. All the above temperature measurements were carried out whilst the furnace tube was sealed by the ceramic fibre covers (i.e. static air condition). Importantly, the heating and cooling intervals were not included in the test time.

Although the testing temperatures had been set to 650, 750, and 850ºC, the temperatures of air measured at the crucible were 643, 743, and 840ºC respectively. The first experiment (i.e. 650ºC) was interrupted, after running for 13 hours, due to furnace trip caused by failure of the control thermocouple. The thermocouple was replaced and the experiment was resumed 18 days later. The subsequent experiments went smoothly without any interruption. The samples and crucibles were weighed after each exposure.

4.3.2 Long-Term Tests

Two chamber furnaces were utilised to conduct the long-term studies. The 650ºC test was carried out in Carbolite furnace (type CSF 11/7) whilst the others were accomplished in Carbolite furnace (type ELF 11/6). The same experimental procedures applied for the short-term tests were followed in the long-term investigation including the use of similar sample dimensions and surface conditions.

The heating and cooling rates of both furnaces are plotted in Appendix B. The furnaces heated up to 650, 750, and 850ºC in 56, 9, and 14 minutes respectively, but, indeed, needed much longer times to cool down. The heating and cooling times were not counted for in the test time.

4.4 Analyses and Results

4.4.1 Short-Term Tests

4.4.1.1 Visual Examination

Figures 4.9-4.11 show the state of the specimens oxidised at 650, 750, and 850ºC after being removed from the furnace.

Visual examination revealed that the 650ºC specimens underwent little oxidation as their surfaces stayed shiny. The surfaces of 35Cr-45Ni and UCX appeared shinier than that of HP, which could possibly be attributed to the higher iron content in HP, which in turn, promoted the formation of more iron oxides at such relatively low temperature. Moreover, localised oxidation (in form of blackish spots) could be observed on the alloys, particularly 35Cr-45Ni and UCX. This might be well caused by either incomplete oxide lateral growth or the relatively inhomogeneous microstructures of the alloys. Localised oxidation might also be the result of varying surface condition [40].

Increasing the exposure temperature to 750ºC led to the formation of denser oxides. Greenish deposits could be seen on the alloys, especially HP and 35Cr-45Ni suggesting the development of chromium-containing oxides. However, the alloy surfaces were not entirely covered by uniform oxides, and some bare alloy surfaces were recognised, Figure 4.10.

Formation of thicker, blackish oxides was pronounced on the alloys after the 850ºC test. However, the oxide layers suffered severe spallation due to the generation of high internal stresses induced by oxides thickening and relatively fast cooling rate. Figure 4.11 reveals the degree of the scale spallation as the oxide particles could be observed scattered within the crucible.

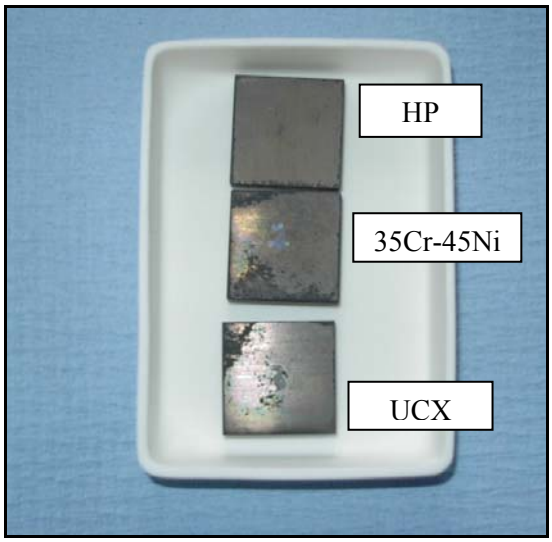

Figure 4.9 Specimens after exposure to air at 650ºC.

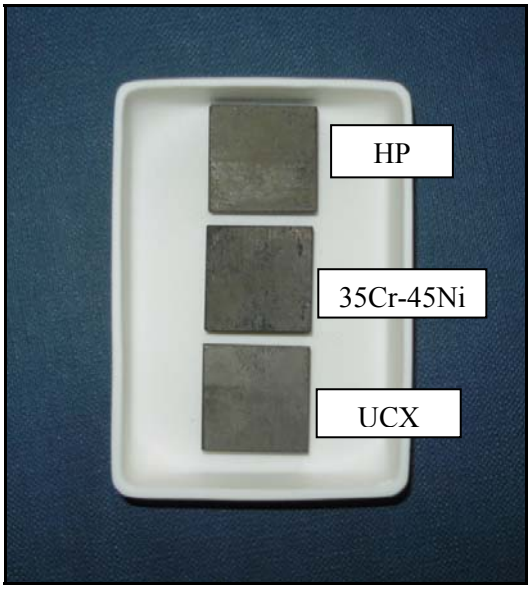

Figure 4.10 Specimens after exposure to air at 750ºC.

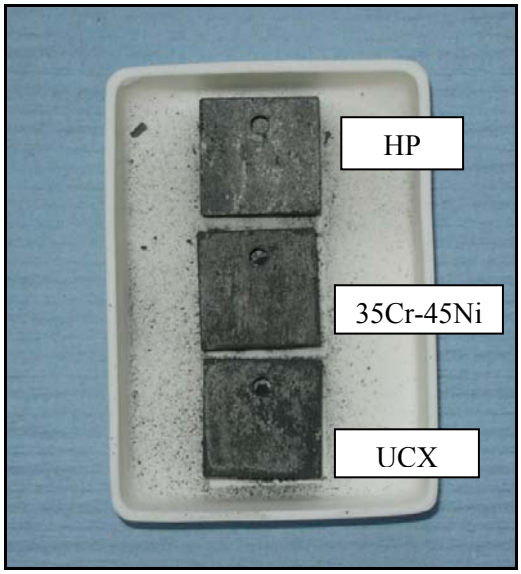

Figure 4.11 Specimens after exposure to air at 850ºC.

4.4.1.2 Weight Change Measurements

The influence of temperature on the oxidation kinetics was investigated by considering the samples' weight change (more details are given in Appendix B). In general, all three alloys experienced increasing weight change with increasing temperature (Figure 4.12).

The specimens exposed at 650ºC did not undergo significant weight change, with UCX gaining the highest, i.e. 0.1004 mg/cm^2, and HP showing no weight change at all. It is worth observing that alloys with higher levels of chromium and nickel (i.e. 35Cr-45Ni and UCX), exhibited more reactivity and thus gained more weight than the iron-based alloy HP.

Oxidising the alloys at 750ºC, however, resulted in more weight gain, with the highest noted on 35Cr-45Ni (0.1507 mg/cm^2). Interestingly, the least weight change, at both temperatures, was observed on HP. The percentage of change (or increase) in weight change (from 650 to 750ºC) was calculated to be 100%, 83%, and 30% for HP, 35Cr-45Ni, and UCX respectively.

Considerably higher weight changes took place on the alloys after the 850ºC exposure. Unlike their behaviour at 650 and 750ºC the alloys experienced weight loss, with HP suffering the highest. The weight loss was most likely due to the generation of internal stresses induced by the formation of thicker oxides which could spall easily at relatively fast cooling rates. Otherwise the oxide layer might be expected to have been intact and more protective if the cooling rate was adequately slow. The percentage increase in the scale thickness was not calculated for the 850ºC samples because of the spallation effect.

Considering the above it is obvious that the oxidation rate had drastically increased in agreement with temperature.

Referring to the visual examination findings and weight change measurements, the formation of a protective oxide layer especially at 650 and 750ºC is indeed questionable. It is worth mentioning, nevertheless, that weight change measurements themselves are not sufficient to evaluate the ability of an alloy to form a protective oxide scale as the level of protection depends on the oxide thickness and, more importantly, on oxide microstructure and morphology.

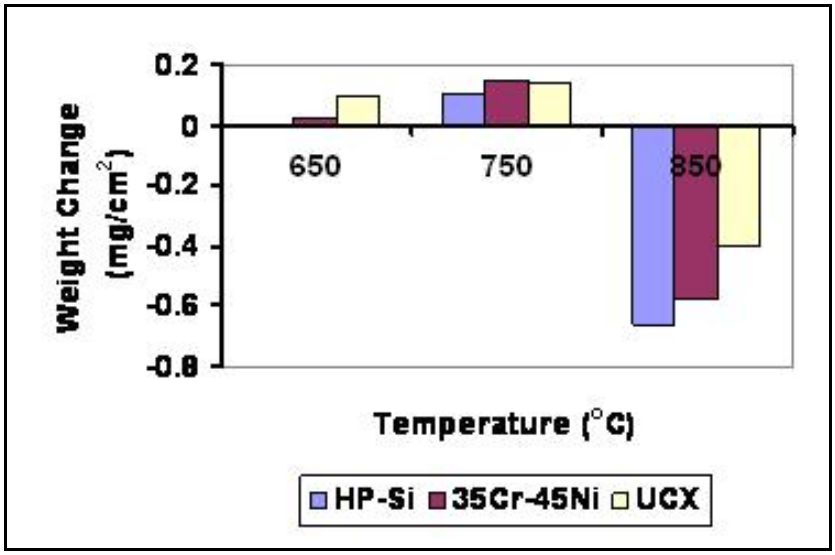

Figure 4.12 **Weight change measurements for the alloys after the exposure at 650, 750, and 850ºC for 100h.**

4.4.1.3 Surface Analyses

Scanning electron analysis (JEOL 5800 LV) was utilised in examining the alloy surfaces. Figures 4.13-4.15 are secondary electron images revealing the surface of the samples after the exposure at the three temperatures (more images are shown in Appendix B).

Small crystallites could generally be observed on the alloys, and their densities and sizes were found to have increased in agreement with temperature. Also, each specimen formed crystallites with appreciably variable size.

On alloy HP oxidised at 650ºC, crystallites with a maximum size of approximately 0.8μm were observed.

However, denser oxides formed on the alloy after the 750ºC exposure, with a maximum crystal size of around 1.5μm. The crystallites grew up to about 2.5μm following the oxidation at 850ºC.

Alloy 35Cr-45Ni formed many crystallites with a maximum size of about 1μm, after the oxidation at 650ºC. The maximum size of the crystallites increased to approximately 1.3μm as a result of increasing the temperature to 750ºC.

Alloy UCX, however, formed fewer, discretely distributed crystallites (~ 0.5μm max) when compared with the others, although at 750ºC the size of oxide crystals was larger than those formed on HP and 35Cr-45Ni (~ 2μm).

It should be pointed out that most oxides formed on specimens tested at 850ºC spalled off and hence their amounts and sizes shown in the micrographs are in fact anticipated to be less than the actual values. To sum up, the above observations clearly illustrate the crucial role of temperature on oxide nucleation and growth on centrifugally cast, heat-resistant alloys.

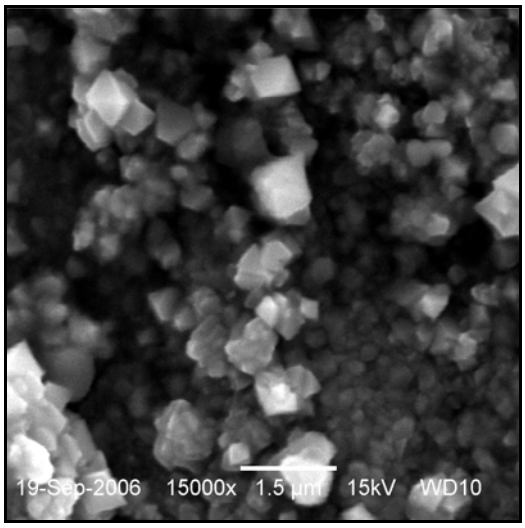

(a)

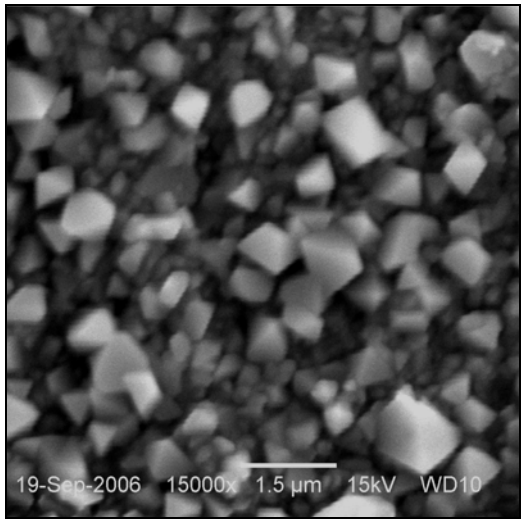

(b)

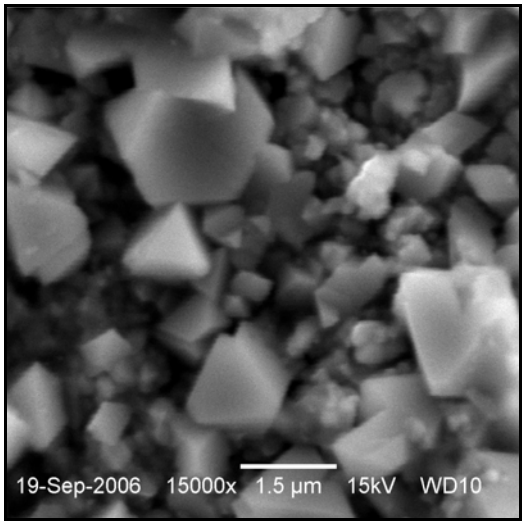

(c)

Figure 4.13 SEM/SE images of alloy HP surfaces exposed at (a) 650ºC, (b) 750ºC, and (c) 850ºC.

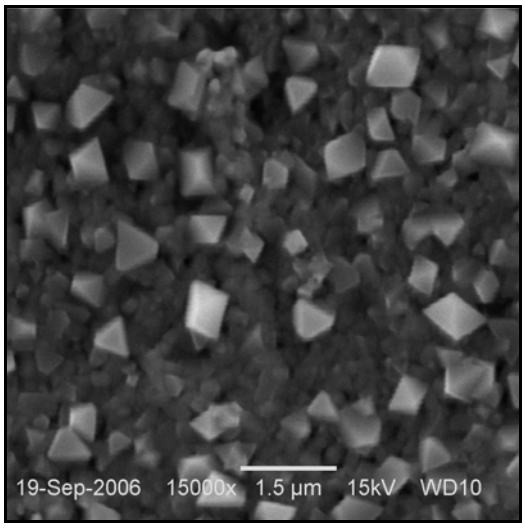

(a)

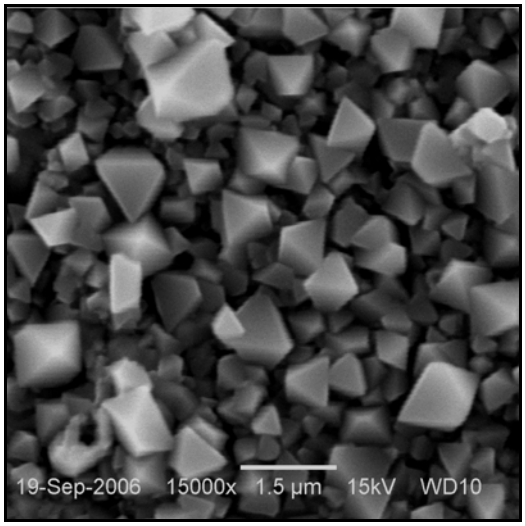

(b)

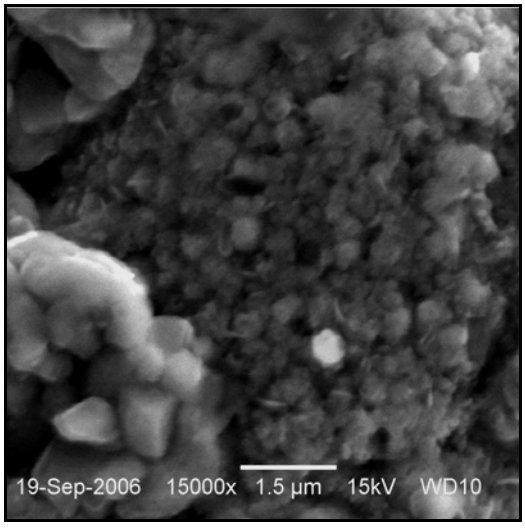

(c)

Figure 4.14 **SEM/SE images of alloy 35Cr-45Ni surfaces exposed at (a) 650ºC, (b) 750ºC, and (c) 850ºC.**

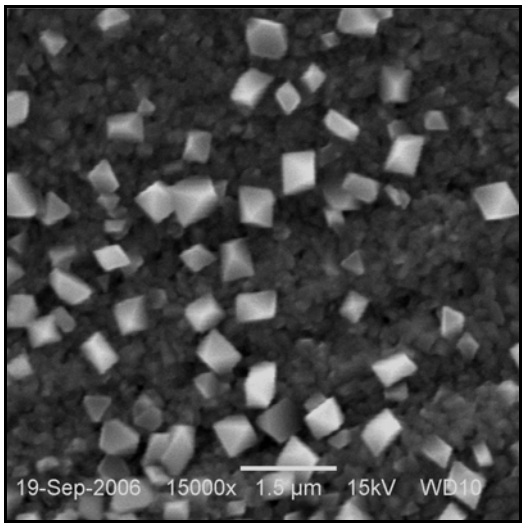

(a)

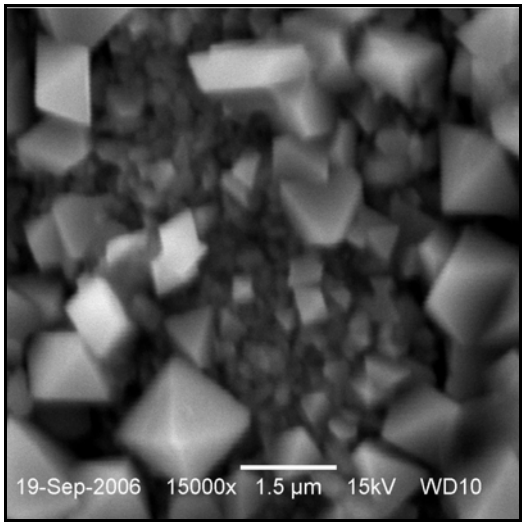

(b)

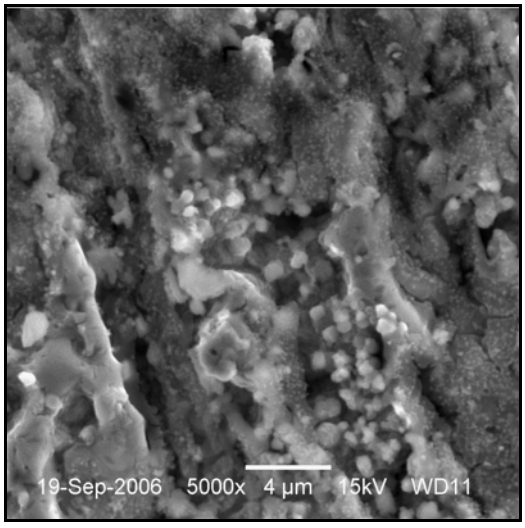

(c)

Figure 4.15 SEM/SE images of alloy UCX surfaces exposed at (a) 650ºC, (b) 750ºC, and (c) 850ºC.

4.4.1.4 XRD Analyses

A Philips vertical diffractometer, PW 1830/00, with Cu Kα radiation, was used to identify the alloys surface composition. The software Philips X'pert Data Collector was used to collect the data whereas Philips X'pert Plus and HighScore Plus were used for peak searching and phase identification. The X-ray diffraction charts and patterns are given in Appendix B. The oxides formed on alloy HP, at both 650 and 750ºC, were composed mainly of chromium oxide (Cr_2O_3) and $Mn_{1.5}Cr_{1.5}O_4$. At 850ºC the alloy formed Cr_2O_3, $NiMn_2O_4$, and some FeO. The oxides on alloy 35Cr-45Ni, exposed at 650ºC, consisted of Cr_2O_3 and $Cr_{1.5}Fe_{0.5}MnO_4$. At higher temperature (i.e. 750ºC), however, $Mn_{1.5}Cr_{1.5}O_4$ formed as well as Cr_2O_3. Chromium oxide (Cr_2O_3), nickel oxide (NiO), and FeO were detected at 850ºC. The alloy UCX showed only the formation of Cr_2O_3 at 650ºC. However, the analysis of specimen exposed at 750ºC confirmed the presence of $Mn_{1.5}Cr_{1.5}O_4$ in addition to Cr_2O_3. Only Cr_2O_3 was detected at 850ºC.

4.4.1.5 Metallographic Examination

Cross sections of the alloys were prepared to study further the oxide layers formed on each alloy. The investigation was carried out using the scanning electron microscope, FEI Quanta 200 SEM with Oxford INCA 250 EDX system attachment.

The samples were mounted in Multifast (manufactured by Struers) that was nonconductive, and therefore copper tapes were used to provide a conductive path from the samples to ground in order to avoid charging. The samples were ground and polished to 9μm using diamond suspension and finally polished to 0.04μm by colloidal silica suspension.

It is important to state that, during the analyses; areas with intact oxide and maximum layer thickness were located and imaged. Backscattered electron imaging and quantitative EDX analyses were utilised to investigate the oxides throughout this study.

An uneven, thin oxide layer was observed to have formed on the alloy HP after the exposure at 650ºC. The thickness of the layer varied from 0.2 to 1µm, with 0.7µm as typical (Figure 4.16). EDX analyses of the two spots, P1 and P2, showed different oxide composition with chromium oxide as the main constituent in both. More nickel, silicon, and iron were detected at point P1, where the layer was less dark than point 2. At point 2, however, more manganese was detected. The line profiling, across the formed layer (along the yellow line in Figure 4.16), revealed the presence of chromium and oxygen peaks suggesting that the scale was mainly composed of chromium oxide. A silicon peak was also observed just beneath the chromium peak suggesting the formation of a silicon oxide layer (~ 0.4µm) below the chromium oxide. Moreover, approximately a 3µm, chromium-depleted zone was also detected in the substrate.

Relatively thicker, more uniform oxide layer, of about 0.5-1.2µm thickness, had formed on the alloy after the oxidation at 750ºC (Figure 4.17). EDX analyses revealed that O, Cr, and Mn were the main constituents of the scale. Interestingly, zirconium was also detected, at the two spots, in considerable amounts (1.11 & 2.88 wt%). Iron and nickel were also observed. The line profiling of the substrate revealed that the predominant oxide was that of chromium, with some iron and silicon-containing oxides formed just near the alloy-oxide interface.

Some intact oxide scale could be found on the alloy after the 850ºC exposure despite the severe spallation caused by a fast cooling rate (Figure 4.18). Much thicker (~2µm), more even, and denser oxide scale had formed on the alloy. The oxide composition was confirmed by EDX as mainly chromium oxide. The lighter grey oxide, however, contained a considerable amount of manganese (~18.81wt%), and traces of silicon and iron. The line profiling analyses showed the distribution of elements across the substrate. Chromium peak detected within the mounting material was probably a result of contamination with alloy particles during the sample preparation.

Collectively, increasing the exposure temperature rendered the oxide layers thicker and denser on HP alloy. It was also noticed that the amount of alloying elements, iron, nickel, and niobium in the oxides, was reduced as the temperature was increased.

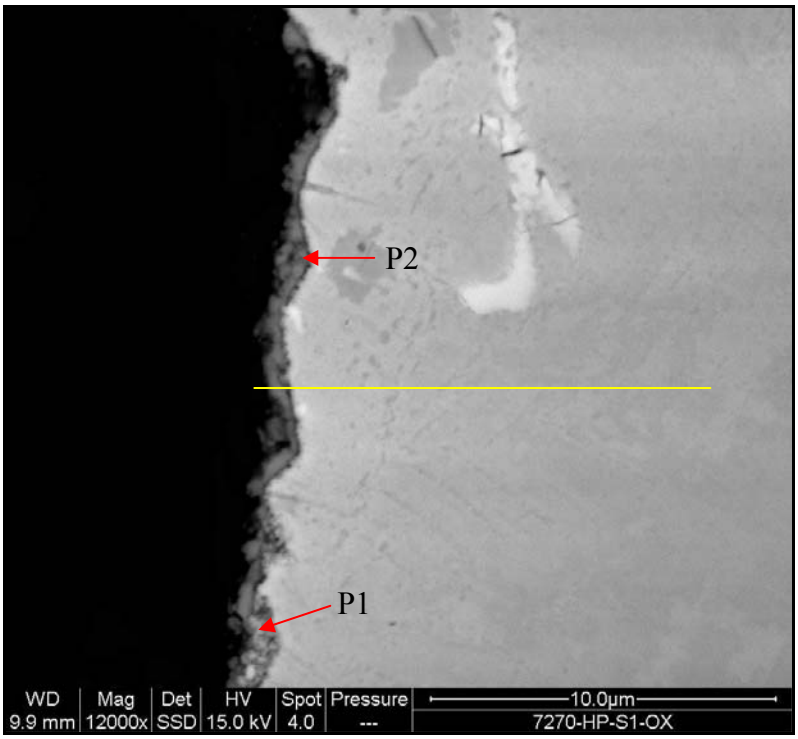

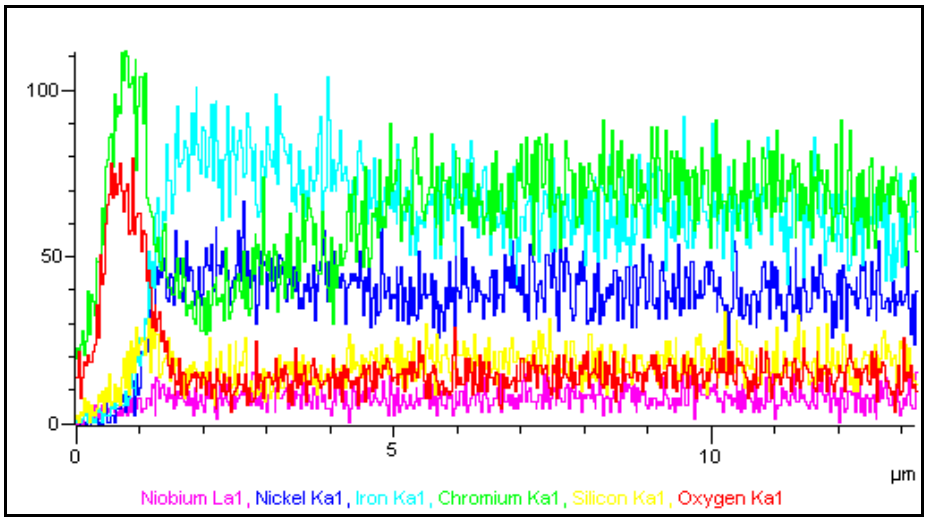

P1

Element	Weight%	Atomic%
C K	9.88	24.95
O K	16.23	30.78
Si K	5.97	6.45
Ca K	0.32	0.24
Cr K	40.45	23.60
Mn K	1.15	0.63
Fe K	4.54	2.47
Ni K	20.29	10.48
Nb L	1.17	0.38
Totals	100.00	

P2

Element	Weight%	Atomic%
C K	15.25	31.53
O K	26.39	40.96
Si K	0.68	0.60
Ca K	0.34	0.21
Cr K	42.70	20.39
Mn K	6.16	2.79
Fe K	3.99	1.77
Ni K	3.60	1.52
Nb L	0.88	0.24
Totals	100.00	

Figure 4.16 Oxide formation on alloy HP exposed to air at 650°C.

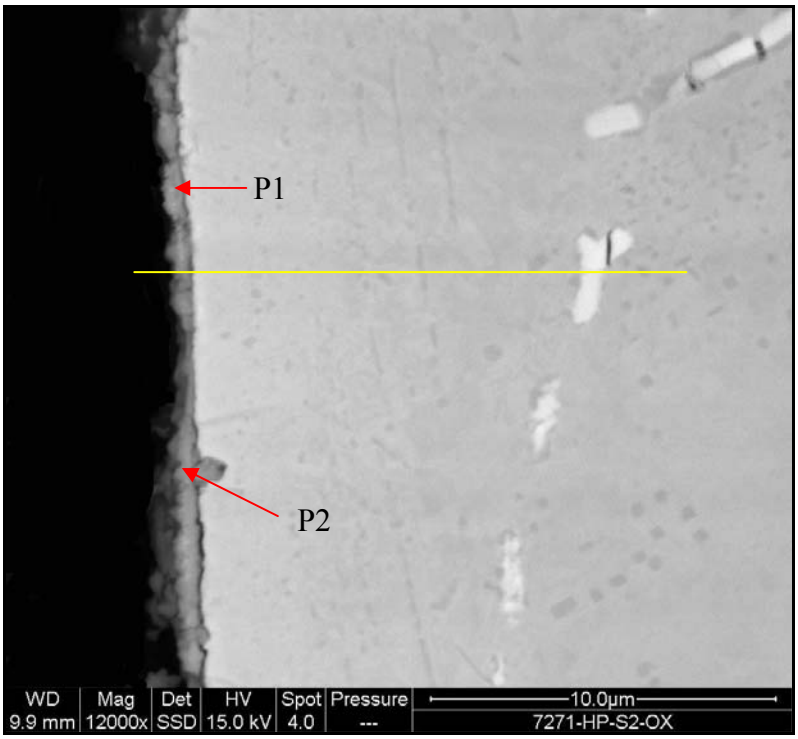

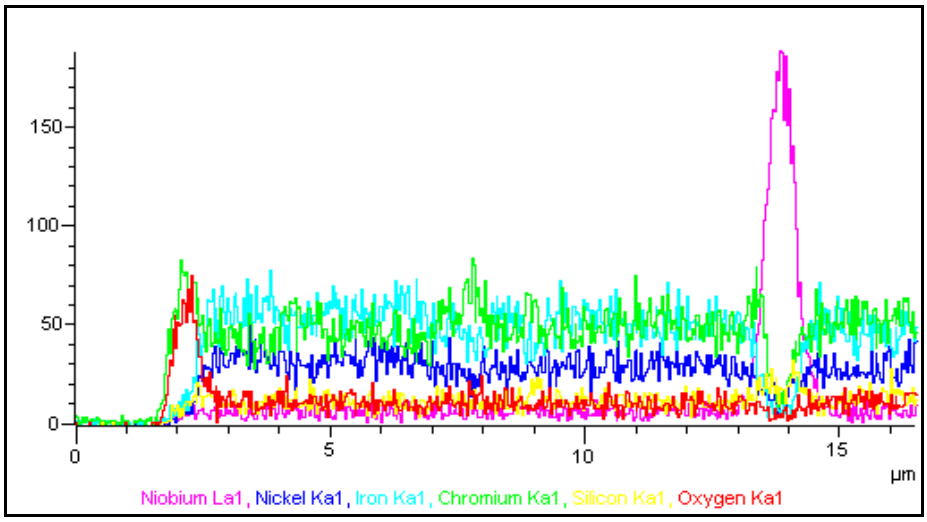

P1

Element	Weight%	Atomic%
C K	14.63	28.90
O K	31.82	47.19
Al K	0.14	0.13
Si K	0.78	0.66
Ca K	0.69	0.41
Cr K	35.67	16.28
Mn K	7.74	3.34
Fe K	3.18	1.35
Ni K	2.47	1.00
Zr L	2.88	0.75
Totals	100.00	

P2

Element	Weight%	Atomic%
C K	13.77	26.63
O K	34.83	50.58
Si K	0.78	0.65
Ca K	0.59	0.34
Cr K	37.65	16.83
Mn K	6.15	2.60
Fe K	2.85	1.18
Ni K	2.28	0.90
Zr L	1.11	0.28
Totals	100.00	

Figure 4.17 Oxide formation on alloy HP exposed to air at 750ºC.

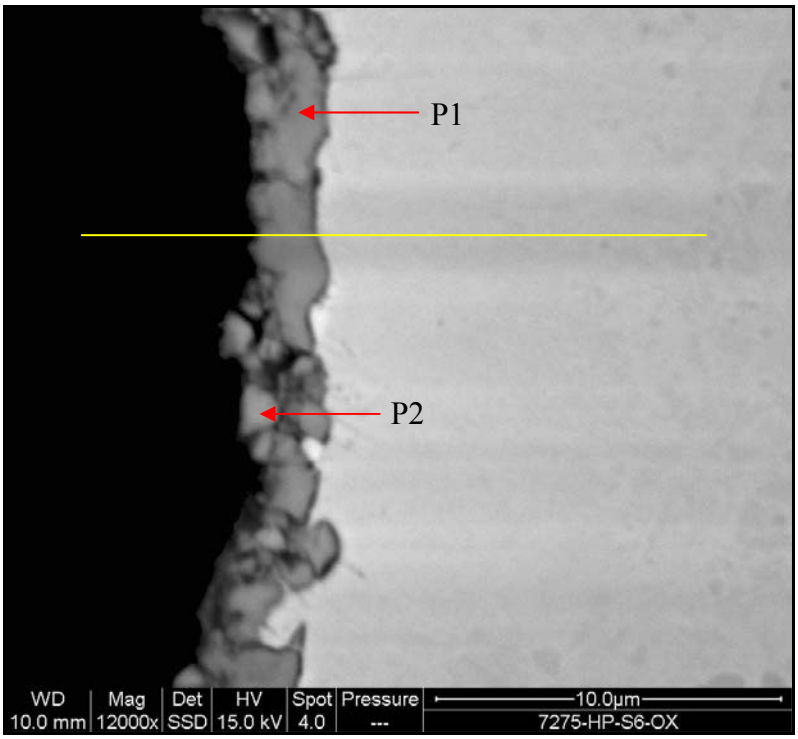

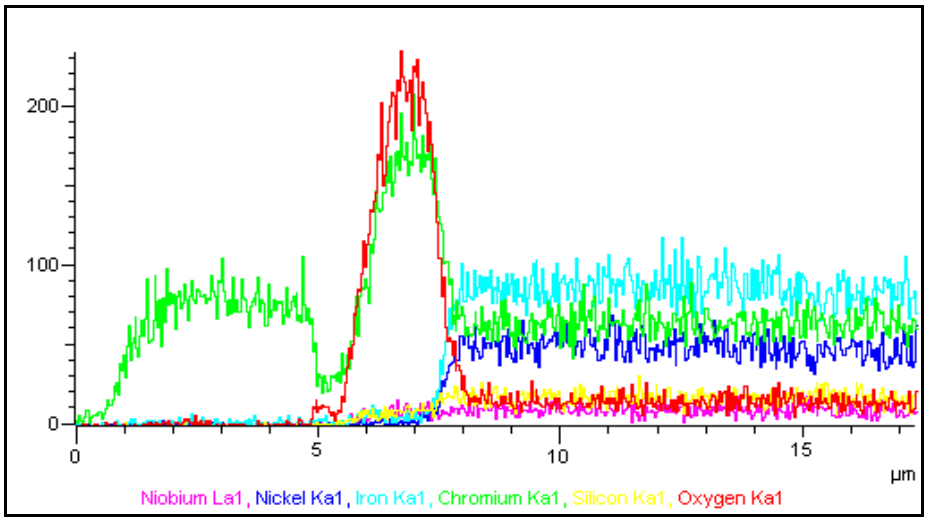

P1

Element	Weight%	Atomic%
C K	3.71	8.16
O K	37.61	62.10
Ca K	0.24	0.16
Cr K	54.10	27.49
Mn K	4.33	2.08
Totals	100.00	

P2

Element	Weight%	Atomic%
C K	17.85	33.55
O K	31.79	44.85
Si K	0.31	0.25
Ca K	0.64	0.36
Cr K	29.86	12.96
Mn K	18.81	7.73
Fe K	0.74	0.30
Totals	100.00	

Figure 4.18 Oxide formation on alloy HP exposed to air at 850ºC.

A thin oxide layer was observed on the 35Cr-45Ni specimen as a result of exposure to air at 650ºC (Figure 4.19). The layer thickness varied from 0.2µm to 1.3µm, with typical thickness of 0.8µm. Elemental analyses showed that O, Cr, and Mn were the major constituents of the scale while Fe, Ni, and Si were the minor. A 2.5µm chromium depleted area was noticed using the line profiling. The niobium peak detected by the line profiling indicated the presence of niobium carbide phase (white precipitates).

Non uniform oxide thickness was also observed on the 35Cr-45Ni specimen as a result of exposure to air at 750ºC (Figure 4.20). The layer thickness varied from 0.2µm to 1.2µm. Elemental analyses showed that the scale was mainly composed of O, Cr, and Mn, with Fe, Ni, and Si in minor amounts. However, higher amounts of Fe and Ni were detected at this temperature. Approximately a 3.5µm chromium-depleted zone was observed by line profiling.

A thicker oxide layer (~3.4µm) was observed on the alloy at 850ºC (Figure 4.21). The layer appeared to be continuous, even, and dense. However, this should not imply that the whole specimen was covered with such oxide as most of it suffered spallation during the cooling down. The oxide layer was found to contain chromium oxide and some manganese-containing spinel. Traces of Fe, Si, and Ni were also detected. The line profiling showed the formation of some silicon oxide at the lower part of the chromium oxide layer.

In short, the alloy 35Cr-45Ni underwent more oxide growth in direct proportion to the exposure temperature. Consequently the oxide layer became denser, more uniform and contained less nonprotective iron and nickel oxides.

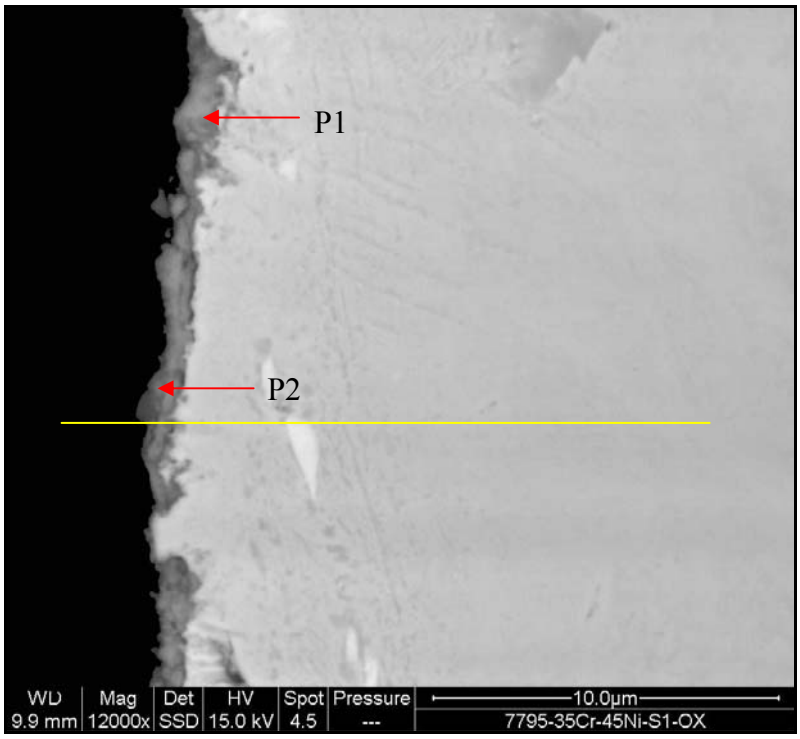

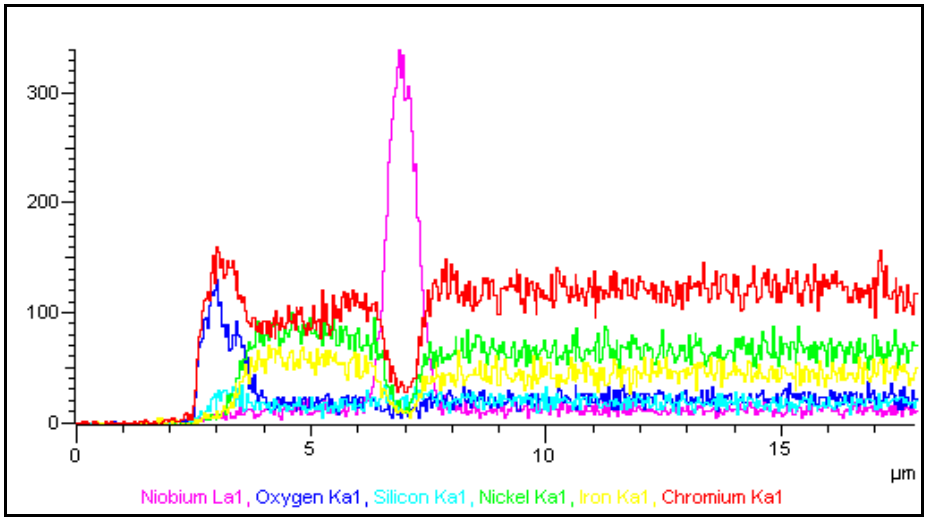

P1

Element	Weight%	Atomic%
C K	8.35	17.90
O K	33.07	53.22
Si K	0.19	0.18
Ca K	0.27	0.17
Cr K	50.19	24.85
Mn K	6.43	3.02
Fe K	0.64	0.29
Ni K	0.85	0.37
Totals	100.00	

P2

Element	Weight%	Atomic%
C K	15.11	30.67
O K	27.90	42.51
Si K	0.40	0.34
Ca K	1.09	0.66
Cr K	48.91	22.93
Mn K	4.65	2.06
Fe K	1.03	0.45
Ni K	0.92	0.38
Totals	100.00	

Figure 4.19 Oxide formation on alloy 35Cr-45Ni exposed to air at 650ºC.

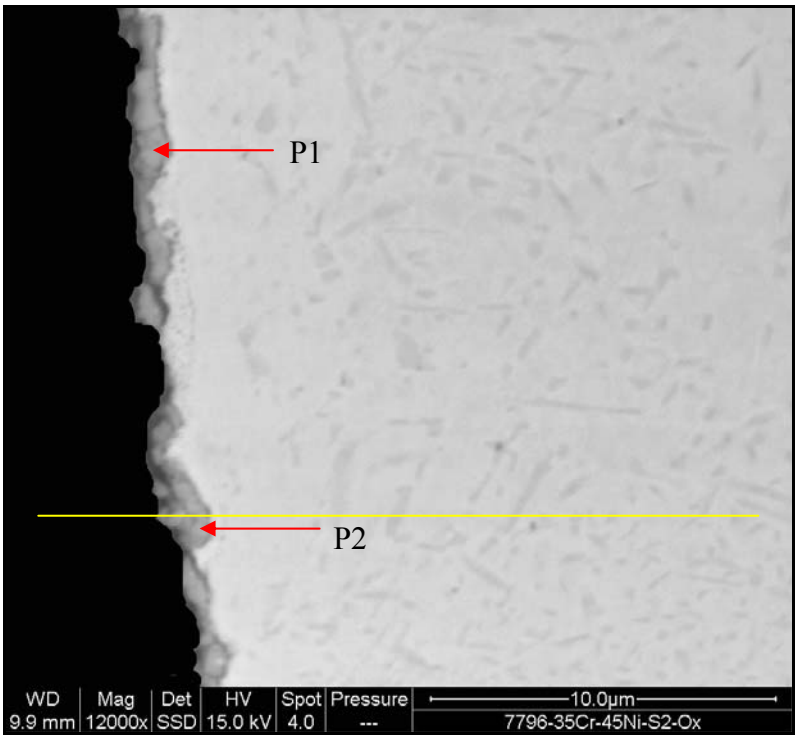

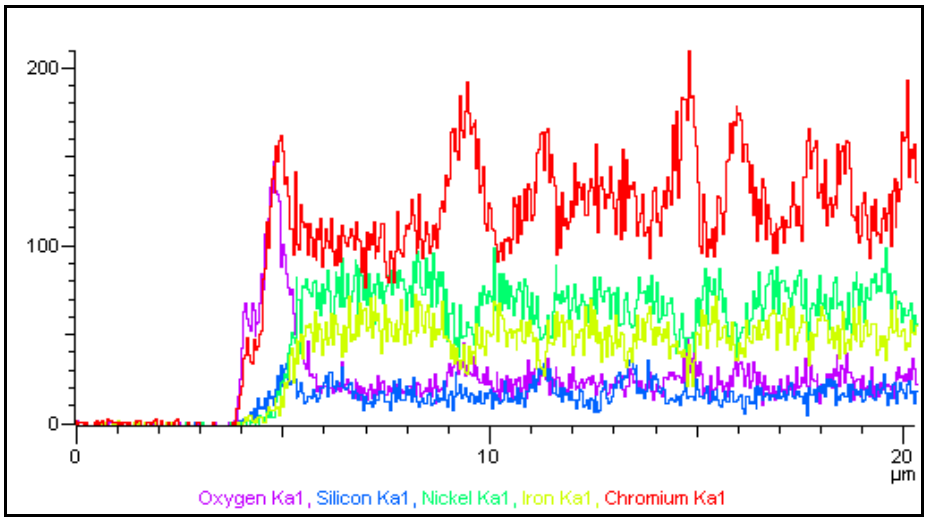

P1

Element	Weight%	Atomic%
C K	9.72	20.92
O K	30.56	49.38
Si K	0.61	0.56
Ca K	0.34	0.22
Cr K	50.72	25.22
Mn K	4.31	2.03
Fe K	1.22	0.56
Ni K	2.52	1.11
Totals	100.00	

P2

Element	Weight%	Atomic%
C K	11.44	24.88
O K	27.27	44.54
Si K	1.08	1.00
Ca K	0.37	0.24
Cr K	41.77	20.99
Mn K	7.02	3.34
Fe K	3.71	1.73
Ni K	7.35	3.27
Totals	100.00	

Figure 4.20 Oxide formation on alloy 35Cr-45Ni exposed to air at 750°C.

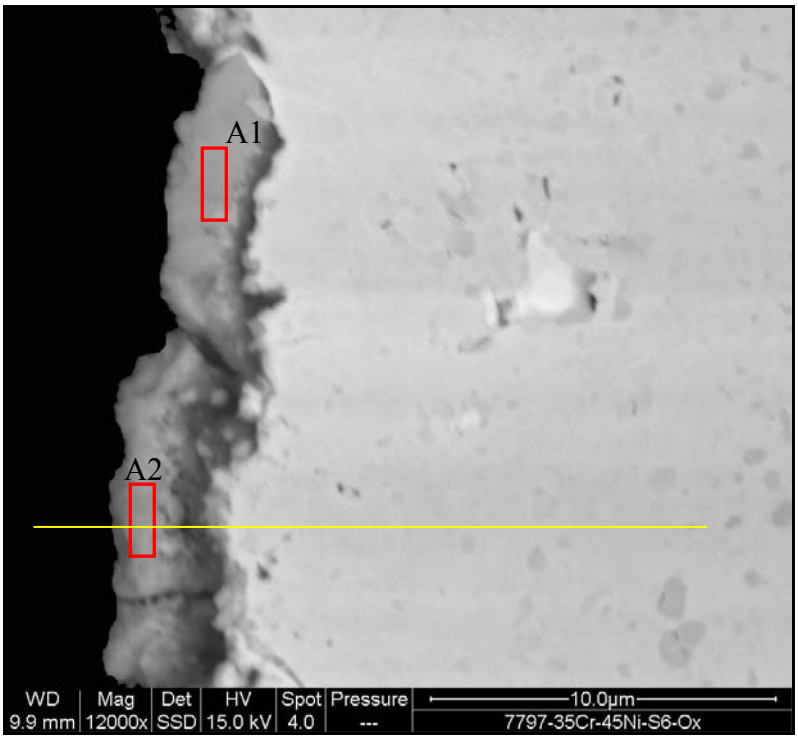

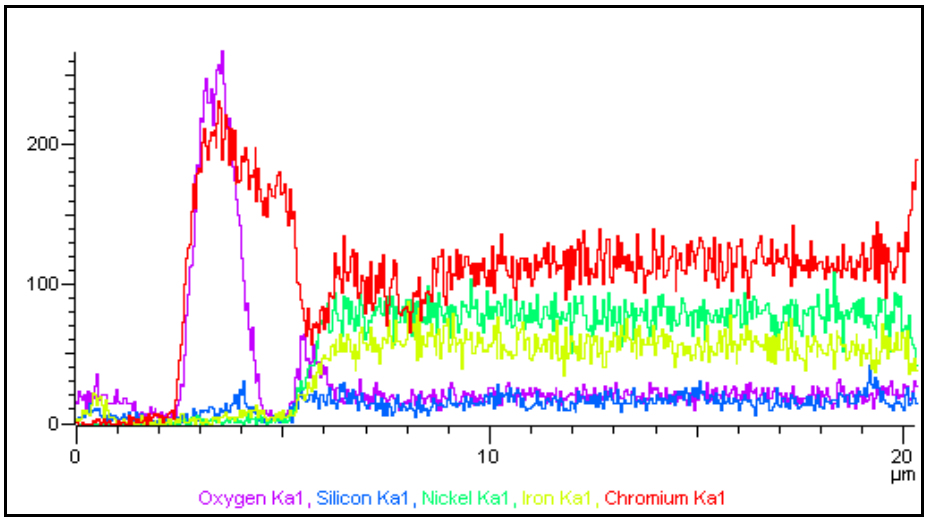

A1

Element	Weight%	Atomic%
C K	2.19	5.17
O K	34.01	60.16
Ca K	0.31	0.22
Cr K	60.23	32.79
Mn K	2.78	1.43
Ni K	0.48	0.23
Totals	100.00	

A2

Element	Weight%	Atomic%
C K	4.99	10.96
O K	35.78	58.97
Si K	0.20	0.18
Ca K	0.26	0.17
Cr K	56.11	28.45
Mn K	2.26	1.09
Fe K	0.39	0.19
Totals	100.00	

Figure 4.21 Oxide formation on alloy 35Cr-45Ni exposed to air at 850°C.

A thin, non uniform oxide layer had formed on the alloy UCX after exposure at 650ºC (Figure 4.22). The layer formed was 0.2µm thick with some localised 1.2µm oxides. A 2.5µm chromium depleted area could be noted at the substrate. The layer was mainly composed of O, Cr, Mn, Fe, and Ni.

A non uniform layer, with thickness varying from about 0.3µm to 1.4µm, had formed on the UCX alloy after the 750ºC test (Figure 4.23). The layer was composed of O, Si, Cr, Mn, and Ni (P1). Compared with oxides formed at 650ºC, this layer contained higher amounts of Si, Mn, and oxygen and lower amounts of Ni, with no iron detected. The elemental analysis of the phase, A1, revealed that it contained mainly chromium-rich carbide with a considerable amount of tungsten. The photomicrograph showed the presence of a chromium-depleted zone of about 5µm in depth.

Much thicker, denser, and more even oxide scale was found to have formed on the alloy at 850ºC, see Figure 4.24. The layer was typically 3µm thick, although there were some localised areas in which thicker oxides formed (~7µm). The oxide layer was mainly chromium oxide with some Mn, Ni, and Si-containing oxides. From the line profiling it is evident that a silicon rich layer had formed just at the alloy/chromium oxide interface. Approximately a 15µm chromium depleted zone was observed at the substrate. From the EDX results, it is obvious that iron and nickel levels in the oxides were reduced as a consequence of increasing the exposure temperature. This was also accompanied by significant scale growth, from 0.2µm to 3µm.

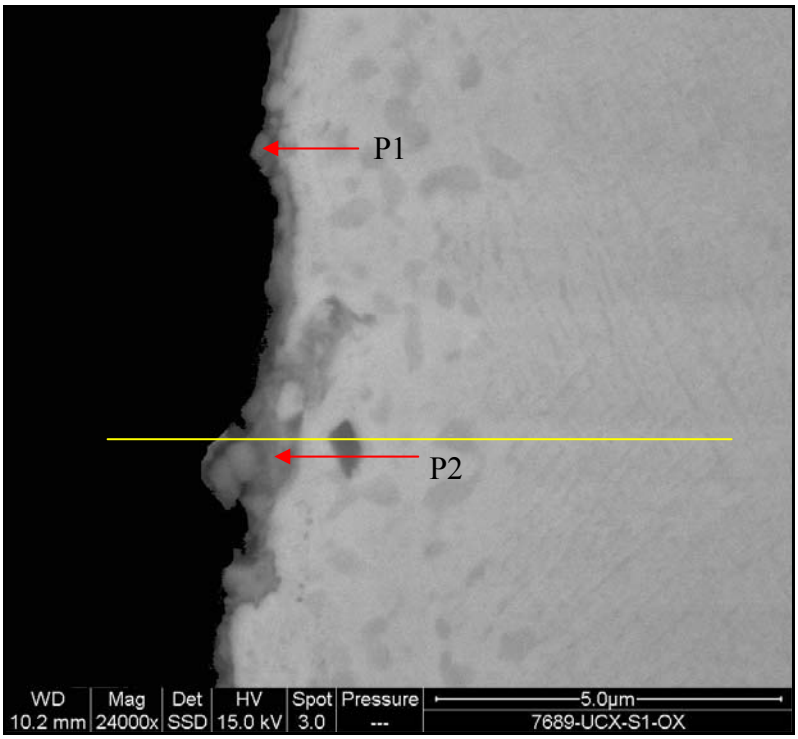

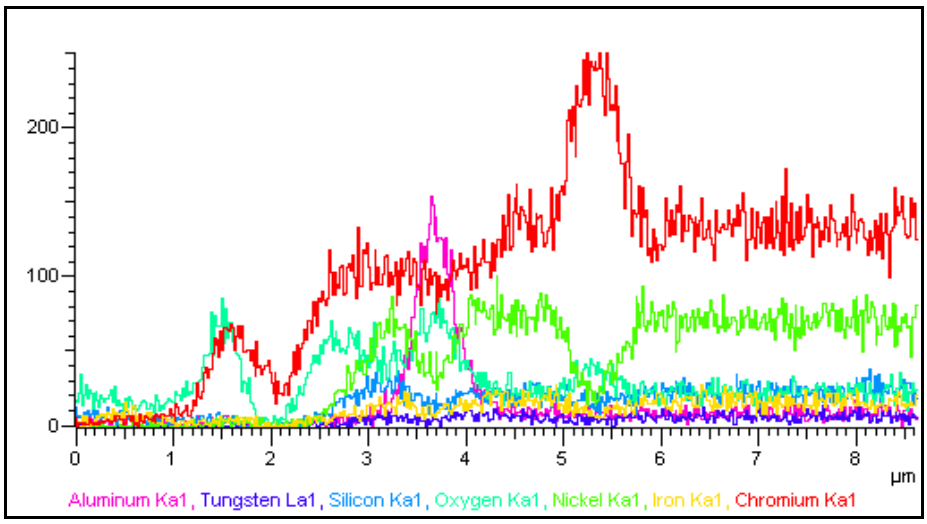

P1

Element	Weight%	Atomic%
C K	23.28	46.29
O K	18.03	26.91
Si K	1.51	1.28
Ca K	1.44	0.86
Cr K	36.04	16.56
Mn K	5.36	2.33
Fe K	1.32	0.56
Ni K	10.27	4.18
Cu K	1.46	0.55
Zn K	1.29	0.47
Totals	100.00	

P2

Element	Weight%	Atomic%
C K	21.55	44.69
O K	16.95	26.38
Si K	1.50	1.33
Ca K	0.58	0.36
Cr K	33.31	15.96
Mn K	5.22	2.37
Fe K	2.19	0.98
Ni K	18.71	7.94
Totals	100.00	

Figure 4.22 Oxide formation on alloy UCX exposed to air at 650ºC.

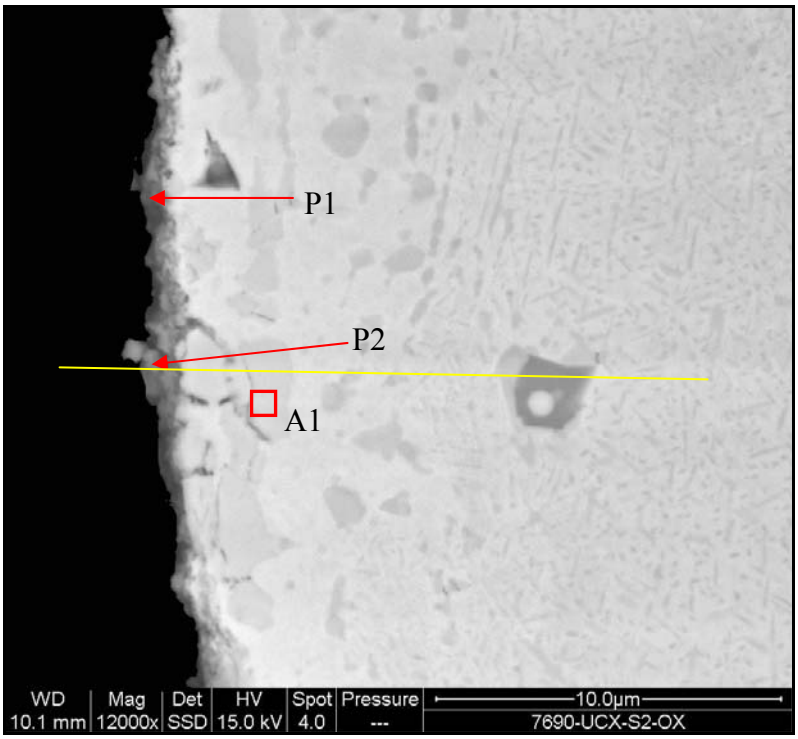

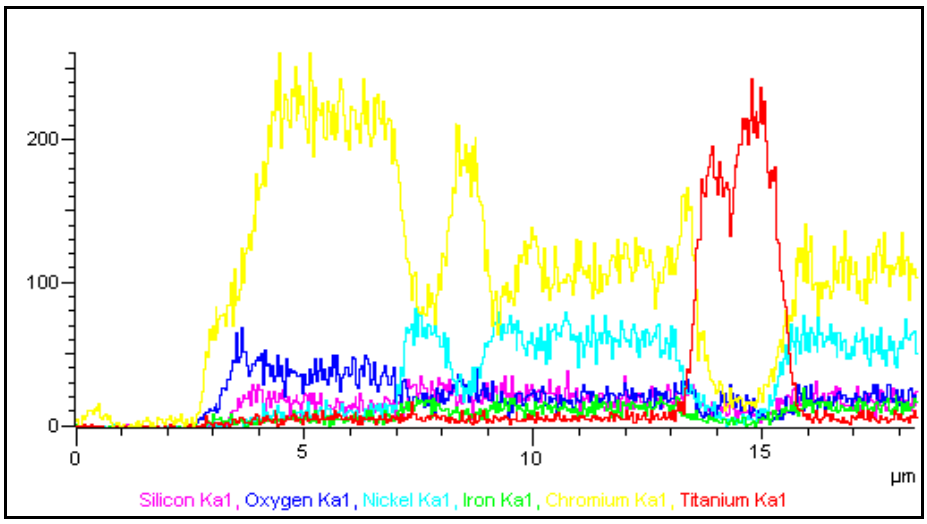

P1

Element	Wt%	At%
C K	27.35	49.21
O K	20.53	27.73
Si K	4.49	3.46
Ca K	0.96	0.52
Cr K	34.96	14.53
Mn K	9.58	3.77
Ni K	2.13	0.78
Totals	100.00	

P2

Element	Wt%	At%
C K	21.24	39.48
O K	27.21	37.98
Mg K	0.16	0.15
Si K	1.37	1.09
Ca K	0.73	0.40
Cr K	39.00	16.75
Mn K	9.10	3.70
Ni K	1.19	0.45
Totals	100.00	

A1

Element	Wt%	At%
C K	6.01	21.25
O K	2.81	7.45
Ca K	0.36	0.38
Cr K	77.22	63.11
Fe K	1.64	1.25
Ni K	7.68	5.56
W M	4.27	0.99
Totals	100.00	

Figure 4.23 Oxide formation on alloy UCX exposed to air at 750ºC.

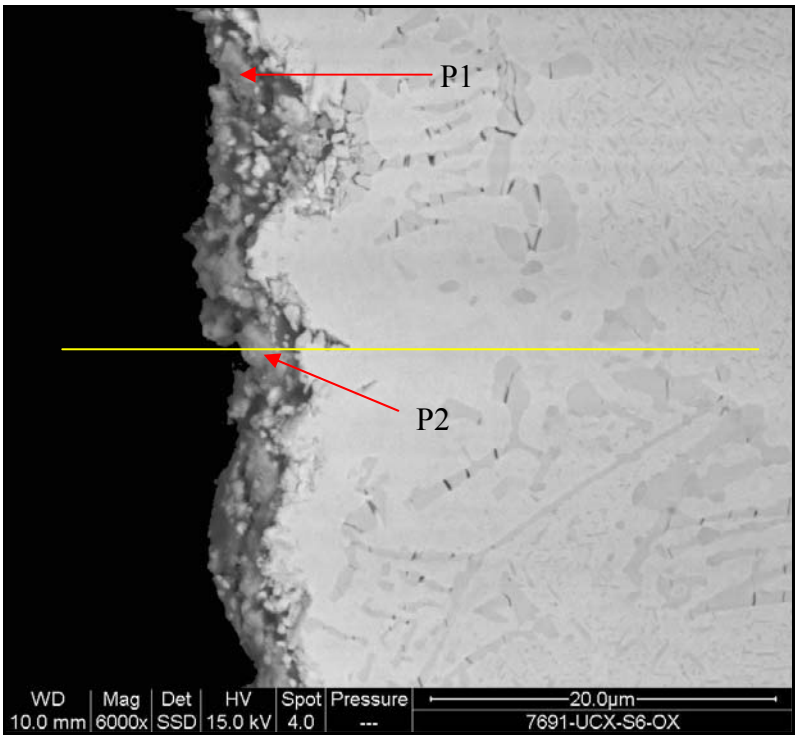

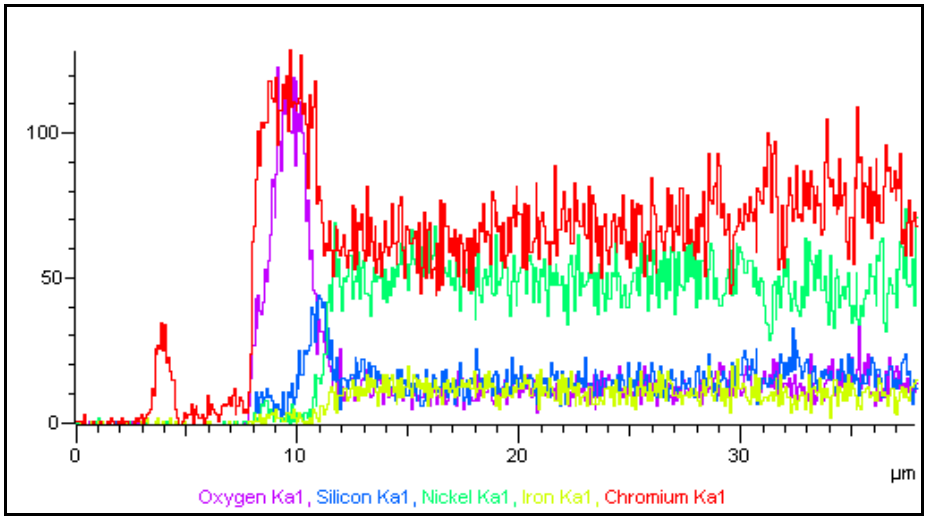

P1		
Element	Weight%	Atomic%
C K	14.47	29.36
O K	28.41	43.27
Si K	2.25	1.95
Ca K	0.30	0.18
Ti K	0.52	0.27
Cr K	46.83	21.94
Mn K	1.23	0.55
Ni K	5.98	2.48
Totals	100.00	

P2		
Element	Weight%	Atomic%
C K	10.37	23.52
O K	25.00	42.55
Si K	0.36	0.35
Cr K	61.14	32.02
Mn K	3.12	1.55
Totals	100.00	

Figure 4.24 Oxide formation on alloy UCX exposed to air at 850ºC.

4.4.2 Long-Term Tests (1000h)

4.4.2.1 Visual Examination

The specimens tested at 650, 750, and 850ºC were visually inspected and photographed, directly after the removal from the furnace.

Blackish deposits covered the alloys oxidised at 650ºC and appeared to be the densest on HP. However, alloys 35Cr-45Ni and UCX were not entirely covered as some shiny areas could be spotted particularly along the edges.

The effect of the exposure time can be understood by referring to the 100h test, where the post exposure examination revealed that the alloys experienced just a little oxidation.

More oxidation took place on the 750ºC specimens, and the surfaces seemed to have been completely covered with blackish oxides that were much denser than those formed after 100h at the same temperature.

The samples, after exposure at 850ºC, were still covered with some oxides despite considerable spallation observed on all of them after furnace cooling. However, the percentage of oxidation varied on the sample surfaces as high densities of localised darker spots were noticed on each alloy suggesting the occurrence of selective oxidation.

Collectively, prolonging the exposure time undoubtedly allowed more oxides to grow on the alloys at the three temperatures. Nevertheless, the degree of oxide growth was apparently, strongly dependent on temperature. As the exposure temperature was increased, the oxide density increased.

4.4.2.2 Weight Change Measurements

The weight change measurements, detailed in Appendix B, generally indicated increasing weight change in agreement with temperature (Figure 4.25).

The alloys behaved somewhat differently at each temperature. Alloy 35Cr-45Ni gained the minimum weight at 650ºC (0.1524 mg/cm^2) and gained the maximum at 750ºC (0.3756 mg/cm^2). HP, however, gained the maximum weight at 650ºC (0.1851 mg/cm^2) whereas the UCX showed the lowest weight change at 750ºC (0.2349 mg/cm^2). Indeed, alloy UCX gained the maximum weight at 850ºC (0.3657 mg/cm^2) in spite of the spallation which occurred and, unlike alloy 35Cr-45Ni which suffered weight loss of -0.2017 mg/cm^2. It should be borne in mind though that the weight change measurements at 850ºC do include the effects of significant spallation that followed cooling. Interestingly, alloy HP experienced a 21% increase in the weight gain by increasing the temperature from 650ºC to 750ºC. Similarly, alloys 35Cr-45Ni and UCX underwent increases by 59% and 25% respectively. The weight gain, after 100h exposure, was appreciably lower than that measured after 1000h. In fact, prolonging the exposure time to 1000h, at 650ºC, led to weight gain increase by 100%, 84%, and 43% on alloys HP, 35Cr-45Ni, and UCX respectively. At 750ºC the weight gain was increased by 54%, 60%, and 39% on HP, 35Cr-45Ni, and UCX respectively.

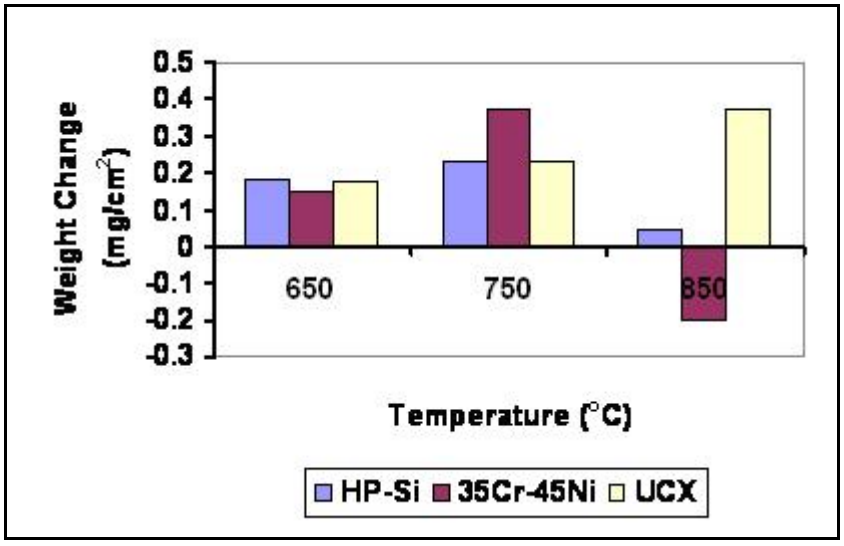

Figure 4.25 Weight change measurements for the alloys exposed at 650, 750, and 850°C.

4.4.2.3 Surface Analyses

SEM secondary electron images of the sample surfaces after the exposure at test temperatures are shown in Figures 4.26-4.28, with additional photomicrographs in Appendix B.

In general, crystallites were observed to have grown on the alloys in different sizes and densities as a result of the exposure at the test temperatures. Raising the temperature produced more crystallite growth that led to the establishment of more cover on the alloy surfaces.

Examining the surfaces of alloy HP revealed that, as the exposure temperature was increased to 750 and 850ºC, the crystallites coarsened and coalesced to form a homogeneous structure. At 650ºC, however, such a continuous layer did not form and a relatively few, distinct crystallites, with maximum size of about 1.2μm, were observed, making no significant difference from what had been noted after the short term test (i.e. 100h).

Denser oxide had grown on alloy 35Cr-45Ni as a consequence of increasing the exposure temperature from 650 to 850ºC. It is worth noticing that the alloy surface, after the exposure at 650ºC, looked almost similar to that exposed at 750ºC after 100h. The extension of exposure time produced greater oxide growth.

Similarly, UCX underwent more oxide growth in agreement with temperature. Interestingly, at 650ºC, the alloy formed denser oxides than HP and 35Cr-45Ni. Additionally, two differently shaped crystallites could be clearly recognized on the alloy after 850ºC.

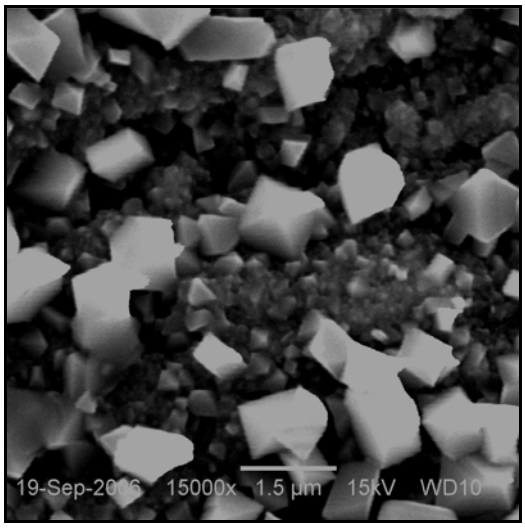

(a)

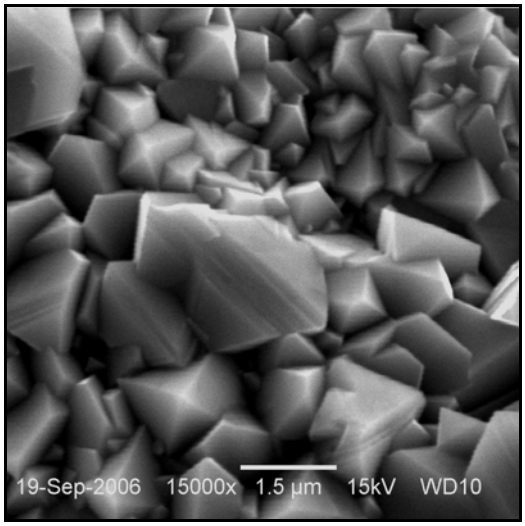

(b)

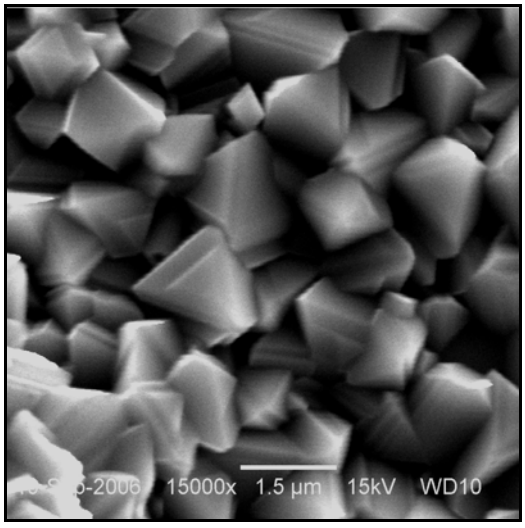

(c)

Figure 4.26 **SEM/SE images of alloy HP surfaces after 1000h exposure at (a) 650ºC, (b) 750ºC, and (c) 850ºC.**

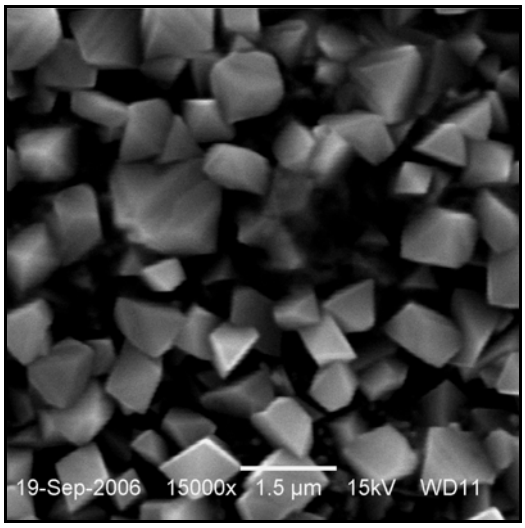

(a)

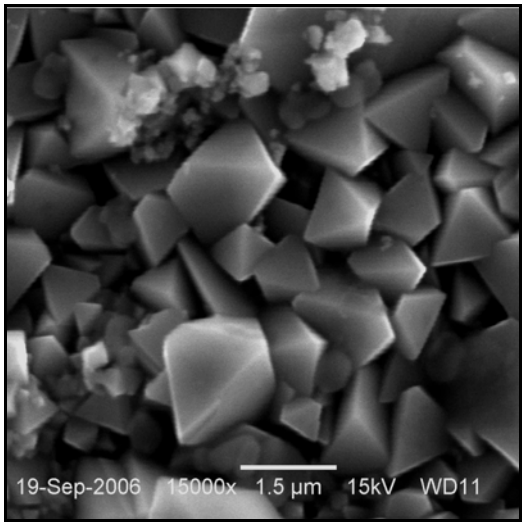

(b)

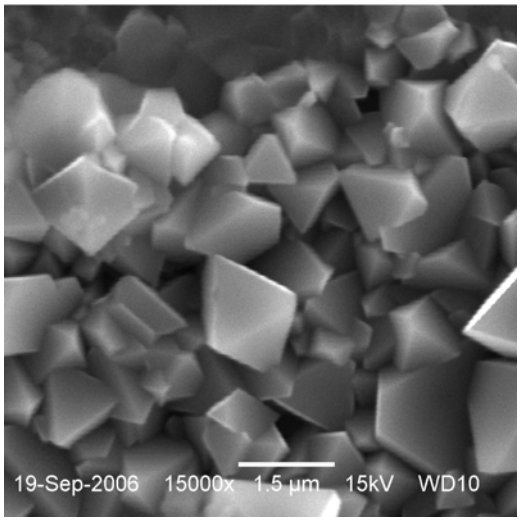

(c)

Figure 4.27 **SEM/SE images of alloy 35Cr-45Ni surfaces after 1000h exposure at (a) 650°C, (b) 750°C, and (c) 850°C.**

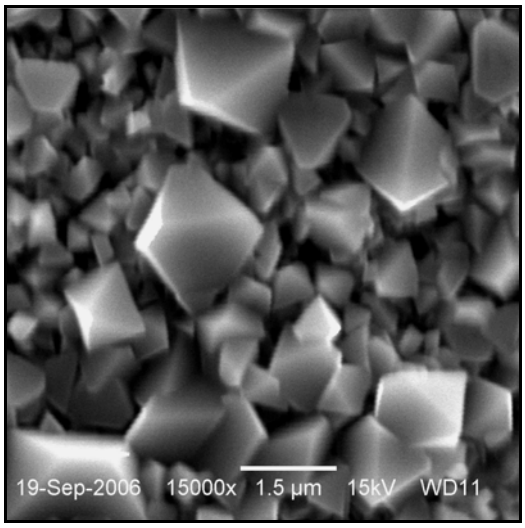

(a)

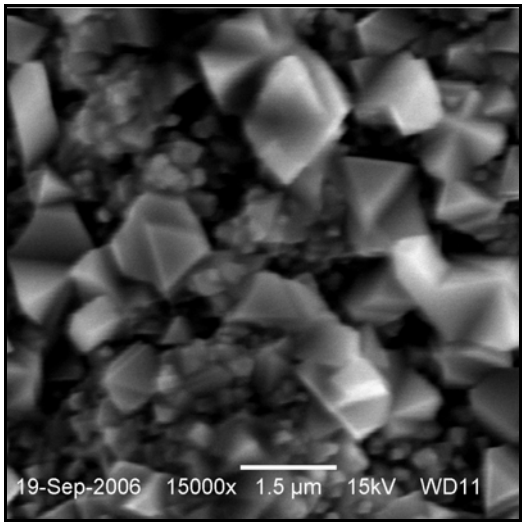

(b)

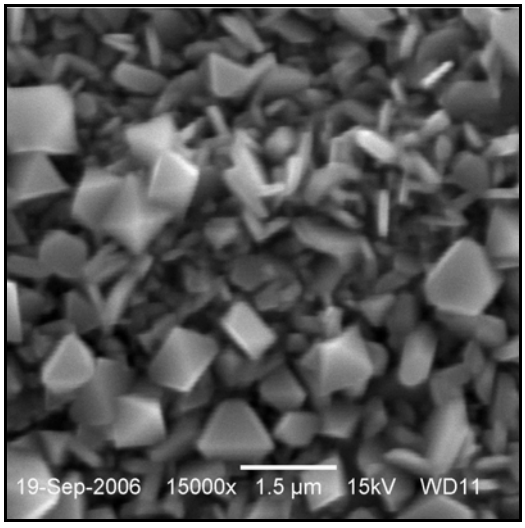

(c)

Figure 4.28 **SEM/SE images of alloy UCX surfaces after 1000h exposure at (a) 650ºC, (b) 750ºC, and (c) 850ºC.**

4.4.2.4 XRD Analysis

The X-ray diffraction patterns recorded from the oxidised samples are shown in Appendix B.

The phases detected on alloy HP at 650ºC were chromium oxide (Cr_2O_3), $NiCrMnO_4$ and silicon oxide. Elevating the temperature to 750ºC and 850ºC led to the formation of $NiMn_{0.5}Cr_{1.5}O_4$ and Cr_2O_3 at both temperatures.

The oxides on alloy 35Cr-45Ni, after the 650ºC exposure, consisted of Cr_2O_3 and $NiFe_{1.95}Mn_{0.05}O_4$. At 750ºC, the layers were composed of Cr_2O_3, $NiCrMnO_4$, and silicon oxide. At 850ºC, the alloy formed Cr_2O_3, $NiMn_2O_4$, and silicon oxide.

Chromium oxide (Cr_2O_3), $NiMn_{0.2}Cr_{1.8}O_4$, and $MnNi_2O_4$ were found to have formed on the alloy UCX at 650ºC. The XRD analysis of the specimen exposed at 750ºC confirmed the presence of $NiCrMnO_4$ and Cr_2O_3. At 850ºC, however, the alloy formed $NiMn_2O_4$ and Cr_2O_3.

4.4.2.5 Metallographic Examination

Alloy samples were cross sectioned and prepared for metallographic examination, Figures 4.29-4.37.

An almost continuous oxide layer developed on alloy HP after exposure at 650ºC with thickness varying from 1µm to 1.5µm. About a 3µm chromium-depleted zone was also observed just beneath the substrate. The EDX analyses were conducted where the layer was found to have contained major amounts of O and Cr, in addition to considerable amounts of iron and nickel.

Compared to the same alloy exposed for 100h at the same temperature, it is obvious that the longer exposure led to the development of a thicker and more even oxide layer. However, generally, there was no major change in the oxide composition.

More uniform oxides seemed to have formed on the specimen after the 750ºC experiment (Figure 4.30). A continuous and adherent scale, about 1-1.7µm in thickness, was established that was considerably thicker than that formed on the same alloy after 100h. Line profiling indicated a chromium depletion zone, approximately 5.5µm deep, underneath the oxide layer. The EDX analyses revealed that the scale was composed mainly of chromium oxide, in addition to some silicon, iron, nickel, and manganese.

A thicker scale (~ 4 up to 14.8µm) formed on the alloy as a result of elevating the temperature to 850ºC, Figure 4.31. The line profiling showed the presence of internal silica layers as well as an ~18µm chromium depletion zone. Two different oxide phases appeared to have formed on the alloy; dark grey and light grey oxides. The EDX analysis of the dark grey layer (P1) showed that it was composed of chromium oxides in addition to appreciable amounts of iron, nickel, and manganese. However, the analysis of lighter grey phase, P2, revealed the oxides were mainly that of chromium with traces of Mn and Fe.

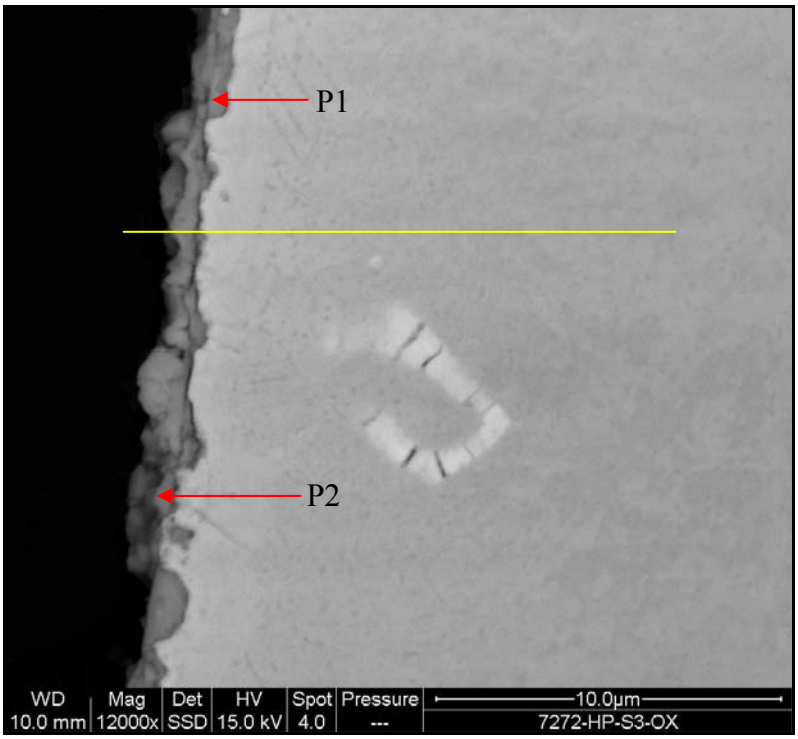

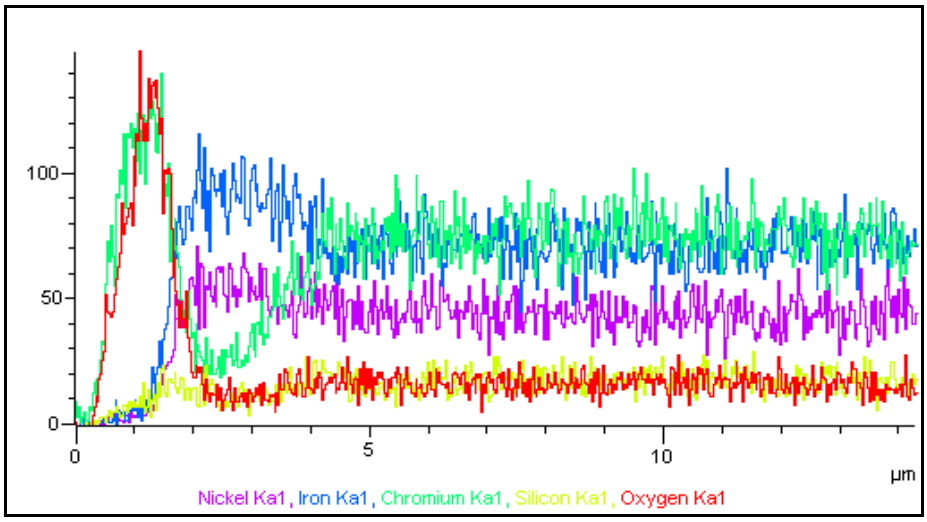

P1

Element	Weight%	Atomic%
C K	14.36	30.58
O K	25.43	40.67
Si K	0.96	0.87
Ca K	0.31	0.20
Cr K	40.06	19.71
Mn K	0.86	0.40
Fe K	5.25	2.41
Ni K	2.01	0.88
Cu K	6.67	2.69
Zn K	4.08	1.60
Totals	100.00	

P2

Element	Weight%	Atomic%
C K	23.46	44.91
O K	22.76	32.70
Si K	0.46	0.38
Ca K	0.42	0.24
Cr K	28.54	12.62
Mn K	1.39	0.58
Fe K	4.29	1.76
Ni K	3.43	1.34
Cu K	9.01	3.26
Zn K	6.24	2.20
Totals	100.00	

Figure 4.29 Oxide formation on alloy HP exposed to air at 650ºC.

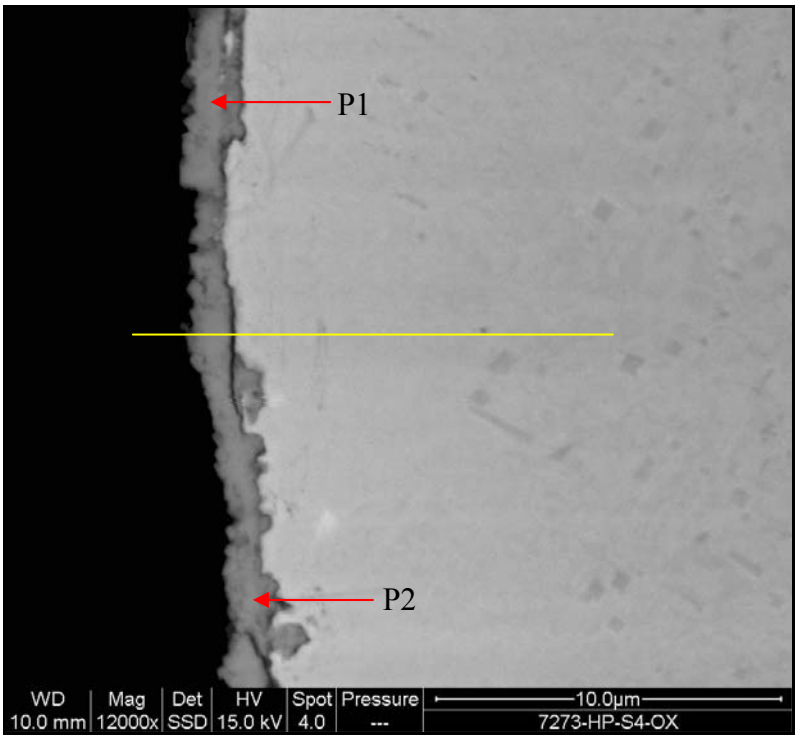

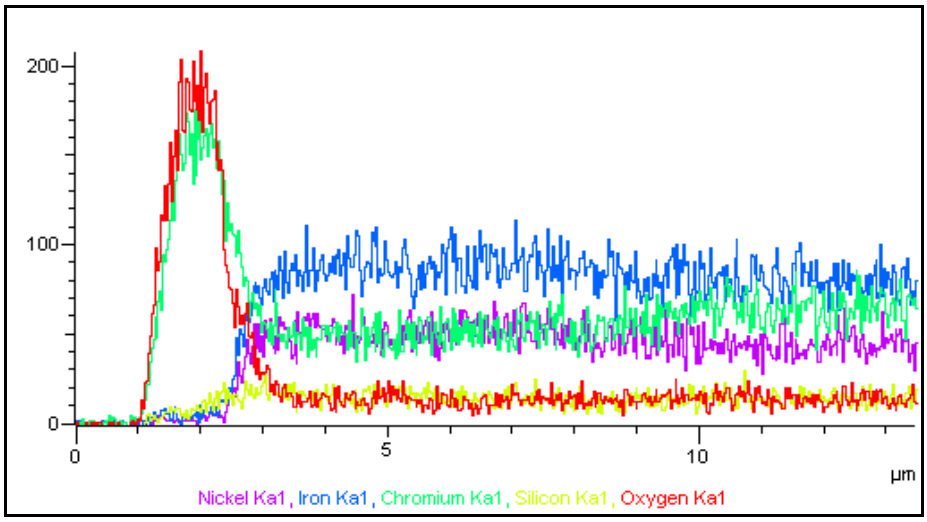

P1

Element	Weight%	Atomic%
C K	4.09	9.20
O K	34.64	58.52
Si K	2.89	2.79
Ca K	0.22	0.15
Cr K	45.25	23.52
Mn K	2.35	1.16
Fe K	3.29	1.59
Ni K	3.39	1.56
Cu K	1.57	0.67
Zn K	1.44	0.60
Nb L	0.86	0.25
Totals	100.00	

P2

Element	Weight%	Atomic%
C K	4.12	9.33
O K	34.37	58.42
Si K	0.79	0.77
Ca K	0.24	0.16
Cr K	54.97	28.75
Mn K	1.69	0.83
Fe K	1.29	0.63
Ni K	0.98	0.45
Cu K	1.55	0.66
Totals	100.00	

Figure 4.30 Oxide formation on alloy HP exposed to air at 750°C.

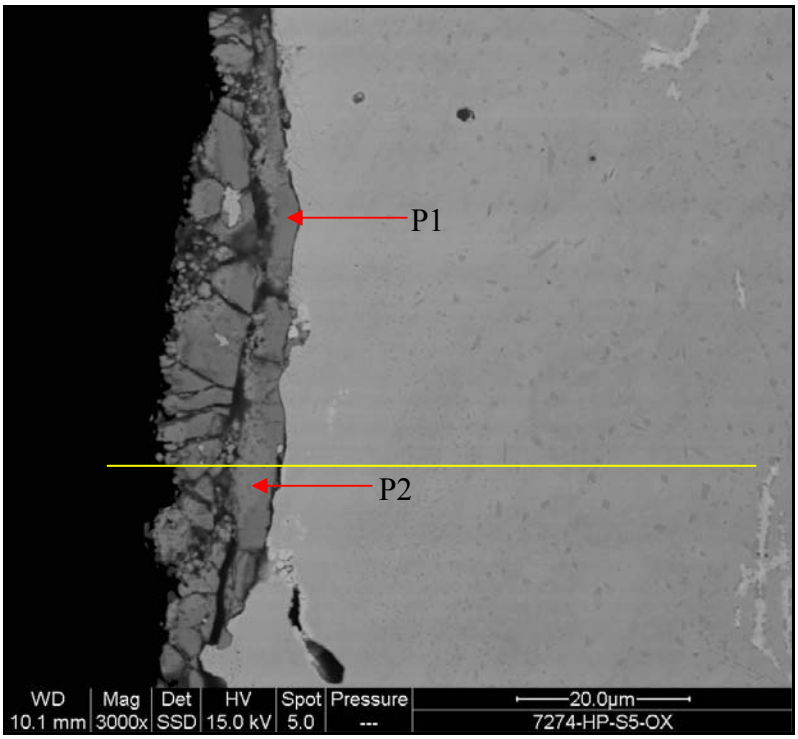

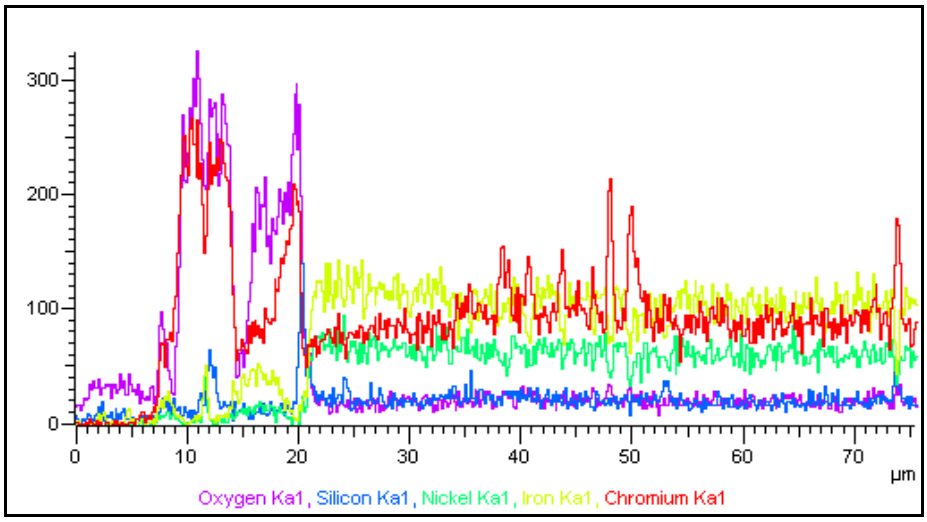

P1

Element	Weight%	Atomic%
C K	1.66	4.10
O K	32.21	59.57
Si K	0.21	0.23
Ca K	0.14	0.10
Cr K	47.23	26.88
Mn K	2.82	1.52
Fe K	3.33	1.76
Ni K	2.82	1.42
Cu K	6.13	2.85
Zn K	3.45	1.56
Totals	100.00	

P2

Element	Weight%	Atomic%
C K	1.03	2.40
O K	36.88	64.33
Cr K	60.60	32.53
Mn K	0.70	0.35
Fe K	0.79	0.39
Totals	100.00	

Figure 4.31 Oxide formation on alloy HP exposed to air at 850°C.

A relatively uneven layer had formed on 35Cr-45Ni after exposure at 650ºC, see Figure 4.32. The layer was found to be very thin in some localised areas (~ 0.4µm) but it was 3µm thick in other areas. Moreover, this layer was thicker than that formed on the same alloy after 100h exposure (i.e. 0.2-1.3µm). The line profiling showed that the layer was mainly composed of chromium oxides and some silicon oxides that produced a chromium depleted zone of about 3µm. The chromium peaks along the scan line indicated the presence of chromium carbides. The EDX spot analyses confirmed that the oxides contained chromium as the major constituent as well as some iron, nickel, and manganese.

After exposure at 750ºC (Figure 4.33) a scale of 4-6µm had formed in a continuous manner and was much thicker than that observed on the alloy after 100h (0.2-1.2µm). Moreover, a chromium-depleted zone, around 14µm, was shown by line scanning. The oxide layer was found to have contained predominantly chromium and oxygen in addition to minor quantities of manganese, iron, and nickel.

Due to severe spallation, the thickness of the oxide layer formed on the alloy after the 850ºC exposure could not be accurately measured, as no area was found intact during the SEM examination, Figure 4.34. However, the oxide contents were determined, by EDX, to have been chromium and nickel in addition to some iron and silicon.

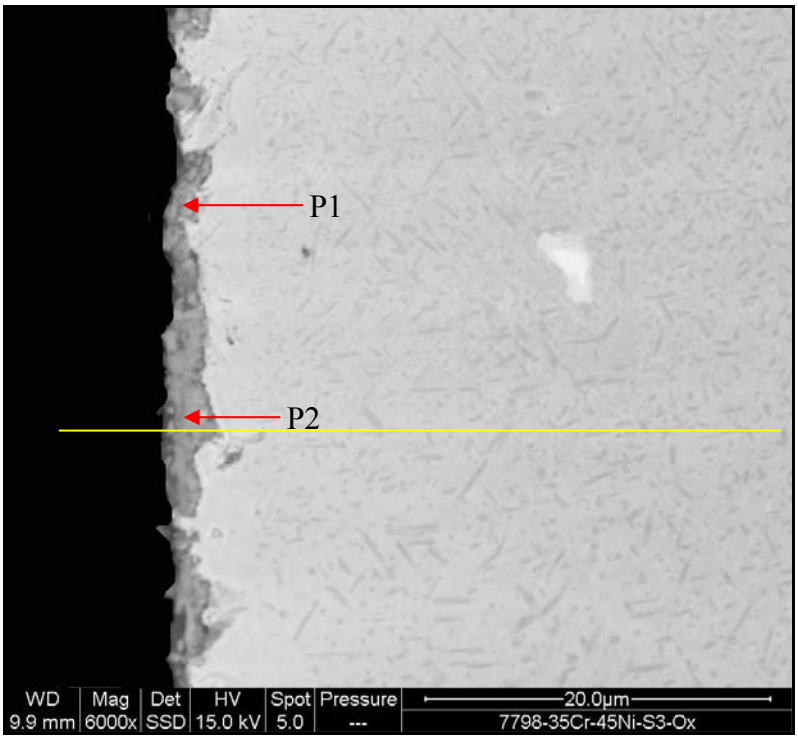

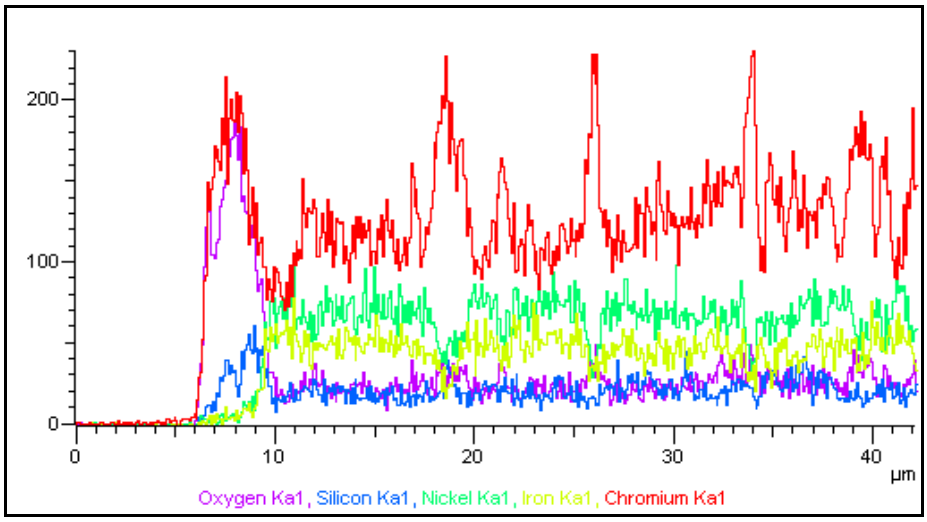

P1

Element	Weight%	Atomic%
C K	8.11	17.18
O K	33.65	53.53
Na K	0.17	0.19
Si K	2.14	1.94
Ca K	0.27	0.17
Cr K	50.86	24.90
Mn K	1.41	0.65
Fe K	1.63	0.74
Ni K	1.37	0.59
Nb L	0.40	0.11
Totals	100.00	

P2

Element	Weight%	Atomic%
C K	4.77	10.49
O K	34.94	57.71
Si K	3.12	2.94
Ca K	0.25	0.16
Cr K	51.35	26.09
Mn K	2.15	1.03
Fe K	1.37	0.65
Ni K	2.05	0.92
Totals	100.00	

Figure 4.32 Oxide formation on alloy 35Cr-45Ni exposed to air at 650ºC.

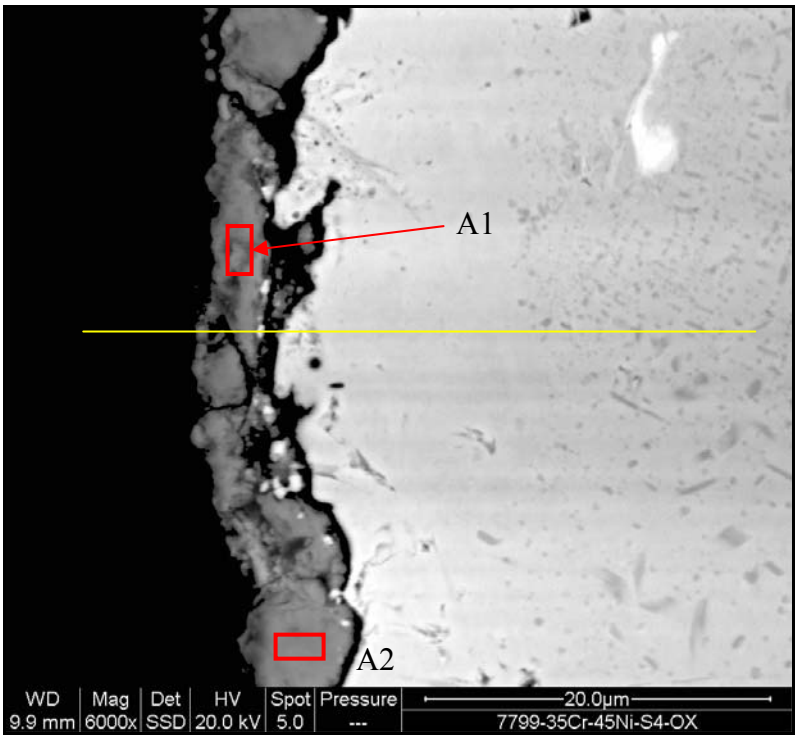

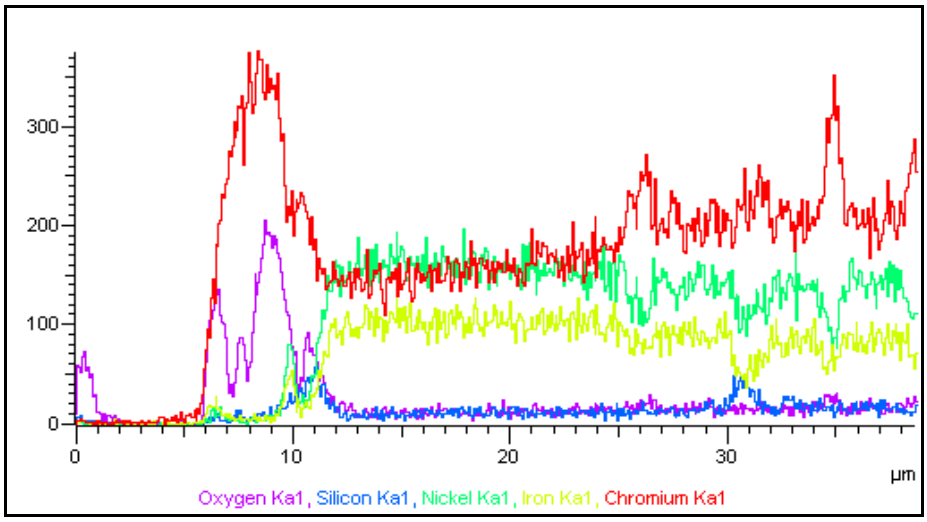

A1

Element	Weight%	Atomic%
C K	3.87	8.96
O K	33.00	57.30
Si K	0.15	0.15
Ca K	0.30	0.21
Cr K	60.14	32.13
Mn K	1.83	0.92
Fe K	0.25	0.13
Ni K	0.46	0.22
Totals	100.00	

A2

Element	Weight%	Atomic%
C K	1.68	3.75
O K	39.15	65.70
Ca K	0.23	0.15
Cr K	57.86	29.88
Mn K	0.48	0.23
Fe K	0.23	0.11
Ni K	0.38	0.17
Totals	100.00	

Figure 4.33 Oxide formation on alloy 35Cr-45Ni exposed to air at 750°C.

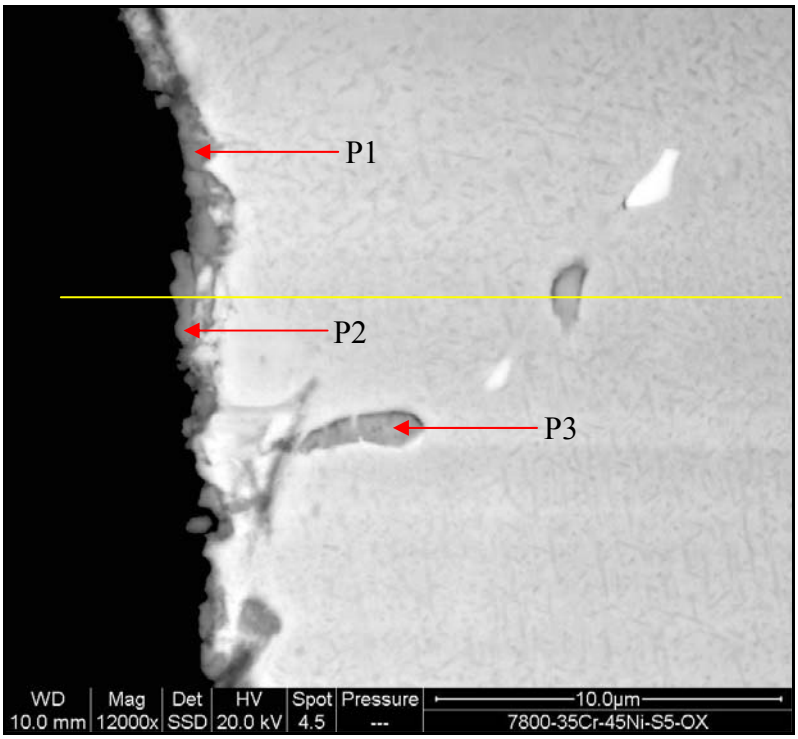

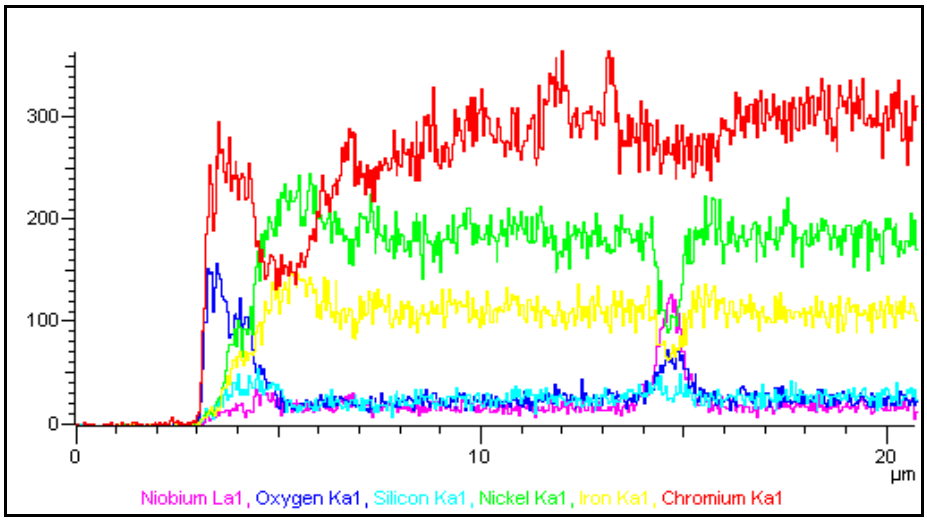

P1

Element	Wt%	At%
C K	19.53	38.02
O K	25.98	37.96
Si K	1.15	0.96
Ca K	0.37	0.22
Cr K	34.02	15.29
Mn K	2.53	1.08
Fe K	4.26	1.78
Ni K	9.06	3.61
Cu K	0.68	0.25
Zn K	2.16	0.77
Nb L	0.27	0.07
Totals	100.0	

P2

Element	Wt%	At%
C K	22.99	43.98
O K	22.31	32.04
Si K	2.00	1.64
Ca K	0.38	0.22
Cr K	31.22	13.80
Mn K	1.89	0.79
Fe K	5.44	2.24
Ni K	12.20	4.77
Cu K	0.50	0.18
Zn K	0.68	0.24
Nb L	0.39	0.10
Totals	100.0	

P3

Element	Wt%	At%
O K	21.14	50.59
Si K	1.30	1.77
Cr K	24.53	18.06
Mn K	3.22	2.25
Fe K	8.24	5.65
Ni K	18.95	12.36
Nb L	22.61	9.32
Totals	100.0	

Figure 4.34 Oxide formation on alloy 35Cr-45Ni exposed to air at 850°C.

As seen in Figure 4.35, UCX alloy formed an oxide layer of varying thickness (0.5-3µm) after exposure at 650ºC for 1000h. Indeed, the layer was thicker and more uniform compared with the layer that formed after 100h, where the thickness was 0.2-1.2µm. The EDX analyses showed that the oxides were mainly chromium-containing with some silicon, manganese, nickel, and iron. The line profiling showed about a 1.5µm chromium-depleted zone.

An approximately 1.3µm thick oxide layer, being ~4µm in some places, was observed on UCX after the exposure at 750ºC (Figure 4.36). This layer was thicker than that formed after 100h (0.3-1.4µm). The line scanning revealed a chromium-depleted zone of about 2µm, and also confirmed that the layer contained chromium, silicon, and some nickel oxides. The EDX analyses (point 2) showed the presence of a high concentration of silicon at the alloy/oxide interface. Oxides of chromium, and some manganese and nickel were detected to be the main constituents of the scale (points 1&3).

Exposing UCX to air at 850ºC led to the growth of a 4.5-10µm scale, mainly composed of chromium oxide with some silica. About an 18µm chromium-depleted zone was also observed (Figure 4.37).

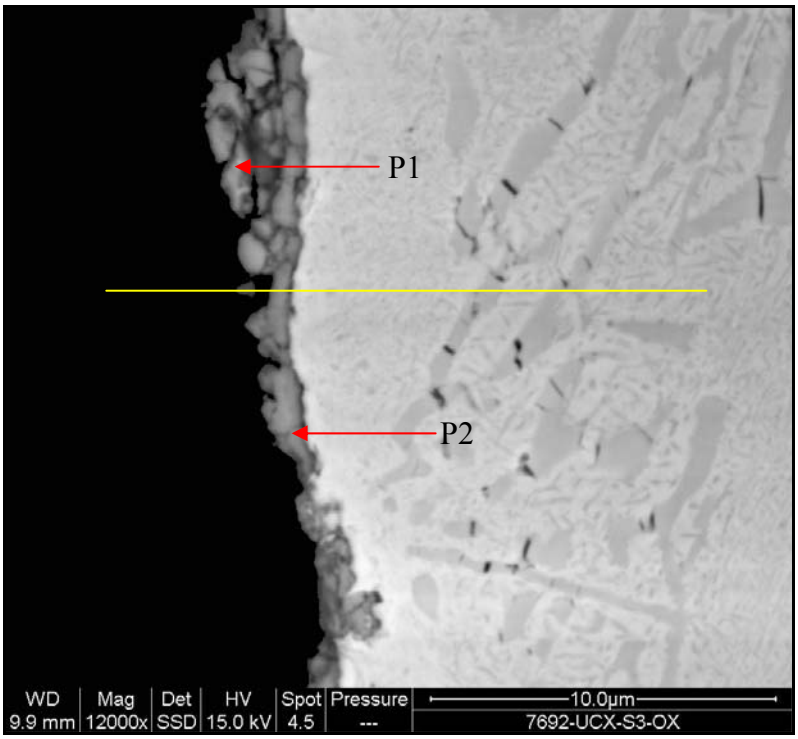

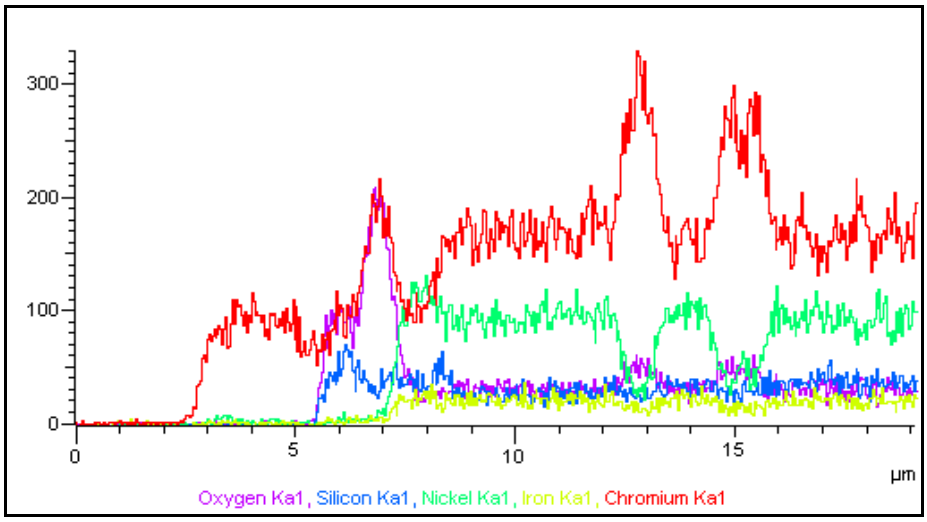

P1

Element	Weight%	Atomic%
C K	20.12	41.79
O K	19.10	29.78
Si K	1.74	1.54
Ca K	0.44	0.27
Cr K	39.32	18.86
Mn K	1.79	0.81
Fe K	0.53	0.24
Ni K	3.34	1.42
Cu K	8.08	3.17
Zn K	5.54	2.11
Totals	100.00	

P2

Element	Weight%	Atomic%
C K	11.06	24.04
O K	29.49	48.11
Si K	0.30	0.28
Ca K	0.23	0.15
Cr K	34.44	17.29
Mn K	1.59	0.76
Ni K	1.21	0.54
Cu K	14.78	6.07
Zn K	6.90	2.75
Totals	100.00	

Figure 4.35 Oxide formation on alloy UCX exposed to air at 650°C.

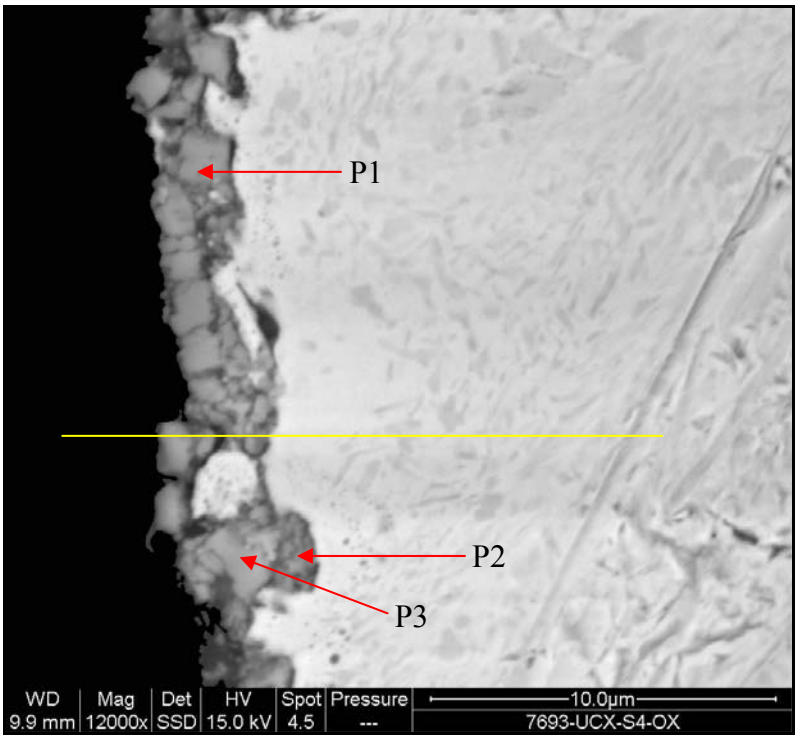

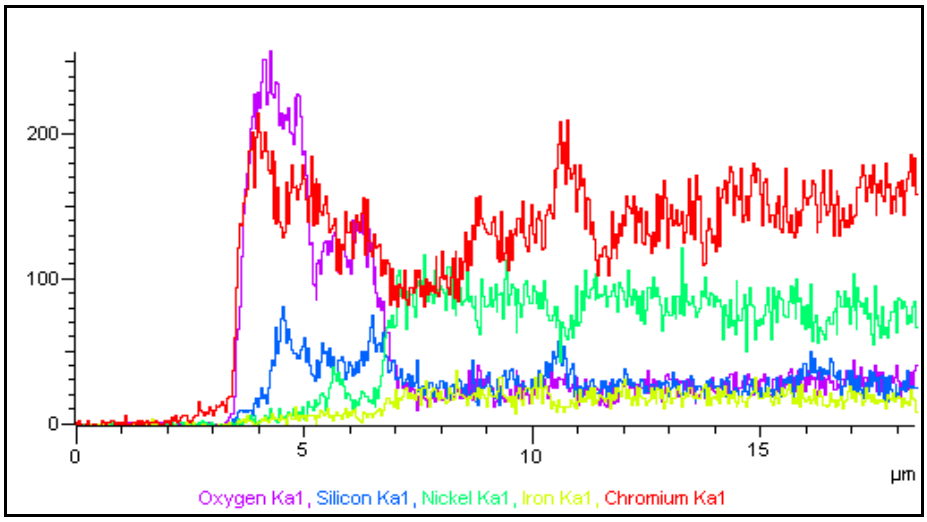

P1

Element	Wt	At%
C K	13.35	29.23
O K	24.14	39.69
Si K	1.39	1.30
Ca K	0.43	0.29
Cr K	44.72	22.63
Mn K	5.19	2.48
Ni K	3.33	1.49
Cu K	3.76	1.56
Zn K	3.15	1.27
W M	0.56	0.08
Totals	100.0	

P2

Element	Wt%	At%
C K	1.85	4.65
O K	27.32	51.60
Si K	6.19	6.66
Ca K	0.23	0.18
Cr K	55.23	32.11
Mn K	3.67	2.02
Fe K	0.62	0.34
Ni K	3.51	1.81
Zn K	1.37	0.63
Totals	100.0	

P3

Element	Wt%	At%
C K	1.63	3.73
O K	37.13	63.77
Si K	0.61	0.59
Ca K	0.29	0.20
Cr K	57.40	30.33
Mn K	1.37	0.69
Ni K	0.66	0.31
Zn K	0.92	0.39
Totals	100.0	

Figure 4.36 Oxide formation on alloy UCX exposed to air at 750ºC.

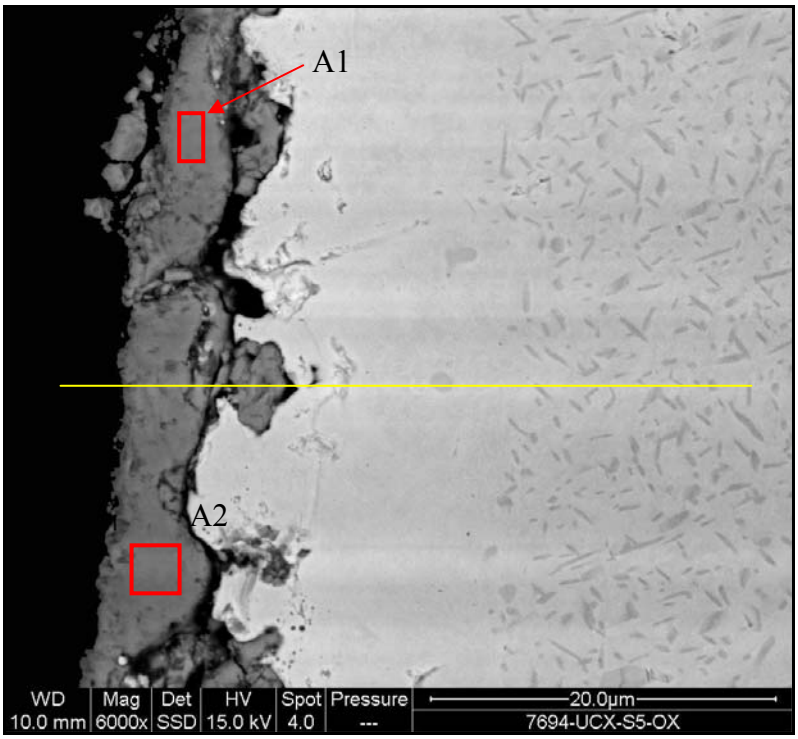

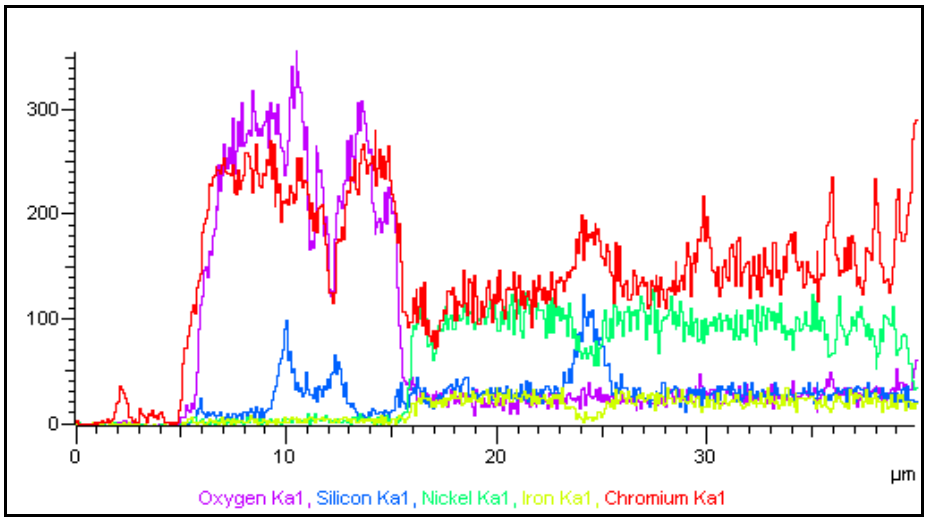

A1

Element	Weight%	Atomic%
C K	1.79	4.08
O K	37.14	63.67
Ca K	0.19	0.13
Cr K	60.89	32.12
Totals	100.00	

A2

Element	Weight%	Atomic%
C K	1.71	3.88
O K	37.71	64.32
Ca K	0.15	0.10
Cr K	59.75	31.36
Mn K	0.69	0.34
Totals	100.00	

Figure 4.37 Oxide formation on alloy UCX exposed to air at 850°C.

4.5 Discussion

Visual examination, weight change measurements, SEM/EDX, and XRD analyses have generally indicated that increasing temperature or time or both resulted in more oxide growth on the three alloys.

The weight gain rate was calculated and found to have decreased as the exposure time was increased, Table 4.1. This might be attributed to a change in the oxidation mechanism from the initial stage to the final stage. In the former, the process involved the formation of individual oxide nuclei which grew laterally to cover the alloy. Once a continuous oxide film had developed the latter stage took place where the reaction could only proceed by solid state diffusion of one or both reactants through the film.

Interestingly, the rate seemed to have increased in agreement with chromium level in the alloys exposed at 650ºC for 100h. This might be interpreted as that, at such relatively low temperature and short time, the diffusion of chromium toward the reaction front was probably quite slow and therefore higher levels of chromium were needed at the surface to form more oxides. Moreover, the calculation showed that elevating the temperature to 750ºC led to faster oxidation kinetics resulted in higher weight gain rate.

Table 4.1 **Weight gain rate was calculated in mg/cm^2 h. The 850ºC samples were not included because of the spallation they suffered.**

Alloy	100h	1000h
HP	**650ºC**	
	<0.0001	1.851 X 10^{-4}
	750ºC	
	1.077 X 10^{-3}	2.353 X 10^{-4}
35Cr-45Ni	**650ºC**	
	2.510 X 10^{-4}	1.524 X 10^{-4}
	750ºC	
	1.507 X 10^{-3}	3.756 X 10^{-4}
UCX	**650ºC**	
	1.004 X 10^{-3}	1.762 X 10^{-4}
	750ºC	
	1.426 X 10^{-3}	2.349 X 10^{-4}

The examination of the oxidised surfaces showed that there was a difference in size of the individual oxide crystallites on the same sample. This variation in crystallite size might be attributed to the distribution of alloying element at the alloy surface and/or the localised surface conditions.

Figures 4.38-4.43 compare the thickness of oxide layers formed on each alloy at the test temperatures (i.e. 650, 750, and 850ºC) for the periods 100 and 1000h. Maximum, minimum, and typical values of each layer were determined using the SEM photomicrographs. The thickness values for alloy 35Cr-45Ni after the 850ºC exposure (Figure 4.41) were not measured as no layer was found intact.

From the figures it is obvious that increasing the time and/or temperature led to pronounced thickening of the scales. A large increase in the oxide layer thickness was observed on the alloys when the test temperature was raised to 850ºC. The diffusion rate of oxide-forming elements toward the alloy/air interface is greatly increased at this temperature. Conversely, there had been no significant influence of increasing the temperature from 650 to 750ºC, except for the alloy 35Cr-45Ni after 1000h, where considerable scale growth was noticed. The minimum layer thickness was observed on alloy HP exposed at 650ºC whilst alloys 35Cr-45Ni and UCX had developed thicker oxides at 650 and 750ºC, that might well be attributed to their higher content of chromium at the substrate.

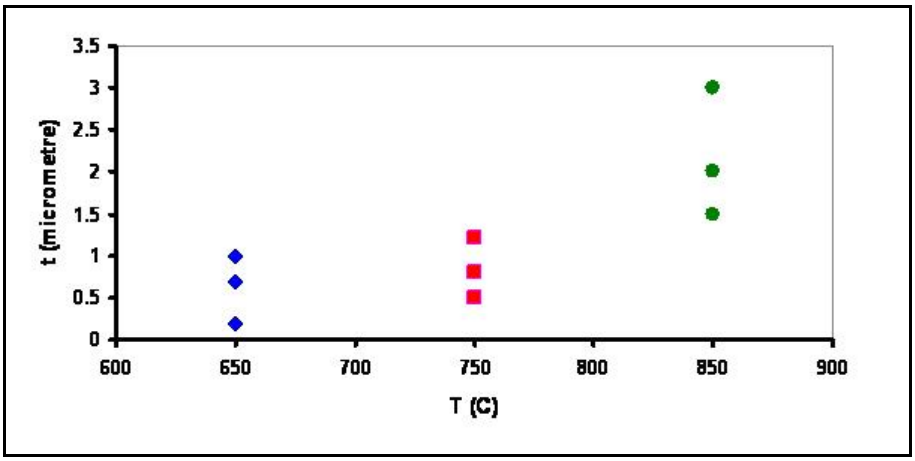

Figure 4.38 Thickness of oxide layer formed on alloy HP after the 100h exposure.

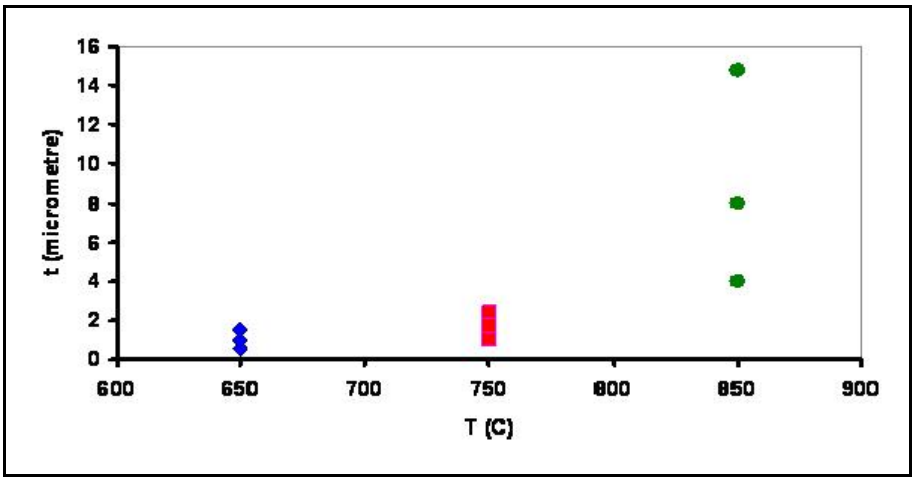

Figure 4.39 Thickness of oxide layer formed on alloy HP after the 1000h exposure.

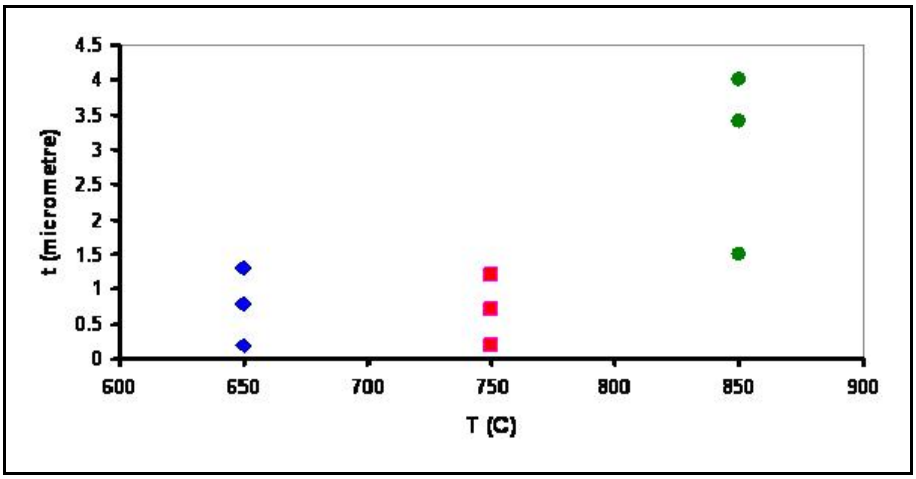

Figure 4.40 Thickness of oxide layer formed on alloy 35Cr-45Ni after the 100h exposure.

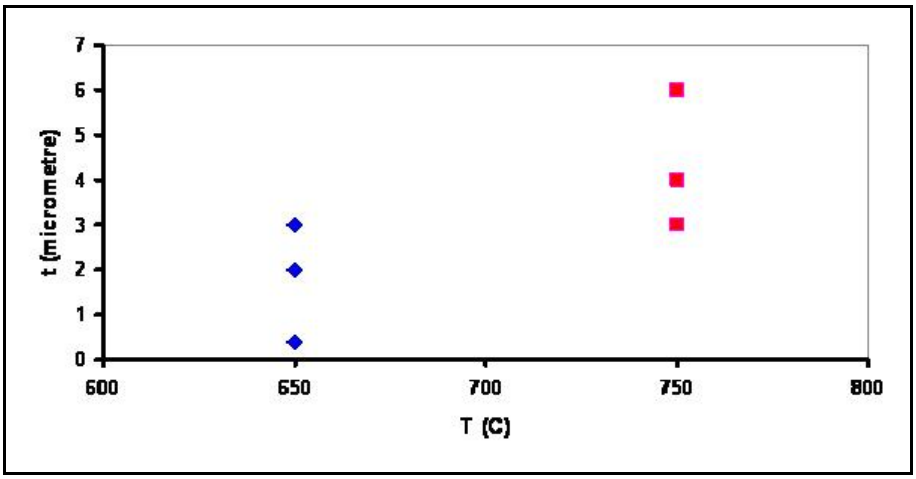

Figure 4.41 Thickness of oxide layer formed on alloy 35Cr-45Ni after the 1000h exposure.

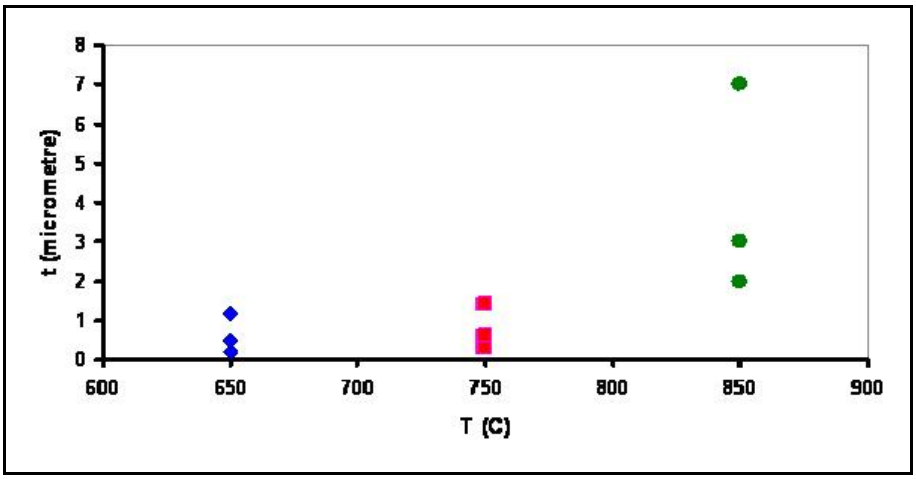

Figure 4.42 Thickness of oxide layer formed on alloy UCX after the 100h exposure.

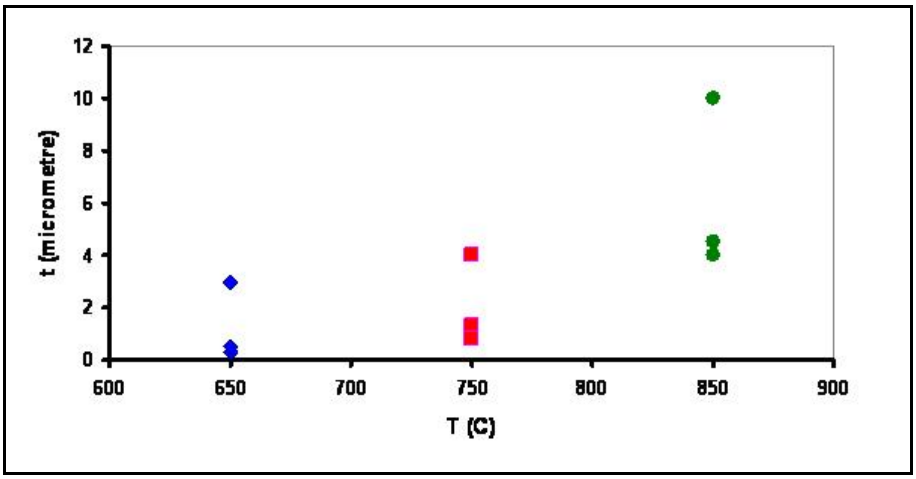

Figure 4.43 Thickness of oxide layer formed on alloy UCX after the 1000h exposure.

The EDX analyses of the oxide layers confirmed that all the alloys generally formed oxides that contained chromium as the main constituent. Also, line profiling showed the formation of silicon oxide layers at the alloy/chromium oxide interface on most samples. Other oxides were also detected including spinels of Mn, Cr, Nb, Fe, and/or Ni. It was evident that the oxides formed on the alloy HP contained the highest amount of iron whereas only traces of iron were detected within the layers formed on the alloy UCX. This was expected owing to the higher iron levels in the former.

Generally, increasing the exposure temperature from 650 to 850ºC resulted in a reduction in the iron content in the oxides formed on alloy HP. However, extending the exposure time from 100h to 1000h, at the same temperature, did not seem to have an effect on the iron content within the oxide.

The oxide layers formed on alloy 35Cr-45Ni, however, contained lower amounts of iron with significantly higher contents of chromium. Iron, in minor amounts, was only detected in oxides formed on alloy UCX after exposure at 650ºC for 100h. Carbon in different amounts was found in most EDX analyses that could be attributed to the contamination by the mounting material.

As elucidated in 4.1.4, the stability of the oxides is important if the alloys are to be exposed to reducing environments such as metal dusting conditions. Chromium, silicon, and manganese oxides are thermodynamically stable in such environments and hence the development of a continuous chromium oxide (Cr_2O_3) scale is known to be an effective method against metal dusting as the scale hinders the carbon ingress to the alloy. However, oxides containing elements like iron and/or nickel may become less protective and may well be reduced.

Several factors may be responsible if the alloys do not to establish a protective scale, particularly at 650ºC. The test temperatures might have been relatively low for such alloys, and therefore, the diffusion of scale-forming element was quite slow. Another possible factor is that the test period was probably not sufficient to allow the formation of a continuous oxide scale.

Also, as elucidated in Chapter 3, the cast alloys have a relatively inhomogeneous microstructure and suffer phase segregation. HP possesses a microstructure composed of an austenitic matrix containing a complex network of chromium and niobium carbides that outlines the boundaries of the original dendrites. These carbides are precipitated and distributed in non uniform manner. The microstructure of alloy 35Cr-45NI is an austenitic with much lower concentration of discontinuous, primary niobium-rich carbides distributed along the grain boundaries in addition to precipitation of titanium nitrides. UCX also has an austenitic microstructure enriched with a network of interdendritic chromium carbides and Zr-Ti-N precipitates. Therefore, alloying element concentration is not expected to be uniform over the alloy surface. This may lead to non-uniform oxide layers, particularly in short-term tests, which may cause localised metal dusting if exposed to carburising environments.

4.6 Conclusion

Increasing the exposure time and/or temperature resulted in an increase of the oxide growth on the alloys and the oxides appeared to have become more continuous, adherent and thicker. It is unlikely though that the alloys formed a completely protective scale, especially at 650ºC, as the oxide layers were uneven and very thin in some areas. It is also suggested that the alloys were still at the initial oxidation stages after exposure for 100h and that lateral growth had not been sufficient to establish a continuous layer. More research may be necessary in order to look at potential, practical methods for improving oxidation kinetics (diffusion of oxide-forming elements) of the alloys in the metal dusting temperature range.

5 EVALUATION OF ALLOY HP PERFORMANCE IN METAL DUSTING CONDITIONS

This chapter reports and discusses the findings concerning the behaviour of the iron-based alloy, HP, that had been exposed to the gas mixture at 650, 750, and 850ºC for periods of 100, 500, and 1000 hours. Details of the experimental apparatus and procedures as well as characterisation methods have already been fully covered in Chapter 2. Moreover, all related XRD patterns and charts, weight change measurements, and EDX spectroscopy are listed in Appendix C. Chapter 8 is dedicated to an overall discussion pertaining to the performance of the three alloys, HP, 35Cr-45Ni, and UCX in the metal dusting conditions.

5.1 Visual Examination

Following each experiment, the samples were removed from the tube and were immediately photographed whilst they were still suspended from the rack. However, despite being drawn out very carefully, the rack movement unavoidably caused some of the carbon deposits on the alloys to fall. The specimens were then detached from the rack and mechanically brushed (by bristle brush) and thoroughly washed in water followed by ultrasonic cleaning in acetone, and were subsequently examined and photographed.

Although Figures 5.1-5.6 show the condition of the three alloys after the experiments, only the behaviour of alloy HP is being described in this chapter as the others are described in chapters 6 and 7.

5.1.1 HP Tested at 650ºC

Exposing the alloys at 650ºC for 100h led to a considerable deposition of carbon on HP that almost covered the sample surface (Figure 5.1). Much growth of carbon filaments, especially on the sample sides, was also observed. It is interesting though to note that the carbon filaments originated on all sides but the upper.

Prolonging the experiment time to 500h appeared to have catalysed more carbon accumulation on the alloy. Interestingly, inverting the sample order did not seem to have a noticeable effect on the carbon deposition. Moreover, the sample exhibited some slight attraction to a magnet suggesting the occurrence of considerable carburisation. Indeed, the alloy surface becomes magnetic when the chromium, at the substrate, is removed from the matrix as a consequence of the precipitation of more chromium carbide. The magnetic transformation of Fe-Ni-Cr alloys is discussed further in Chapter 8.

A denser, thicker, blackish layer had developed on the sample as a consequence of the exposure for 1000h. Some localised, pronounced growth of carbon was also noticed on both faces of the specimen. Furthermore, the sample edges experienced less carbon deposition.

Figure 5.2 shows the alloy after being cleaned. Although the same cleaning procedure had been followed for all samples, some deposit was found easier to remove than the other. For instance, the specimen tested for 500h formed adhesive, “sticky” deposits that could not be entirely removed whereas a more “loose” layer formed on the sample exposed for 100h.

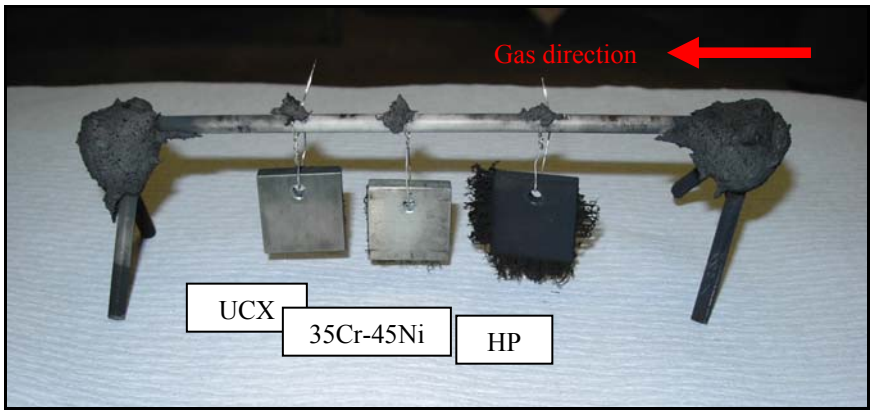

(a) Samples condition after 100h

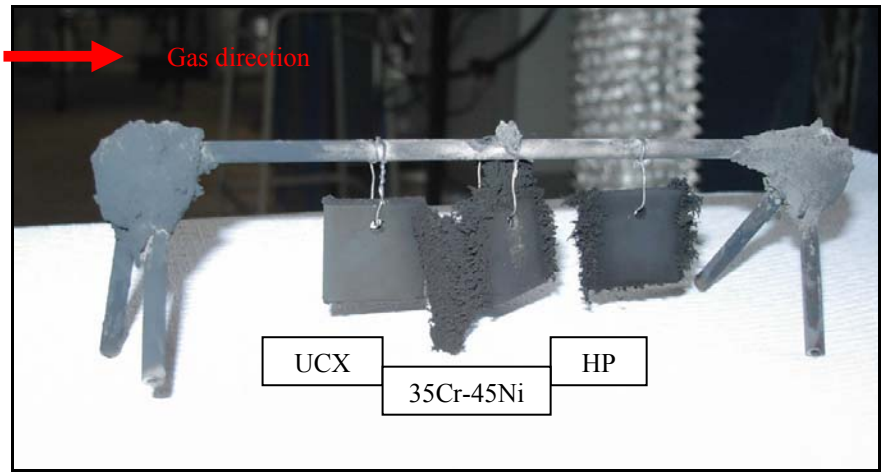

(b) Samples condition after 500h

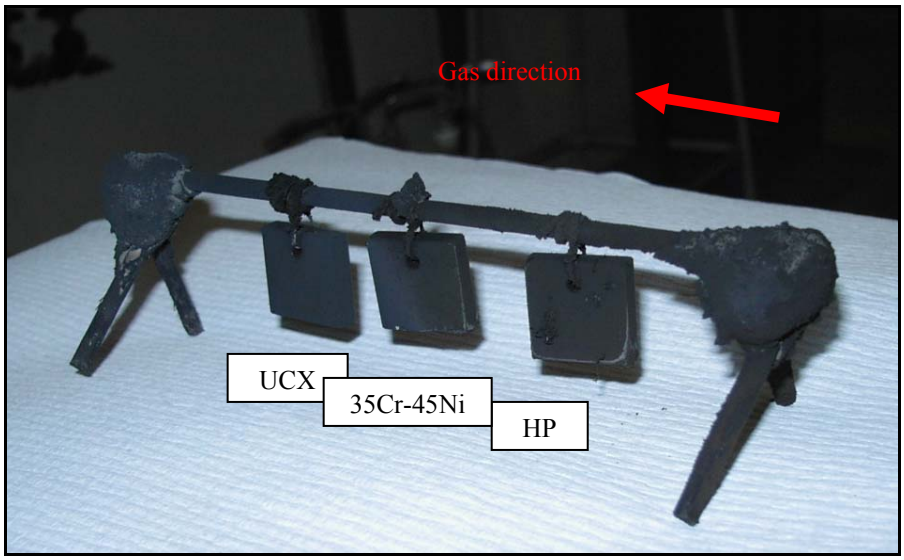

(c) Samples condition after 1000h

Figure 5.1 General photos of the alloys after the exposures at 650°C.

(a) Alloy condition after 100h

(b) Alloy condition after 500h

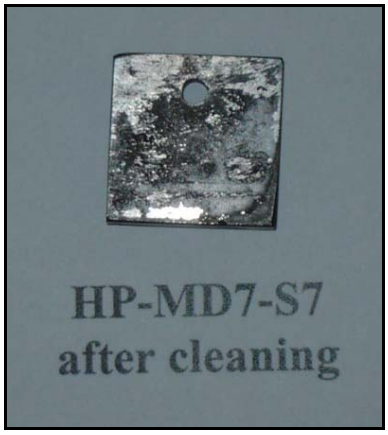

(c) Alloy condition after 1000h

Figure 5.2 Photos of the alloy after exposed at 650ºC after cleaning.

5.1.2 HP Tested at 750ºC

In general, increasing the test temperature to 750ºC resulted in a relatively low carbon deposition (Figure 5.3). Also, more carbon accumulation appeared to have occurred as a result of prolonging the experiment time.

No significant carbon filament growth was observed on the sample after 100h of testing, and the degree of carbon deposition appeared to be considerably less than that took place at the 650ºC. However, comparatively dense carbon layers could be noticed on the sides of the sample.

The sample exposed for 500h did not appear to experience appreciable carbon build up, despite some growth of carbon filament on two sides of the sample. The alloy surface, however, seemed to be mostly covered with a greyish layer.

Extending the exposure time to 1000h allowed a deposition of a thick, loose, blackish layer that could be removed effortlessly from the surface.

It is worth noting that the carbon deposition was gradually lessening in agreement with the gas flow direction, as seen in Figure 5.3 b & c. Most carbon deposition was observed on alloy UCX, which had been the first to see the gas, during the 500h experiment. In contrast, the least deposition was seen on alloy HP which was the last on the rack (Figure 5.3 b). Alloy 35Cr-45Ni, however, appeared to have experienced different levels of deposition as the specimen first half (next to UCX) showed more carbon accumulation than the other half (near HP). Similar behaviour was also noticed on the samples exposed for 1000h despite the reversion of their order on the rack. In short, the inversion of the samples order might well have influenced their interaction with the environment. Moreover, none of the samples exhibited any strong attraction to the magnet. The sample's condition after cleaning is shown in Figure 5.4.

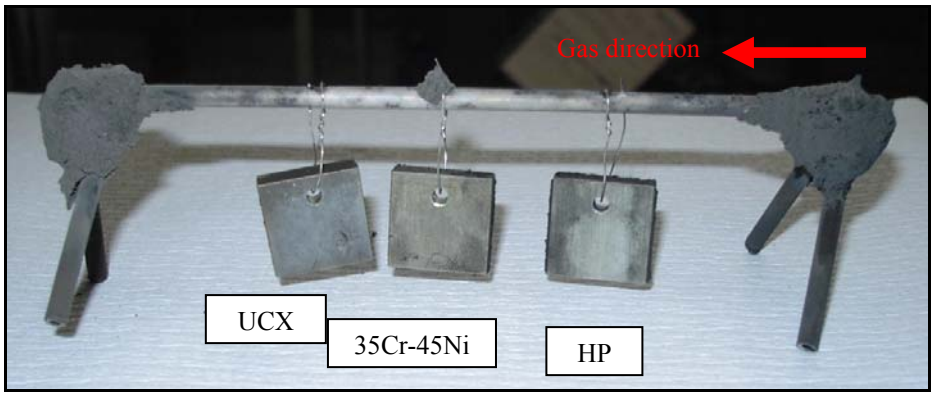

(a) Samples condition after 100h

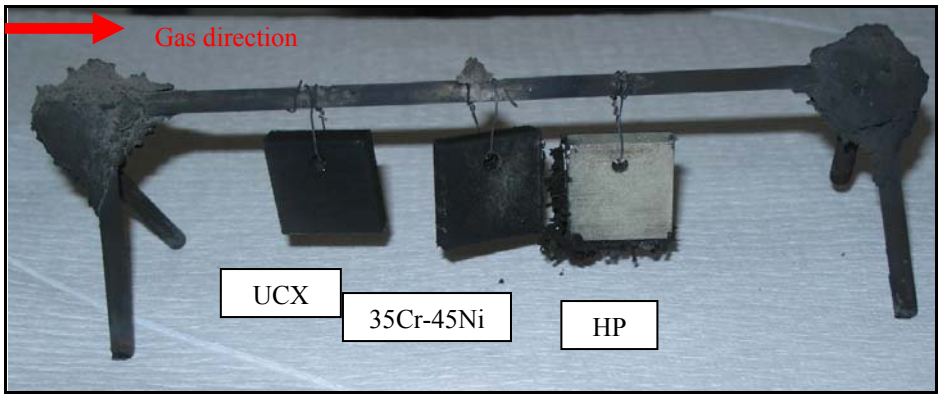

(b) Samples condition after 500h

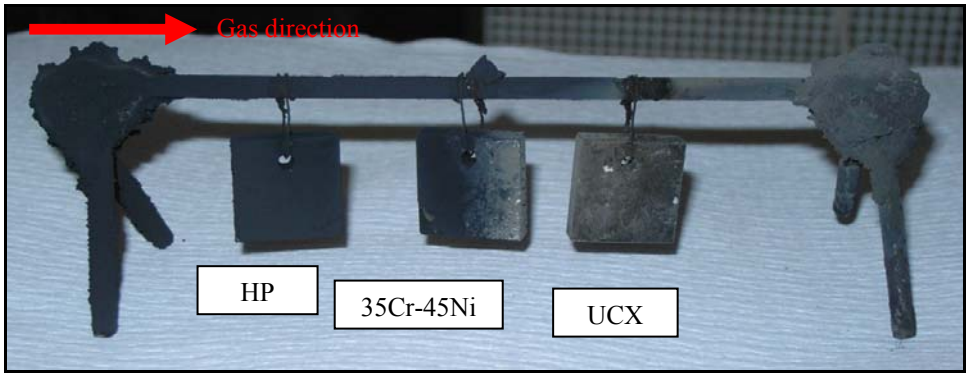

(c) Samples condition after 1000h

Figure 5.3 General photos of the alloys after the exposures at 750°C.

(a) Alloy condition after 100h

(b) Alloy condition after 500h

(c) Alloy condition after 1000h

Figure 5.4 Photos of the alloy after exposed at 750ºC after cleaning.

5.1.3 HP Tested at 850ºC

It was very obvious that increasing the temperature from 650 to 850ºC was accompanied by a remarkable decrease in carbon deposition. Photos of the samples tested at the latter temperature are shown in Figure 5.5.

The alloy experienced extremely low carbon deposition following the exposure for 100h at 850ºC. Indeed, the carbon deposition was more prevalent at the sample sides. The surface of the alloy was mainly covered with a grey layer.

Two different areas, shown by grey and lighter grey layers, were noticed on the sample exposed for the period of 500h. In addition, some small blackish spots were also observed on the alloy.

The sample subjected at 850ºC for 1000h formed a mixture of greyish and greenish layers (Figure 5.5 c). No samples showed any attraction to a magnet. The samples after cleaning are shown in Figure 5.6.

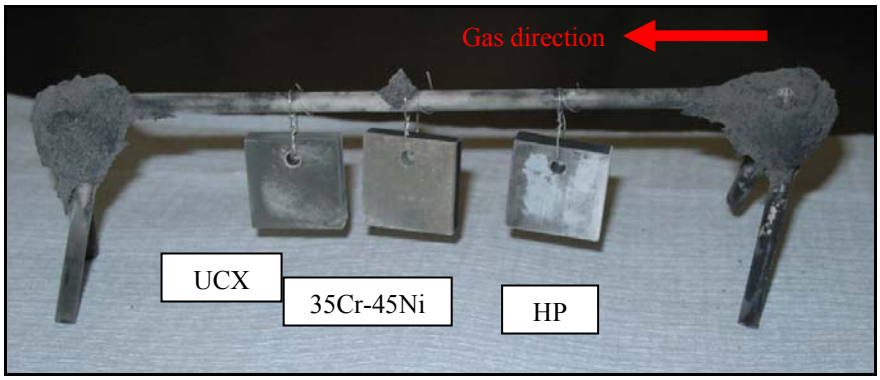

(a) Samples condition after 100h

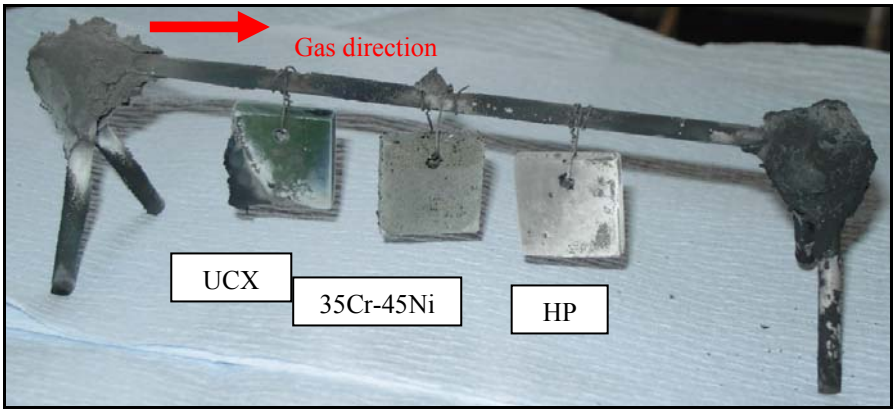

(b) Samples condition after 500h

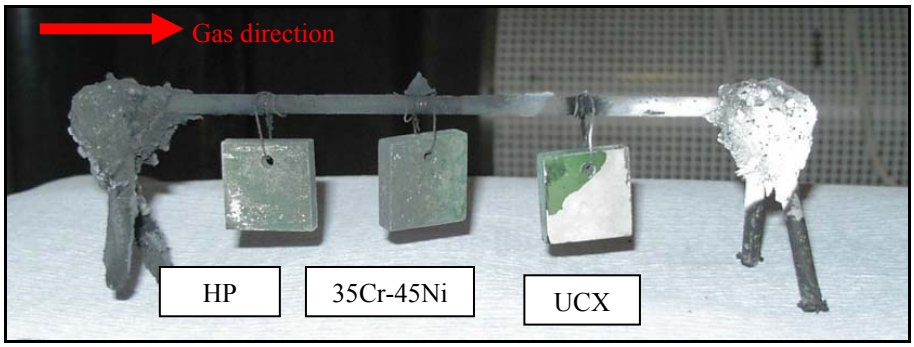

(c) Samples condition after 1000h

Figure 5.5 General photos of the alloys after the exposures at 850°C.

(a) Alloy condition after 100h

(b) Alloy condition after 500h

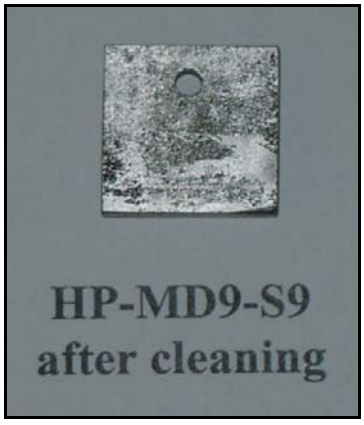

(c) Alloy condition after 1000h

Figure 5.6 Photos of the alloy after exposed at 850ºC after cleaning.

5.2 Weight Change Measurements

After each test, any deposits on the samples were mechanically removed by bristle brush. Subsequently, the specimens were thoroughly washed in water and finally, ultrasonically cleaned in acetone for 40 minutes. Despite this procedure the sample surfaces still appeared to retain some deposits that were very adhering such that they could not be removed. Indeed, cleaning the samples was an uneasy task as a compromise was required and care was taken not to damage the surface features in order to allow for further investigation.

The specimens were weighed to determine the resultant weight change, Table 5.1. The measurements indicated weight change fluctuations, varying from weight gain to weight loss, at the same temperature but at different exposure times. Indeed, the weight change would be the product of a complex interaction of several processes including oxidation, oxides volatility, carburisation, carbon intake, and metal wastage which, in turn, had been influenced by the exposure temperature and duration. Therefore, the occurrence and/or extent of metal dusting could not be fully predicted using only this technique.

Table 5.1 Weight change (mg/cm^2) of the alloy after the exposure at different temperatures for different periods of time.

Temperature (°C)	100h	500h	1000h
650	-0.1529	-3.0928	0.3081
750	1.0128	-2.9568	0.1093
850	0.3099	0.9083	-0.2468

5.3 X ray Diffraction Results

All the alloy surfaces, as well as the deposits if there were sufficient, were analysed by XRD. In fact, all samples that experienced the gas mixture at 650 and 750ºC formed sufficient amounts of deposits that could be collected and analysed. The XRD patterns and charts are given in Appendix C.

Exposing the alloy at 650ºC for 100h resulted in the formation of Fe_3O_4 and C in addition to chromium and iron-containing carbides. Analysing the deposit removed from this sample revealed the presence of C, SiO_2, Cr_2O_3, Fe_2O_3, and (Fe,Ni). Extending the test time to 500h led to the formation of chromium and iron-containing carbides. Carbon, Cr_2O_3, $FeNi_3$, and $Ni_{0.6}Fe_{2.4}O_4$ were detected in the deposit collected from this sample. The 1000h exposure, however, led to the formation of C, Cr_2O_3, niobium carbides, and chromium and iron-containing carbides. The carbon gathered from this alloy was found to contain SiO_2 and Fe, as well as carbon.

Increasing the exposure temperature to 750ºC (for 100h) promoted the formation of $Cr_{0.5}Fe_{1.5}MnO_4$, SiO_2, and chromium and iron-bearing carbides on the alloy surface. The analysis of the deposits found on this sample revealed the presence of (Fe,Ni), SiO_2, and carbon. Prolonging the experiment time to 500h resulted in the development of $Mn_{0.43}Fe_{2.57}O_4$, SiO_2, and chromium and iron-containing carbides. The deposit removed from this specimen was confirmed to consist of Cr_2O_3, FeNi, SiO_2, and carbon. Increasing the exposure time to 1000h led to the formation of Cr_2O_3 and $Mn_{1.5}Cr_{1.5}O_4$. The deposit removed from this sample contained SiO_2 and carbon.

The alloy formed $CrFeMnO_4$, SiO_2, chromium, and chromium and iron-containing carbides after being exposed at 850ºC for 100h. Increasing the testing period to 500h led to the formation of SiO_2 and chromium and iron-containing carbides. The 1000h exposure caused the alloy to form $Mn_{1.5}Cr_{1.5}O_4$, C, $Fe_{1.34}Si_{0.66}$, and chromium carbides. Not enough deposit could be collected from the alloys exposed at 850ºC.

5.4 SEM/EDX Deposits Analysis

The chemical composition of the deposits removed from the alloys was confirmed using SEM/EDX, see Figures 5.7-5.12.

5.4.1 HP-650ºC-100h

As shown in Figure 5.7, three areas were analysed to identify the constituents of the deposit gathered from the alloy exposed at 650ºC for 100h. Beside carbon as the main element, considerable levels of oxygen and silicon were detected suggesting the presence of silicon oxide. Furthermore, traces of chromium and iron, and relatively high nickel content were also found.

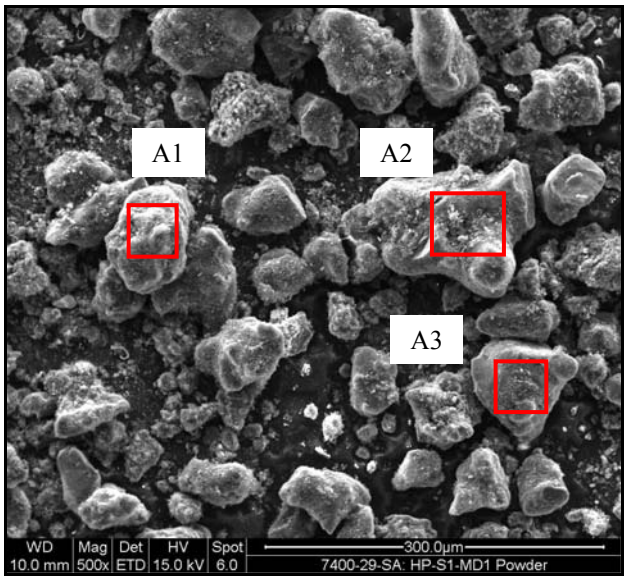

A1

Element	Wt%	At%
C K	86.07	91.07
O K	9.35	7.43
Si K	2.11	0.96
Cr K	0.29	0.07
Fe K	0.84	0.19
Ni K	1.34	0.29
Totals	100.00	

A2

Element	Wt%	At%
C K	76.07	84.43
O K	13.09	10.91
Si K	8.83	4.19
Cr K	0.23	0.06
Fe K	0.83	0.20
Ni K	0.95	0.22
Totals	100.00	

A3

Element	Wt%	At%
C K	68.62	78.63
O K	16.53	14.22
Si K	14.36	7.03
Ni K	0.49	0.11
Totals	100.00	

Figure 5.7 Chemical analysis of deposits removed from the alloy surface after the exposure at 650ºC for 100h.

5.4.2 HP-650ºC-500h

Figure 5.8 shows an image of the deposit removed from the alloy after the exposure at 650ºC for 500h. Four areas were analysed and confirmed to contain significant amounts of oxygen, iron, nickel, silicon, and chromium. It is worth noting that the concentrations of alloying elements detected in this deposit are higher than those found in deposit removed from the alloy tested for 100h, meaning that more reactions might have taken place as a result of prolonging the exposure time. It is also interesting to observe that the concentrations of silicon, iron, and nickel were higher than chromium.

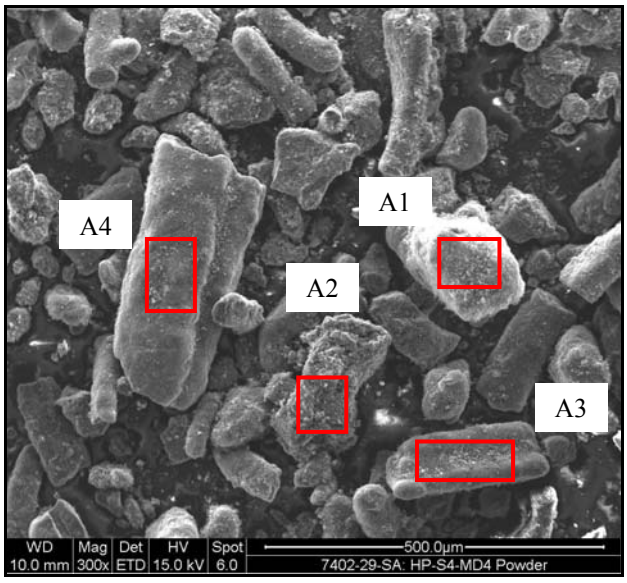

A1

	Wt%	At%
C K	73.99	81.95
O K	16.67	13.86
Si K	8.36	3.96
Fe K	0.54	0.13
Ni K	0.44	0.10
Totals	100.0	

A2

	Wt%	At%
C K	78.34	90.73
O K	5.64	4.90
Si K	1.45	0.72
S K	0.18	0.08
Cr K	2.94	0.79
Fe K	5.41	1.35
Ni K	6.04	1.43
Totals	100.0	

A3

	Wt%	At%
C K	89.12	92.75
O K	8.15	6.37
Si K	1.25	0.56
Fe K	0.50	0.11
Ni K	0.98	0.21
Totals	100.0	

A4

	Wt%	At%
C K	81.22	88.15
O K	9.66	7.87
Si K	8.06	3.74
Fe K	0.39	0.09
Ni K	0.67	0.15
Totals	100.0	

Figure 5.8 Chemical analysis of deposits removed from the alloy surface after the exposure at 650ºC for 500h.

5.4.3 HP-650ºC-1000h

Three regions on the deposit removed from the sample exposed at 650ºC for 1000h (Figure 5.9) were also analysed and found to contain considerable levels of oxygen, nickel, silicon, iron, and chromium. It is also worth noting that, unlike other areas, the area with the highest concentrations of iron and nickel appeared porous and somewhat level. In general, the deposits removed from the alloy after the three periods of exposure contained appreciable concentrations of alloying elements implying that the alloy may have suffered some metal wastage. The increase in the elements level in the deposit, as the exposure time was increased, may indicate that the sample underwent further metal loss.

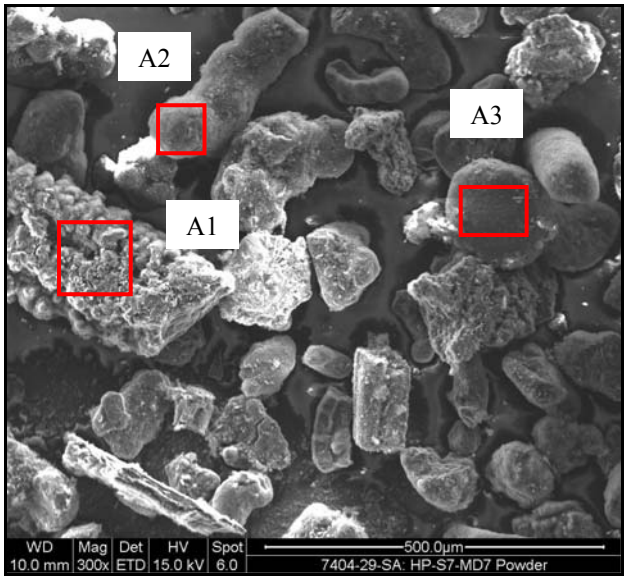

A1

Element	Wt%	At%
C K	84.87	92.64
O K	6.53	5.35
Si K	0.27	0.12
Cr K	0.95	0.24
Fe K	2.72	0.64
Ni K	4.22	0.94
Mo L	0.43	0.06
Totals	100.00	

A2

Element	Wt%	At%
C K	88.30	92.02
O K	9.22	7.21
Si K	1.03	0.46
Ni K	1.45	0.31
Totals	100.00	92.02

A3

Element	Wt%	At%
C K	86.29	92.43
O K	5.78	4.65
Si K	4.68	2.15
Cl K	0.41	0.15
Ni K	2.83	0.62
Totals	100.00	

Figure 5.9 Chemical analysis of deposits removed from the alloy surface after the exposure at 650ºC for 1000h.

5.4.4 HP-750ºC-100h

Exposing the alloy at 750ºC for 100h led to the formation of a deposit (rock-like particles) containing mainly carbon, oxygen, and silicon, suggesting the presence of some silicon oxides. Additionally, traces of nickel and iron were also detected in one area, Figure 5.10.

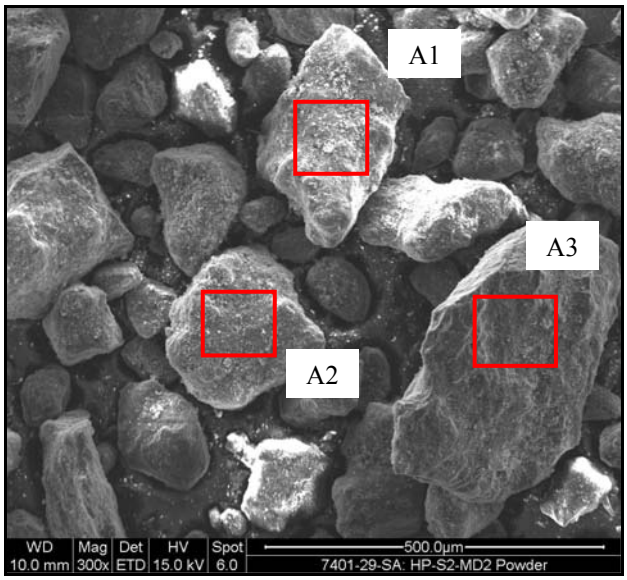

A1			A2			A3		
Element	Wt%	At%	Element	Wt%	At%	Element	Wt%	At%
C K	67.48	76.53	C K	52.13	63.95	C K	84.63	89.39
O K	21.01	17.89	O K	27.57	25.39	O K	11.90	9.44
Si K	11.51	5.58	Si K	20.31	10.66	Si K	1.85	0.84
						Fe K	0.31	0.07
						Ni K	0.36	0.08
						Cu K	0.95	0.19
Totals	100.00		Totals	100.00		Totals	100.00	

Figure 5.10 Chemical analysis of deposits removed from the alloy surface after the exposure at 750ºC for 100h.

5.4.5 HP-750ºC-500h

Extending the exposure time to 500h at 750ºC led to the development of deposits that were composed of carbon as main constituent and oxygen as the major element. Moreover, considerable amounts of iron, nickel, chromium, and silicon were also discovered, Figure 5.11.

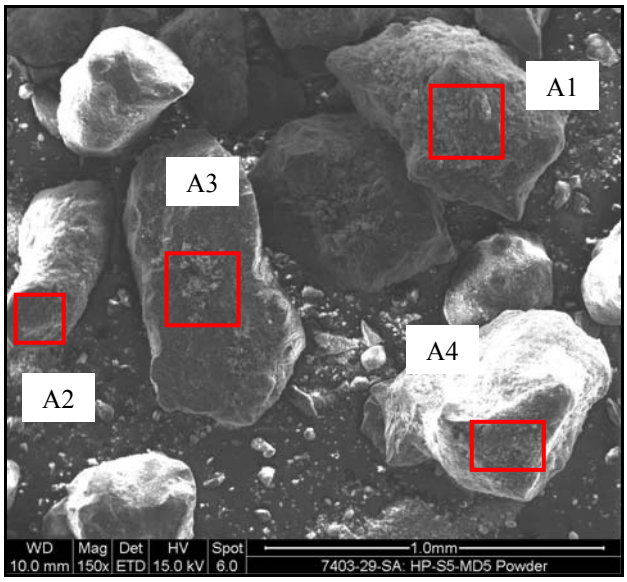

A1			A2			A3			A4		
	Wt%	At%		Wt%	At%		Wt%	At%		Wt%	At%
C K	82.41	88.43	C K	88.64	91.94	C K	86.42	92.46	C K	89.01	92.48
O K	11.97	9.65	O K	9.63	7.49	O K	7.31	5.87	O K	8.50	6.63
Si K	2.67	1.22	Si K	0.84	0.37	Si K	1.03	0.47	Si K	1.50	0.67
Cr K	1.42	0.35	Fe K	0.51	0.11	Cr K	1.07	0.26	Fe K	0.41	0.09
Fe K	0.78	0.18	Ni K	0.38	0.08	Fe K	1.81	0.42	Ni K	0.57	0.12
Ni K	0.75	0.16				Ni K	2.37	0.52			
Totals	100.0		Totals	100.0		Totals	100.0		Totals	100.0	

Figure 5.11 Chemical analysis of deposits removed from the alloy surface after the exposure at 750ºC for 500h.

5.4.6 HP-750ºC-1000h

The flake-like deposit found on the sample after the testing at 750ºC for 1000h was composed mainly of carbon, and some oxygen and silicon. Additionally, traces of nickel and chromium were also detected (Figure 5.12). In short, testing the alloy at both 650 and 750ºC led to the deposition and accumulation of carbon deposits that contained different levels of alloying elements suggesting the occurrence of metal wastage.

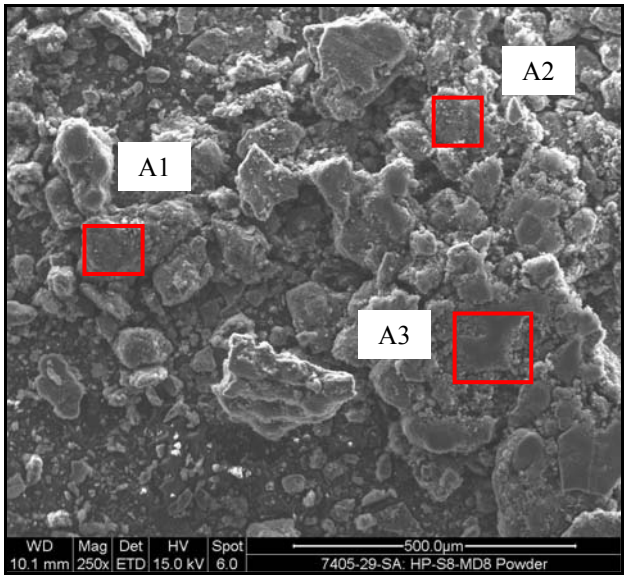

A1

Element	Wt%	At%
C K	87.62	91.41
O K	9.11	7.14
Si K	3.26	1.46
Totals	100.00	

A2

Element	Wt%	At%
C K	89.21	92.74
O K	7.75	6.05
Si K	2.46	1.09
Ni K	0.58	0.12
Totals	100.00	

A3

Element	Wt%	At%
C K	84.71	90.53
O K	8.07	6.47
Si K	5.88	2.69
Cr K	0.58	0.14
Ni K	0.77	0.17
Totals	100.00	

Figure 5.12 Chemical analysis of deposits removed from the alloy surface after the exposure at 750ºC for 1000h.

5.5 Surface Analyses

The alloy surfaces were thoroughly examined using SEM/EDX. Any surface features such as localised attack, carbon and/or oxide layers were identified and analysed.

5.5.1 HP-650ºC-100h

Examination of the alloy surface exposed to the gas mixture for 100h revealed the presence of a dense layer that was subsequently confirmed to be composed mainly of carbon, oxygen, silicon, chromium, iron, nickel, and some manganese (Figure 5.13). Some localised, darker deposits were also observed and found to contain major amounts of carbon, oxygen, and silicon in addition to traces of iron, chromium, and nickel.

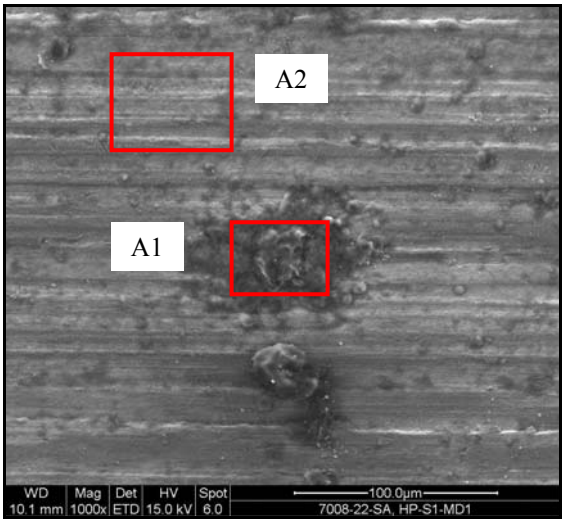

A1

Element	Weight%	Atomic%
C K	53.79	66.44
O K	25.30	23.46
Si K	16.63	8.79
S K	0.13	0.06
Cl K	0.15	0.06
K K	0.19	0.07
Ca K	0.94	0.35
Cr K	1.05	0.30
Fe K	1.06	0.28
Ni K	0.76	0.19
Totals	100.00	

A2

Element	Weight%	Atomic%
C K	17.02	36.08
O K	19.78	31.47
Si K	7.54	6.83
Cr K	19.17	9.38
Mn K	2.36	1.09
Fe K	17.72	8.08
Ni K	16.13	6.99
Nb L	0.28	0.08
Totals	100.00	

Figure 5.13 General image of the alloy surface after the exposure for 100h.

The layer was found flaked off in some areas, possibly by the cleaning process, allowing further examination of the surface underneath (Figure 5.14). Tiny pits, with a maximum size of about 1µm, could be seen spreading across the substrate. EDX analysis of the pit contents showed the presence of higher levels of carbon than the surrounding areas.

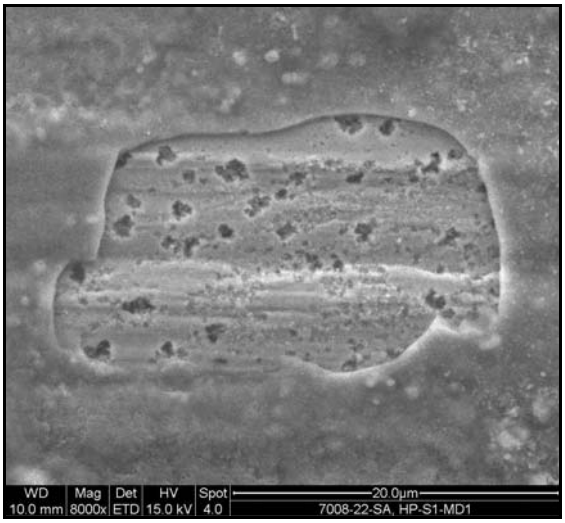

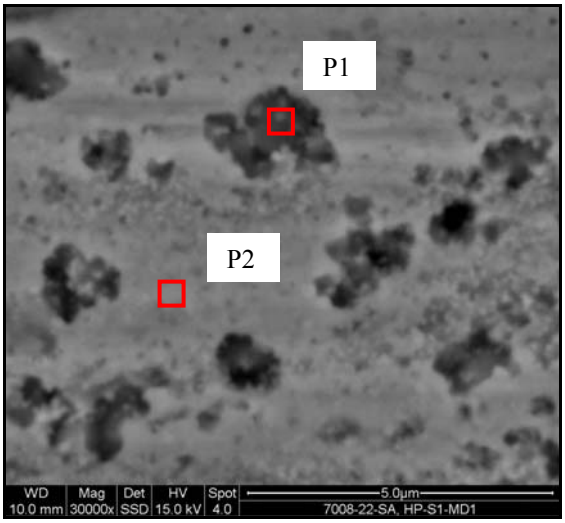

P1

Element	Weight%	Atomic%
C K	4.89	17.63
O K	3.97	10.75
Si K	1.17	1.80
Ca K	1.23	1.33
Cr K	17.48	14.56
Fe K	36.51	28.30
Ni K	34.75	25.63
Totals	100.00	

P2

Element	Weight%	Atomic%
C K	2.10	8.34
O K	3.06	9.14
Si K	2.36	4.01
Cr K	15.39	14.14
Fe K	38.92	33.30
Ni K	38.17	31.06
Totals	100.00	

Figure 5.14 The alloy suffered pitting attack after the 100h experiment.

5.5.2 HP-650ºC-500h

A layer had also established on the sample exposed for 500h, as seen in Figure 5.15 below. The layer appeared to be composed of two phases; grey and lighter grey. Analysing the light greyish phases confirmed that it was basically composed of carbon and some oxides of silicon, chromium, and manganese. Iron was also detected in that phase. The darker phases, on the other hand, contained more carbon but much lower levels of chromium and manganese. Distinctive, randomly distributed islands of deposit (P1) were also noticed to have formed on the alloy. Their elemental analysis confirmed that they were composed mainly of carbon and some silicon oxide.

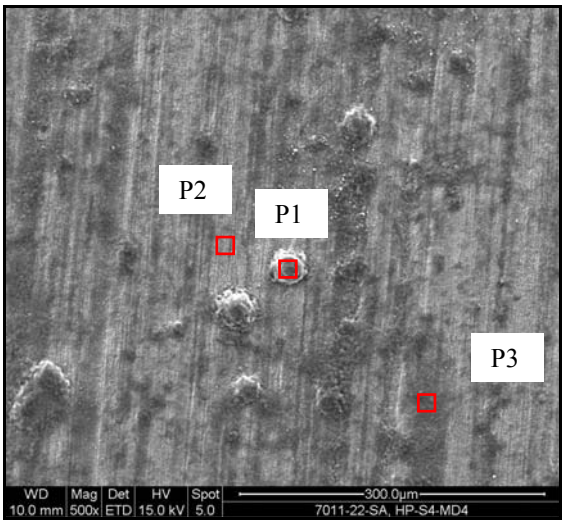

P1

Element	Wt%	At%
C K	52.84	64.17
O K	28.90	26.35
Si K	18.26	9.48
Totals	100.00	

P2

Element	Wt%	At%
C K	15.19	28.62
O K	30.40	43.00
Si K	13.23	10.66
Cr K	33.09	14.40
Mn K	5.97	2.46
Fe K	2.12	0.86
Totals	100.00	

P3

Element	Wt%	At%
C K	45.08	58.43
O K	29.71	28.91
Si K	19.69	10.91
Ca K	1.43	0.55
Cr K	2.62	0.79
Mn K	1.47	0.42
Totals	100.00	

Figure 5.15 Formation of dense layer on the alloy after the 500h test.

Although most of the sample had been covered with the dense layer, some alloy surface could be seen exposed in some areas. As seen Figures 5.16 and 5.17, some of the underlying alloy surface appeared intact whereas other areas suffered localised pitting that might be deemed to be initiation points of metal dusting. EDX analysis of the surface layer revealed significant variation in its chemical composition from one area to the other. The composition of the layer at A1 was dominated by carbon and silicon oxides whilst the layer at A2 contained much higher levels of chromium and appreciable amount of manganese suggesting the formation of protective oxides. Considerable levels of iron and nickel were also found in the latter. The bare surface composition was more or less identical to that of the base metal. However, no manganese could be detected indicating it might well be consumed at the surface.

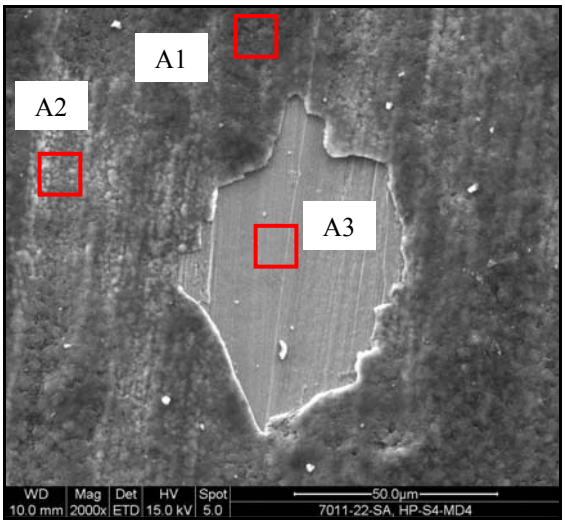

A1

Element	Wt%	At%
C K	43.13	57.45
O K	28.33	28.32
Si K	20.71	11.79
Ca K	0.43	0.17
Cr K	6.46	1.99
Mn K	0.95	0.28
Totals	100.00	

A2

Element	Wt%	At%
C K	10.23	20.75
O K	32.91	50.13
Si K	7.18	6.23
Cr K	38.81	18.19
Mn K	3.40	1.51
Fe K	4.07	1.77
Ni K	3.41	1.41
Totals	100.00	

A3

Element	Wt%	At%
C K	2.75	10.89
O K	2.35	7.00
Si K	1.90	3.23
Cr K	20.52	18.81
Fe K	35.49	30.29
Ni K	36.20	29.38
Nb L	0.79	0.40
Totals	100.00	

Figure 5.16 EDX analyses of the layer formed after 500h.

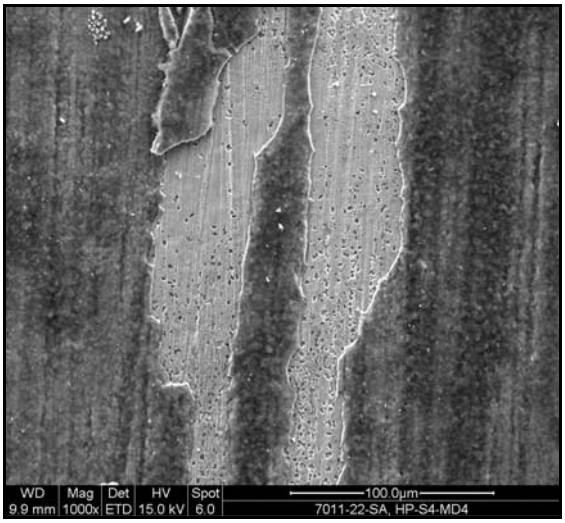

Figure 5.17 Tiny pits on the alloy surface following the exposure for 500h.

5.5.3 HP-650ºC-1000h

Two distinctive scales were observed to have developed on the alloy as a consequence of the exposure for 1000h; one blackish layer formed on top of another greyish layer (Figure 5.18).

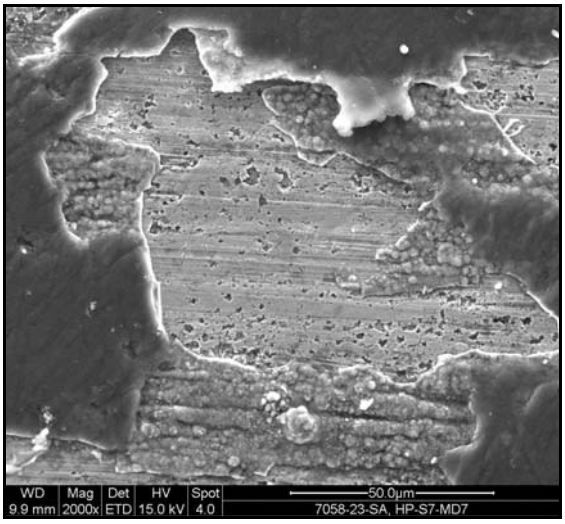

Figure 5.18 Two different layers were observed on the alloy after 1000h of exposure.

Moreover, localised attack in form of relatively large pits was noticed (Figure 5.19). Some of the pits were full of material containing calcium, oxygen, and carbon that was subsequently confirmed, using EDX, to have come from the glue used to attach the samples to the XRD machine holder. The glue was so 'sticky' and apparently could not be removed by the cleaning process followed the XRD analysis. However, Figure 5.19 b shows another area, on the same sample, where the attack took place.

The blackish layer (A4) was analysed by EDX and found to be carbon-based, with some traces of chromium, iron, and silicon. The greyish layer, however, was composed mainly of chromium and some silicon oxides in addition to carbon as a major element.

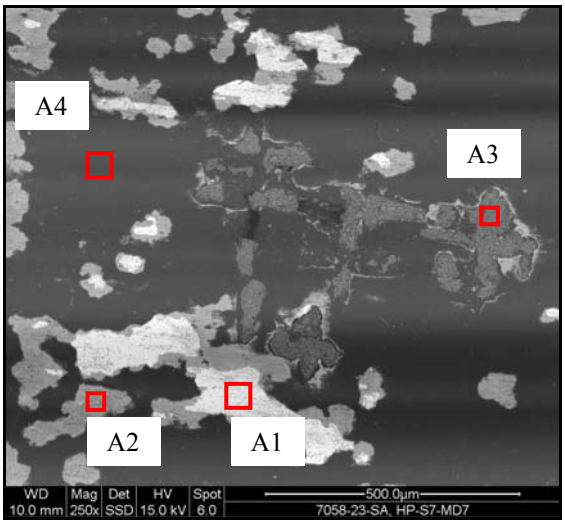

(a) Backscattered electron image of a localised attack.

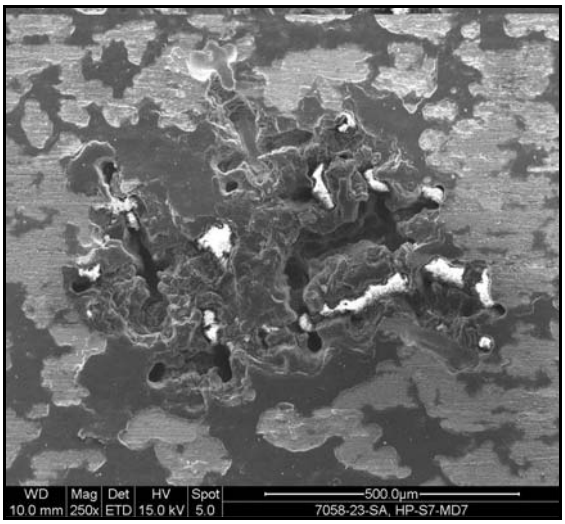

(b) Secondary electron image showing another attacked area.

A1

	Wt%	At%
C K	5.29	18.29
O K	5.05	13.10
Si K	3.31	4.89
Cr K	17.80	14.22
Fe K	33.21	24.69
Ni K	34.61	24.48
Nb L	0.73	0.33
Totals	100.0	

A2

	Wt%	At%
C K	14.47	28.29
O K	31.28	45.90
Si K	4.01	3.35
Ca K	0.73	0.43
Cr K	40.56	18.31
Mn K	3.16	1.35
Fe K	3.09	1.30
Ni K	2.70	1.08
Totals	100.0	

A3

	Wt%	At%
C K	15.46	26.24
O K	40.15	51.16
Si K	0.34	0.25
Ca K	43.55	22.15
Cr K	0.51	0.20
Totals	100.0	

A4

	Wt%	At%
C K	89.49	92.98
O K	7.56	5.90
Si K	1.66	0.74
S K	0.29	0.11
Cl K	0.16	0.06
Ca K	0.25	0.08
Cr K	0.33	0.08
Fe K	0.27	0.06
Totals	100.0	

Figure 5.19 Localised attack was noticed on the alloy after the 1000h experiment.

The alloy substrate, just under the greyish layer, was exposed in some areas permitting more examination to be carried out. As seen in Figure 5.20, the surface experienced pitting with pits of varying size, which probably represented the attack onset sites. The deposits inside the pits were analysed and found to contain high amount of calcium suggest the presence of some glue material that mentioned in the previous paragraph. In addition, major concentrations of chromium, iron, and nickel were also detected. Comparatively huge, deep pits were also noticed on the sample, with sizes of about 100µm, Figure 5.21.

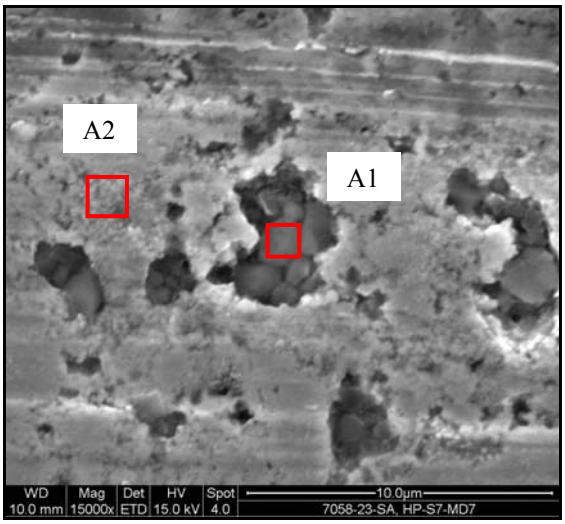

A1

Element	Weight%	Atomic%
C K	16.79	33.16
O K	26.03	38.59
Si K	3.18	2.69
Ca K	15.09	8.93
Cr K	11.62	5.30
Fe K	14.49	6.16
Ni K	12.79	5.17
Totals	100.00	

A2

Element	Weight%	Atomic%
C K	8.05	24.65
O K	6.30	14.49
Si K	2.05	2.68
Cr K	66.74	47.23
Fe K	11.53	7.59
Ni K	5.34	3.35
Totals	100.00	

Figure 5.20 Pits with varying sizes occurred on the alloy after 1000h.

Collectively, testing the alloy at 650ºC in the gas mixture led to the formation of layers with mixtures of oxides, carbon, and possibly alloying elements. The attack seemed to have taken place after a relatively short time (less than 100h) of exposure and been increased at times longer. The corrosion was localised and appeared to have been initiated from tiny pits that subsequently linked up forming groove-like patterns.

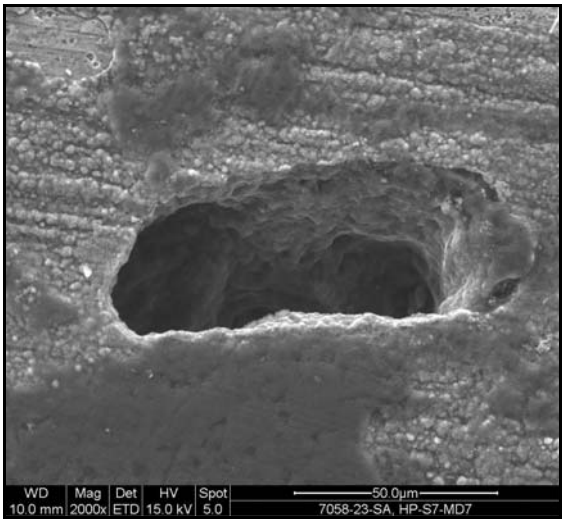

Figure 5.21 Relatively big and deep pits on the alloy exposed for 1000h.

5.5.4 HP-750ºC-100h

Figure 5.22 shows the alloy surface after exposure at 750ºC for the period of 100h. Almost all the sample had been coated with a layer that was adherent enough not to be entirely removed during the cleaning procedure. Chemical analyses of the layer showed the presence of high levels of oxygen suggesting that it was composed mainly of oxides of chromium, manganese, and silicon. However, the presence of some free alloying elements (or carbides) such as iron and nickel could not be ruled out. A considerable amount of carbon was also detected within this layer. What seemed to be localised, thicker layers (A2) were found to contain higher levels of carbon with lower amounts of iron and nickel. The substrate, just underneath the layers, appeared to contain relatively low levels of the alloying elements, iron and nickel. Figure 5.23 shows a higher magnification image of the alloy surface revealing the presence of some localised metal removal sites.

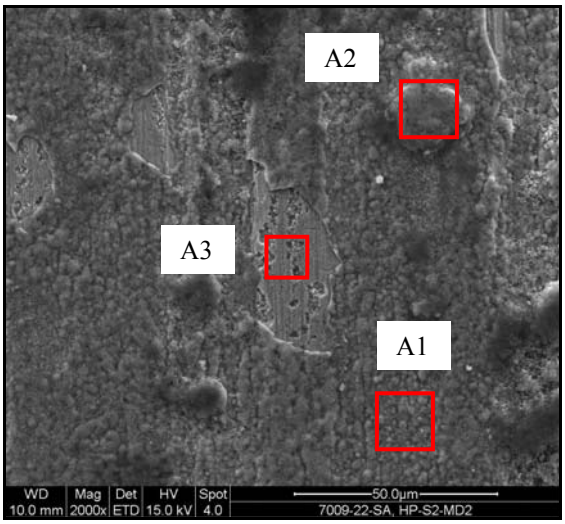

A1

Element	Wt%	At%
C K	7.86	16.95
O K	30.29	49.05
Si K	9.89	9.12
Ca K	0.28	0.18
Cr K	25.37	12.64
Mn K	7.03	3.31
Fe K	9.87	4.58
Ni K	9.42	4.16
Totals	100.00	

A2

Element	Wt%	At%
C K	14.12	25.92
O K	35.01	48.25
Si K	12.31	9.66
Ca K	0.75	0.41
Cr K	27.80	11.79
Mn K	6.58	2.64
Fe K	1.97	0.78
Ni K	1.46	0.55
Totals	100.00	

A3

Element	Wt%	At%
C K	6.31	19.62
O K	8.73	20.37
Si K	4.73	6.29
Ca K	0.87	0.81
Cr K	21.78	15.64
Fe K	28.05	18.75
Ni K	28.38	18.05
Nb L	1.17	0.47
Totals	100.00	

Figure 5.22 The alloy surface condition after the exposure at 750ºC for 100h.

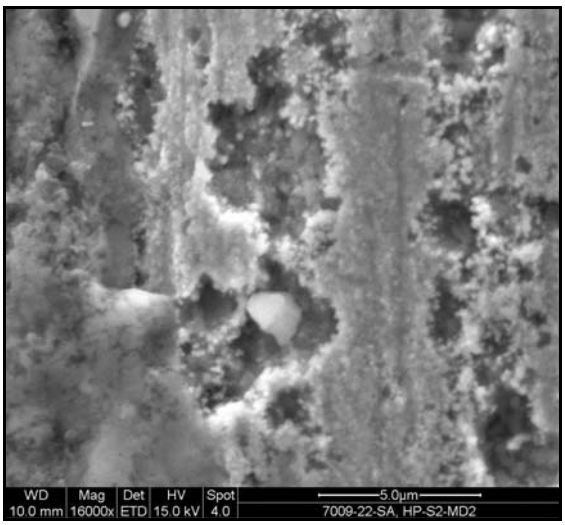

Figure 5.23 Localised attack was observed on the alloy substrate.

5.5.5 HP-750ºC-500h

Oxides of different composition were found on the alloy as a result of increasing the exposure time to 500h, Figure 5.24.

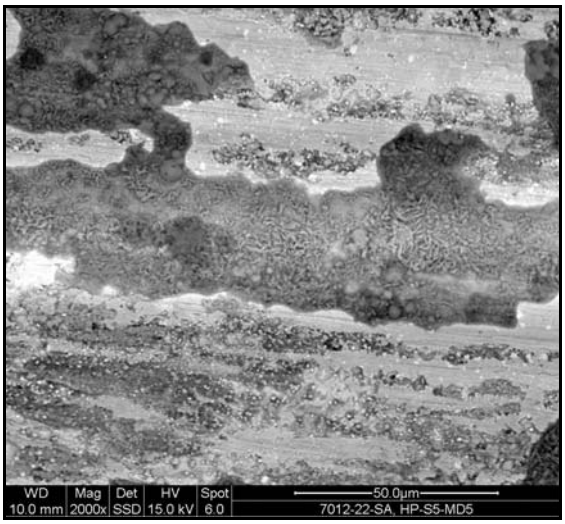

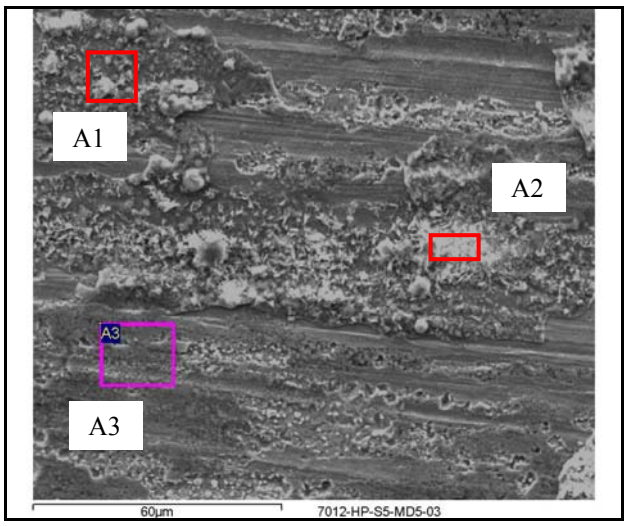

A1

Element	Wt%	At%
C K	2.13	4.74
O K	33.51	56.06
Si K	16.43	15.66
Cr K	20.75	10.68
Mn K	7.78	3.79
Fe K	9.87	4.73
Ni K	9.54	4.35
Totals	100.00	

A2

Element	Wt%	At%
C K	2.42	4.99
O K	38.95	60.28
Si K	18.40	16.23
Cr K	17.25	8.21
Mn K	19.16	8.64
Fe K	2.04	0.91
Ni K	1.77	0.75
Totals	100.00	

A3

Element	Wt%	At%
C K	5.54	15.81
O K	13.42	28.74
Si K	8.10	9.88
Cr K	38.54	25.39
Fe K	15.62	9.58
Ni K	17.09	9.97
Nb L	1.67	0.62
Totals	100.00	

Figure 5.24 General view of the alloy surface following the exposure for 500h.

A higher magnification photomicrograph of the area (A2) in Figure 5.24 is shown in Figure 5.25. Needle-like crystallites could be observed growing on the surface. This layer was manly composed of oxygen, silicon, chromium, manganese, and some iron.

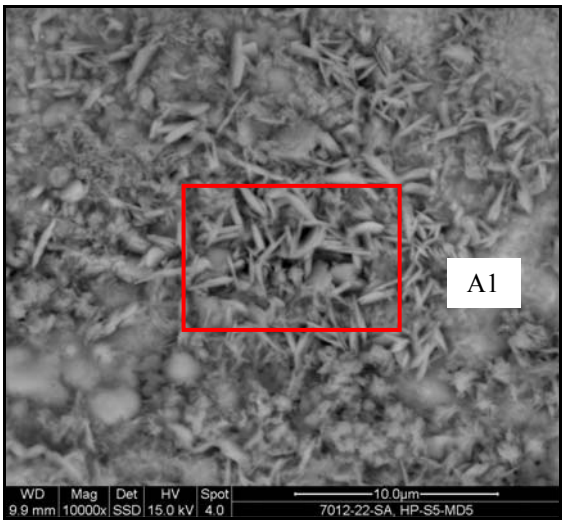

A1

Element	Weight%	Atomic%
O K	40.53	64.06
Si K	18.44	16.60
Cr K	18.78	9.13
Mn K	17.76	8.18
Fe K	4.49	2.03
Totals	100.00	

Figure 5.25 Needle-like oxides were seen on the alloy.

Further analysis of the alloy surface revealed significant variations in the chemical composition from one point to the other. As seen in Figure 5.26, the level of oxygen was considerably higher at area A1, suggesting the establishment of more oxides at this site. Moreover, some areas had suffered some metal removal in the pitted areas.

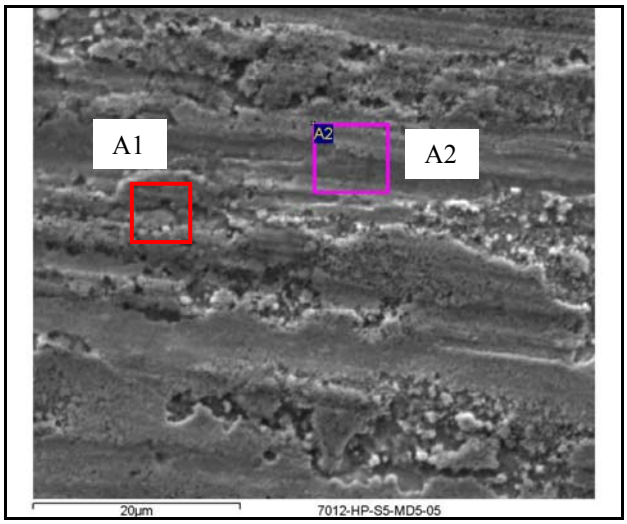

A1

Element	Weight%	Atomic%
C K	4.59	13.13
O K	14.22	30.56
Si K	9.52	11.66
Cr K	34.51	22.82
Fe K	17.30	10.65
Ni K	17.82	10.44
Nb L	2.04	0.75
Totals	100.00	

A2

Element	Weight%	Atomic%
C K	2.18	8.57
O K	3.29	9.71
Si K	2.93	4.92
Cr K	20.97	19.04
Fe K	33.47	28.30
Ni K	35.75	28.75
Nb L	1.41	0.72
Totals	100.00	

Figure 5.26 Some metal removal could be noticed to take place on the alloy.

5.5.6 HP-750°C-1000h

Figure 5.27 shows an image of the alloy surface after the 1000h experiment. A layer of oxides of chromium, silicon, and manganese seemed to have formed on the alloys (A1). Carbon was also available as a minor element. The sample surface also experienced some localised attack in the form of scattered pits. The pits contained appreciable levels of carbon and oxides. EDX of area (A3) revealed relatively lower chromium content than that expected in the base metal. This might be attributed to the chromium diffusion and consumption in the oxide layer. No oxygen was detected in that area.

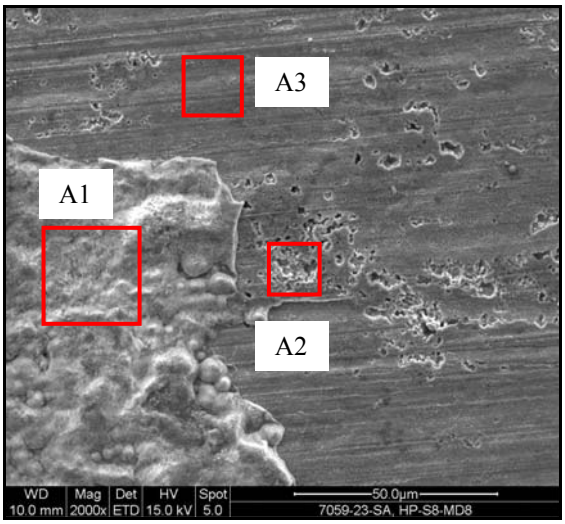

A1

Element	Wt%	At%
C K	2.82	6.33
O K	36.24	61.04
Si K	2.77	2.66
Cr K	51.57	26.73
Mn K	6.60	3.24
Totals	100.00	

A2

Element	Wt%	At%
C K	4.72	15.50
O K	7.59	18.72
Si K	4.14	5.82
Cr K	39.81	30.20
Fe K	20.92	14.78
Ni K	21.43	14.40
Nb L	1.38	0.59
Totals	100.00	

A3

Element	Wt%	At%
C K	1.76	7.63
Si K	2.52	4.68
Cr K	16.60	16.65
Fe K	36.19	33.81
Ni K	40.07	35.61
Nb L	2.87	1.61
Totals	100.00	

Figure 5.27 The alloy surface condition after being exposed at 750ºC for 1000h.

Investigating other areas on that alloy confirmed the presence of mixtures of oxides and carbon (and some possible carbides or elements). The area A1 shown in Figure 5.28 appeared to be a large pit that contained more carbon than the adjacent areas. Significantly higher manganese was also detected within this area.

In summary, raising the experimental temperature to 750ºC resulted in a noticeable reduction in carbon deposition and more formation of oxides. However, signs of some metal removal on the alloy surface could be observed suggesting that the alloy was probably still susceptible to metal wastage.

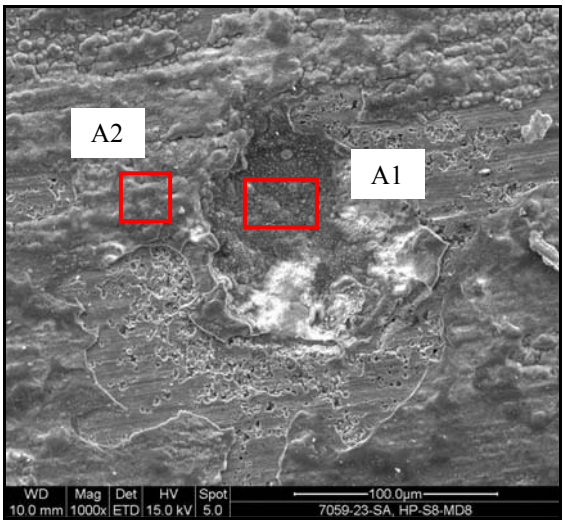

A1

Element	Weight%	Atomic%
C K	18.09	34.01
O K	29.21	41.22
Si K	6.49	5.22
Cr K	24.26	10.53
Mn K	21.95	9.02
Totals	100.00	

A2

Element	Weight%	Atomic%
C K	8.03	16.57
O K	36.17	56.06
Si K	2.31	2.04
Cr K	46.61	22.23
Mn K	6.89	3.11
Totals	100.00	

Figure 5.28 Alloy surface after 1000h at 750ºC.

5.5.7 HP-850ºC-100h

Little carbon was detected on the alloy surface after exposure at 850ºC for 100h. Instead, very high levels of silicon were detected. Figure 5.29 is an image of the alloy surface where two phases could be clearly distinguished. Mainly silicon oxide had formed at area A1, where the layer appeared to be thicker, whereas in the darker region, A2, much more chromium and manganese were detected in addition to iron and nickel as minor elements. The area under the scale was also analysed and found to bear less oxygen but much higher levels of iron, nickel, and chromium, which, however, did not reach their concentrations in the base metal.

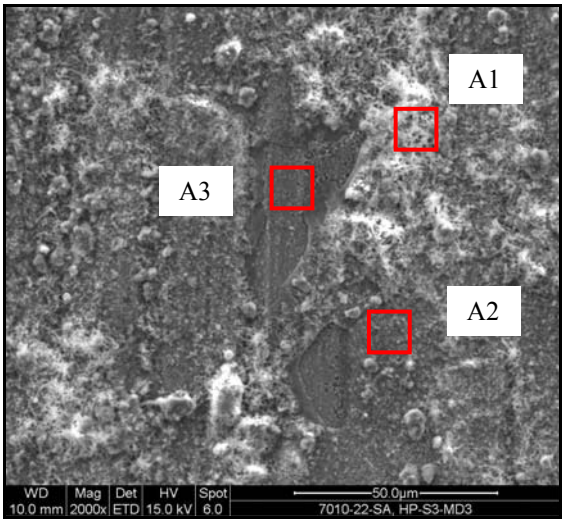

A1

Element	Wt%	At%
C K	3.19	5.37
O K	50.35	63.61
Si K	39.34	28.31
Ca K	0.47	0.24
Cr K	2.22	0.86
Mn K	3.29	1.21
Fe K	0.61	0.22
Ni K	0.52	0.18
Totals	100.00	

A2

Element	Wt%	At%
C K	2.00	3.90
O K	42.40	62.20
Si K	24.15	20.18
Cr K	14.84	6.70
Mn K	11.84	5.06
Fe K	2.81	1.18
Ni K	1.97	0.79
Totals	100.00	

A3

Element	Wt%	At%
C K	2.00	6.17
O K	14.12	32.69
Si K	8.64	11.39
Cr K	24.40	17.38
Mn K	1.10	0.74
Fe K	22.94	15.21
Ni K	24.67	15.56
Nb L	2.14	0.85
Totals	100.00	

Figure 5.29 Condition of the alloy after the testing at 850°C for the period of 100h.

A higher magnification micrograph, shown in Figure 5.30, revealed the presence of fibre-like, silicon-based oxides. These oxides contained considerable amounts of chromium, iron, and nickel with traces of manganese. However, the analysis of the round, protruding deposit (A1) confirmed that it contained higher levels of chromium and manganese and almost no iron and nickel. Moreover, a noticeably higher percentage of carbon was also detected.

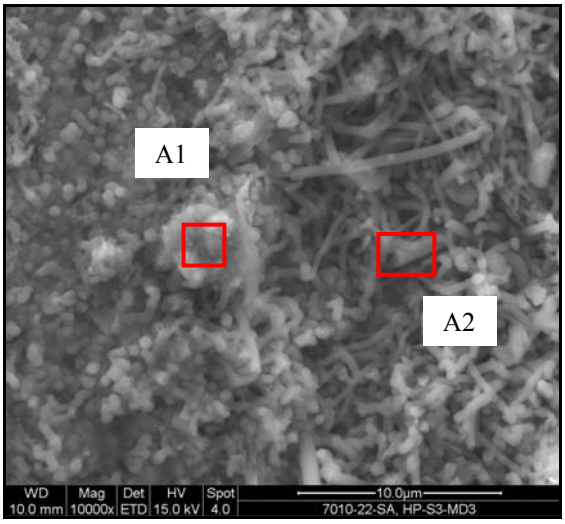

A1

Element	Weight%	Atomic%
C K	12.71	21.45
O K	43.33	54.88
Si K	20.37	14.70
Ca K	0.15	0.08
Cr K	11.94	4.65
Mn K	10.69	3.94
Fe K	0.81	0.30
Totals	100.00	

A2

Element	Weight%	Atomic%
C K	1.09	1.96
O K	48.16	64.92
Si K	35.01	26.89
Cr K	7.52	3.12
Mn K	0.98	0.39
Fe K	3.92	1.52
Ni K	3.32	1.22
Totals	100.00	

Figure 5.30 Fibre-like crystallites formed on the alloy after 100h exposure at 850ºC.

Figure 5.31 shows another area where the underlying surface could be seen. Indeed, two layers could be observed to have formed on the alloy; the above-mentioned silicon-based oxide layer and a chromium-based oxide layer, where the latter developed directly on the alloy substrate while the former formed above it.

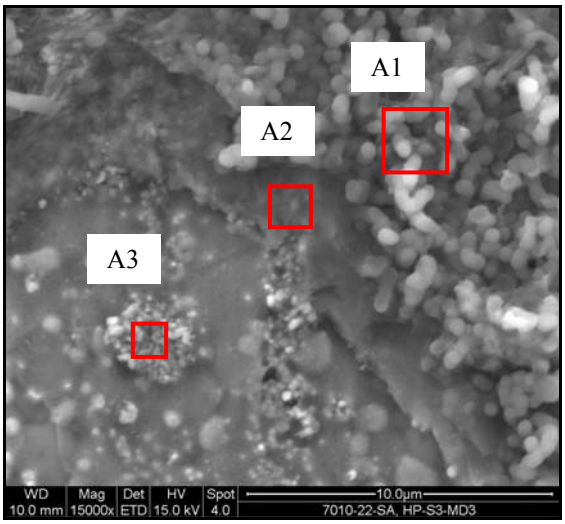

A1

Element	Wt%	At%
C K	2.83	5.19
O K	45.90	63.22
Si K	27.74	21.76
Cr K	17.41	7.38
Mn K	4.62	1.85
Fe K	1.51	0.59
Totals	100.00	

A2

Element	Wt%	At%
C K	1.51	3.92
O K	24.87	48.37
Si K	10.10	11.19
Cr K	38.50	23.04
Mn K	8.00	4.53
Fe K	7.43	4.14
Ni K	8.12	4.31
Nb L	1.46	0.49
Totals	100.00	

A3

Element	Wt%	At%
C K	6.52	19.87
O K	8.28	18.94
Si K	3.71	4.83
Cr K	64.74	45.58
Fe K	10.28	6.74
Ni K	6.47	4.04
Totals	100.00	

Figure 5.31 **Two different layer were observed to have grown on the alloy after 100h exposure at 850º.**

5.5.8 HP-850ºC-500h

A micrograph of the alloy that had been exposed to the gas mixture at 850ºC for 500h is shown in Figure 5.32. It was evident that more layer growth occurred as a consequence of the temperature rise. EDX confirmed that the layer that had been established on the alloy contained high levels of oxygen, silicon, manganese and carbon. Only about 3 wt% of chromium was detected at both areas; A1 and A2. The sub-surface under this layer was also analysed and found to contain levels of chromium (~36 wt%) that were considerably higher than that in the base metal. However, the iron and nickel contents were found to be less than those expected in bulk alloy. The presence of appreciable amount of carbon at that region may well suggest the presence of some alloy carbides.

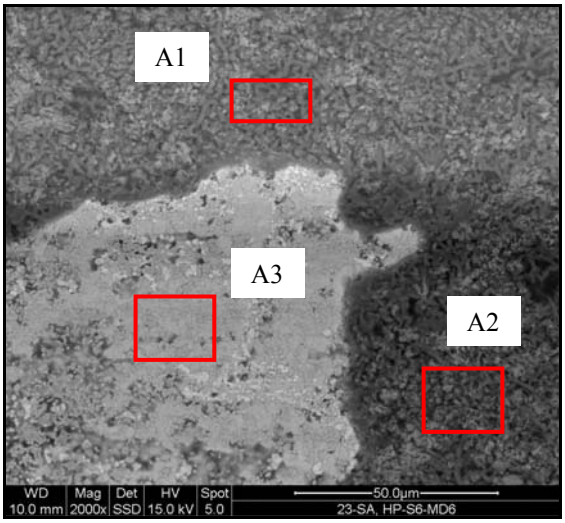

A1

Element	Wt%	At%
C K	13.10	21.38
O K	43.81	53.67
Si K	27.83	19.42
Ca K	0.20	0.10
Cr K	3.03	1.14
Mn K	11.56	4.13
Fe K	0.46	0.16
Totals	100.00	

A2

Element	Wt%	At%
C K	5.35	9.38
O K	46.28	60.93
Si K	30.25	22.69
Cr K	3.70	1.50
Mn K	13.36	5.12
Fe K	0.54	0.20
Ni K	0.53	0.19
Totals	100.00	

A3

Element	Wt%	At%
C K	3.31	12.28
O K	3.90	10.85
Si K	2.64	4.19
Cr K	36.20	31.03
Fe K	26.56	21.20
Ni K	26.22	19.90
Nb L	1.18	0.56
Totals	100.00	

Figure 5.32 The alloy status after the 500h experiment.

Higher magnification images of the alloy surface confirmed the formation of two distinct phases (Figure 5.33). A phase of dark grey crystallites was clearly observed apparently growing on lighter grey layers. The former was analysed to contain silicon and oxygen as main constituents. The latter, however, contained high amounts of chromium and manganese in addition to silicon and oxygen.

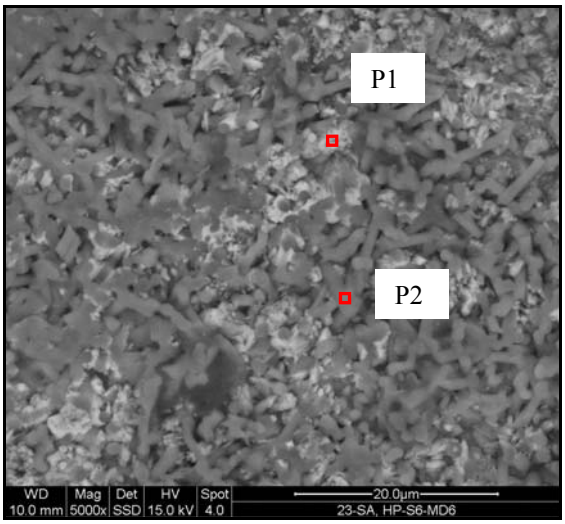

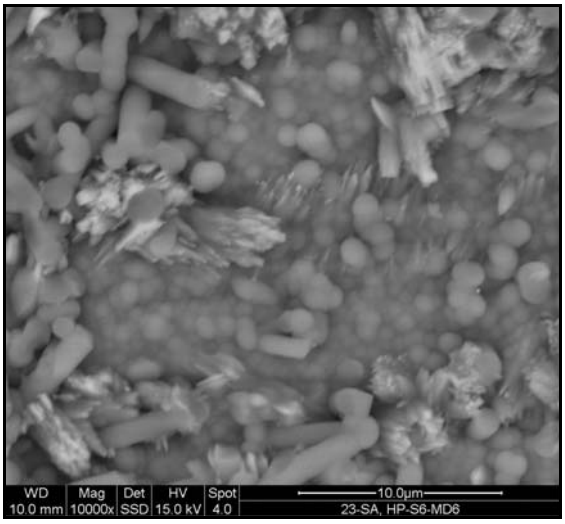

P1

Element	Weight%	Atomic%
C K	1.36	2.83
O K	39.31	61.34
Si K	20.02	17.80
Cr K	7.69	3.69
Mn K	30.05	13.65
Fe K	0.96	0.43
Ni K	0.62	0.26
Totals	100.00	

P2

Element	Weight%	Atomic%
C K	1.43	2.36
O K	54.38	67.22
Si K	42.13	29.67
Cr K	0.69	0.26
Mn K	0.93	0.33
Fe K	0.45	0.16
Totals	100.00	

Figure 5.33 Tubular crystallites had formed on the surface.

Clusters of chromium-based carbides (A3) could be seen on the alloy substrate, Figure 5.34. In addition to chromium, considerable amounts of iron, nickel, manganese, and oxygen were also detected (area A3). However, the whitish, isolated islands spreading on the surface were confirmed to contain high levels of niobium, nickel, and silicon

suggesting some partial transformation of NbC to nickel-niobium silicide, $Ni_{16}Nb_6Si_7$, also named, G-phase.

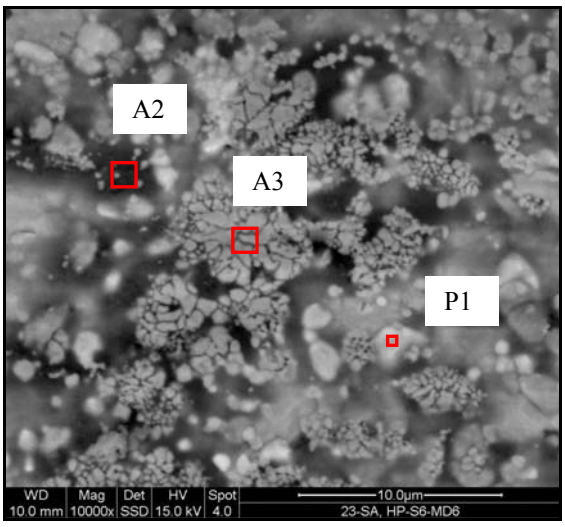

P1

Element	Wt%	At%
C K	2.17	9.01
O K	2.22	6.93
Si K	8.82	15.67
Cr K	11.14	10.69
Fe K	8.88	7.94
Ni K	44.41	37.75
Nb L	22.36	12.01
Totals	100.00	

A2

Element	Wt%	At%
C K	2.35	4.92
O K	35.64	55.90
Si K	25.48	22.77
Cr K	12.13	5.85
Fe K	12.75	5.73
Ni K	10.72	4.58
Nb L	0.92	0.25
Totals	100.00	

A3

Element	Wt%	At%
C K	5.89	18.65
O K	7.02	16.70
Si K	2.63	3.57
Cr K	72.95	53.38
Fe K	7.52	5.13
Ni K	3.98	2.58
Totals	100.00	

Figure 5.34 Clusters of carbides on the substrate.

5.5.9 HP-850°C-1000h

Increasing exposure time to 1000h led to the development of a layer that consisted mainly of oxygen, silicon, chromium, manganese, and carbon (Figure 5.35). The Figure shows slightly different surface conditions between the matrix and grain boundaries, as it appeared that the surface at the latter (indicated by the arrows) became rougher and porous, suggesting that they were more susceptible to the reaction with the surrounding environment. Interestingly, the chemical analysis of the surface was almost identical to that of the base alloy. However, no niobium or manganese was detected. In addition, there appeared to be no significant chromium depletion from the substrate. Moreover, silicon-based oxides seemed to have formed at the grain boundaries (A1). Chromium, iron, and nickel in considerable concentrations were also detected at this area.

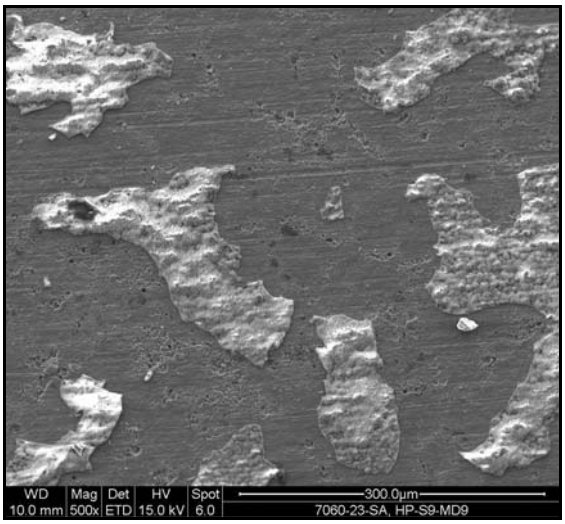

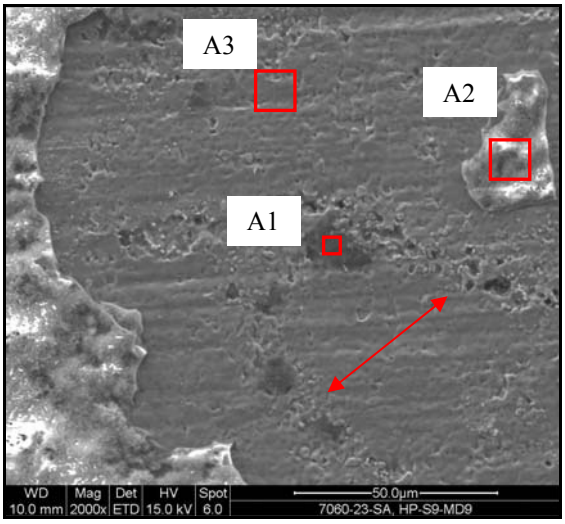

A1

Element	Wt%	At%
C K	1.08	1.99
O K	46.55	64.12
Si K	33.71	26.45
Cr K	6.18	2.62
Fe K	7.18	2.83
Ni K	5.29	1.99
Totals	100.00	

A2

Element	Wt%	At%
C K	3.60	7.40
O K	39.34	60.65
Si K	12.94	11.36
Cr K	31.93	15.15
Mn K	10.55	4.74
Fe K	0.87	0.39
Ni K	0.76	0.32
Totals	100.00	

A3

Element	Wt%	At%
C K	1.18	5.22
Si K	1.52	2.87
Cr K	20.33	20.70
Fe K	38.54	36.54
Ni K	38.43	34.66
Totals	100.00	

Figure 5.35 Images of the specimen after the exposure at 850ºC for 1000h.

The nature of the oxide layer formed on the alloy can be seen in Figure 5.36. Dense, "whisker-like" oxides had developed on the surface after the 1000h exposure. The analysis indicated that it was composed mainly of oxides of chromium, manganese, and silicon.

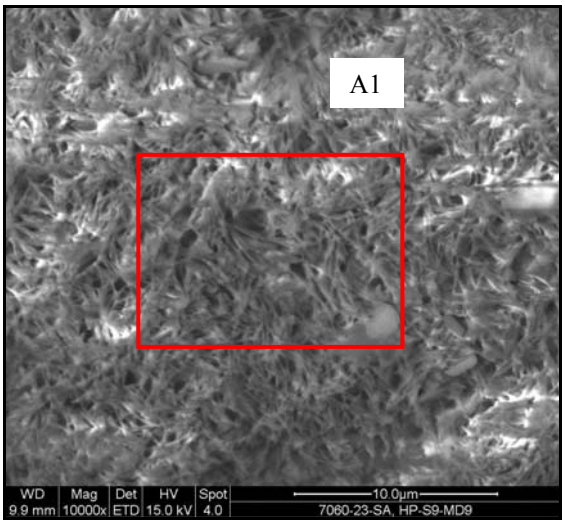

A1

Element	Weight%	Atomic%
C K	1.93	4.33
O K	36.08	60.78
Si K	7.16	6.87
Cr K	40.35	20.91
Mn K	14.48	7.10
Totals	100.00	

Figure 5.36 Whisker-like oxides after 1000h at 850ºC.

5.6 Metallographic Examination

The specimens were cross-sectioned, mounted, ground, polished and then examined using SEM/EDX. The sample preparation and investigation procedures have already been covered in Chapter 2.

5.6.1 HP-650ºC-100h

The reaction front of the sample exposed for 100h revealed the presence of randomly distributed pits, with different sizes and shapes, Figure 5.37. The depth of the pits varied from approximately 20µm to around 40µm. It was also noticed that some of the pits had linked up forming bigger perforation. The pits appeared to have initiated at the matrix rather than the carbides (Figure 5.38). The pits shown in this micrograph were about 13µm

in depth and 30μm in diameter. Some pits were also observed to contain some alloy particles surrounded with carbon, Figure 5.39. These alloy particles might have been separated from the alloy during the sample preparation.

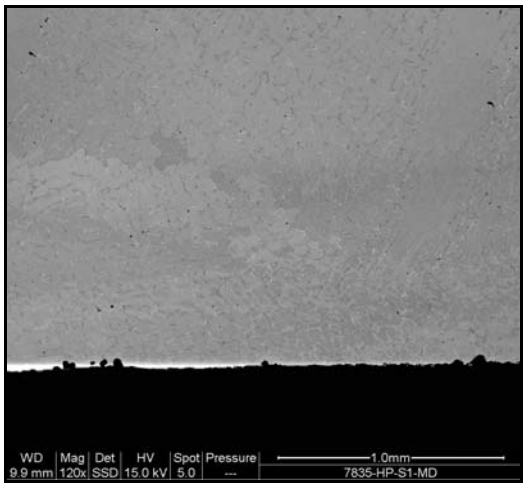

Figure 5.37 Pitting at the alloy surface after the exposure for 100h.

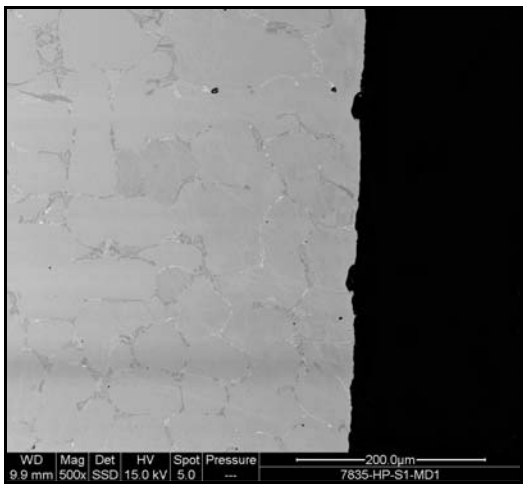

Figure 5.38 Relatively wide pits were observed on the alloy.

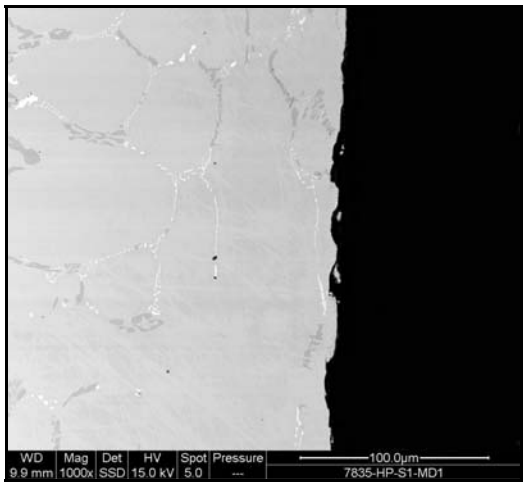

Figure 5.39 Some pits contained alloy particles surrounded with carbon.

The two pits, shown in Figure 5.40 below, had almost grown together as the alloy separating them seemed to have disintegrated and was about to be detached from the alloy. It was not clear that whether the disintegration was caused by corrosion, sample preparation or both. Higher magnification micrographs of the pit bottom are shown in Figure 5.41.

"Strips" of carbides appeared to have formed at the reaction zone, just below the reaction front, running almost parallel to the alloy substrate.

A thin layer, about 0.5μm, had also established at the substrate and was found to be composed mainly of mixtures of oxides, carbon, alloying elements, and possibly carbides. It seemed that the alloy particles were removed from the alloy by simultaneous interaction of oxides and carbon that led to the particle (A1 and A2) been contained and detached.

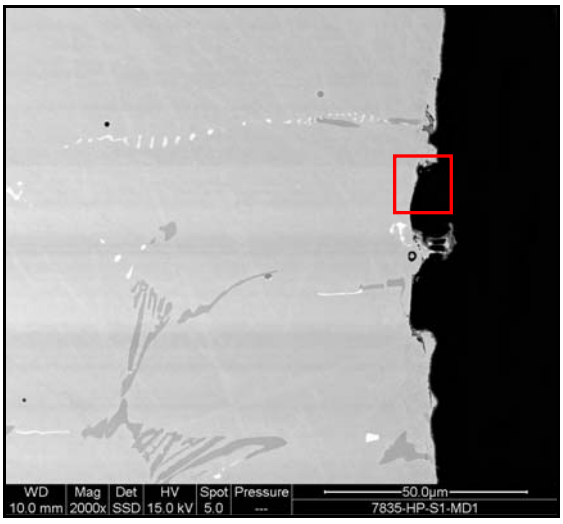

Figure 5.40 Pits seemed to link up forming bigger pit.

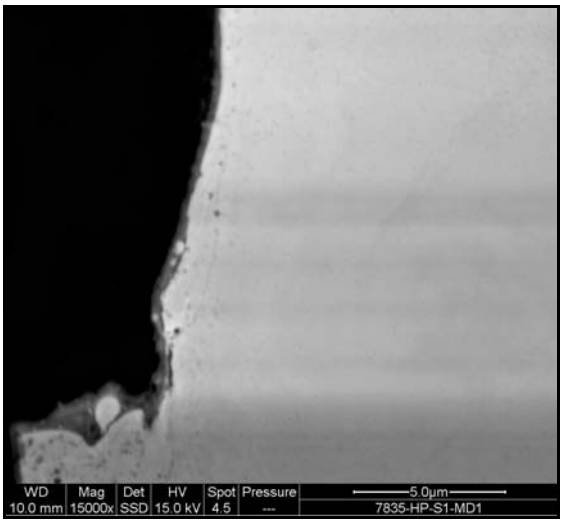

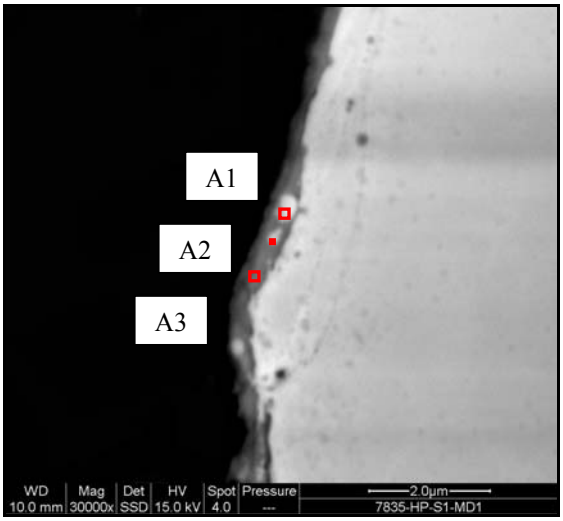

A1

Element	Wt%	At%
C K	12.83	33.57
O K	11.75	23.09
Si K	3.51	3.93
Cr K	11.15	6.74
Mn K	0.41	0.24
Fe K	25.06	14.10
Ni K	27.17	14.54
Cu K	5.71	2.82
Zn K	1.07	0.52
Nb L	1.33	0.45
Totals	100.00	

A2

Element	Wt%	At%
C K	12.59	30.51
O K	17.06	31.03
Si K	4.45	4.61
Cr K	19.86	11.11
Mn K	0.88	0.47
Fe K	19.31	10.06
Ni K	17.21	8.53
Cu K	4.96	2.27
Zn K	2.07	0.92
Nb L	1.61	0.50
Totals	100.00	

A3

Element	Wt%	At%
C K	5.18	17.88
O K	6.26	16.21
Si K	2.01	2.97
Cr K	14.39	11.48
Mn K	0.56	0.42
Fe K	31.10	23.09
Ni K	30.98	21.88
Cu K	8.76	5.72
Nb L	0.76	0.34
Totals	100.00	

Figure 5.41 Micrographs and EDX analysis of the pit bottom squared in Figure 5.40.

Very wide pits (~55µm wide and ~21µm deep) were also seen to have developed on the alloy after only 100h of exposure, Figure 5.42. It is interesting to observe that the attack tended to be more favourable through the bulk material rather than the carbides. This behaviour could be clearly seen as the attack appeared to firstly grow vertically till it reached the grain boundary, where most of the primary carbides precipitated, and then turned to grow laterally through the matrix.

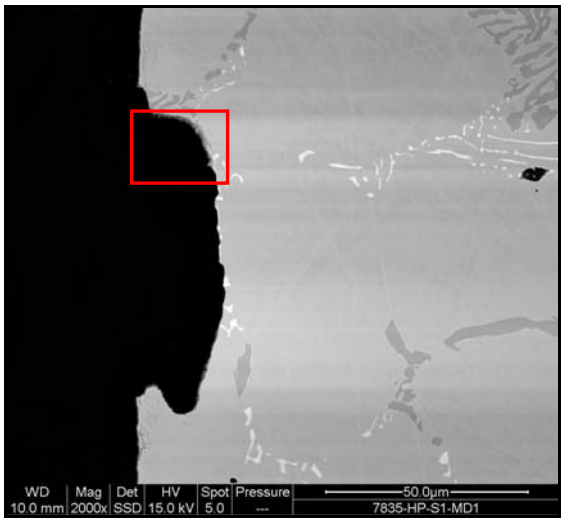

Figure 5.42 Wide pits were also found on the alloy surface after the 100h test.

Figure 5.43 shows higher magnification photomicrographs of the reaction front. A layer of fibrous and filament-like product had formed at the alloy substrate. Moreover, some carburisation was also observed at the reaction zone. As shown by line profiling, a mixture of alloying elements and carbon was detected at the reaction front. The concentration of carbon within the layer was more in the lower part while more alloying elements, especially chromium, were found at the upper layer. It is also worth noting that there was almost no oxygen at that layer suggesting little formation of oxides.

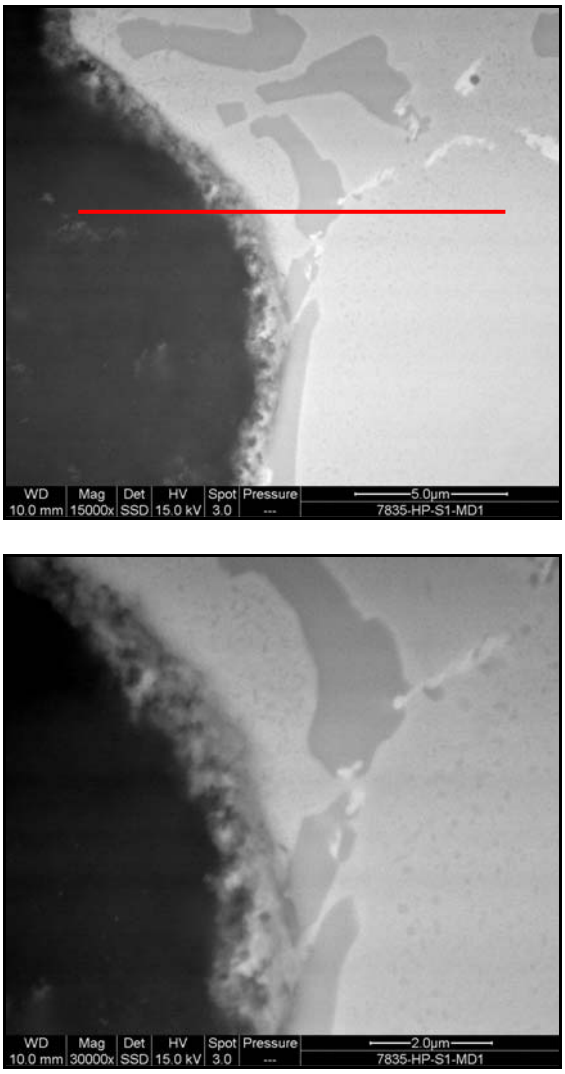

Figure 5.43 A layer of fibrous and filament-like product had formed at the reaction front.

Deeper pits were also observed on the sample. Figure 5.44 shows a pit that was about 52µm in depth. It is interesting to notice the niobium carbide (white phase) precipitates protruding from the reaction front which may imply that such carbides are more resistant to the environment than the matrix. EDX analysis of the reaction front (A4) showed that it was composed mainly of carbon and some oxides. Analysing area, A3, showed that it contained oxygen and iron as main constituents suggesting that the particle was iron-based oxides. It is also worth noting that the substrate chemical composition (A2) contained carbon as the main constituent with levels of the major alloying elements well below those in the base metal. This may suggest that the substrate was supersaturated with carbon that had diffused from the surrounding environment.

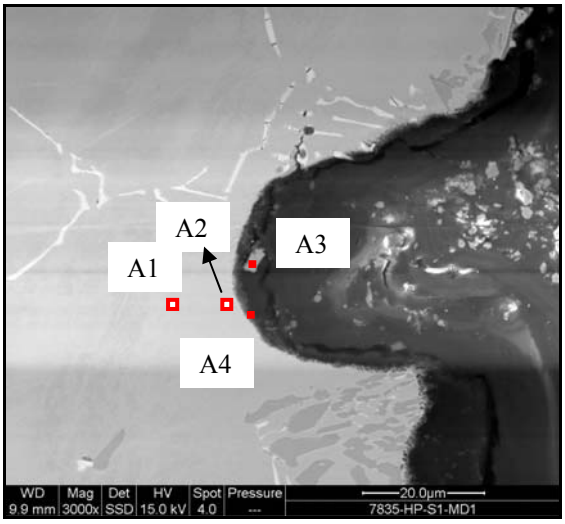

A1

	Wt%	At%
C K	3.51	13.98
O K	1.08	3.22
Si K	1.39	2.36
Cr K	22.32	20.51
Mn K	1.11	0.97
Fe K	35.93	30.75
Ni K	34.66	28.21
Totals	100.0	

A2

	Wt%	At%
C K	31.97	63.51
O K	6.65	9.92
Si K	0.91	0.77
Cr K	13.95	6.40
Fe K	23.64	10.10
Ni K	22.88	9.30
Totals	100.0	

A3

	Wt%	At%
C K	8.62	18.33
O K	34.84	55.60
Si K	0.42	0.38
Cr K	1.71	0.84
Fe K	53.31	24.37
Ni K	1.10	0.48
Totals	100.0	

A4

	Wt%	At%
C K	71.66	78.98
O K	24.09	19.93
Si K	0.29	0.14
Cr K	1.63	0.42
Fe K	1.49	0.35
Ni K	0.83	0.19
Totals	100.0	

Figure 5.44 Deep pits were observed forming on the alloy.

5.6.2 HP-650ºC-500h

As observed in Figure 5.45, a relatively superficial localised attack took place on the alloy following the extension of the exposure time to 500h. Pits, about 4µm deep, were noticed spreading through the cross section. Furthermore, comparatively deeper and more concentrated pits, of about 50µm maximum depth, were also observed on another area of the surface (Figure 5.46).

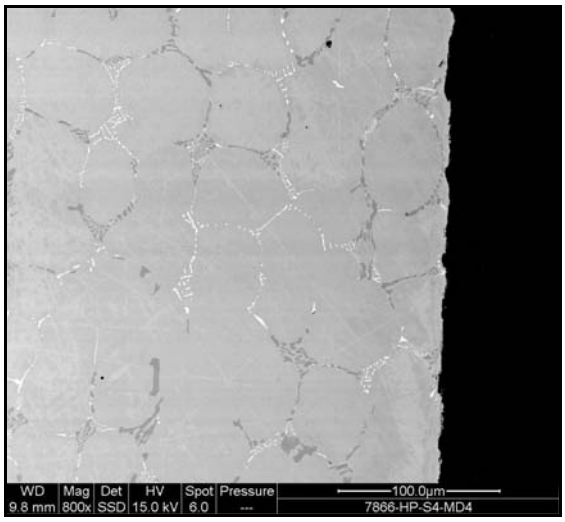

Figure 5.45 **Superficial localised attack took place on the alloy following the extension of the exposure time to 500h.**

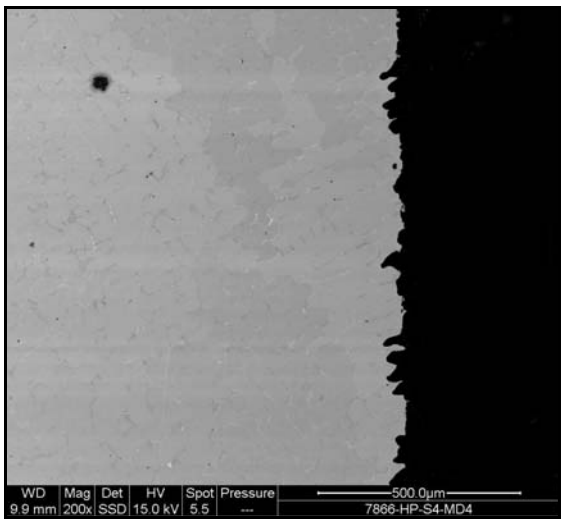

Figure 5.46 **Deeper and more concentrated pits were observed on another area of the alloy.**

It appeared that some of the pits combined together forming bigger pits, Figure 5.47. Particles observed embedded within the carbon deposits were chemically analysed and found to contain some oxides of chromium, iron, nickel, manganese, and silicon. However, the presence of some free element could not be ruled out either.

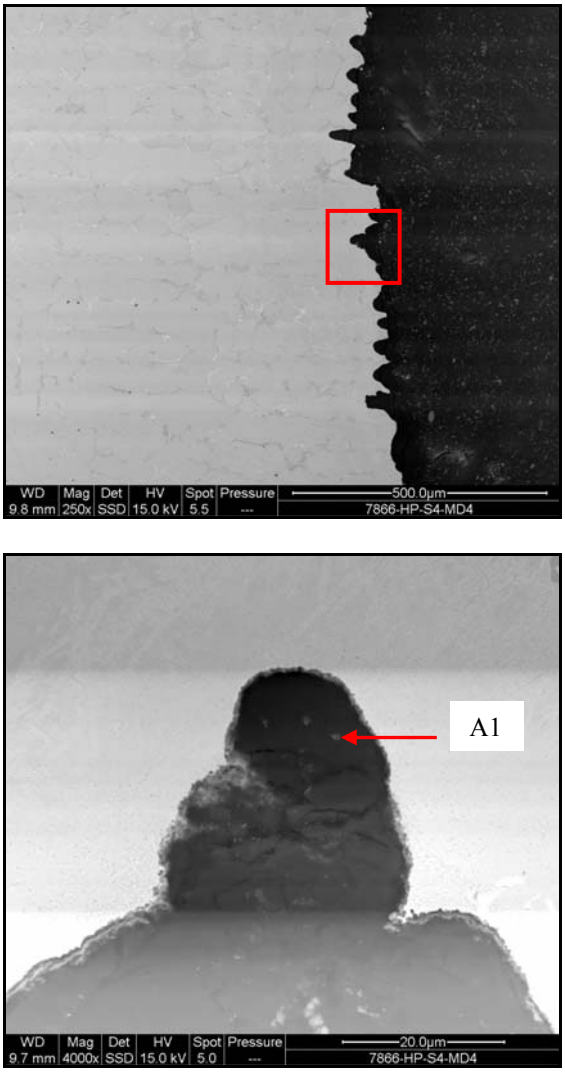

A1

Element	Weight%	Atomic%
C K	72.14	84.29
O K	13.38	11.73
Si K	0.78	0.39
Cr K	8.01	2.16
Mn K	0.34	0.09
Fe K	4.64	1.16
Ni K	0.72	0.17
Totals	100.00	

Figure 5.47 Some of the pits combined forming bigger pits.

A higher magnification micrograph of the reaction front is shown in Figure 5.48. It is evident that some carbide had formed at the reaction zone (just below the reaction front) and yet it appeared that the metal had subsequently, disintegrated into a porous, sponge-like product. EDX area analysis conducted on the latter (A1) showed that it was composed mainly of carbon in addition to chromium, nickel, iron, silicon, and manganese. Analysis of the reaction front, just adjacent to the alloy surface, revealed the presence of higher parentages of chromium, manganese, iron, and nickel. Interestingly, almost the same level of oxygen was detected at both areas.

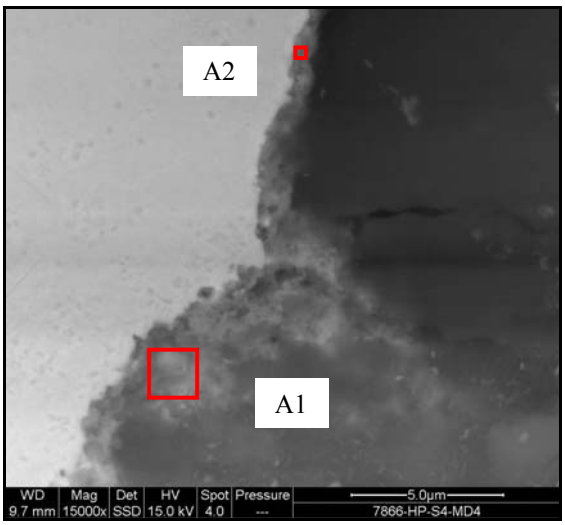

A1

Element	Weight%	Atomic%
C K	53.33	77.53
O K	8.97	9.79
Si K	2.04	1.27
Cr K	15.52	5.21
Mn K	2.83	0.90
Fe K	9.95	3.11
Ni K	7.36	2.19
Totals	100.00	

A2

Element	Weight%	Atomic%
C K	31.72	62.44
O K	6.67	9.87
Si K	2.15	1.81
Cr K	29.46	13.40
Mn K	4.23	1.82
Fe K	13.85	5.86
Ni K	11.92	4.80
Totals	100.00	

Figure 5.48 A higher magnification micrograph of the reaction front first shown in Figure 5.48.

The nature of the reaction front can also be seen in the higher magnification micrograph shown in Figure 5.49. It seems that the attack progressed through the formation of micropits, caused by carbon diffusion into the substrate, which probably acted to weaken the alloy chunks between them, and eventually detach them into very small particles.

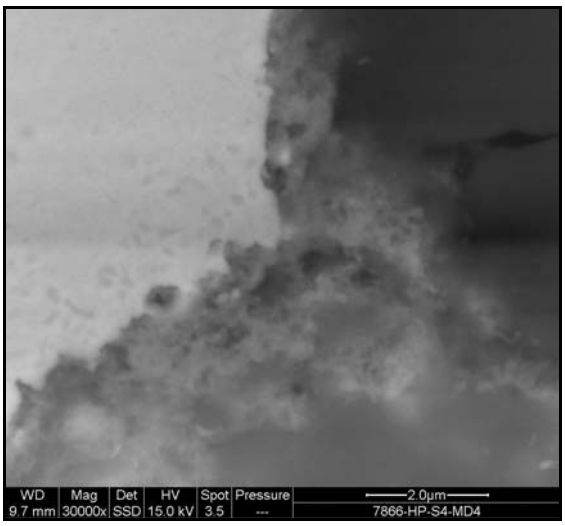

Figure 5.49 Photomicrograph showing the nature of the reaction front.

One of the shallow attacks observed on the alloy surface is shown Figure 5.50. A portion of the alloy that seemed to have been confined with chromium oxide detached (probably during sample preparation) leaving shallow pit. Strips of carbides, running in different orientations, seemed to have precipitated at the reaction zone. Line profiling analysis showing the composition of this area is shown in Figure 5.51.

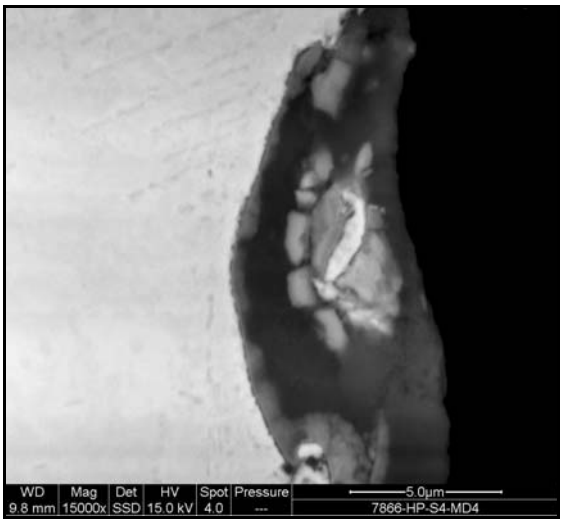

Figure 5.50 Shallow attacks observed on the alloy surface after the 500h exposure.

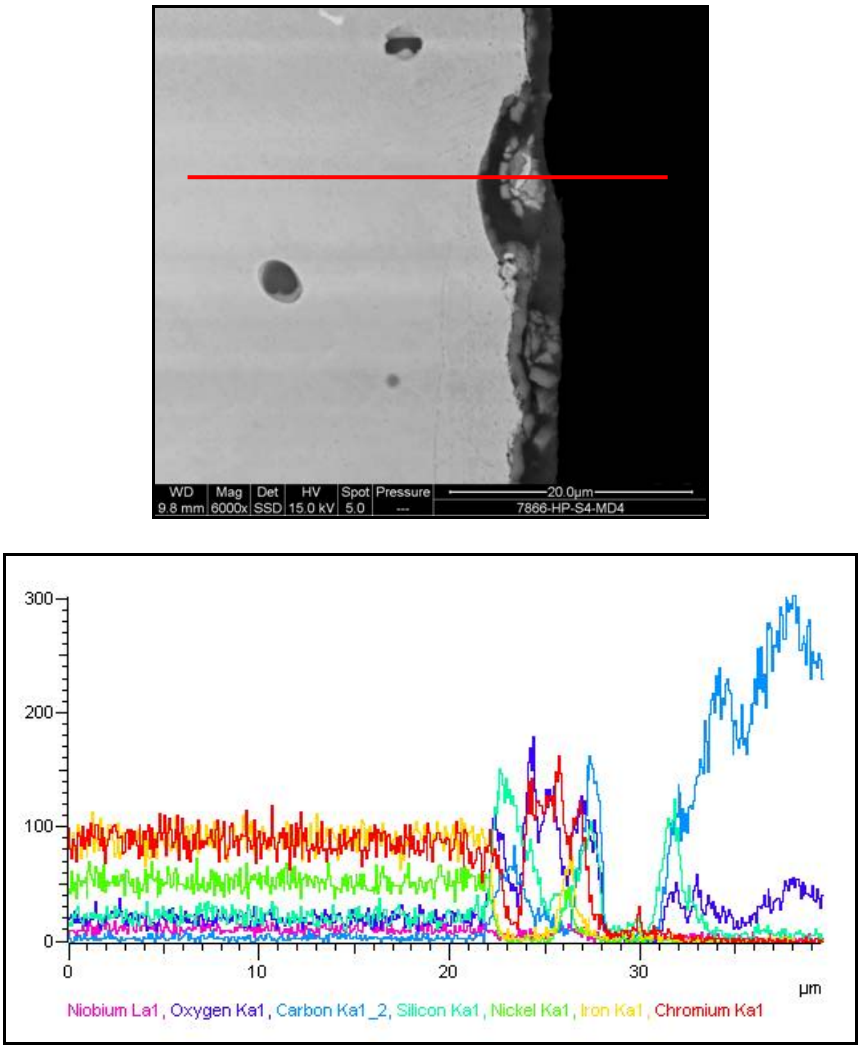

Figure 5.51 Line profiling analysis of the shallow pit.

5.6.3 HP-650ºC-1000h

Extending the experiment time to 1000h obviously aggravated the metal dusting attack through the formation of deeper and wider pits (Figure 5.52). It is interesting to notice that the corrosion propagation was much easier through the matrix compared to the carbides. Moreover, because of that reason, it appeared that the carbide distribution had controlled and guided the attack direction. The maximum depth of penetration was about 140µm with a total width of approximately 420µm.

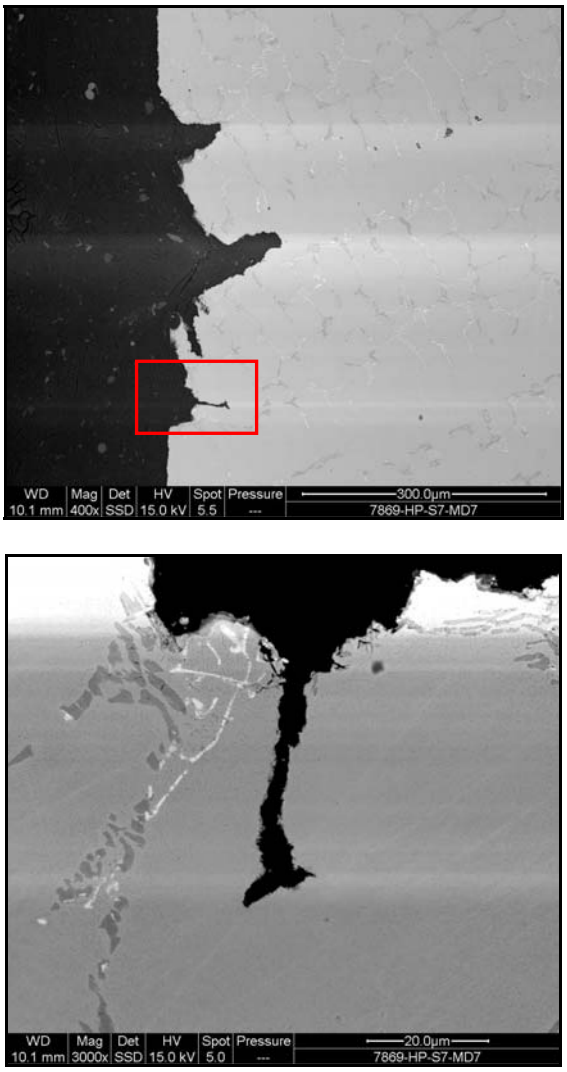

Figure 5.52 Formation of deep and wide groove-like attacks after the 1000h experiment.

Figure 5.53 is a higher magnification micrograph detailing the attack "tip". The pit contents were analysed by EDX at the points shown on that Figure. The chemical composition of the deposit at the reaction tip was dominated by carbon. Considerable levels of oxygen, chromium, nickel, and iron, however, were also detected. Analysing the grey layer (at point 4) revealed that it contained a mixture of carbon, oxide(s), and perhaps alloying elements. Small particles could be observed to have readily been detached from that layer (point 3 for example).

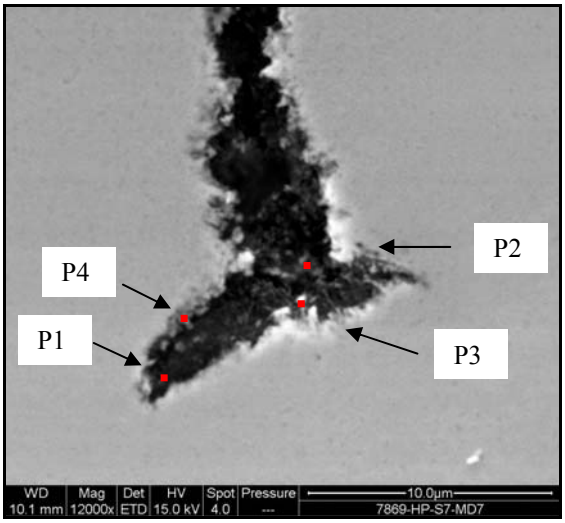

P1

	Wt%	At%
C K	74.08	89.05
O K	6.29	5.67
Si K	0.59	0.30
Cr K	6.41	1.78
Fe K	6.84	1.77
Ni K	5.79	1.42
Totals	100.0	

P2

	Wt%	At%
C K	57.38	76.36
O K	15.37	15.36
Si K	0.70	0.40
Cr K	15.11	4.65
Mn K	0.58	0.17
Fe K	8.00	2.29
Ni K	2.86	0.78
Totals	100.0	

P3

	Wt%	At%
C K	71.05	87.23
O K	7.53	6.94
Si K	0.43	0.22
S K	0.22	0.10
Cr K	5.47	1.55
Fe K	8.26	2.18
Ni K	7.04	1.77
Totals	100.0	

P4

	Wt%	At%
C K	36.75	66.83
O K	8.23	11.24
Si K	1.17	0.91
Cr K	12.06	5.07
Mn K	0.80	0.32
Fe K	20.08	7.85
Ni K	20.92	7.78
Totals	100.0	

Figure 5.53 Detailed analysis of the attack "tip" (from Figure 5.52).

An uneven and apparently discontinuous layer was also noticed on the same sample, Figure 5.54. The line profiling showed that the layer was composed mainly of chromium and silicon oxides in addition to carbon. Branch-like chromium-based carbides could be seen at the reaction zone. Additionally, some isolated carbide islands were also observed just below the layer.

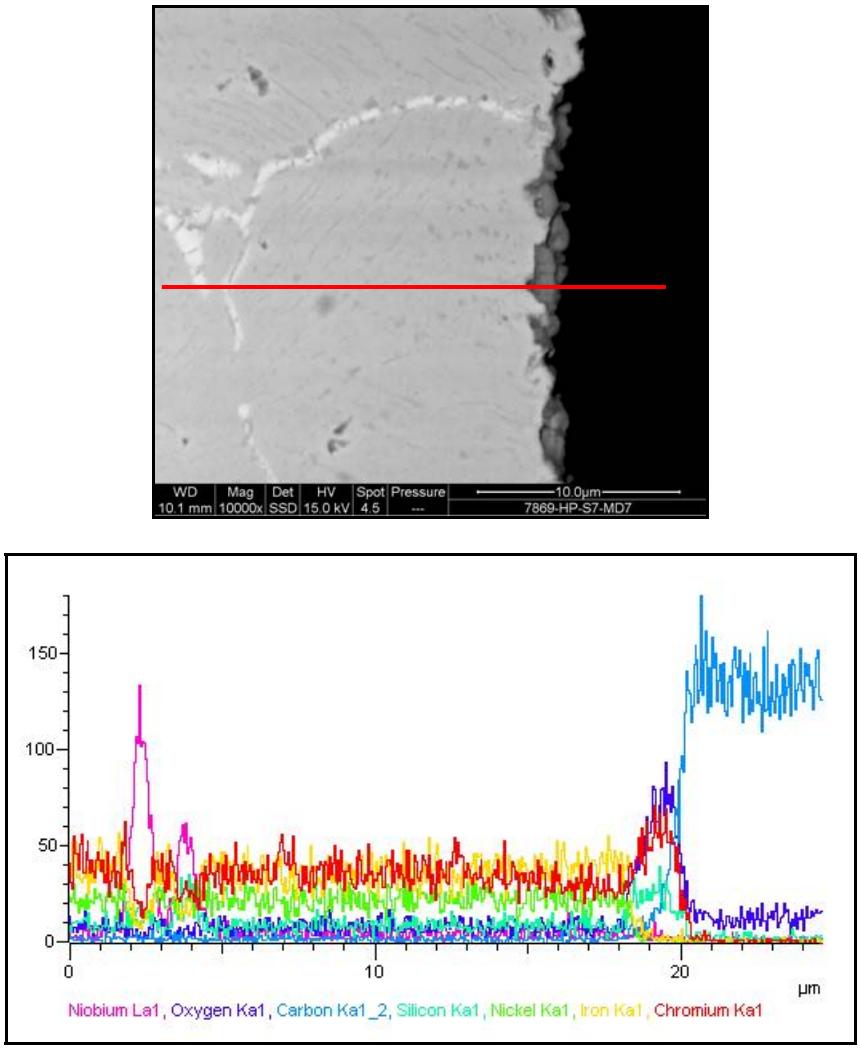

Figure 5.54 Formation of uneven and discontinuous oxide layer on the alloy.

5.6.4 HP-750ºC-100h

In general, exposing the alloy to the gas mixture at this temperature led to a remarkably less aggressive attack that manifested as a reduction in the number and sizes of the localised corrosion sites.

Only comparatively superficial metal removal was observed on the sample exposed for 100h (Figures 5.55-5.59). As seen in Figure 5.55, a layer of about 1µm typical thickness had grown on the alloy and was confirmed to contain oxides of mainly silicon, chromium, manganese, in addition to some iron and nickel. Interestingly, some darker phases were

also observed embedded within that layer and were shown to contain significantly higher levels of carbon (A2).

Shallow, localised corrosion took place on the alloy and chunks of the base metal could be observed detached at some pits (Figure 5.56). EDX analysis of the alloy substrate showed no significant reduction in the chromium level, which would have been expected to be consumed to produce oxides. However, there was no manganese detected in this area.

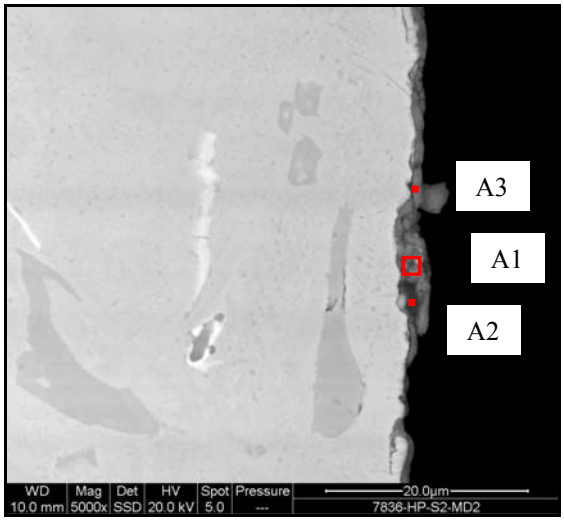

A1

Element	Wt%	At%
C K	14.79	25.14
O K	43.16	55.08
Na K	0.28	0.25
Si K	10.02	7.28
Ca K	0.41	0.21
Cr K	19.83	7.79
Mn K	9.28	3.45
Fe K	1.27	0.46
Ni K	0.97	0.34
Totals	100.00	

A2

Element	Wt%	At%
C K	29.53	43.96
O K	36.11	40.35
Mg K	0.12	0.09
Si K	13.37	8.51
Ca K	0.52	0.23
Cr K	14.19	4.88
Mn K	3.48	1.13
Fe K	1.60	0.51
Ni K	1.09	0.33
Totals	100.00	

A3

Element	Wt%	At%
C K	16.84	29.55
O K	37.74	49.73
Na K	0.22	0.20
Si K	7.75	5.81
Ca K	0.29	0.15
Cr K	20.79	8.43
Mn K	6.35	2.44
Fe K	4.91	1.85
Ni K	5.10	1.83
Totals	100.00	

Figure 5.55 Layer grown on the alloy after the exposure at 750ºC for 100h.

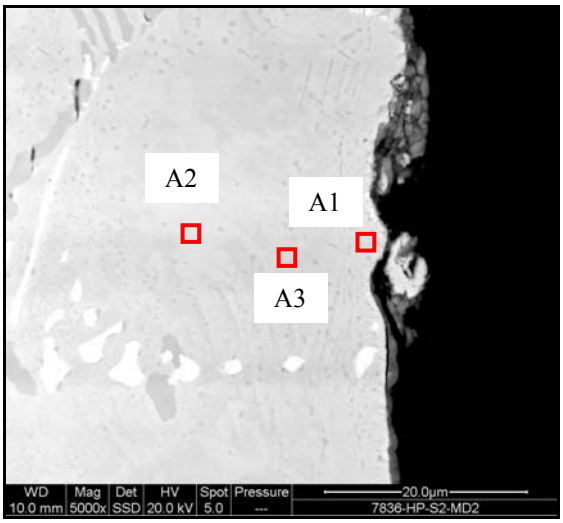

A1

Element	Wt%	At%
C K	2.78	11.14
O K	1.77	5.32
Si K	1.64	2.81
Ca K	0.22	0.26
Cr K	21.52	19.90
Fe K	36.24	31.21
Ni K	35.83	29.35
Totals	100.00	

A2

Element	Wt%	At%
C K	1.94	8.02
O K	1.61	4.98
Si K	1.60	2.83
Cr K	23.30	22.20
Mn K	0.92	0.83
Fe K	35.54	31.53
Ni K	35.09	29.61
Totals	100.00	

A3

Element	Wt%	At%
C K	2.13	8.72
O K	1.58	4.83
Si K	1.99	3.49
Cr K	25.14	23.72
Mn K	0.93	0.83
Fe K	32.62	28.65
Ni K	35.62	29.76
Totals	100.00	

Figure 5.56 **Localised corrosion took place on the alloy and detached chunks of the base metal could be observed.**

A higher magnification micrograph of the pit is shown in Figure 5.57. Bands of carbides, precipitating in different directions, could be observed to have formed at the reaction zone, just beneath the pit. The product formed in the pit was composed of carbon and an oxides mixture in addition to possible free elements. The alloy chunk did not contain any manganese (or niobium) suggesting that they were consumed during the oxidation process. Figure 5.58 also shows one area where superficial attack took place. It seemed that the scale built up and accumulated around the alloy portion eventually leading to disintegration. However, the sample preparation might also have led to the detachment of the layer.

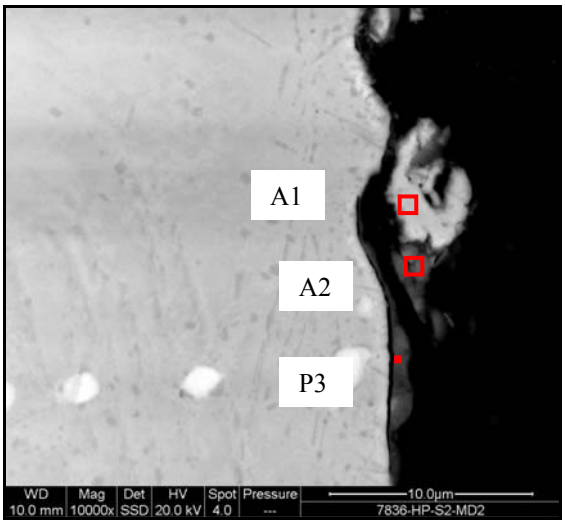

A1

Element	Wt%	At%
C K	3.65	13.82
O K	3.06	8.69
Si K	1.90	3.07
Ca K	0.43	0.49
Cr K	21.49	18.78
Fe K	35.04	28.51
Ni K	34.44	26.65
Totals	100.00	

A2

Element	Wt%	At%
C K	24.44	39.83
O K	35.00	42.82
Na K	0.16	0.14
Si K	7.22	5.03
Ca K	0.57	0.28
Cr K	17.97	6.76
Mn K	8.43	3.00
Fe K	3.50	1.23
Ni K	2.70	0.90
Totals	100.00	

P3

Element	Wt%	At%
C K	15.95	28.88
O K	36.12	49.11
Si K	7.43	5.75
Ca K	0.30	0.17
Cr K	20.92	8.75
Mn K	5.81	2.30
Fe K	6.24	2.43
Ni K	6.71	2.49
Nb L	0.51	0.12
Totals	100.00	

Figure 5.57 Bands of carbides, precipitating in different directions.

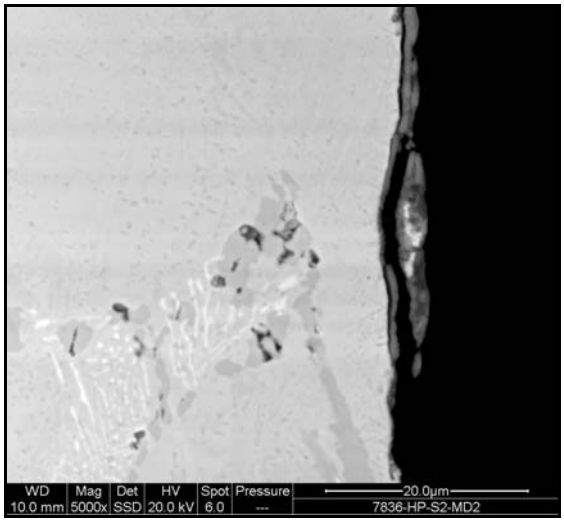

Figure 5.58 Product accumulated around the alloy portion leading to disintegration.

As stated above, relatively large portions of the alloy were observed to be isolated and detached from the base metal. Figure 5.59 shows alloy chunk that was not completely separated from the alloy. It seems that the attack was probably facilitated by the precipitation of some carbide bands that then created internal stresses and increased the substrate brittleness leading to carbon diffusion and oxidation assisted crack propagation.

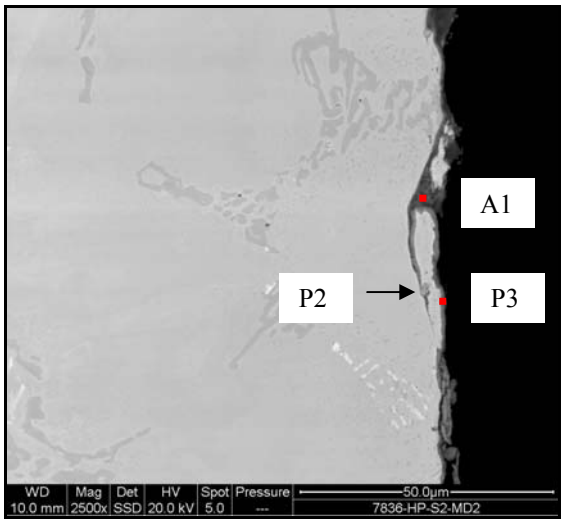

A1

Element	Wt%	At%
C K	37.25	52.21
O K	32.42	34.11
F K	0.63	0.56
Na K	0.17	0.12
Mg K	0.28	0.20
Si K	9.20	5.51
Ca K	9.34	3.92
Cr K	6.48	2.10
Mn K	1.66	0.51
Fe K	1.39	0.42
Ni K	1.17	0.33
Totals	100.00	

P2

Element	Wt%	At%
C K	7.08	19.12
O K	15.49	31.41
Si K	4.19	4.84
S K	0.14	0.14
Ca K	0.33	0.27
Cr K	50.34	31.40
Mn K	2.42	1.43
Fe K	11.89	6.91
Ni K	8.12	4.49
Totals	100.00	

P3

Element	Wt%	At%
C K	26.48	40.05
O K	41.76	47.42
Si K	5.25	3.40
Ca K	0.20	0.09
Cr K	20.60	7.20
Mn K	1.88	0.62
Fe K	2.12	0.69
Ni K	1.70	0.53
Totals	100.00	40.05

Figure 5.59 A micrograph showing the progress of metal removal process.

5.6.5 HP-750°C-500h

Relatively wide pits were observed on the alloy cross section following the exposure for 500h, Figure 5.60. Analysing the particles embedded within the carbon deposit (P1, P2, and P3) revealed the presence of oxygen, chromium, silicon, with minor levels of nickel, manganese, and iron. Chromium-based oxides were also detected at the reaction front (P4). No significant differences in the chemical composition of the alloy were detected at the

areas; A5 and A6, suggesting that only mild oxidation had taken place. A relatively uniform, heavily carburised zone, of about 20µm was discovered surrounding the pit.

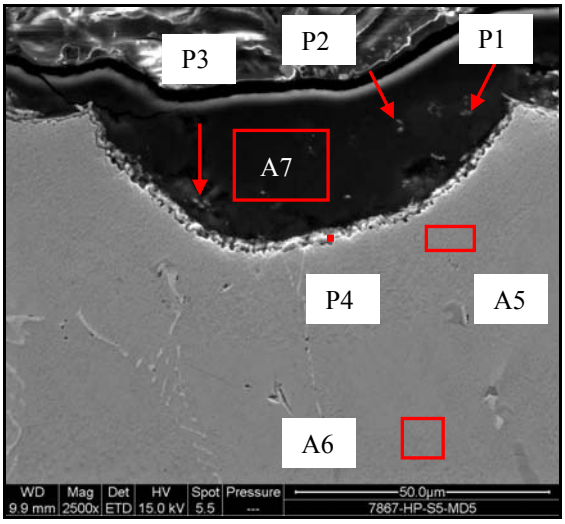

P1

	Wt%	At%
C K	67.10	82.40
O K	11.84	10.91
Si K	3.22	1.69
Cr K	14.73	4.18
Fe K	2.22	0.59
Ni K	0.89	0.22
Totals	100.0	

P2

	Wt%	At%
C K	75.52	84.59
O K	13.47	11.32
Si K	5.94	2.85
Cr K	2.18	0.56
Fe K	1.53	0.37
Ni K	1.37	0.31
Totals	100.0	

P3

	Wt%	At%
C K	55.24	72.00
O K	20.71	20.27
Si K	2.45	1.37
Cr K	15.48	4.66
Mn K	1.27	0.36
Fe K	3.48	0.98
Ni K	1.38	0.37
Totals	100.0	

P4

	Wt%	At%
C K	39.24	57.64
O K	28.01	30.88
Si K	1.71	1.07
Cr K	25.34	8.60
Mn K	3.50	1.12
Fe K	1.66	0.52
Ni K	0.54	0.16
Totals	100.0	

A5

Element	Wt%	At%
C K	2.61	10.61
O K	1.44	4.40
Si K	1.34	2.33
Cr K	23.20	21.77
Mn K	0.88	0.78
Fe K	35.24	30.79
Ni K	35.29	29.33
Totals	100.00	

A6

Element	Wt%	At%
C K	2.54	10.31
O K	1.46	4.45
Si K	1.49	2.59
Cr K	22.72	21.34
Mn K	0.93	0.83
Fe K	35.82	31.33
Ni K	35.04	29.15
Totals	100.00	

A7

Element	Wt%	At%
C K	87.33	92.22
O K	7.53	5.97
Si K	2.89	1.31
Cr K	0.44	0.11
Fe K	1.14	0.26
Ni K	0.67	0.14
Totals	100.00	

Figure 5.60 Wide pit was observed on the alloy cross section following the exposure for 500h.

Further investigation of the reaction front, shown in Figure 5.60, revealed a shark's teeth-like pattern suggesting that the metal wastage process was progressing through the formation of a high number of micropits (Figure 5.61). The EDX analysis of the grey product at the pits confirmed the presence of oxides, carbon, and probably some free

elements and/or carbides. The darker product (P2), however, comprised more carbon, nickel, and iron and less chromium. Interestingly, the niobium-based carbide protruding from the reaction front (P3) seemed to be more resistant to the attack as the alloy around it had already been eaten away.

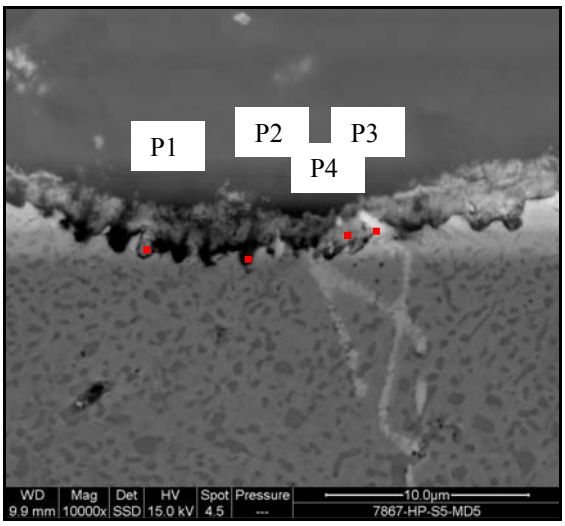

P1

	Wt%	At%
C K	12.04	27.49
O K	19.56	33.53
Si K	9.00	8.79
Cr K	38.33	20.22
Fe K	13.05	6.41
Ni K	6.88	3.22
Nb L	1.14	0.34
Totals	100.0	

P2

	Wt%	At%
C K	17.63	38.99
O K	15.75	26.15
Si K	7.78	7.36
Cr K	6.53	3.33
Fe K	24.34	11.58
Ni K	25.79	11.67
Cu K	2.19	0.91
Totals	100.0	

P3

	Wt%	At%
C K	13.86	31.51
O K	26.23	44.78
Si K	2.99	2.91
Cr K	12.71	6.68
Fe K	3.38	1.65
Ni K	2.72	1.26
Nb L	38.11	11.20
Totals	100.0	

P4

	Wt%	At%
C K	10.37	25.90
O K	18.37	34.44
Si K	2.86	3.05
Cr K	50.61	29.19
Mn K	1.12	0.61
Fe K	5.29	2.84
Ni K	1.52	0.78
Nb L	9.84	3.18
Totals	100.0	

Figure 5.61 **Metal wastage process seemed to progress through the formation of high number of micropits at the reaction front.**

5.6.6 HP-750ºC-1000h

Figure 5.62 shows the alloy cross section after the 1000h test where the specimen experienced shallow pitting. It is worth noting that the chromium carbide particle shown in this Figure did not seem to be attacked but, instead, was surrounded by some silicon-containing oxides.

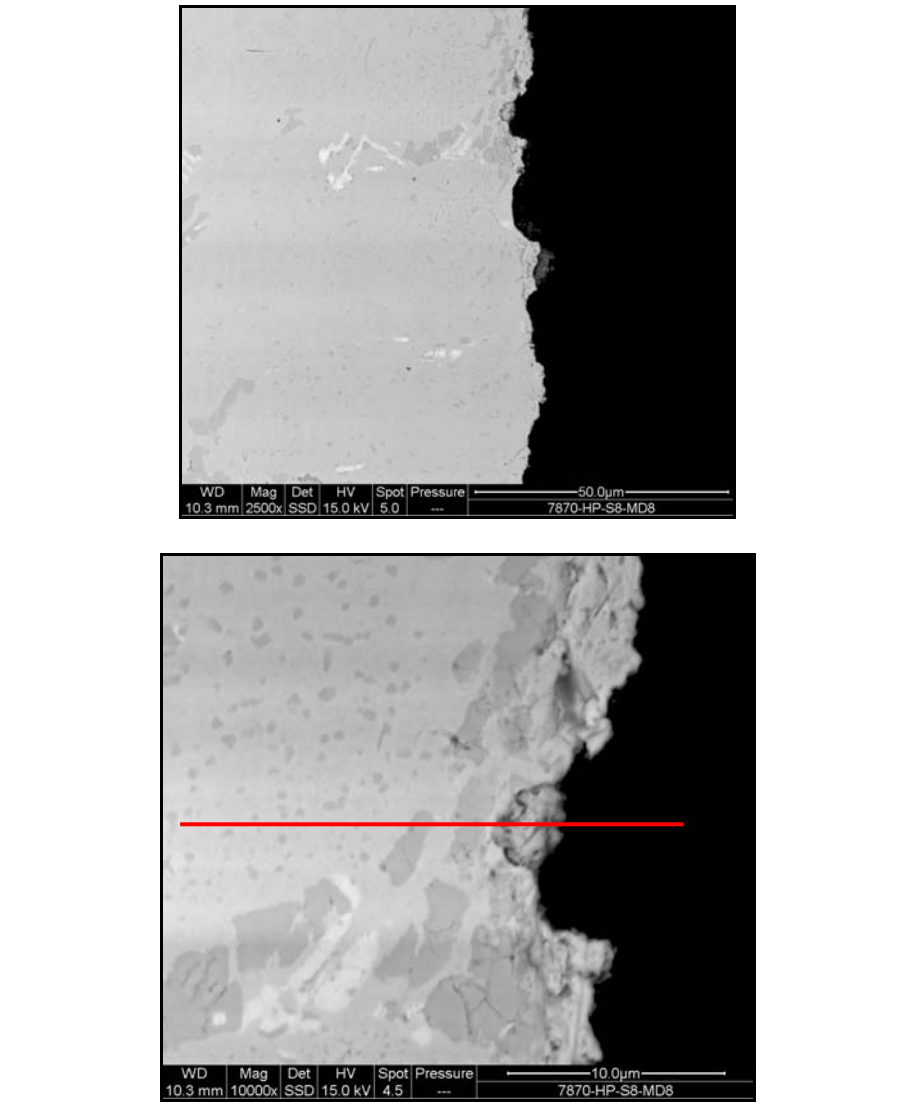

Figure 5.62 The alloy cross section after the 1000h test where shallow pitting occurred.

5.6.7 HP-850ºC-100h

A cross section of the alloy exposed to the gas mixture at 850ºC for 100h is shown in Figure 5.63. The alloy surface revealed no significant metal removal despite the presence of some shallow pits. However, very distinctive strips of carbides appeared to have formed at the reaction zone. Moreover, the alloy was covered with what appeared to be a nonhomogeneous layer. Elemental analysis of the substrate (A1) did not show significant depletion of the oxide-forming elements.

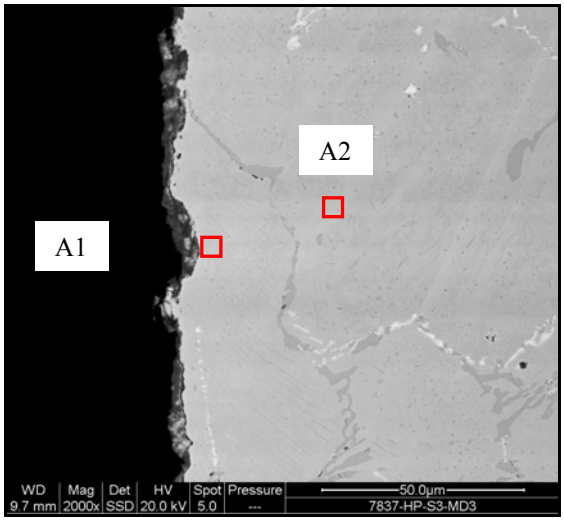

A1

Element	Weight%	Atomic%
C K	1.91	7.99
O K	1.25	3.93
Si K	1.24	2.22
Cr K	20.54	19.87
Mn K	0.60	0.55
Fe K	38.02	34.24
Ni K	36.43	31.21
Totals	100.00	

A2

Element	Weight%	Atomic%
C K	1.93	7.98
O K	1.55	4.82
Si K	1.37	2.43
Cr K	22.50	21.53
Mn K	0.71	0.64
Fe K	37.13	33.09
Ni K	34.81	29.51
Totals	100.00	

Figure 5.63 A cross section of the alloy exposed to the gas mixture at 850ºC for 100h

A higher magnification micrograph of a pit is shown in Figure 5.64. The different phases of the layer were analysed. An internal layer (P3), of about 1µm, was observed at the alloy substrate and EDX confirmed this to be a chromium-based oxide scale. An external darker, thicker, layer that contained more silicon oxides and carbon had formed above the oxide

scale. Some chromium, manganese, and silicon oxide particles were also observed embedded within the layer formed at the pit (P1).

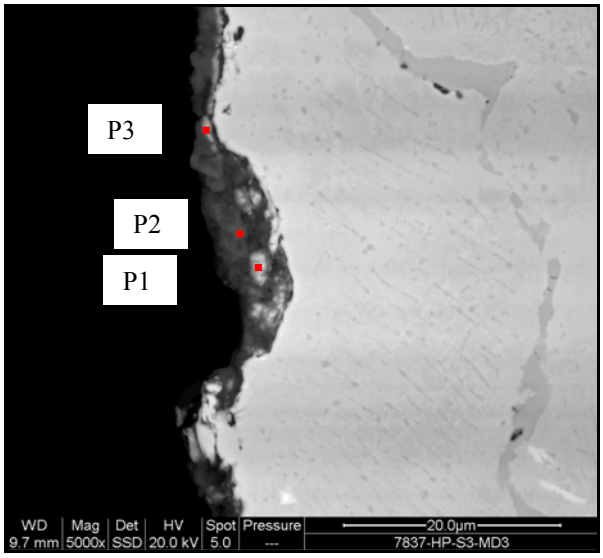

P1

Element	Wt%	At%
C K	12.71	25.37
O K	29.60	44.36
Si K	10.06	8.59
Ca K	0.32	0.19
Cr K	35.52	16.38
Mn K	8.48	3.70
Fe K	2.40	1.03
Ni K	0.90	0.37
Totals	100.00	

P2

Element	Wt%	At%
C K	28.69	38.48
O K	48.14	48.48
F K	1.04	0.88
Mg K	0.22	0.15
Si K	19.75	11.33
Ca K	0.40	0.16
Cr K	0.69	0.21
Mn K	0.33	0.10
Fe K	0.43	0.13
Ni K	0.32	0.09
Totals	100.00	

P3

Element	Wt%	At%
C K	17.70	31.09
O K	36.09	47.59
Si K	8.27	6.21
Ca K	0.47	0.25
Cr K	24.20	9.82
Mn K	9.27	3.56
Fe K	2.33	0.88
Ni K	1.67	0.60
Totals	100.00	

Figure 5.64 Presence of some shallow pits on the alloy after 100h.

A further investigation of the pit bottom is shown in Figure 5.65. The EDX analysis of the area, A1, at the tip under the alloy chunk showed the presence of considerable levels of iron and nickel in addition to oxides of probably chromium, silicon, and manganese. The substrate also appeared to contain lower levels of alloying elements, especially iron and nickel, than the base metal.

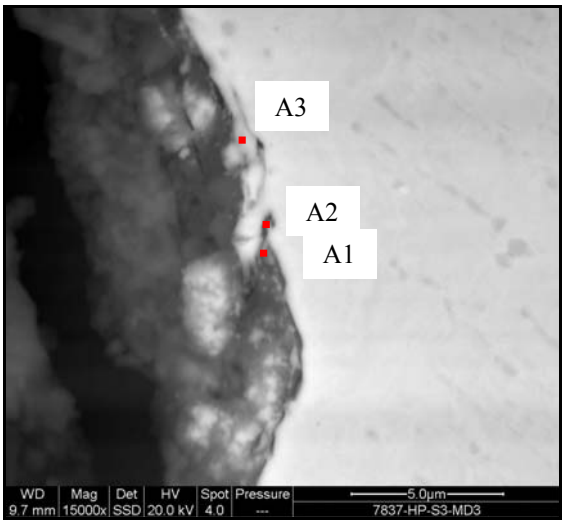

A1

Element	Wt%	At%
C K	8.00	17.53
O K	27.05	44.50
Si K	14.00	13.11
Ca K	0.37	0.24
Cr K	26.23	13.28
Mn K	6.24	2.99
Fe K	10.00	4.71
Ni K	8.11	3.64
Totals	100.00	

A2

Element	Wt%	At%
C K	4.22	14.04
O K	7.18	17.95
Si K	6.16	8.77
Ca K	0.21	0.21
Cr K	21.67	16.67
Mn K	0.94	0.69
Fe K	29.87	21.40
Ni K	29.75	20.27
Totals	100.00	

A3

Element	Wt%	At%
C K	4.66	14.87
O K	8.59	20.59
Si K	7.13	9.73
Ca K	0.27	0.26
Cr K	19.91	14.69
Mn K	0.98	0.68
Fe K	29.30	20.13
Ni K	29.17	19.06
Totals	100.00	

Figure 5.65 Higher magnification micrograph of the pit bottom.

5.6.8 HP-850°C-500h

Somewhat different attack process was observed to have taken place on the alloy after the exposure for both 500 and 1000h. Localised sites seemed to have been subject to severe, dual actions of oxidation and carburisation. Figure 5.66 showed one of the sites attacked on the alloy after 500h. Two different zones were observed just beneath the reaction front; a carbide depleted zone and a carburised zone that occurred just below it. This may suggest a simultaneous action of oxidation and carburisation. The attack depth was approximately 35µm.

As shown in Figure 5.67, the outer layer (~ 1µm) formed on the alloy was analysed (at P1) and found to be composed of chromium, manganese, and silicon oxides in addition to some minor levels of iron. The alloy portions observed within the corrosion product (P2 and P4) were composed mainly of iron and nickel in addition to much lower chromium levels.

Moreover, one of the alloy chunks (P3) contained high level of niobium suggesting that it was originally niobium-rich carbide.

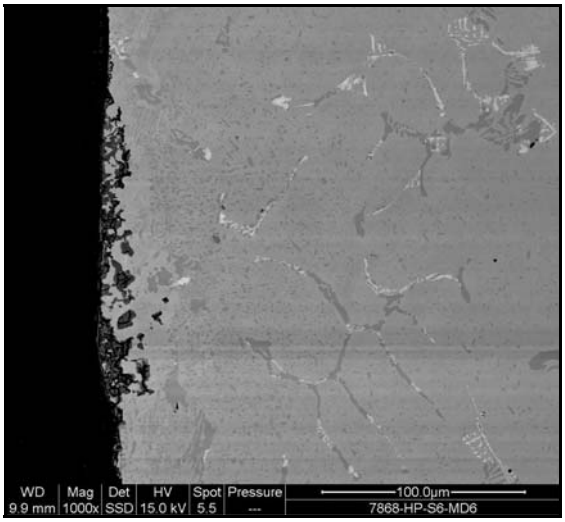

Figure 5.66 Attacks observed on the alloy after 500h of exposure.

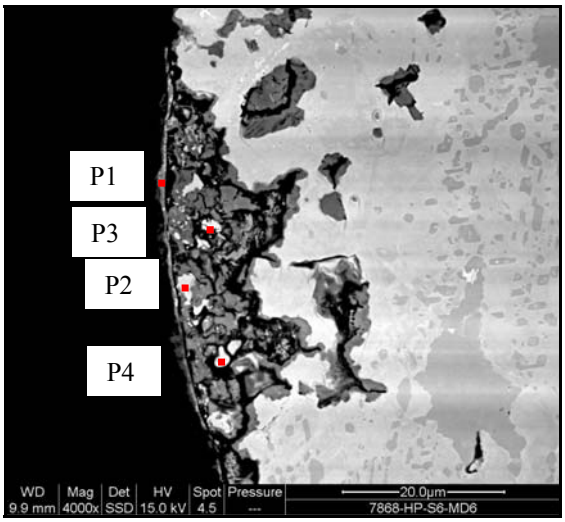

P1

	Wt%	At%
C K	6.78	14.82
O K	29.98	49.22
Si K	10.34	9.67
Cr K	37.87	19.13
Mn K	12.21	5.84
Fe K	2.82	1.32
Totals	100.0	

P2

	Wt%	At%
C K	1.81	7.81
O K	1.20	3.90
Cr K	5.09	5.08
Fe K	45.12	41.89
Ni K	46.78	41.32
Totals	100.0	

P3

	Wt%	At%
C K	6.23	20.96
O K	11.23	28.37
Si K	2.75	3.95
Cr K	2.79	2.17
Fe K	20.27	14.66
Ni K	20.63	14.20
Nb L	36.10	15.70
Totals	100.0	

P4

	Wt%	At%
C K	2.05	7.46
O K	6.92	18.91
Si K	4.29	6.68
Cr K	9.60	8.07
Fe K	37.37	29.26
Ni K	39.76	29.61
Totals	100.0	

Figure 5.67 Catastrophic oxidation and carburisation noticed on the alloy

More investigation of the localised corrosion is shown in Figure 5.68. It was confirmed that most of the product at the site was, basically, oxides with some alloy and carbide particles embedded within.

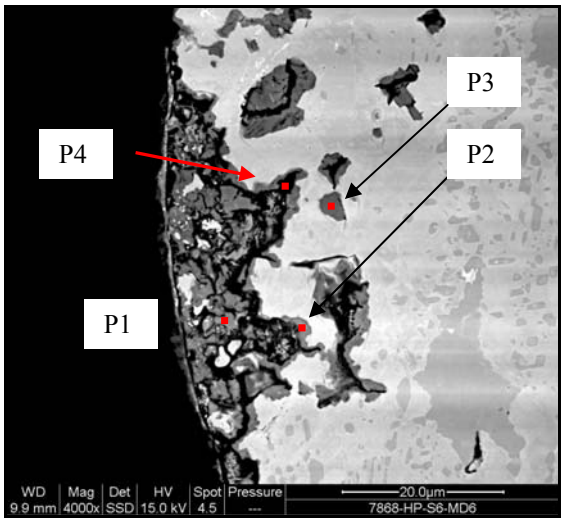

P1

	Wt%	At%
C K	1.20	2.82
O K	35.27	62.44
Si K	1.77	1.78
Cr K	39.60	21.57
Mn K	19.37	9.99
Fe K	1.60	0.81
Ni K	1.20	0.58
Totals	100.0	

P2

	Wt%	At%
C K	1.90	4.48
O K	33.16	58.70
Si K	5.41	5.46
Cr K	41.00	22.33
Mn K	11.61	5.99
Fe K	3.62	1.83
Ni K	1.11	0.54
Nb L	2.20	0.67
Totals	100.0	

P3

	Wt%	At%
C K	1.36	3.07
O K	38.21	65.05
Si K	1.18	1.14
Cr K	55.62	29.13
Mn K	0.84	0.42
Fe K	1.07	0.52
Ni K	0.92	0.43
Nb L	0.81	0.24
Totals	100.0	

P4

	Wt%	At%
O K	51.96	68.09
Si K	36.80	27.47
Cr K	8.18	3.30
Mn K	0.69	0.27
Fe K	1.65	0.62
Ni K	0.71	0.25
Totals	100.0	

Figure 5.68 **Corrosion products at the site were basically oxides with some alloy and carbide particles embedded within.**

5.6.9 HP-850ºC-1000h

Similarly, localised corrosion was observed on the alloy following the exposure for 1000h (Figure 5.69). A layer of about 3μm was observed to have developed on the alloy surface. However, no appreciable localised concentration of carbides could be seen around the corroded area (in the reaction zone).

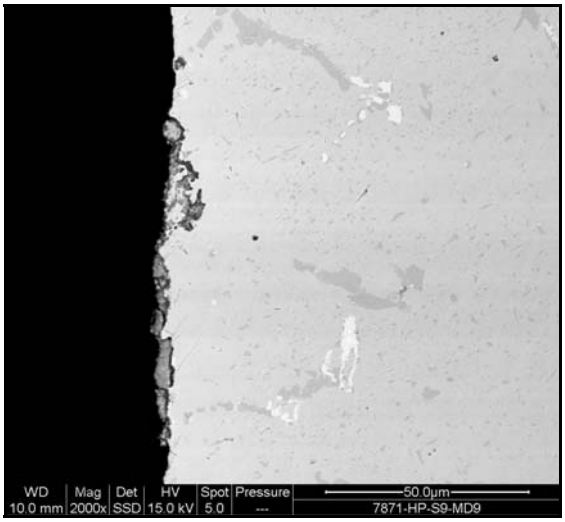

Figure 5.69 Localised corrosion was observed on the alloy following the exposure for 1000h.

Further investigation of the attack (shown in Figure 5.69) revealed that the pit contents were mainly oxides of chromium and silicon (Figures 5.70 and 5.71). The external oxide layer was analysed and found to be chromium, silicon, and manganese-containing oxides. It is worth mentioning that considerable amounts of iron and nickel were also detected within the oxides at the pit.

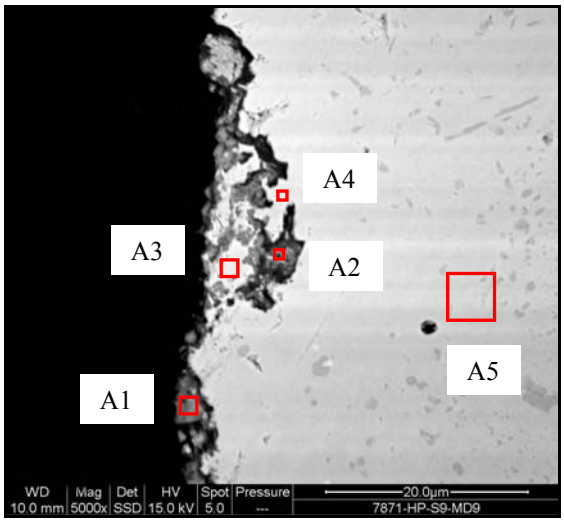

A1

Element	Wt%	At%
C K	5.65	12.21
O K	34.26	55.60
Si K	5.96	5.51
Ca K	0.23	0.15
Cr K	39.14	19.55
Mn K	14.77	6.98
Totals	100.00	

A2

Element	Wt%	At%
C K	7.30	16.79
O K	25.44	43.94
Si K	8.01	7.88
Ca K	0.75	0.51
Cr K	53.68	28.53
Fe K	3.18	1.58
Ni K	1.63	0.77
Totals	100.00	

A3

Element	Wt%	At%
C K	1.71	6.99
O K	2.85	8.76
Si K	0.47	0.82
Cr K	21.34	20.16
Mn K	0.69	0.61
Fe K	37.50	32.99
Ni K	35.45	29.67
Totals	100.00	

A4

Element	Weight%	Atomic%
C K	1.89	7.74
O K	2.06	6.36
Si K	1.58	2.78
Cr K	19.45	18.45
Fe K	38.54	34.03
Ni K	36.48	30.64
Totals	100.00	

A5

Element	Weight%	Atomic%
C K	1.61	6.81
O K	1.36	4.30
Si K	1.27	2.28
Cr K	21.55	20.99
Fe K	36.99	33.53
Ni K	37.22	32.10
Totals	100.00	

Figure 5.70 The pit contents were mainly oxides of chromium and silicon

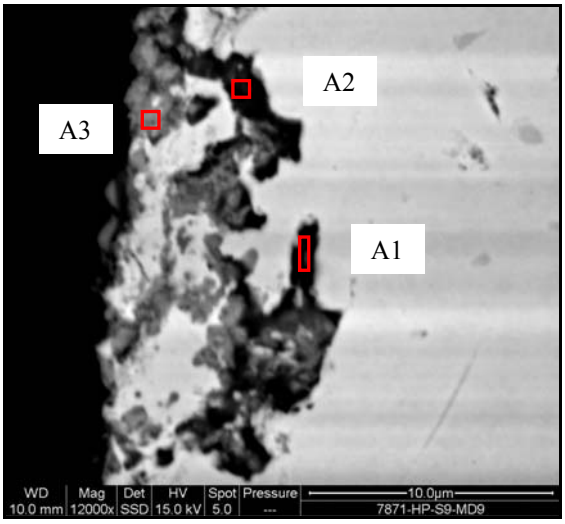

A1

Element	Wt%	At%
C K	2.90	6.49
O K	29.99	50.43
Si K	20.13	19.28
Ca K	0.56	0.38
Cr K	33.66	17.42
Fe K	7.04	3.39
Ni K	5.72	2.62
Totals	100.00	

A2

Element	Wt%	At%
C K	3.78	7.44
O K	38.29	56.64
Si K	26.21	22.08
Ca K	0.75	0.44
Cr K	13.37	6.08
Fe K	10.10	4.28
Ni K	7.51	3.03
Totals	100.00	

A3

Element	Wt%	At%
C K	2.22	5.42
O K	30.60	55.96
Si K	3.00	3.13
Ca K	0.26	0.19
Cr K	50.36	28.34
Mn K	1.02	0.54
Fe K	6.66	3.49
Ni K	5.88	2.93
Totals	100.00	

Figure 5.71 Mixtures of oxides had formed within the localised corrosion.

6 EVALUATION OF ALLOY 35Cr-45Ni PERFORMANCE IN METAL DUSTING CONDITIONS

This chapter describes the findings pertaining to the behaviour of the nickel-based alloy, 35Cr-45Ni, that had been exposed to the gas mixture at 650, 750, and 850ºC for periods of 100, 500, and 1000 hours.

6.1 Visual Examination

6.1.1 35Cr-45Ni Tested at 650ºC

Photos of the alloy after the removal from the furnace are shown in Figure 5.1 (Chapter 5).

Apart from a few carbon filaments seen on the sides, the sample tested at 650ºC for 100h did not experience an appreciable carbon deposition.

However, increasing the experimental time to 500h appeared to have allowed much more carbon accumulation on the alloy surface. Additionally, carbon filaments were observed to grow on the sample sides.

A denser, thicker, blackish layer had developed on the specimen as a consequence of exposure for 1000h at the same temperature. Some localised, pronounced growth of carbon filaments was also noticed on both faces of the specimen. Furthermore, the sample edges seemed to have experienced less carbon deposition.

Figure 6.1 shows the alloy samples after cleaning. It is worth noting that increasing the exposure time generally led to the formation of more adherent deposits that were more difficult to remove.

(a) Alloy condition after 100h

(b) Alloy condition after 500h

(c) Alloy condition after 1000h

Figure 6.1 Photos of the alloy after exposed at 650ºC after cleaning.

6.1.2 35Cr-45Ni Tested at 750ºC

Figure 5.3 (Chapter 5) shows photos of the alloy samples after the removal from the furnace.

Visual inspection of the exposed specimens revealed a little carbon deposition that had taken place on the sample after 100h of testing. However, comparatively denser carbon layers were seen on the sides of the sample. No carbon filaments appeared to have grown on the alloy.

Increasing the exposure time to 500h apparently caused an accumulation of a blackish, carbon deposit on the specimen. Moreover, the extent of the carbon deposition seemed to vary across the sample with less carbon deposition observed on the sample half near the HP alloy (with reference to the samples' order on the rack).

Extension of exposure time to 1000h allowed more deposition of a thicker, loose, blackish layer on the alloy surface. Interestingly, the carbon accumulation appeared to be decreasing across the sample as most deposition was observed on the sample's half, just next to alloy HP, whilst the least carbon was seen on the sample's half near UCX. This behaviour is discussed further in Chapter 8.

The samples' condition after cleaning is shown in Figure 6.2. It is obvious that increasing the exposure time led to the formation of more adherent layer(s) on the alloy surfaces that might be attributed to more carbon diffusion into the alloy substrate giving rise to stronger bonding between layers.

(a) Alloy condition after 100h

(b) Alloy condition after 500h

(c) Alloy condition after 1000h

Figure 6.2 Photos of the alloy after exposed at 750ºC after cleaning.

6.1.3 35Cr-45Ni Tested at 850ºC

In general, increasing the temperature to 850ºC was accompanied by a remarkable reduction in carbon deposition. Photographs of the samples after the removal from the furnace are shown in Figure 5.5 (Chapter 5).

The alloy experienced almost no carbon deposition after exposure for 100h at 850ºC. However, a little carbon deposition was observed on the sample sides. Also, the surface of the alloy was covered mainly with a light greenish layer that was probably composed of oxides.

Grey and greenish layers had formed on the sample exposed for 500h. In addition, distinctive, small black spots were also observed on the alloy.

The specimen subjected to 850ºC for 1000h also formed a mixture of greyish and greenish layers that appeared to be thicker than that formed on the alloy after 500h.

The samples after cleaning are shown in Figure 6.3. It seems that the alloy formed more oxides at this temperature (i.e. 850ºC) and experienced the least carbon deposition.

(a) Alloy condition after 100h

(b) Alloy condition after 500h

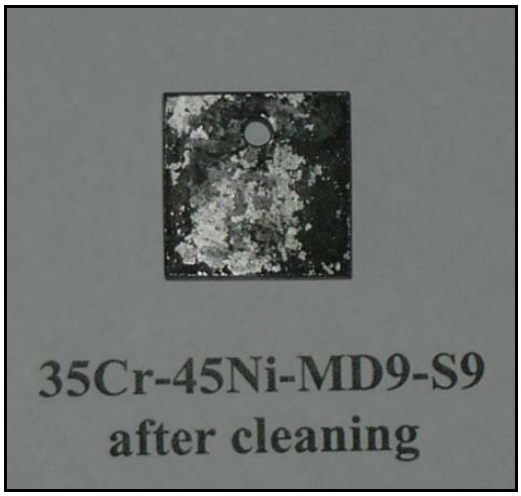

(c) Alloy condition after 1000h

Figure 6.3 Photos of the alloy after exposed at 850°C after cleaning.

6.2 Weight Change Measurements

The specimens were then weighed in order to calculate the weight change (Table 6.1). The measurements showed that the samples experienced weight gain in most experiments. Weight loss, however, was observed on the sample exposed at 650ºC for 500h.

In general, the weight change might well be the result of oxidation, carburisation, metal dusting, carbon deposition, or a combination of some or all of these. In view of that, we can say that, although the weight gain may not prove whether the alloy experienced metal wastage, the weight loss, nonetheless, might indicate that the alloy suffered metal dusting, especially for the samples exposed at relatively low temperatures (650 and 750ºC) where the formation (and spallation) of thick oxide scales is unlikely.

Table 6.1 Weight change (mg/cm^2) of the alloy after the exposure at different temperatures for different periods of time.

Temperature (ºC)	100h	500h	1000h
650	0.1060	-0.8335	0.3519
750	0.4392	0.5191	0.1907
850	0.3741	0.3855	0.1427

6.3 X ray Diffraction Results

All the alloy surfaces, as well as any sufficient amount of deposits, were analysed by XRD. The XRD patterns and charts are reported in Appendix C.

Analysis of the alloy after exposure at 650ºC for 100h showed the presence of carbon, niobium carbides, and chromium and iron-containing carbides. It was also possible to collect a small amount of the deposit that was found to contain carbon, chromium carbides, chromium, and silicon oxide.

Carbides of niobium and chromium-iron were detected in the sample exposed for 500h at the same temperature. The deposit removed from this sample contained carbon, Cr_2O_3, and alloy particles (Cr_2Ni_3).

Increasing the test time to 1000h resulted in the formation of silicon oxide, carbon, and niobium and chromium-iron carbides on the alloy surface. The deposit extracted from this alloy was found to contain mainly carbon and silicon oxide.

$MnCr_2O_4$ and chromium-iron carbides had formed on the alloy as a result of exposure at 750ºC for 100h. The deposit removed from this specimen was composed of carbon, silicon oxide, and Fe_3Ni_2.

Extending the exposure time to 500h resulted in the formation of $Cr_{1.5}Fe_{0.5}MnO_4$, Cr_2O_3, silicon oxides, and chromium-iron-carbides on the alloy surface. Not enough deposit was found on this sample to be analysed.

Prolonging the experiment time to 1000h led to the formation of $CrMn_{1.5}O_4$ and Cr_2O_3 on the alloy. The analysis of the deposit removed from this sample showed the presence of carbon, silicon oxide, and Ni-Si particles.

Carbon and $CrMn_{1.5}O_4$ were detected on the sample as a consequence of exposure at 850ºC for 100h. However, $Cr_{0.5}Fe_{1.5}MnO_4$ was found on the alloy after increasing the exposure time to 500h. Increasing the experiment time further, to 1000h, led to the production of $CrMn_{1.5}O_4$, Cr_2O_3, and $Mn_{1.7}Fe_{1.3}O_4$ on the sample surface.

6.4 SEM/EDX Deposits Analysis

The chemical composition of the deposits removed from the alloys was examined using SEM/EDX.

6.4.1 35Cr-45Ni-650ºC-100h

EDX of the deposit removed from this sample showed that it was composed mainly of carbon, silicon, and oxygen with traces of chromium and nickel (Figure 6.4). Indeed, the presence of alloying elements such as chromium, nickel, and/or iron in the deposit might well suggest the onset of metal dusting.

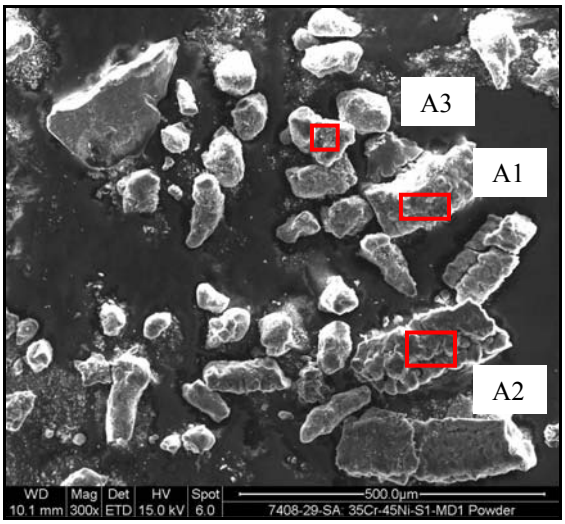

A1

Element	Wt%	At%
C K	63.69	74.64
O K	19.34	17.02
Si K	16.34	8.19
Ni K	0.64	0.15
Totals	100.00	

A2

Element	Wt%	At%
C K	79.99	86.92
O K	11.72	9.56
Si K	6.57	3.05
Cl K	0.51	0.19
Cr K	0.46	0.12
Ni K	0.74	0.17
Totals	100.00	

A3

Element	Wt%	At%
C K	62.74	73.85
O K	19.73	17.43
Si K	17.06	8.59
Cr K	0.47	0.13
Totals	100.00	

Figure 6.4 Chemical analysis of deposits removed from the alloy surface after exposure at 650ºC for 100h.

6.4.2 35Cr-45Ni-650ºC-500h

Greater concentrations of the alloying elements, nickel and iron, were indeed detected in the deposit removed from the sample after exposure at 650ºC for 500h (Figure 6.5).

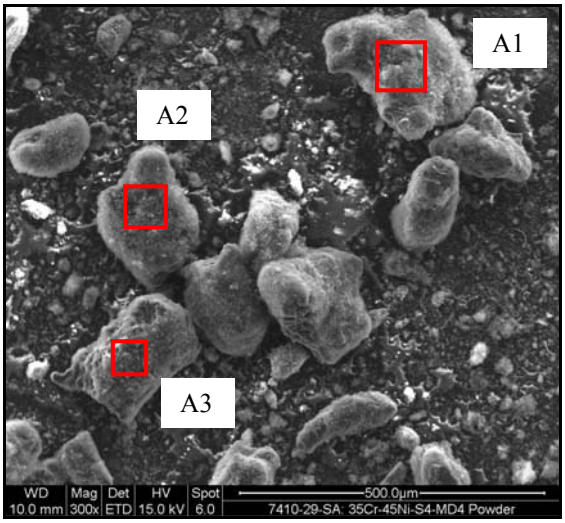

A1

Element	Wt%	At%
C K	87.37	91.38
O K	9.76	7.66
Si K	1.46	0.65
Fe K	0.34	0.08
Ni K	1.08	0.23
Totals	100.00	

A2

Element	Wt%	At%
C K	88.79	93.09
O K	7.21	5.68
Si K	1.64	0.74
Fe K	0.34	0.08
Ni K	1.37	0.29
Cu K	0.64	0.13
Totals	100.00	

A3

Element	Wt%	At%
C K	89.76	93.77
O K	6.56	5.15
Si K	1.20	0.54
Cr K	0.32	0.08
Fe K	0.71	0.16
Ni K	1.45	0.31
Totals	100.00	

Figure 6.5 Chemical analysis of deposits removed from the alloy surface after exposure at 650ºC for 500h.

6.4.3 35Cr-45Ni-750ºC-100h

The deposit removed from the specimen exposed at 750ºC for 100h was composed mainly of carbon, silicon, and oxygen suggesting the presence of silicon oxides (Figure 6.6). No alloying elements were detected at the three areas, A1, A2, and A3.

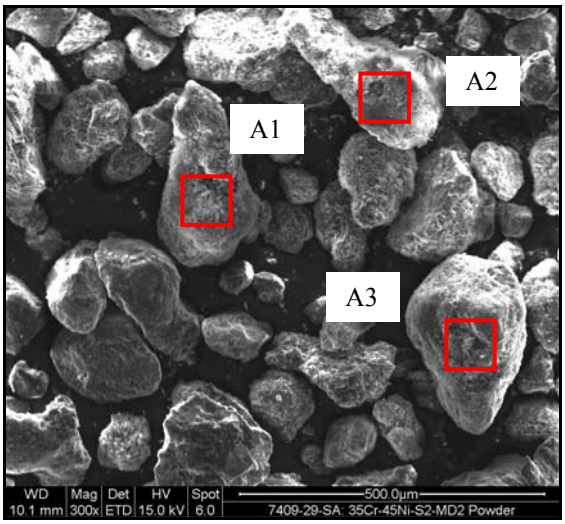

A1

Element	Wt%	At%
C K	35.44	47.33
O K	37.17	37.26
Si K	26.65	15.22
Cu K	0.74	0.19
Totals	100.00	

A2

Element	Wt%	At%
C K	29.50	41.08
O K	37.61	39.33
Si K	32.89	19.59
Totals	100.00	

A3

Element	Wt%	At%
C K	46.26	58.20
O K	31.71	29.95
Si K	22.03	11.85
Totals	100.00	

Figure 6.6 Chemical analysis of deposits removed from the alloy surface after exposure at 750ºC for 100h.

6.4.4 35Cr-45Ni-750ºC-1000h

Considerable amounts of manganese and nickel were detected in the deposit removed from this sample. It is also worth noting the change in the deposit shape as it became flake like (Figure 6.7).

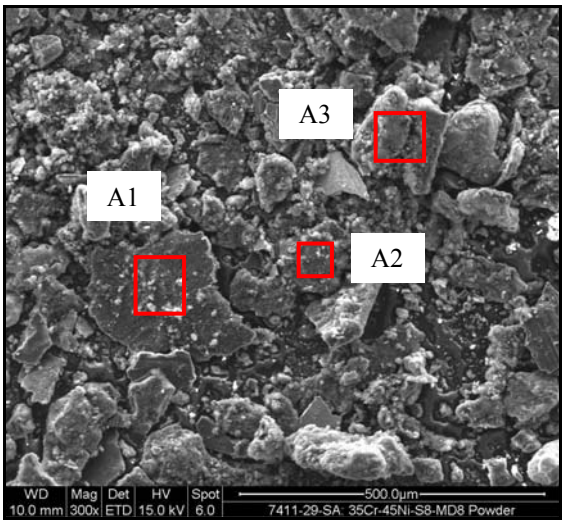

A1

Element	Wt%	At%
C K	84.91	91.04
O K	8.38	6.75
Si K	3.04	1.39
Mn K	1.26	0.30
Ni K	2.41	0.53
Totals	100.00	

A2

Element	Wt%	At%
C K	81.73	87.64
O K	11.49	9.25
Si K	6.78	3.11
Totals	100.00	

A3

Element	Wt%	At%
C K	89.17	92.80
O K	7.61	5.95
Si K	2.43	1.08
Ni K	0.79	0.17
Totals	100.00	

Figure 6.7 Chemical analysis of deposits removed from the alloy surface after exposure at 750ºC for 1000h.

6.5 Surface Analyses

6.5.1 35Cr-45Ni-650ºC-100h

As seen in Figure 6.8, the alloy surface had been covered with a layer that was found (at A1) to contain mainly chromium and oxygen suggesting the development of Cr_2O_3. Also, large amounts of silicon, nickel, and manganese were detected. The alloy surface was uncovered at some areas, perhaps due to cleaning, which allowed further investigation.

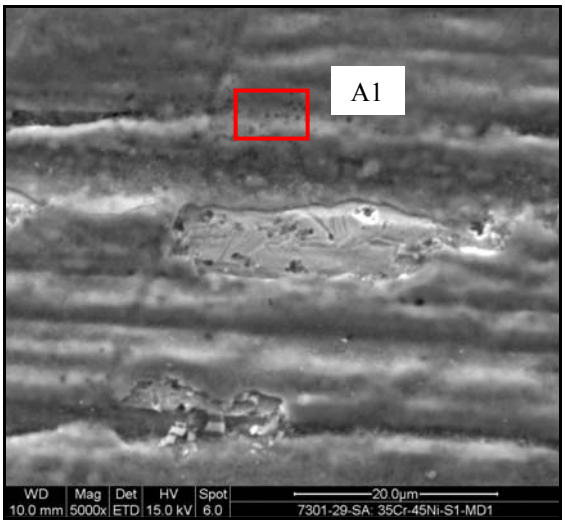

A1

Element	Wt%	At%
C K	1.52	3.43
O K	34.98	59.21
Na K	0.29	0.35
Si K	11.16	10.76
Cr K	35.85	18.67
Mn K	4.99	2.46
Fe K	3.38	1.64
Ni K	7.09	3.27
Nb L	0.73	0.21
Totals	100.00	

Figure 6.8 Alloy surface after exposure at 650ºC for 100h.

A higher magnification image of the exposed surface is shown in Figure 6.9. Considerable depletion of chromium at the substrate was confirmed by analysing the area A2. Only 24.9 wt% of chromium was detected compared to the base metal concentration of

~35 wt% chromium. Examination of the surface also revealed the presence of small pits with a maximum size of approximately 2.5µm. EDX of the pitted area (A1) detected higher amounts of carbon, oxygen, and silicon.

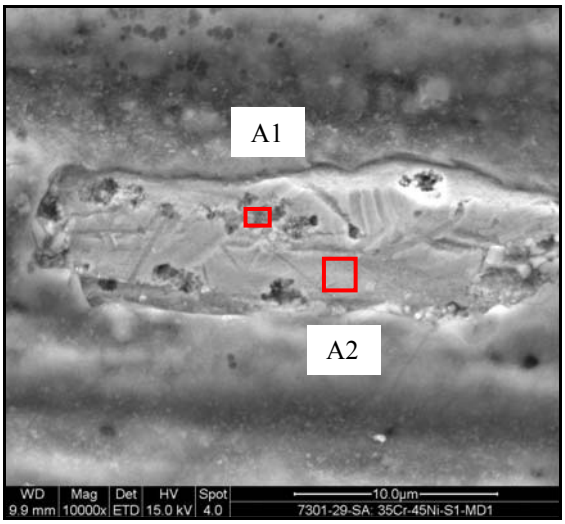

A1

Element	Wt%	At%
C K	4.92	16.55
O K	6.83	17.26
Si K	3.58	5.16
Cr K	24.92	19.38
Fe K	17.05	12.35
Ni K	42.32	29.15
Nb L	0.38	0.17
Totals	100.00	

A2

Element	Wt%	At%
C K	2.56	10.43
O K	1.78	5.44
Si K	0.95	1.65
Cr K	24.88	23.44
Fe K	20.45	17.94
Ni K	49.04	40.92
Nb L	0.35	0.18
Totals	100.00	

Figure 6.9 Small pits were observed on the alloy surface.

6.5.2 35Cr-45Ni-650ºC-500h

Two layers appeared to have formed on the alloy due to the extension of exposure time to 500h (Figure 6.10). The composition of the outer layer, which was darker and apparently thicker, was dominated by carbon in addition to silicon oxide (A1). Only traces of other alloying elements were detected in this layer. The underlying layer (A2) was, however, composed of oxides of chromium, silicon, and manganese with minor amounts of iron and nickel. The amount of carbon in this layer was detected to be much lower than that found in the upper layer. The alloy surface, under this layer (A3), was also analysed

and found to contain less oxides and more alloying elements. It is worth noting that the level of chromium at this area (i.e. 26.8 wt%) was significantly less than that of the base metal (i.e. ~35 wt%) suggesting little diffusion of chromium to the substrate.

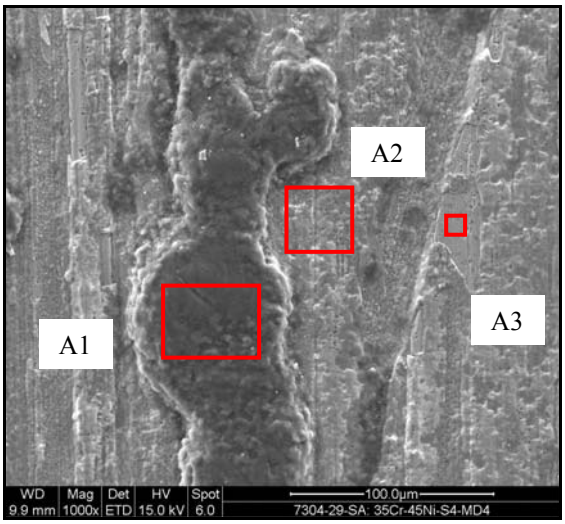

A1

Element	Wt%	At%
C K	59.73	71.65
O K	21.54	19.40
Si K	16.14	8.28
Cl K	0.26	0.11
Ca K	0.22	0.08
Cr K	0.48	0.13
Fe K	0.36	0.09
Ni K	0.75	0.18
Mo L	0.52	0.08
Totals	100.00	

A2

Element	Wt%	At%
C K	4.34	9.02
O K	38.13	59.52
Si K	10.11	8.99
Cr K	37.79	18.15
Mn K	7.30	3.32
Fe K	0.82	0.37
Ni K	1.52	0.65
Totals	100.00	

A3

Element	Wt%	At%
C K	2.31	8.47
O K	6.25	17.23
Si K	2.92	4.59
Cr K	26.75	22.69
Mn K	1.01	0.81
Fe K	17.45	13.78
Ni K	42.93	32.25
Nb L	0.39	0.18
Totals	100.00	

Figure 6.10 Two layers formed on the alloy after exposure at 650ºC for 500h.

A higher magnification image of the alloy surface revealed the occurrence of localised attack in the form of pits (Figure 6.11). The pits appeared to be randomly distributed with a maximum size of around 4µm.

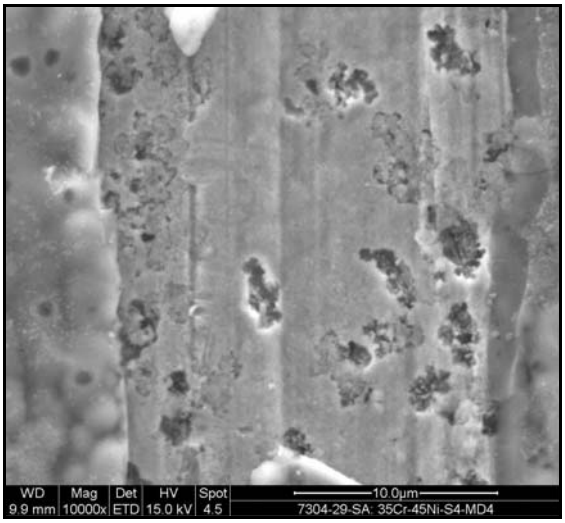

Figure 6.11 **Pitting observed on the alloy surface as a consequence to exposure at 650ºC to the gas mixture for 500h.**

6.5.3 35Cr-45Ni-650ºC-1000h

Localised islands of deposit were observed on the alloy surface (A1) after increasing the exposure time to 1000h (Figure 6.12). EDX confirmed that they were composed of carbon and silicon oxides. The layer formed on the surface (A2) was also analysed and was found to contain a mixture of carbon and oxides of chromium and silicon in addition to traces of nickel and manganese. Pitting was seen on the alloy surface, under that layer, distributed in a random manner. The substrate was also analysed (A3) and found to be depleted of chromium and manganese possibly due to oxidation. The concentrations of nickel and iron were, however, almost identical to those of the base metal.

A higher magnification image of the pitted area on the alloy surface is shown in Figure 6.13. Analysing that area showed the presence of significant amounts of carbon, oxygen, silicon, and niobium. However, compared to the base metal, low concentrations of chromium were detected, implying severe depletion of that element at the surface as a consequence of oxidation. Also, no manganese was found. The detection of a comparatively high concentration of niobium might be attributed to either formation of

more niobium-containing carbides or selective attack that was more favourable in the matrix rather than carbides that led to an increase in the concentration of carbides at the pitted area.

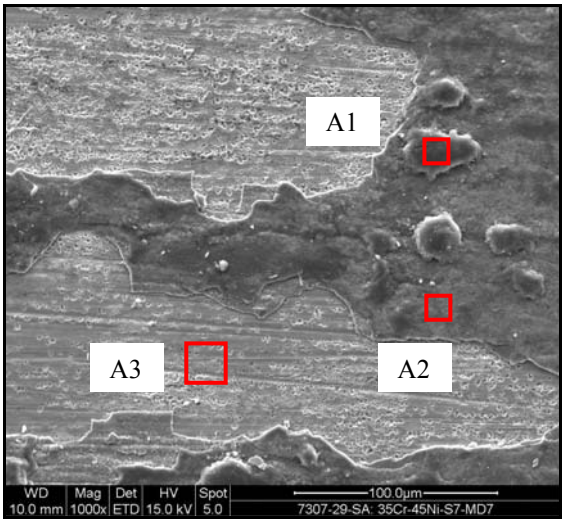

A1

Element	Wt%	At%
C K	62.55	73.56
O K	21.00	18.54
Si K	15.08	7.58
Cl K	0.20	0.08
Cr K	0.53	0.14
Mo L	0.64	0.09
Totals	100.00	

A2

Element	Wt%	At%
C K	26.81	43.01
O K	31.30	37.69
Si K	12.13	8.32
Cr K	28.19	10.45
Mn K	0.82	0.29
Ni K	0.75	0.25
Totals	100.00	

A3

Element	Wt%	At%
C K	3.02	10.97
O K	5.79	15.77
Si K	3.70	5.74
Cr K	22.36	18.75
Fe K	18.30	14.28
Ni K	45.82	34.02
Nb L	1.00	0.47
Totals	100.00	

Figure 6.12 Image of the alloy surface after exposure at 650°C for 1000h.

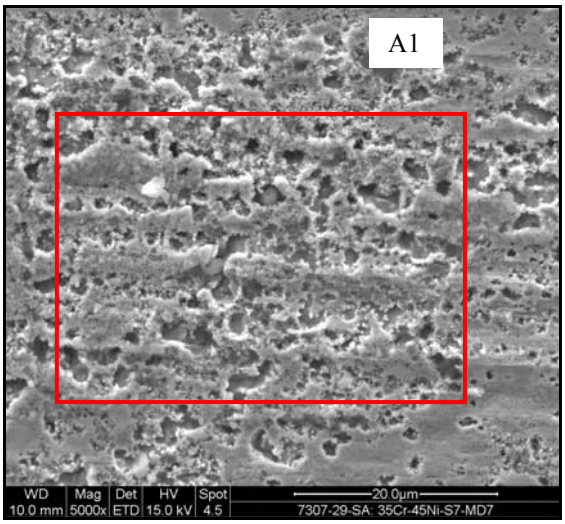

A1

Element	Wt%	At%
C K	10.43	31.25
O K	6.27	14.10
Si K	4.83	6.19
Ca K	0.23	0.21
Cr K	14.97	10.36
Fe K	14.67	9.46
Ni K	42.55	26.09
Nb L	6.07	2.35
Totals	100.00	

Figure 6.13 Pitting observed on the alloy surface.

6.5.4 35Cr-45Ni-750ºC-100h

The condition of the alloy surface after exposure at 750ºC for 100h is shown in Figure 6.14. There appeared to be two layers formed on the alloy. Although the outer layer was almost entirely removed by cleaning, it was possible to locate some residuals (A1) that were analysed and found to be a mixture of carbon and silicon oxide in addition to traces of alloying element. The layer that directly formed on the alloy (A2), however, was seen to contain oxides of chromium, silicon, and manganese with a much lower amount of carbon. EDX of the alloy bare surface is also shown in Figure 6.14. A higher magnification micrograph of the surface is shown in Figure 6.15 where some pitting can be observed.

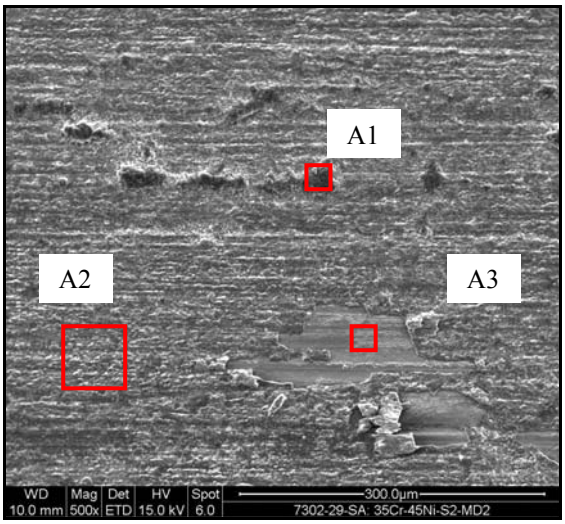

A1

Element	Wt%	At%
C K	43.23	56.25
O K	31.70	30.97
Si K	20.38	11.34
S K	0.14	0.07
Cl K	0.14	0.06
Ca K	0.31	0.12
Cr K	2.52	0.76
Mn K	0.55	0.16
Fe K	0.60	0.17
Ni K	0.44	0.12
Totals	100.00	

A2

Element	Wt%	At%
C K	3.84	7.80
O K	39.76	60.69
Si K	13.15	11.44
Cr K	35.19	16.53
Mn K	6.52	2.90
Fe K	0.62	0.27
Ni K	0.93	0.39
Totals	100.00	

A3

Element	Wt%	At%
C K	3.14	9.88
O K	12.20	28.78
Si K	6.93	9.31
Cr K	22.38	16.25
Fe K	15.63	10.56
Ni K	38.32	24.65
Nb L	1.41	0.57
Totals	100.00	

Figure 6.14 Alloy surface after exposure at 750ºC for 100h.

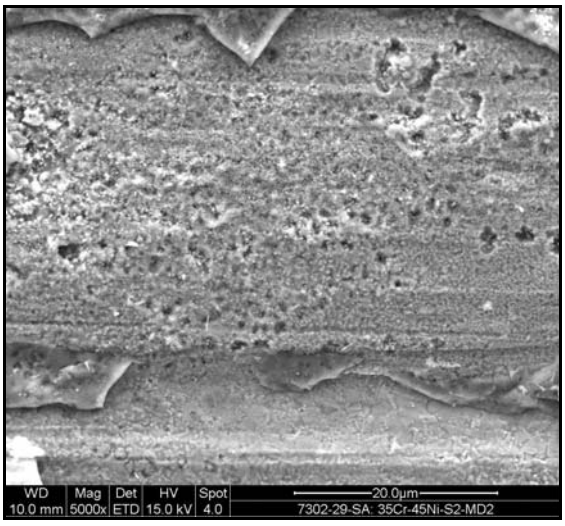

Figure 6.15 An image of the alloy surface (A3 in Figure 6.14).

6.5.5 35Cr-45Ni-750°C-500h

The layers formed on the alloy after 500h are shown in Figure 6.16. The outer layer (A1) contained higher amounts of carbon and silicon whereas the inner layer (A2) comprised considerably more chromium and manganese. The alloy underlying surface (A3) was also analysed and found to contain carbon and some oxides in addition to the alloying elements. Figure 6.17 shows a higher magnification image that reveals the presence of pitting.

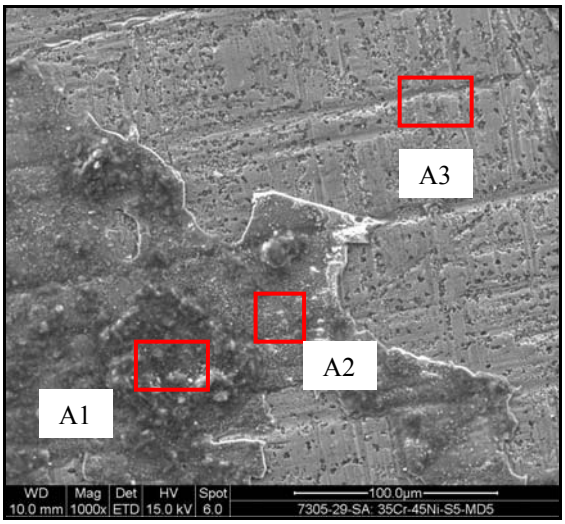

A1

Element	Wt%	At%
C K	35.21	49.75
O K	32.03	33.97
Na K	0.16	0.12
Si K	19.94	12.05
Ca K	1.84	0.78
Cr K	6.69	2.18
Mn K	3.17	0.98
Mo L	0.97	0.17
Totals	100.00	

A2

Element	Wt%	At%
C K	14.13	26.47
O K	33.72	47.41
Si K	10.46	8.37
Ca K	0.46	0.26
Cr K	26.93	11.65
Mn K	13.57	5.56
Ni K	0.73	0.28
Totals	100.00	47.41

A3

Element	Wt%	At%
C K	11.43	31.96
O K	8.25	17.31
Al K	0.13	0.16
Si K	3.78	4.52
Ca K	1.17	0.98
Cr K	27.28	17.61
Fe K	12.53	7.54
Ni K	33.80	19.33
Nb L	1.62	0.59
Totals	100.00	

Figure 6.16 The alloy surface after exposure at 750°C for 500h.

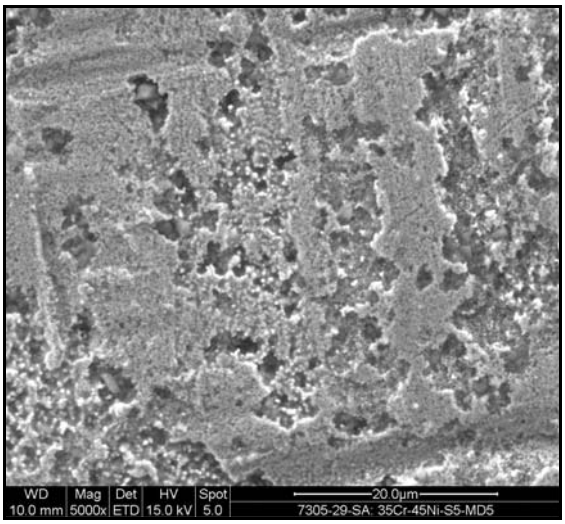

Figure 6.17 The degree of the pitting attack on the alloy surface.

6.5.6 35Cr-45Ni-750ºC-1000h

Examination of the alloy surface after the 1000h exposure showed that the layer formed (A1 and A2) contained a mixture of carbon and oxides of chromium, manganese and silicon (Figure 6.18). Much more oxide was observed to have formed at the lower part of the layer compared to the upper part. The surface under these layers was also analysed and found to contain lower concentrations of iron, nickel, and chromium than those of the base metal. However, relatively high levels of niobium, carbon and silicon oxides were also detected. The alloy surface is revealed in Figure 6.19 where pitting occured.

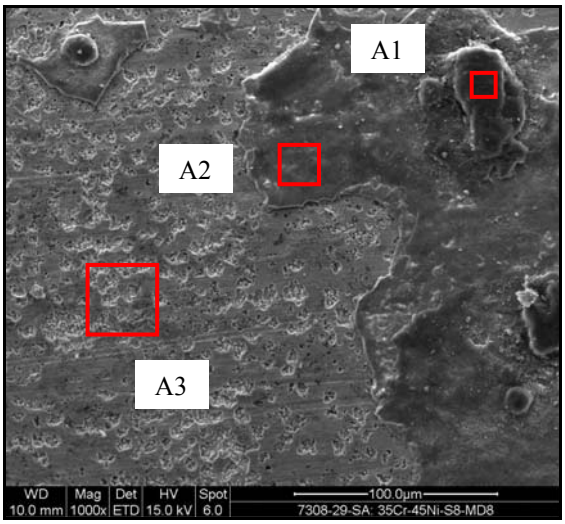

A1

Element	Wt%	At%
C K	82.84	88.83
O K	10.72	8.63
Si K	4.69	2.15
Cr K	0.39	0.10
Ni K	1.36	0.30
Totals	100.00	

A2

Element	Wt%	At%
C K	11.10	22.16
O K	33.39	50.05
Si K	6.30	5.38
Cr K	37.36	17.23
Mn K	11.85	5.17
Totals	100.00	

A3

Element	Wt%	At%
C K	5.55	17.06
O K	10.34	23.83
Si K	6.34	8.33
Cr K	26.07	18.50
Fe K	13.11	8.66
Ni K	35.87	22.54
Nb L	2.72	1.08
Totals	100.00	

Figure 6.18 The alloy surface after exposure for 1000h at 750ºC.

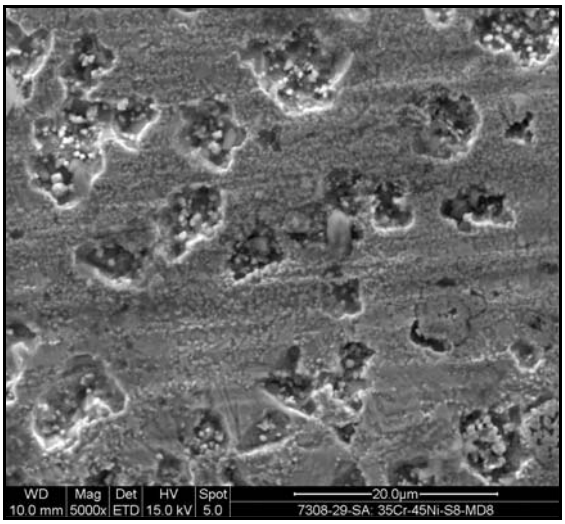

Figure 6.19 Pitting observed on the substrate.

6.5.7 35Cr-45Ni-850ºC-100h

A mixture of oxides and carbon was detected on the alloy after exposure at 850ºC for 100h (Figure 6.20). A higher magnification image of the alloy bare surface is shown in Figure 6.21. Unusually high levels of silicon oxides were observed to have formed on all alloys, especially at 750 and 850ºC, by comparison with the alloy's silicon content of below 2.5 wt%. Therefore, it is unlikely that all the silicon in the oxide had come from the alloy. It is possible, however, that the silicon oxides (SiO) were produced by reaction(s) that took place between the mullite furnace tube and the gas mixture and transferred in a vapour phase form to deposit on the alloy surface. A further discussion of this process is given in Chapter 8.

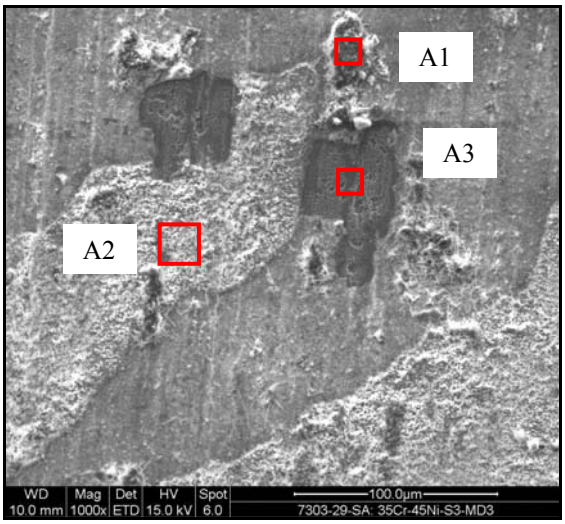

A1

Element	Wt%	At%
C K	25.54	36.15
O K	43.14	45.83
Si K	28.15	17.04
Ca K	0.59	0.25
Cr K	0.76	0.25
Mn K	0.46	0.14
Fe K	0.39	0.12
Ni K	0.49	0.14
Mo L	0.49	0.09
Totals	100.00	

A2

Element	Wt%	At%
C K	2.47	4.39
O K	48.35	64.50
Si K	31.74	24.12
Cr K	10.60	4.35
Mn K	5.51	2.14
Fe K	0.53	0.20
Ni K	0.79	0.29
Totals	100.00	

A3

Element	Wt%	At%
C K	1.96	6.52
O K	11.36	28.42
Al K	0.32	0.47
Si K	3.63	5.18
Cr K	31.90	24.55
Mn K	4.85	3.53
Fe K	11.95	8.57
Ni K	32.27	22.00
Nb L	1.74	0.75
Totals	100.00	

Figure 6.20 The alloy surface after exposure for 100h at 850ºC.

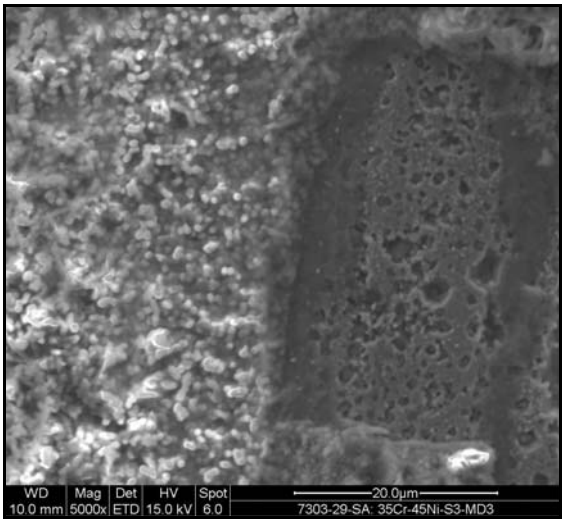

Figure 6.21 The alloy substrate under the outer layers.

6.5.8 35Cr-45Ni-850ºC-500h

The specimen exposed for 500h at 850ºC formed a layer that contained high levels of chromium, manganese, silicon, and oxygen in addition to carbon (Figure 6.22). The chemical composition of the layer was found to be changing from A1 to A2, as a higher carbon amount was detected in the former.

A higher magnification image of that layer (A2 in Figure 6.22) is shown in Figure 6.23. It seems that the alloy formed a more protective layer when the temperature was raised from 650 to 850ºC and the scale appeared to have become more continuous and denser. EDX and an image of the bare alloy surface can be seen in Figure 6.24.

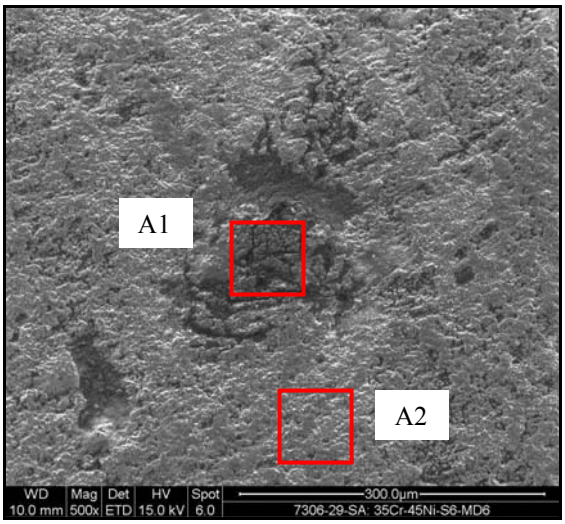

A1

Element	Wt%	At%
C K	16.54	29.95
O K	35.00	47.57
Si K	7.46	5.77
Ca K	0.21	0.11
Cr K	20.82	8.71
Mn K	18.80	7.44
Fe K	0.56	0.22
Ni K	0.62	0.23
Totals	100.00	

A2

Element	Wt%	At%
C K	2.57	5.77
O K	34.83	58.58
Si K	9.60	9.20
Cr K	18.64	9.65
Mn K	33.64	16.48
Ni K	0.71	0.33
Totals	100.00	

Figure 6.22 The alloy surface after exposure for 500h at 850ºC.

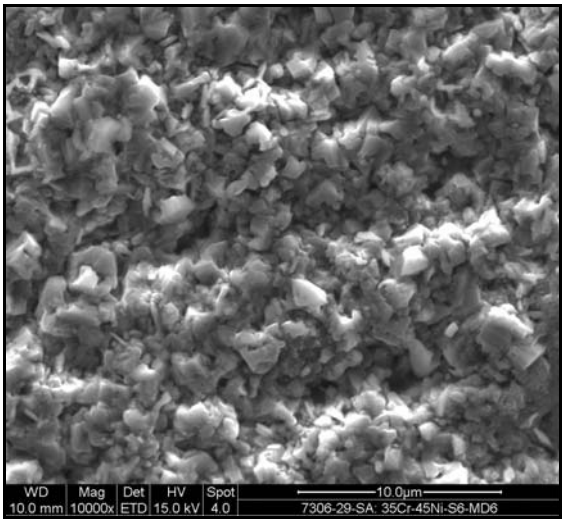

Figure 6.23 The layer formed on the alloy appeared to be continuous.

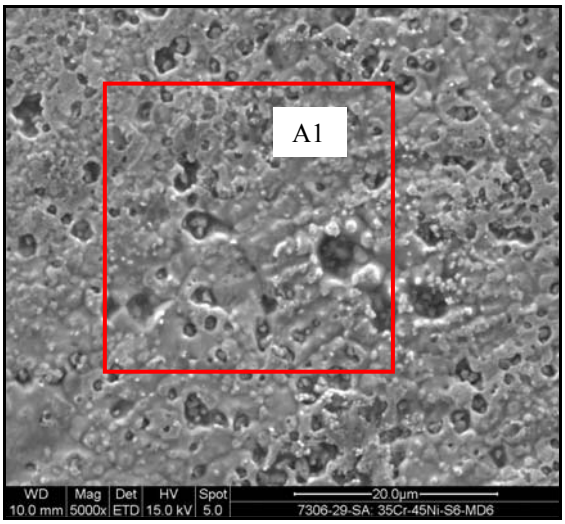

A1

Element	Wt%	At%
C K	7.32	24.31
O K	4.60	11.47
Si K	2.22	3.15
Ca K	0.36	0.35
Cr K	29.69	22.77
Mn K	1.17	0.85
Fe K	14.35	10.24
Ni K	38.22	25.96
Nb L	2.07	0.89
Totals	100.00	

Figure 6.24 Image and EDX analysis of exposed alloy surface.

6.5.9 35Cr-45Ni-850ºC-1000h

Figure 6.25 shows the alloy surface after exposure at 850ºC for 1000h. An oxide layer that was composed mainly of chromium, silicon, and manganese had developed on the alloy (A2). Considerable amounts of carbon deposition were also detected at another darker area on the surface (A1). A higher magnification image of the alloy bare surface is shown in Figure 6.26. Examination of the exposed surface revealed no pitting. A higher magnification image of the needle-like oxides formed on the alloy is shown in Figure 6.27.

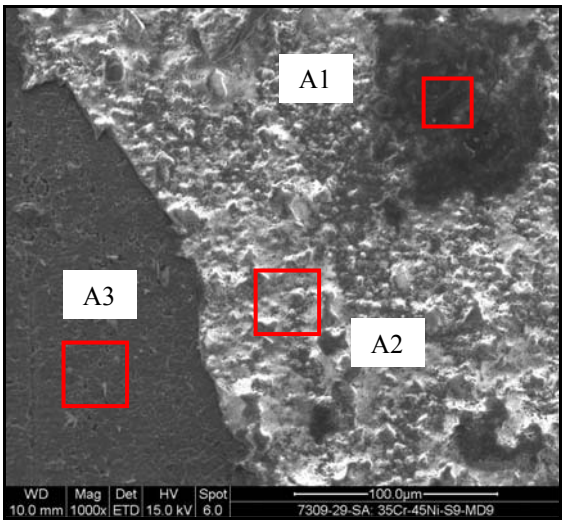

A1

Element	Wt%	At%
C K	35.94	54.14
O K	27.79	31.43
Si K	6.63	4.27
Ca K	0.26	0.12
Cr K	20.05	6.98
Mn K	8.71	2.87
Ni K	0.63	0.19
Totals	100.00	

A2

Element	Wt%	At%
C K	3.90	8.40
O K	36.66	59.22
Si K	7.84	7.22
Cr K	34.37	17.08
Mn K	16.12	7.59
Fe K	0.49	0.23
Ni K	0.61	0.27
Totals	100.00	

A3

Element	Wt%	At%
C K	1.04	4.07
O K	4.79	14.10
Si K	3.85	6.45
Cr K	28.57	25.89
Fe K	16.25	13.71
Ni K	43.03	34.53
Nb L	2.48	1.26
Totals	100.00	

Figure 6.25 The alloy surface after exposure at 850ºC for 1000h.

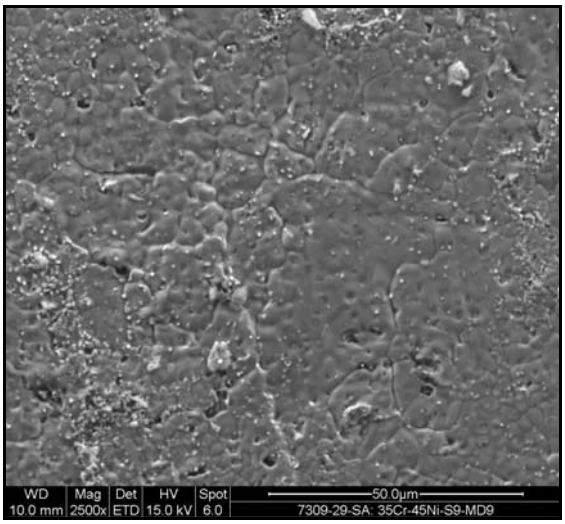

Figure 6.26 A higher magnification image of A3 shown in Figure 6.25.

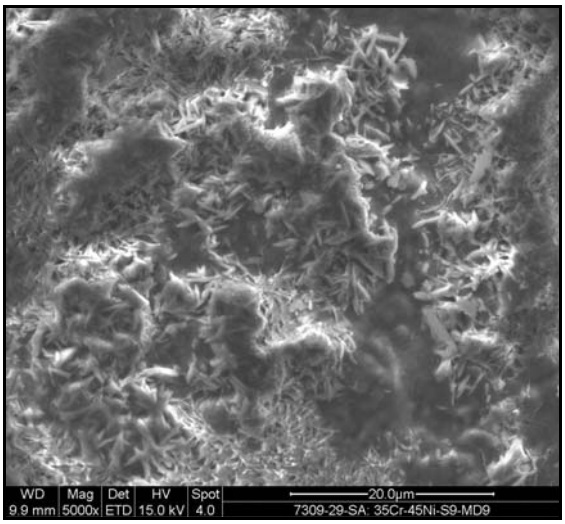

Figure 6.27 A higher magnification image of A2 shown in Figure 6.25.

6.6 Metallographic Examination

6.6.1 35Cr-45Ni-650°C-100h

A few pits were observed along the sample cross section as a result of exposure at 650 for 100h. Figures 6.28 and 6.29 summarise a detailed investigation carried out on one of the pits that was ~9µm deep. The pit appeared to grow in different directions within the alloy. The deposits and layers inside the pit were analysed (A1, A2, A3 and A4) and found to contain mixtures of carbon and oxides. Examination of the micrograph showed that the substrate suffered carburisation as a high concentration of carbides was noticed surrounding the pit. A thin layer, approximately 0.5µm, was also observed to have formed on the alloy and found to be composed of carbon and oxides (A8 in Figure 6.29).

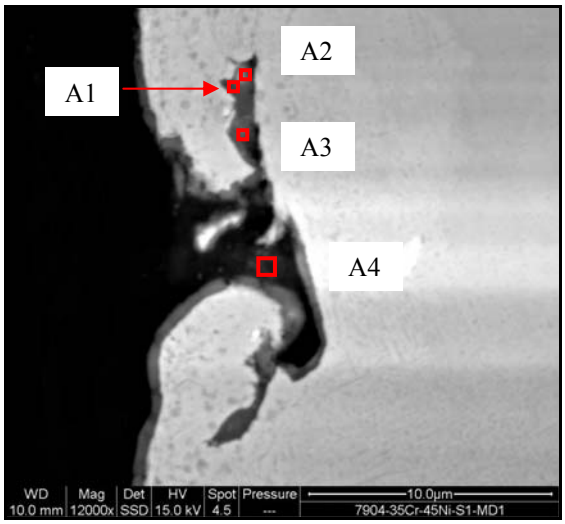

A1

	Wt%	At%
C K	1.45	3.70
O K	26.15	50.17
Si K	9.77	10.67
Ca K	0.26	0.20
Cr K	31.70	18.71
Mn K	8.92	4.98
Fe K	7.33	4.03
Ni K	14.43	7.54
Totals	100.0	

A2

	Wt%	At%
C K	1.58	4.76
O K	16.49	37.26
Si K	6.25	8.05
Ca K	0.32	0.29
Cr K	32.91	22.88
Mn K	6.40	4.21
Fe K	11.24	7.27
Ni K	24.82	15.28
Totals	100.0	

A3

	Wt%	At%
C K	9.76	25.24
O K	15.06	29.25
Si K	4.82	5.33
Ca K	0.45	0.35
Cr K	32.99	19.71
Mn K	9.93	5.62
Fe K	7.95	4.42
Ni K	19.05	10.08
Totals	100.0	

A4

	Wt%	At%
C K	36.79	57.39
O K	21.20	24.83
Si K	8.98	5.99
S K	0.21	0.12
Ca K	2.25	1.05
Cr K	17.43	6.28
Mn K	1.62	0.55
Fe K	6.69	2.24
Ni K	4.82	1.54
Totals	100.0	

Figure 6.28 Localised attack took place on the alloy after 100h at 650°C.

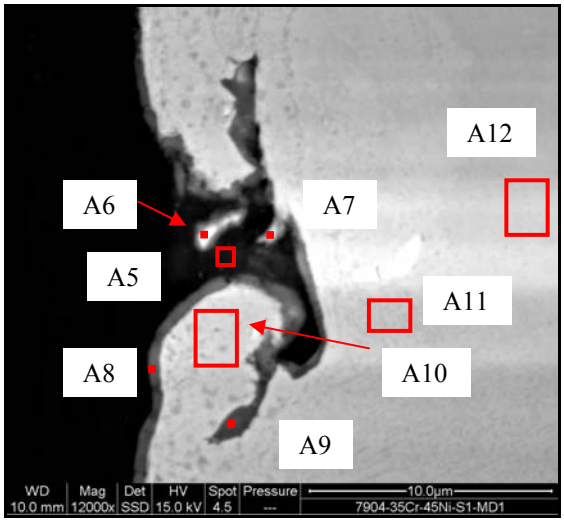

A5

	Wt%	At%
C K	50.42	65.86
O K	24.02	23.56
Si K	11.46	6.40
Ca K	0.82	0.32
Cr K	7.85	2.37
Mn K	0.75	0.22
Fe K	1.98	0.56
Ni K	2.69	0.72
Totals	100.0	

A6

	Wt%	At%
C K	48.87	66.50
O K	21.28	21.73
Si K	10.01	5.83
Ca K	0.36	0.15
Cr K	8.63	2.71
Mn K	0.60	0.18
Fe K	3.32	0.97
Ni K	6.92	1.93
Totals	100.0	

A7

	Wt%	At%
C K	17.87	40.82
O K	10.32	17.69
Si K	6.80	6.64
Ca K	10.37	7.09
Cr K	29.93	15.79
Mn K	4.33	2.16
Fe K	11.47	5.63
Ni K	8.91	4.16
Totals	100.0	

A8

	Wt%	At%
C K	4.27	15.13
O K	5.55	14.74
Si K	2.22	3.37
Ca K	0.27	0.29
Cr K	24.63	20.15
Fe K	17.40	13.25
Ni K	45.66	33.08
Totals	100.0	

A9

	Wt%	At%
C K	2.12	8.64
O K	1.97	6.01
Si K	1.42	2.47
Cr K	31.80	29.91
Fe K	17.64	15.44
Ni K	45.05	37.53
Totals	100.0	

A10

	Wt%	At%
C K	7.78	20.32
O K	17.92	35.15
Si K	5.22	5.83
Ca K	0.28	0.22
Cr K	25.24	15.23
Mn K	3.33	1.90
Fe K	10.78	6.05
Ni K	27.21	14.54
Nb L	2.24	0.76
Totals	100.0	

A11

	Wt%	At%
C K	1.87	7.75
O K	1.69	5.26
Si K	1.30	2.30
Cr K	33.20	31.76
Mn K	1.65	1.49
Fe K	16.65	14.82
Ni K	42.55	36.04
Nb L	1.09	0.58
Totals	100.0	

A12

	Wt%	At%
C K	1.60	6.68
O K	1.72	5.40
Si K	1.33	2.38
Cr K	32.98	31.78
Mn K	1.41	1.29
Fe K	16.79	15.06
Ni K	43.31	36.96
Nb L	0.85	0.46
Totals	100.0	

Figure 6.29 Further analysis to the layers formed within the attack area.

6.6.2 35Cr-45Ni-650ºC-500h

Prolonging the exposure time to 500h led to the formation of a higher concentration of pits, with a maximum size of approximately 13µm, which were randomly distributed across the alloy surface (Figure 6.30).

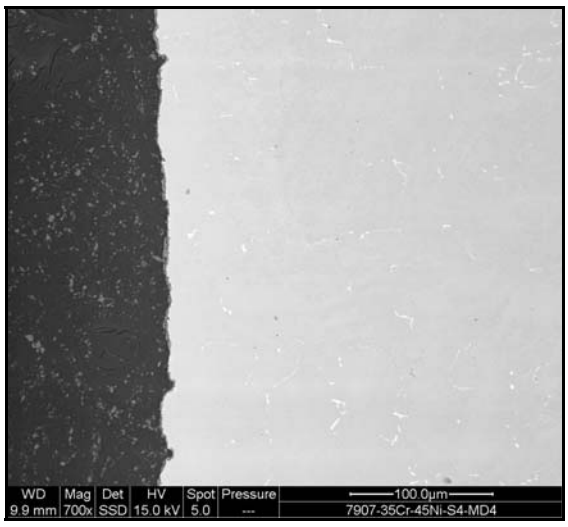

Figure 6.30 Pitting observed on the alloy surface after 500h at 650ºC.

A higher magnification image of one of the pits is shown in Figure 6.31. The pit was approximately 7µm deep and appeared to contain an isolated alloy portion. A layer of approximately 1µm had also developed on the alloy surface and found (A2) to contain a mixture of carbon and oxides of chromium, manganese, and silicon in addition to minor amounts of iron and nickel. Interestingly, there was no significant depletion of the oxide-forming elements detected in the substrate at the pit's bottom (A1).

A further investigation of the pit contents was carried out (Figure 6.32). It is obvious that the area around the pit was heavily carburised and carbides, as "strips", were observed to have precipitated. Also, the layers surrounding the alloy portion (A5 and A6) were analysed and found to contain carbon and oxides of chromium, silicon, and manganese. Considerable amounts of nickel and iron were also detected at the two areas. The analysis

of the alloy portion embedded in the pit indicated low levels of chromium and manganese (A4) suggesting that they had been consumed during oxidation. A higher magnification photomicrograph showing the reaction front and the degree of carburisation can be seen in Figure 6.33.

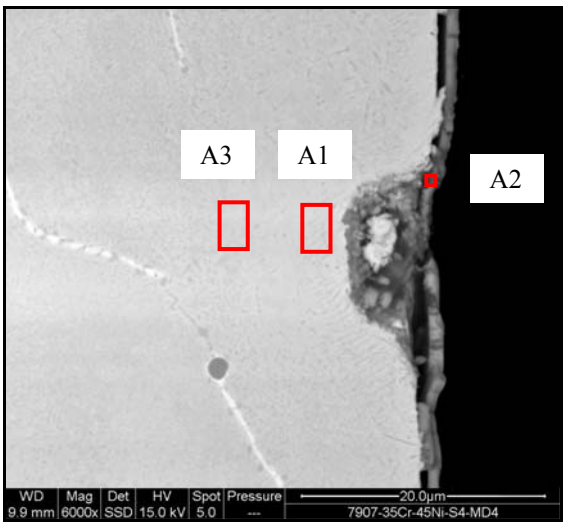

A1

Element	Wt%	At%
C K	1.57	6.60
O K	1.53	4.82
Si K	0.92	1.65
Cr K	31.17	30.29
Mn K	0.71	0.65
Fe K	18.52	16.76
Ni K	45.58	39.23
Totals	100.00	

A2

Element	Wt%	At%
C K	24.34	42.01
O K	28.91	37.46
Si K	6.17	4.56
Ca K	0.21	0.11
Cr K	33.11	13.20
Mn K	3.09	1.17
Fe K	1.75	0.65
Ni K	2.42	0.85
Totals	100.00	

A3

Element	Wt%	At%
C K	1.16	4.96
O K	1.50	4.80
Si K	1.01	1.85
Cr K	32.01	31.48
Mn K	1.10	1.02
Fe K	18.63	17.05
Ni K	44.59	38.84
Totals	100.00	

Figure 6.31 Investigation of one of the pits observed on alloy after 500h at 650°C.

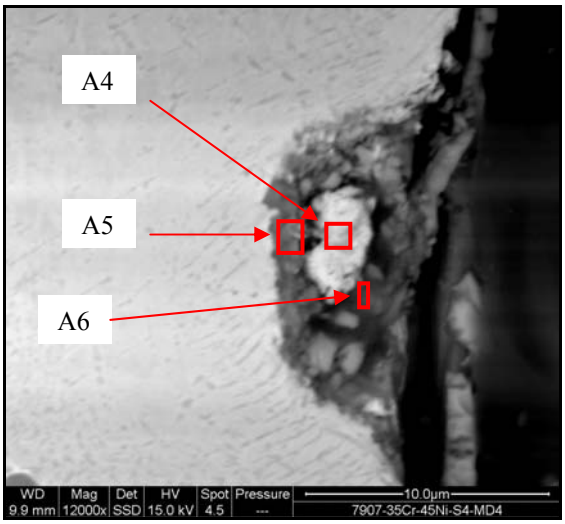

A4

Element	Wt%	At%
C K	3.68	13.99
O K	3.44	9.80
Si K	1.18	1.92
Cr K	22.72	19.93
Fe K	19.64	16.04
Ni K	49.33	38.32
Totals	100.00	

A5

Element	Wt%	At%
C K	28.78	44.62
O K	35.05	40.81
Si K	5.72	3.79
Ca K	0.25	0.12
Cr K	24.70	8.85
Mn K	2.26	0.76
Fe K	1.28	0.43
Ni K	1.97	0.62
Totals	100.00	

A6

Element	Wt%	At%
C K	8.14	17.34
O K	31.60	50.56
Si K	7.29	6.64
Cr K	39.02	19.21
Mn K	2.82	1.32
Fe K	3.32	1.52
Ni K	7.81	3.40
Totals	100.00	

Figure 6.32 Alloy portion detached at the pit.

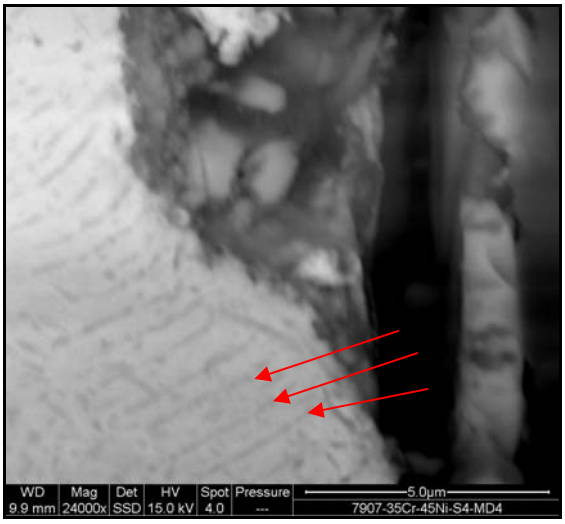

Figure 6.33 Carburisation (in form of parallel strips indicated by arrows) was observed at the substrate (under the pit).

6.6.3 35Cr-45Ni-650ºC-1000h

A layer of approximately 4µm maximum thickness had formed on the alloy as a result of exposure for 1000h at 650ºC (Figure 6.34). The layer was analysed (P1) and found to contain oxides of chromium, silicon, and manganese in addition to carbon.

Furthermore, localised attacks were observed on the alloy cross section where oxidation and carburisation seemed to have occurred simultaneously (Figure 6.35). Catastrophic localised oxidation was confirmed by EDX to have taken place at the corroded area (Figure 6.36). Heavy carburisation was also observed at the reaction zone, just below the localised oxidation. In addition, carbon was detected in considerable amounts within the oxides (P1 and P2).

Interestingly, a decarburised zone was also noticed at the substrate of another localised attack suggesting either a different corrosion mechanism or a different stage of the corrosion process (Figure 6.37). The carbide concentration at the reaction zone was less that that of the adjacent base metal. A higher magnification micrograph of the attack is shown in Figure 6.38. EDX analysis showed that the pit contents were mainly oxides, carbon, and carbides. Chromium carbide was detected at P1, P2, and P4 whereas chromium and manganese oxides were found at P5. Considerable carbon was also detected especially at the outer layer (P6). More silicon oxides were found to have formed internally (P3) in addition to chromium and manganese oxides. Significant concentrations of iron and nickel were also detected at this point.

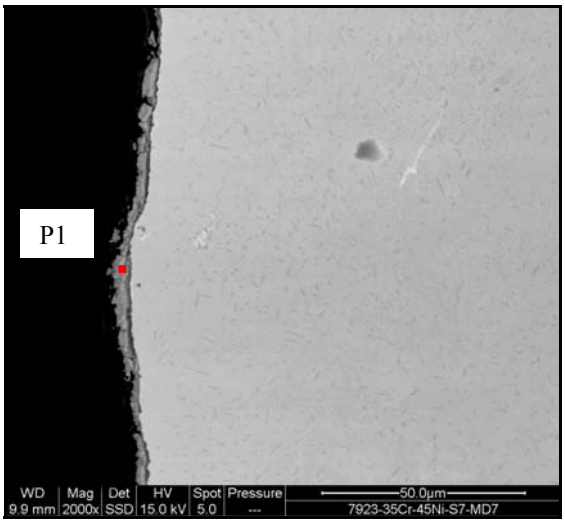

P1

Element	Wt%	At%
C K	3.91	8.20
O K	36.98	58.19
Si K	13.02	11.67
Ca K	0.49	0.31
Cr K	28.37	13.74
Mn K	17.23	7.89
Totals	100.00	

Figure 6.34 Oxide layer observed to form on the alloy after 1000h at 650ºC.

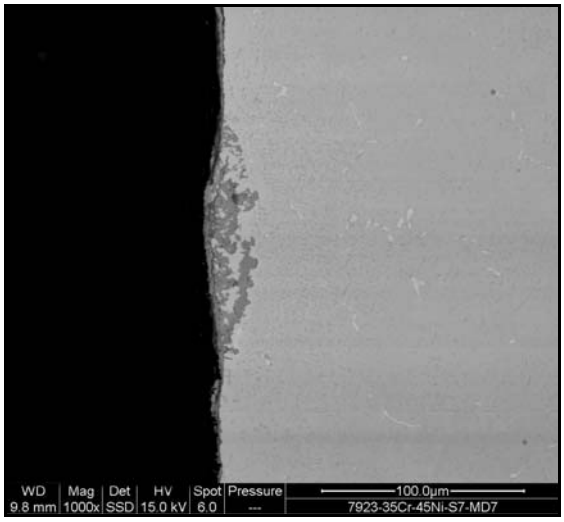

Figure 6.35 Localised attack seen on alloy cross section.

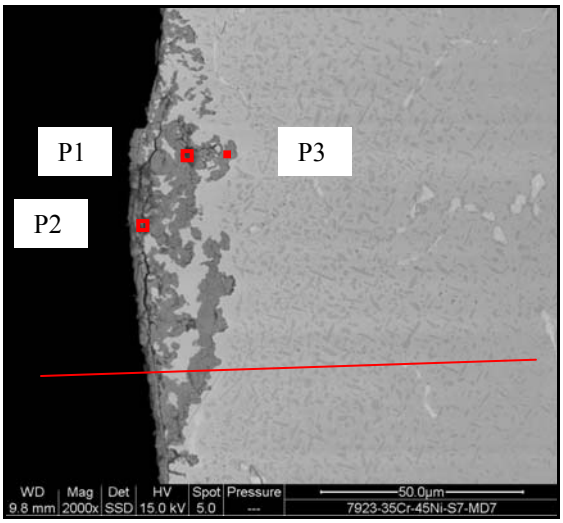

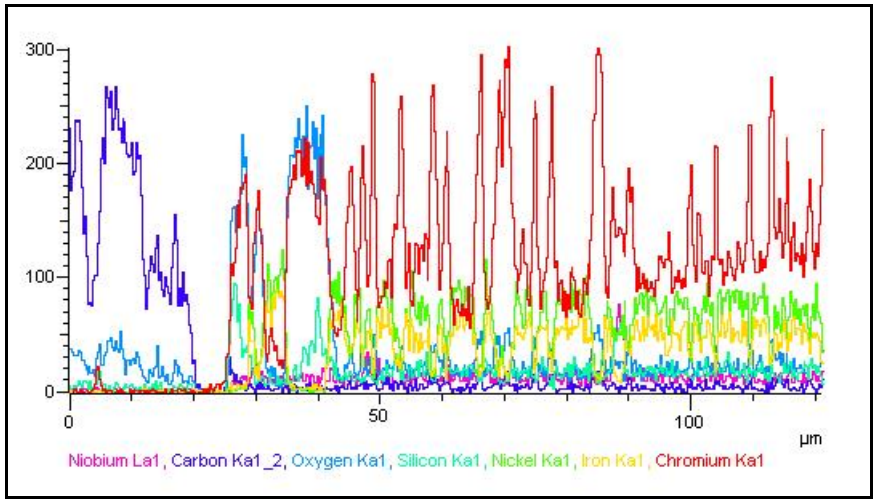

P1

Element	Wt%	At%
C K	12.09	27.05
O K	21.34	35.82
Na K	0.55	0.65
Mg K	0.50	0.55
Si K	5.01	4.80
S K	0.44	0.37
Ca K	2.27	1.52
Cr K	45.09	23.30
Mn K	1.61	0.79
Fe K	3.80	1.83
Ni K	7.30	3.34
Totals	100.00	

P2

Element	Wt%	At%
C K	7.30	16.06
O K	31.96	52.74
Na K	0.22	0.26
Si K	1.54	1.45
Ca K	0.41	0.27
Cr K	42.58	21.62
Mn K	11.19	5.38
Fe K	2.61	1.24
Ni K	2.18	0.98
Totals	100.00	

P3

Element	Wt%	At%
C K	1.07	2.49
O K	35.97	62.67
Na K	0.21	0.26
Si K	3.04	3.02
Cr K	55.03	29.51
Mn K	1.15	0.59
Fe K	0.72	0.36
Ni K	1.54	0.73
Nb L	1.27	0.38
Totals	100.00	

Figure 6.36 Analysis of the localised attack.

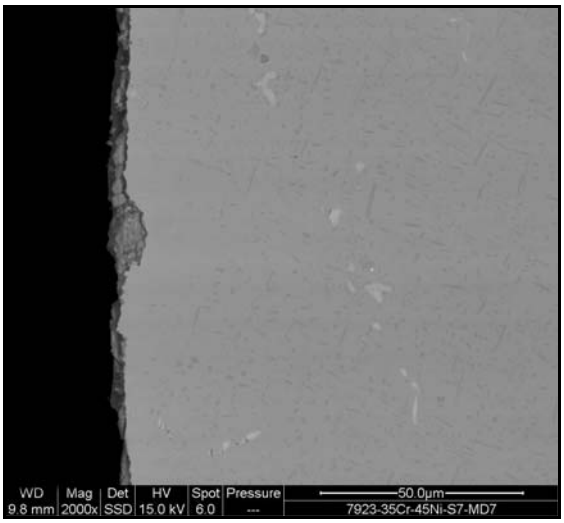

Figure 6.37 Another localised attack observed on the alloy after 1000h at 650ºC.

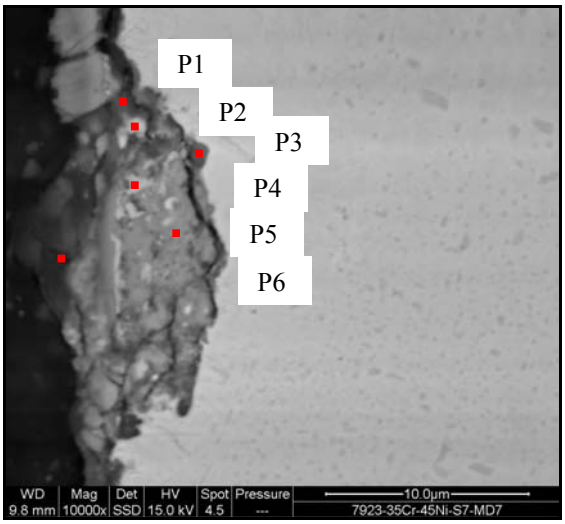

P1

Element	Wt%	At%
C K	8.44	23.74
O K	10.26	21.67
Si K	4.31	5.18
Ca K	1.30	1.10
Cr K	58.80	38.22
Mn K	6.71	4.13
Fe K	3.37	2.04
Ni K	6.81	3.92
Totals	100.00	

P2

Element	Wt%	At%
C K	12.65	29.99
O K	16.80	29.91
Si K	3.90	3.96
Ca K	0.61	0.43
Cr K	56.27	30.82
Mn K	2.56	1.32
Fe K	2.68	1.37
Ni K	4.53	2.20
Totals	100.00	

P3

Element	Wt%	At%
C K	2.97	6.85
O K	29.31	50.68
Si K	16.57	16.32
Ca K	0.68	0.47
Cr K	25.57	13.60
Mn K	6.41	3.23
Fe K	6.25	3.10
Ni K	12.24	5.77
Totals	100.00	

P4

Element	Wt%	At%
C K	8.07	23.08
O K	10.56	22.67
Si K	1.66	2.03
Cr K	72.65	47.99
Fe K	3.19	1.96
Ni K	3.86	2.26
Totals	100.00	

P5

Element	Wt%	At%
C K	2.74	6.59
O K	31.67	57.09
Si K	1.48	1.52
Cr K	41.29	22.90
Mn K	18.74	9.84
Fe K	2.02	1.05
Ni K	2.06	1.01
Totals	100.00	

P6

Element	Wt%	At%
C K	28.63	47.79
O K	24.46	30.66
Mg K	3.49	2.88
Al K	1.11	0.82
Si K	2.73	1.95
K K	0.48	0.24
Ca K	6.90	3.45
Cr K	22.10	8.52
Mn K	10.11	3.69
Totals	100.00	

Figure 6.38 Analysis of the content of the pit shown in Figure 6.37.

6.6.4 35Cr-45Ni-750ºC-100h

Two layers appeared on the alloy after 100h exposure at 750ºC (Figure 6.39). The layers were almost separated from the alloy although this may have been caused during sample preparation. EDX of the external layer, A1, which was around 1.5µm thick, confirmed the presence of carbon and oxides. The internal layer (A2), however, contained considerably less amounts of carbon but higher levels of oxide-forming elements such as chromium, manganese, and silicon.

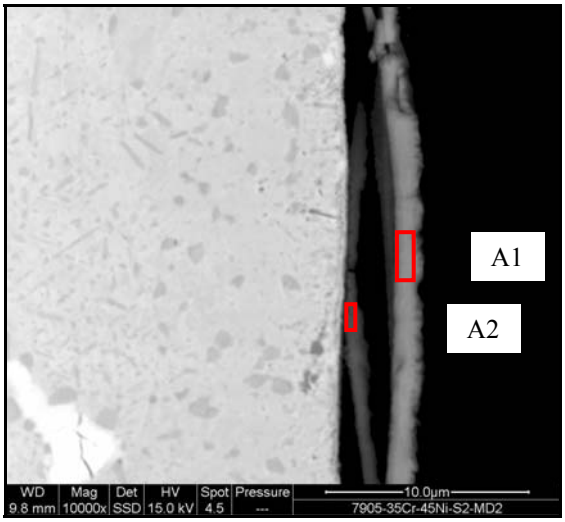

A1

Element	Wt%	At%
C K	32.76	46.48
O K	39.84	42.44
Mg K	0.17	0.12
Si K	7.65	4.64
Ca K	0.68	0.29
Cr K	9.52	3.12
Mn K	8.99	2.79
Ni K	0.40	0.12
Totals	100.00	

A2

Element	Wt%	At%
C K	13.23	22.98
O K	42.69	55.67
Si K	11.42	8.49
Ca K	0.71	0.37
Cr K	18.03	7.23
Mn K	12.44	4.72
Fe K	0.62	0.23
Ni K	1.00	0.35
Totals	100.00	

Figure 6.39 Specimen cross section after exposure at 750ºC for 100h.

Localised attack, approximately 7µm deep, was also observed on this sample (Figures 6.40 and 6.41). EDX of the areas, A1 and A2, was carried out to investigate any change in

the composition at the reaction zone. No significant reduction in scale-forming elements, particularly chromium, was detected meaning that only mild oxidation might have taken place at the pit bottom. Spherical chromium carbides were also observed at the reaction zone (A3). A higher magnification micrograph is shown in Figure 6.41 where the layer was further analysed. Three areas on the layer (A4, A5 and A6), which was approximately 1.2µm thick, were analysed and found to have different composition. For example, in the area A5, a high level of carbon (37.7 wt%) was detected whereas only a minor amount (2 wt%) was found at A6 and the same applied for chromium. EDX of the needle-like phase (A7) showed that it contained a high level of chromium suggesting that it was composed of chromium-containing carbides.

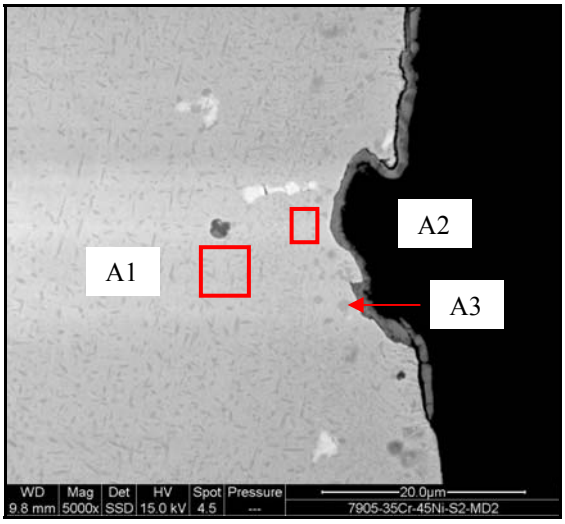

A1

Element	Wt%	At%
C K	1.41	5.90
O K	1.80	5.65
Si K	1.45	2.59
Cr K	32.59	31.49
Mn K	1.65	1.51
Fe K	17.09	15.38
Ni K	43.41	37.15
Nb L	0.60	0.33
Totals	100.00	

A2

Element	Wt%	At%
C K	2.35	8.76
O K	5.58	15.62
Si K	2.35	3.75
Cr K	29.86	25.74
Mn K	1.21	0.99
Fe K	16.26	13.05
Ni K	41.35	31.58
Nb L	1.04	0.50
Totals	100.00	

A3

Element	Wt%	At%
C K	1.34	5.30
O K	3.10	9.16
Si K	0.52	0.87
Ca K	0.29	0.34
Cr K	73.58	66.93
Fe K	8.26	7.00
Ni K	12.90	10.39
Totals	100.00	

Figure 6.40 Localised corrosion seen on the alloy after 100h at 750°C.

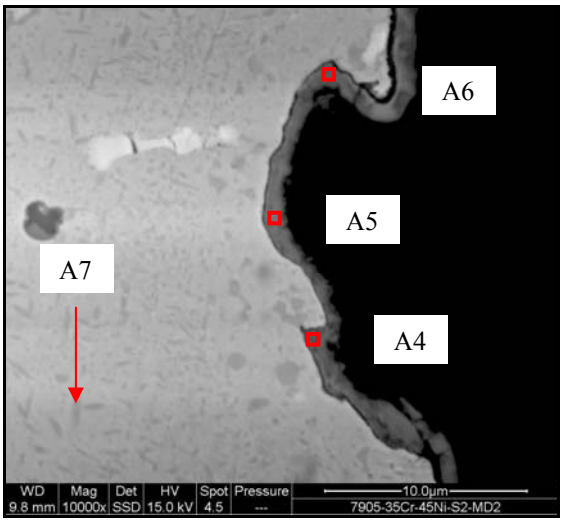

A4			A5			A6			A7		
	Wt%	At%		Wt%	At%		Wt%	At%		Wt%	At%
C K	6.42	13.87	C K	37.69	53.44	C K	2.00	5.73	C K	1.33	5.53
O K	32.10	52.00	O K	33.17	35.31	O K	18.84	40.52	O K	2.06	6.42
Mg K	0.17	0.18	Si K	6.97	4.22	Si K	7.52	9.21	Si K	0.91	1.61
Si K	9.69	8.95	Ca K	0.27	0.11	Ca K	0.30	0.26	Cr K	40.69	38.98
Ca K	0.50	0.32	Cr K	8.18	2.68	Cr K	28.62	18.94	Mn K	1.56	1.42
Cr K	29.91	14.91	Mn K	13.25	4.11	Mn K	4.02	2.52	Fe K	16.34	14.57
Mn K	10.99	5.19	Ni K	0.47	0.14	Fe K	9.93	6.12	Ni K	37.11	31.48
Fe K	3.29	1.53				Ni K	28.03	16.43			
Ni K	6.93	3.06				Nb L	0.73	0.27			
Totals	100.0		Totals	100.0		Totals	100.0		Totals	100.0	

Figure 6.41 Investigation of the pit's reaction front.

6.6.5 35Cr-45Ni-750ºC-500h

Larger pits were observed on the alloy as a consequence of increasing the exposure time to 500h (Figure 6.42). A higher magnification image of the pit is shown in Figure 6.43. The pit was approximately 25µm deep and was full of carbon. A layer, ~2µm thick, was also observed on the alloy surface. EDX of the carbon deposit (A1) detected no alloying elements or oxides. However, analysing the carbon near the substrate (A2) confirmed the presence of appreciable amounts of chromium, nickel, and iron. The layer developed on the alloy was also analysed (A3) and found to contain carbon as a main constituent. EDX of the substrate (A4), just beneath the pit bottom, revealed no depletion of oxide-forming elements suggesting only a little oxidation had taken place.

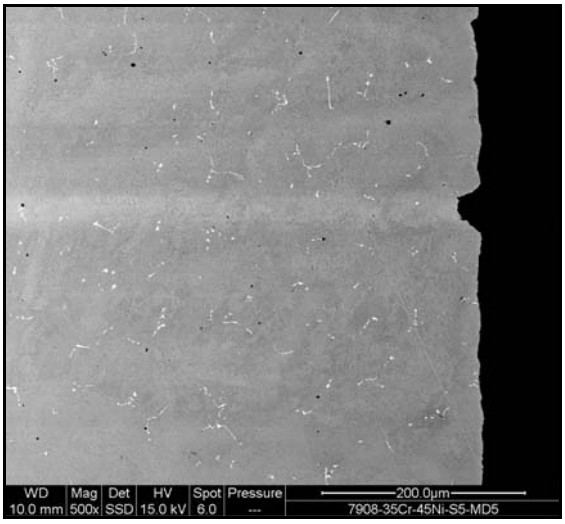

Figure 6.42 Pitting observed on the sample after 500h at 750ºC.

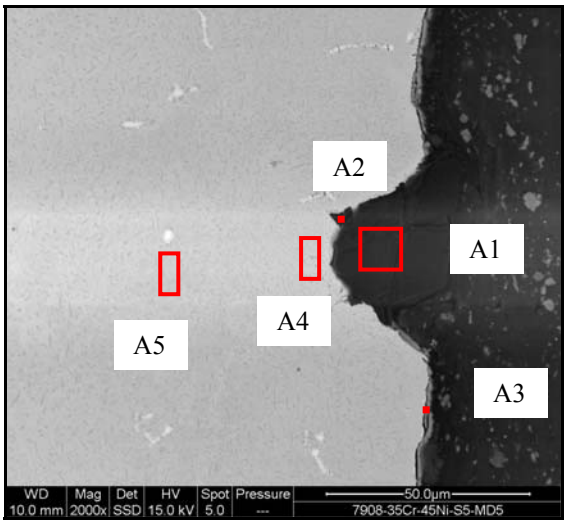

A1

Element	Wt%	At%
C K	95.32	96.44
O K	4.68	3.56
Totals	100.00	

A2

Element	Wt%	At%
C K	89.05	95.69
O K	3.03	2.45
Cr K	3.49	0.87
Fe K	1.70	0.39
Ni K	2.73	0.60
Totals	100.00	

A3

Element	Wt%	At%
C K	27.68	58.24
O K	7.21	11.39
Si K	2.03	1.83
Ca K	0.44	0.28
Cr K	18.42	8.95
Fe K	12.33	5.58
Ni K	31.88	13.72
Totals	100.00	

A4

Element	Wt%	At%
C K	3.01	11.98
O K	1.78	5.31
Si K	1.07	1.83
Cr K	32.34	29.75
Mn K	1.26	1.10
Fe K	17.29	14.81
Ni K	43.24	35.22
Totals	100.00	

A5

Element	Wt%	At%
C K	1.11	4.72
O K	1.79	5.68
Si K	1.23	2.23
Cr K	33.27	32.55
Mn K	1.23	1.14
Fe K	17.76	16.18
Ni K	42.73	37.03
Nb L	0.88	0.48
Totals	100.00	

Figure 6.43 EDX analysis to the pit content and reaction zone.

6.6.6 35Cr-45Ni-750ºC-1000h

Relatively shallow but wider pits were observed on the alloy after exposure for 1000h at 750ºC (Figure 6.44).

The layer formed on the alloy (A1 in Figure 6.45) was around 2.3µm thick and found to contain small amounts of oxide. The layer, instead, was rich with carbon and contained high levels of iron, nickel, and chromium. Analysing the substrate (A2) confirmed that it was not depleted of chromium suggesting a mild oxidation, if any, to have taken place on the alloy.

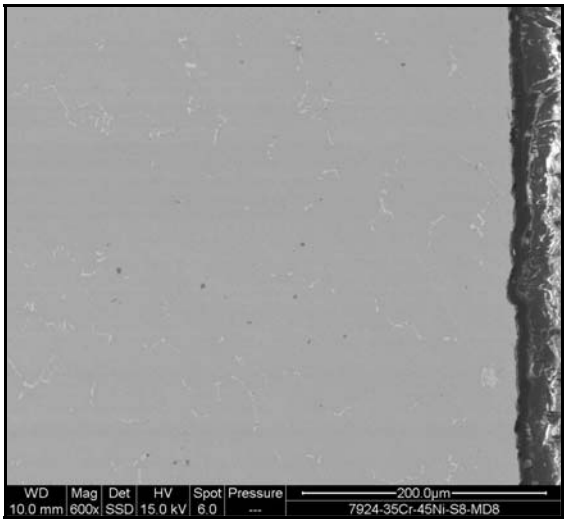

Figure 6.44 Alloy cross section after 1000h at 750ºC.

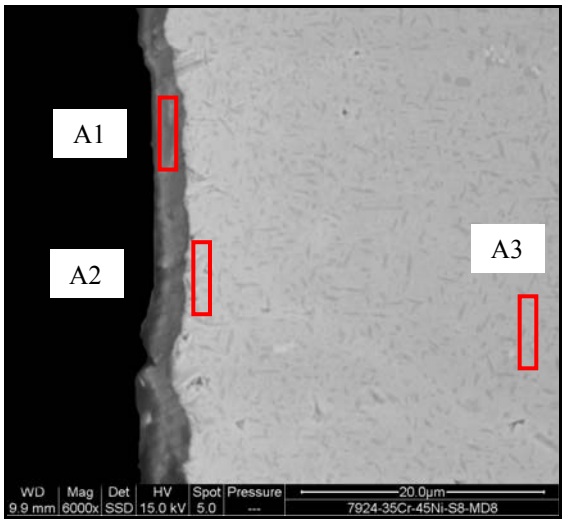

A1

Element	Wt%	At%
C K	18.07	49.04
O K	1.72	3.51
Si K	0.08	0.10
Ca K	0.36	0.29
Cr K	32.23	20.21
Mn K	2.68	1.59
Fe K	12.41	7.25
Ni K	32.45	18.02
Totals	100.00	

A2

Element	Wt%	At%
C K	2.67	10.80
O K	1.64	4.98
Si K	1.16	2.00
Cr K	30.41	28.46
Mn K	1.59	1.41
Fe K	17.20	14.98
Ni K	44.67	37.02
Nb L	0.67	0.35
Totals	100.00	

A3

Element	Wt%	At%
C K	1.77	7.33
O K	1.86	5.77
Si K	1.26	2.24
Cr K	33.46	31.98
Mn K	1.56	1.41
Fe K	16.81	14.96
Ni K	42.23	35.75
Nb L	1.04	0.56
Totals	100.00	

Figure 6.45 EDX analysis to the alloy reaction front.

6.6.7 35Cr-45Ni-850ºC-100h

As seen in Figure 6.46, the alloy experienced pitting after exposure to the gas mixture for 100h at 850ºC. A higher magnification image of two pits is shown in Figure 6.47. The maximum depth of the pits was approximately 8µm. The pits were randomly distributed across the specimen cross section. Examination of the pits revealed the presence of different layers that formed (or deposited) on the alloy surface.

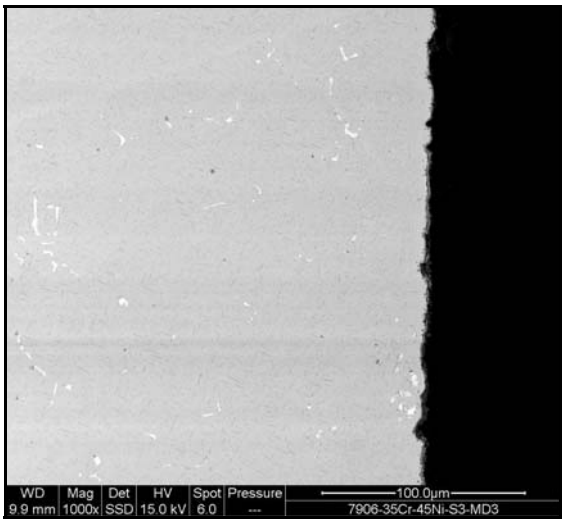

Figure 6.46 Pitting was seen on the alloy surface after 100h at 850ºC.

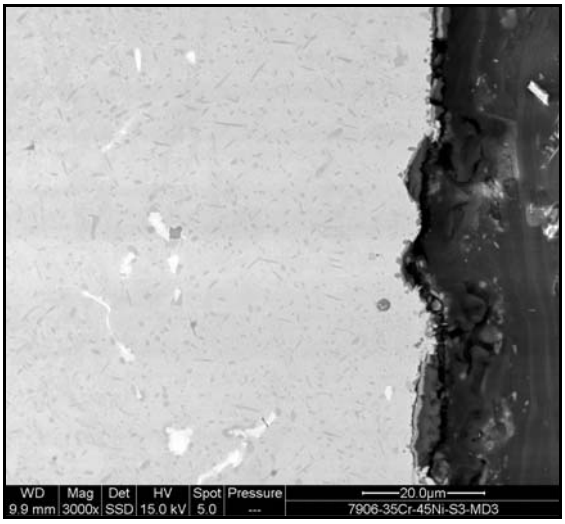

Figure 6.47 A higher magnification image of the pits.

Internal islands of oxides (A4 in Figure 6.48) were noticed to grow into the reaction zone at the bottom of the pits. These islands contained large amounts of chromium and manganese oxides. The layer formed in the pit bottom (A3) was also found to contain chromium and manganese oxides. Higher carbon levels were detected at the darker areas (A1 and A2). The area, A5, located between two oxide islands, was analysed and found to contain high concentration of chromium.

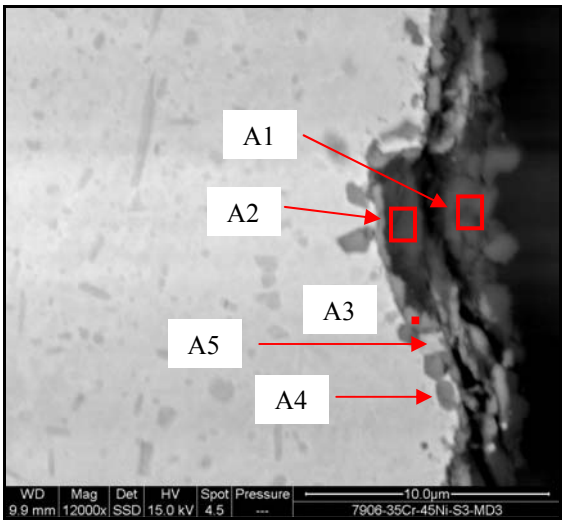

A1

Element	Wt%	At%
C K	29.53	39.39
O K	47.79	47.85
Mg K	0.24	0.16
Si K	21.59	12.31
Ca K	0.38	0.15
Cr K	0.47	0.15
Totals	100.00	

A2

Element	Wt%	At%
C K	4.12	6.49
O K	58.72	69.38
Si K	34.30	23.09
Ca K	0.16	0.07
Cr K	2.08	0.76
Mn K	0.62	0.21
Totals	100.00	

A3

Element	Wt%	At%
C K	1.48	3.35
O K	36.15	61.47
Si K	6.77	6.56
Ca K	0.33	0.22
Cr K	37.82	19.79
Mn K	15.73	7.79
Fe K	0.75	0.37
Ni K	0.96	0.45
Totals	100.00	

A4

Element	Wt%	At%
C K	1.51	3.89
O K	28.48	54.98
Si K	1.47	1.62
Ca K	0.26	0.20
Ti K	0.29	0.19
Cr K	38.44	22.83
Mn K	17.83	10.03
Fe K	3.89	2.15
Ni K	7.83	4.12
Totals	100.00	

A5

Element	Wt%	At%
C K	1.45	4.61
O K	13.86	33.12
Si K	0.95	1.29
Ca K	0.39	0.37
Cr K	70.90	52.12
Mn K	4.77	3.32
Fe K	5.27	3.61
Ni K	2.42	1.57
Totals	100.00	

Figure 6.48 EDX of a pit caused by exposure at 850°C for 100h.

Figure 6.49 shows a high magnification micrograph of the alloy substrate (not a pitting site) where two phases could be clearly seen. The layer, which was in total ~2.3µm thick, was analysed to identify the composition of the two phases. The darker, outer layer (A1) was composed mainly of carbon and silicon oxides. The inner layer (A2), however, comprised chromium, manganese, and silicon oxides with comparatively lower amount of carbon.

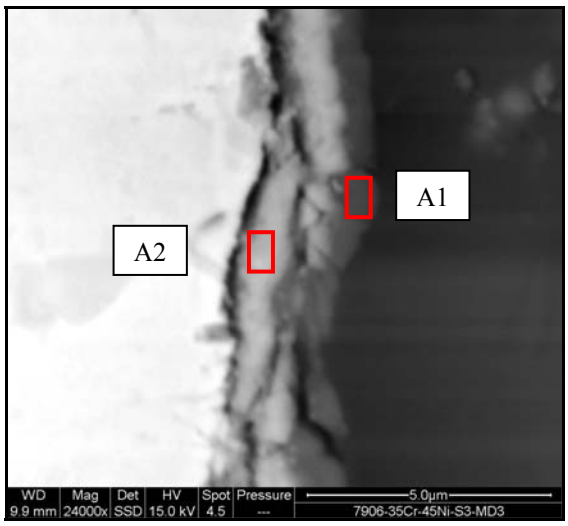

A1

Element	Wt%	At%
C K	45.48	56.34
O K	37.42	34.80
F K	0.98	0.77
Na K	0.17	0.11
Mg K	0.43	0.26
Al K	0.12	0.07
Si K	13.15	6.97
Ca K	0.53	0.20
Cr K	1.32	0.38
Mn K	0.39	0.11
Totals	100.00	

A2

Element	Wt%	At%
C K	8.15	15.69
O K	39.57	57.21
Si K	10.90	8.98
Ca K	0.33	0.19
Cr K	28.64	12.74
Mn K	10.71	4.51
Fe K	0.74	0.31
Ni K	0.96	0.38
Totals	100.00	

Figure 6.49 Layer formed on the alloy surface after 100h at 850ºC.

6.6.8 35Cr-45Ni-850ºC-500h

A micrograph of the cross section of the sample exposed for 500h at 850ºC is shown in Figure 6.50. Pitting was observed along the alloy cross section and the pits appeared to have different shapes and sizes. A higher magnification image of one of the pits is shown in Figure 6.51. EDX of the pit contents (A1) showed the presence of minor amounts of chromium, iron, and nickel.

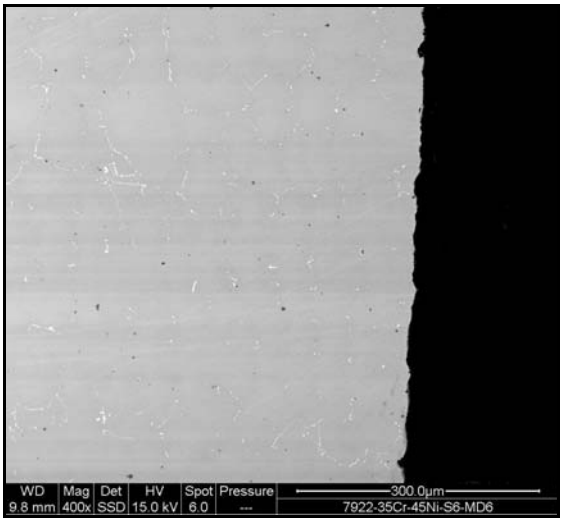

Figure 6.50 Cross section of the alloy after 500h at 850ºC.

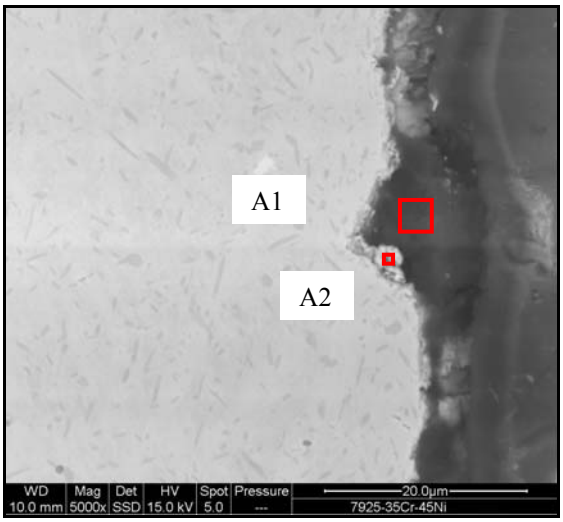

A1

Element	Wt%	At%
C K	76.55	84.35
O K	16.57	13.70
Al K	0.18	0.09
Si K	0.72	0.34
S K	0.20	0.08
Ca K	0.53	0.17
Cr K	2.16	0.55
Fe K	1.55	0.37
Ni K	1.56	0.35
Totals	100.00	

A2

Element	Wt%	At%
C K	31.33	63.58
O K	5.39	8.21
Si K	1.27	1.10
Ca K	0.24	0.15
Cr K	20.71	9.71
Mn K	1.08	0.48
Fe K	11.39	4.97
Ni K	28.18	11.70
Nb L	0.41	0.11
Totals	100.00	

Figure 6.51 Analysis of a pit formed on the alloy.

6.6.9 35Cr-45Ni-850ºC-1000h

Similarly, the sample exposed for 1000h at 850ºC exhibited pitting (Figure 6.52). A micrograph of localised corrosion, which was also seen on the sample, is shown in Figure 6.53. It seemed that the alloy suffered localised catastrophic oxidation in addition to carburisation. It is worth noting that although a relatively high concentration of carbides was observed surrounding the attack area, a decarburised zone could also be seen at the substrate. This may suggest the occurrence of a simultaneous oxidation and carburisation process.

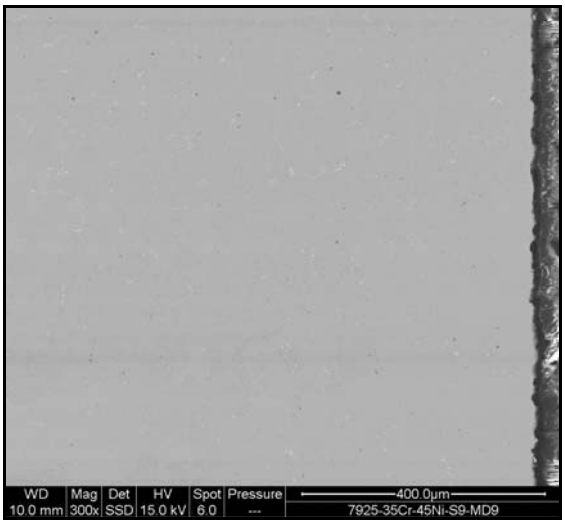

Figure 6.52 Cross section of the alloy after 1000h at 850ºC.

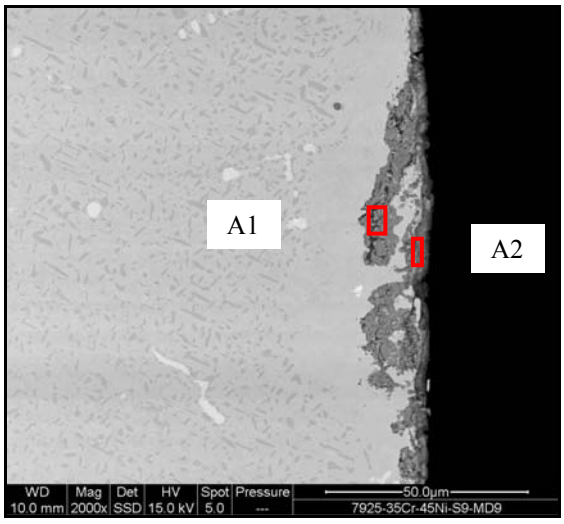

A1

Element	Wt%	At%
C K	2.50	5.71
O K	34.68	59.40
Si K	4.39	4.28
Cr K	53.24	28.06
Mn K	3.62	1.81
Ni K	1.57	0.73
Totals	100.00	

A2

Element	Wt%	At%
C K	12.37	38.22
O K	1.35	3.14
Si K	1.47	1.94
Ca K	0.67	0.62
Cr K	27.56	19.67
Mn K	1.28	0.86
Fe K	18.17	12.07
Ni K	37.14	23.48
Totals	100.00	

Figure 6.53 Localised corrosion observed to take place.

7 EVALUATION OF ALLOY UCX PERFORMANCE IN METAL DUSTING CONDITIONS

This chapter presents the findings relating to the performance of the nickel-based alloy, UCX, that had been exposed to the gas mixture at 650, 750, and 850ºC for periods of 100, 500, and 1000 hours.

7.1 Visual Examination

7.1.1 UCX Tested at 650ºC

Photos of the alloy after the removal from the furnace are shown in Figure 5.1 (Chapter 5).

Visual inspection of the sample subjected to the gas mixture for 100h at 650ºC revealed extremely low carbon deposition. However, increasing the exposure time to 500h resulted in an accumulation of a blackish layer that appeared to cover the entire specimen surface. An apparently thicker, denser, blackish layer had formed on the alloy as consequence of extending the exposure time to 1000h.

Photos of the samples after cleaning are shown in Figure 7.1. The alloy surface had become darker as the exposure time was increased suggesting the formation of more adherent carbon layers.

(a) Alloy condition after 100h

(b) Alloy condition after 500h

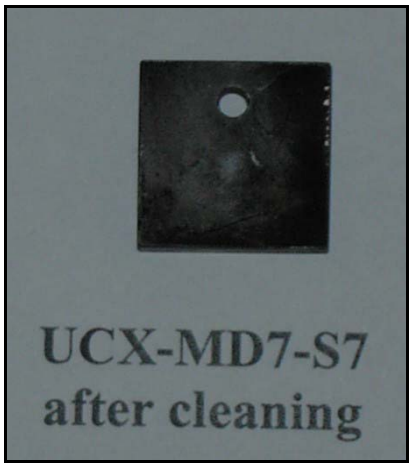

(c) Alloy condition after 1000h

Figure 7.1 Photos of the alloy after exposed at 650°C after cleaning.

7.1.2 UCX Tested at 750ºC

Figure 5.3 (Chapter 5) shows the alloys after removal from the furnace. Mild carbon deposition was observed on the sample following the 100h experiment. A blackish layer, however, was seen on the specimen exposed for 500h. The sample exposed for 1000h was covered with light grey and dark grey layers.

Figure 7.2 shows the samples after cleaning. The alloy experienced more adherent carbon deposition after 500 and 1000h. Indeed, the sample tested for 500h showed the most carbon accumulation although that might be attributed to the inversion of the sample order where UCX became the first to experience the gas mixture (i.e. during the 500h experiment). This behaviour is discussed further in Chapter 8.

7.1.3 UCX Tested at 850ºC

Photographs of the samples after the removal from the furnace are shown in Figure 5.5 (Chapter 5). A grey layer, which had been lighter in some places, was observed to have formed on the sample exposed for 100h. Extending the experiment time to 500h resulted in the formation of a distinctive green layer on the alloy surface. In addition, some whitish deposits were also observed in some places on the surface. Considerable growth of carbon had also taken place on the sample side that was the first to see the gas. After exposure for 1000h, the alloy formed a very greenish layer which seemed to have spalled off after cooling. Photos of the samples after cleaning are shown in Figure 7.3.

(a) Alloy condition after 100h

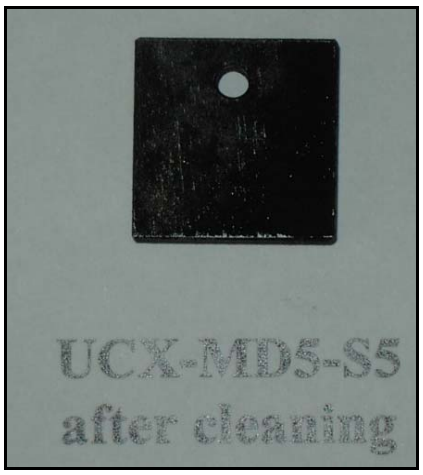

(b) Alloy condition after 500h

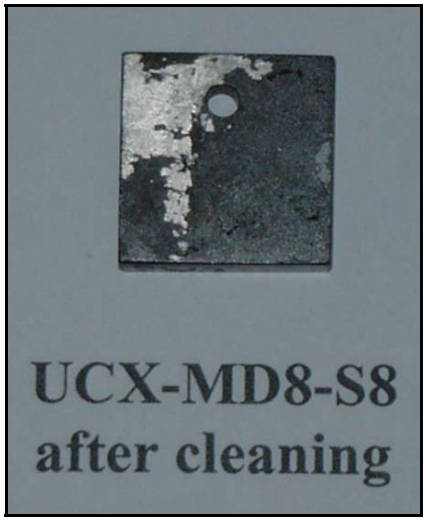

(c) Alloy condition after 1000h

Figure 7.2 Photos of the alloy after exposed at 750ºC after cleaning.

(a) Alloy condition after 100h

(b) Alloy condition after 500h

(c) Alloy condition after 1000h

Figure 7.3 The alloy after exposed at 850ºC after cleaning.

7.2 Weight Change Measurements

The weight change measurements showed that the samples experienced weight gain in most experiments (Table 7.1). Weight loss, however, was observed on the sample exposed at 850ºC for 1000h.

Table 7.1 Weight change (mg/cm^2) of the alloy after the exposure at different temperatures for different periods of time.

Temperature (ºC)	100h	500h	1000h
650	0.1696	0.5072	0.4541
750	0.4358	1.3245	0.5104
850	0.2677	0.3818	-0.8227

7.3 X ray Diffraction Results

XRD of the alloy after exposure at 650ºC for 100h showed the presence of carbon and chromium and iron-containing carbides. Chromium-containing carbides, Cr_2O_3, and silicon oxide were found on the sample exposed for 500h at the same temperature. The deposit removed from this sample contained carbon, Cr_2O_3, silicon oxide, Fe_2O_3, and tungsten carbides. Increasing the test time to 1000h resulted in the formation of chromium-iron carbides on the alloy surface.

Chromium-iron carbides had formed on the alloy as a result of the exposure at 750ºC for 100h. Extending the exposure time to 500h resulted in the formation of $Cr_{1.3}Fe_{0.7}O_4$, $Cr_{1.5}Mn_{1.5}O_4$, silicon oxides, and chromium-iron carbides on the alloy surface. Prolonging the experiment interval to 1000h led to the formation of chromium-iron carbides.

Chromium-iron carbides formed on the sample as a consequence of exposure at 850ºC for 100h. However, $CrMn_{1.5}O_4$, carbon, Cr_2NiO_4, chromium and chromium-iron carbides were detected after increasing the exposure time to 500h. Deposits removed from this sample contained silicon oxide, magnetite, and carbon. Increasing the experiment time further, to 1000h, led to the formation of chromium-iron carbides on the sample surface.

7.4 SEM/EDX Deposits Analysis

Enough deposits were only found on the specimens exposed at 650ºC for 500h and at 850ºC for 500h.

7.4.1 UCX-650ºC-500h

The deposit removed from this sample contained traces of iron and nickel (Figure 7.4). However, the main elements detected in the deposit were carbon, silicon, and oxygen.

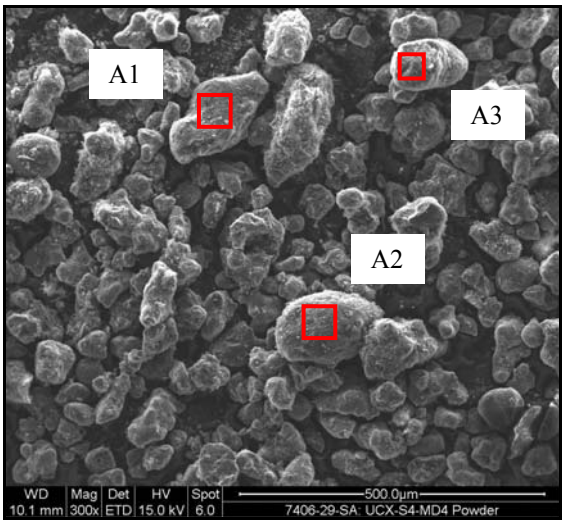

A1

Element	Wt%	At%
C K	69.95	79.09
O K	18.09	15.36
Si K	11.03	5.33
Fe K	0.46	0.11
Ni K	0.47	0.11
Totals	100.00	

A2

Element	Wt%	At%
C K	68.18	77.49
O K	19.50	16.64
Si K	11.87	5.77
Ni K	0.45	0.10
Totals	100.00	

A3

Element	Wt%	At%
C K	68.28	77.16
O K	20.96	17.78
Si K	10.20	4.93
Ni K	0.56	0.13
Totals	100.00	

Figure 7.4 EDX of deposits removed from the alloy surface after 500h at 650ºC.

7.4.2 UCX-850ºC-500h

SEM image of the deposit collected from the alloy after exposure at 850ºC for 500h is shown in Figure 7.5. The deposit resembled flakes and contained “chip”-like portions that were confirmed (A1) to contain high amounts of chromium and carbon suggesting they were essentially chromium carbides. Small amounts of titanium, nickel, iron, silicon, and oxygen were also found at that area. The other areas (A2 and A3) on the deposit were composed mainly of carbon and silicon oxides.

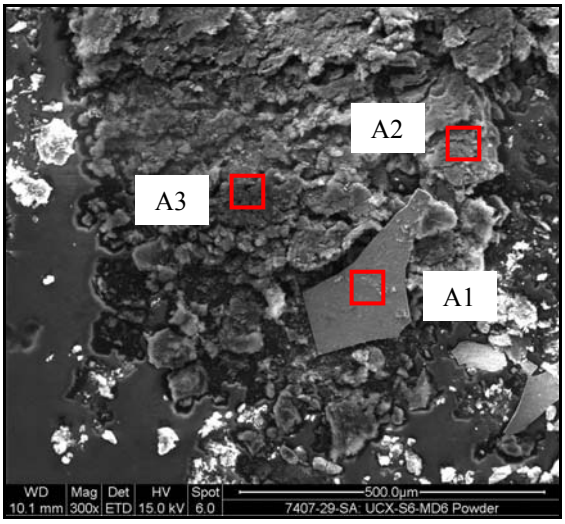

A1

Element	Wt%	At%
C K	15.93	40.38
O K	7.51	14.29
Si K	1.34	1.45
Ti K	0.50	0.32
Cr K	71.46	41.85
Fe K	0.64	0.35
Ni K	2.62	1.36
Totals	100.00	

A2

Element	Wt%	At%
C K	75.78	82.53
O K	17.59	14.38
Si K	6.62	3.08
Totals	100.00	

A3

Element	Wt%	At%
C K	87.25	91.20
O K	9.20	7.22
Si K	3.55	1.59
Totals	100.00	

Figure 7.5 EDX of deposits removed from the alloy surface after 500h at 850ºC.

7.5 Surface Analyses

7.5.1 UCX-650ºC-100h

Figures 7.6 and 7.7 show the surface of the alloy after exposure at 650ºC for 100h. The alloy was completely covered with a layer that was analysed and found to be composed of oxides of chromium, silicon, and manganese (A3 in Figure 7.6). Considerable amounts of nickel (11.9 wt%) and iron (1.8 wt%) were also detected. Some deposit islands that seemed to be residuals from an external layer, which was possibly removed by cleaning, were also analysed (A1 and A2) and found to have carbon as the main constituent with comparatively low oxygen levels.

The alloy surface beneath the layer could not be examined as no area was found exposed. Indeed, the layer chemical composition has varied from one place to the other (A2 and A3 in Figure 7.7). More carbon was detected mixing with the oxides at A2 unlike that found at A3 where more oxides had developed.

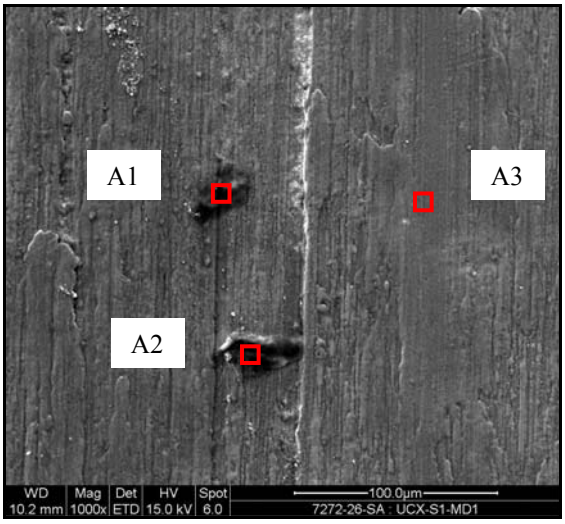

A1

Element	Wt%	At%
C K	42.07	58.45
N K	11.11	13.24
O K	15.10	15.76
Na K	0.46	0.34
Si K	7.66	4.55
S K	0.30	0.16
Cl K	0.48	0.23
K K	0.23	0.10
Ca K	0.27	0.11
Cr K	18.60	5.97
Mn K	2.42	0.73
Ni K	1.29	0.37
Totals	100.00	

A2

Element	Wt%	At%
C K	35.79	64.75
O K	5.54	7.53
Na K	0.38	0.36
Si K	9.11	7.05
S K	0.38	0.26
Cl K	0.67	0.41
Ca K	0.23	0.13
Cr K	34.43	14.39
Mn K	4.52	1.79
Fe K	1.28	0.50
Ni K	7.67	2.84
Totals	100.00	

A3

Element	Wt%	At%
C K	0.86	1.99
O K	34.21	59.21
Si K	11.46	11.30
Cr K	32.92	17.53
Mn K	6.90	3.48
Fe K	1.76	0.88
Ni K	11.88	5.61
Totals	100.00	

Figure 7.6 The alloy surface after 100h at 650°C.

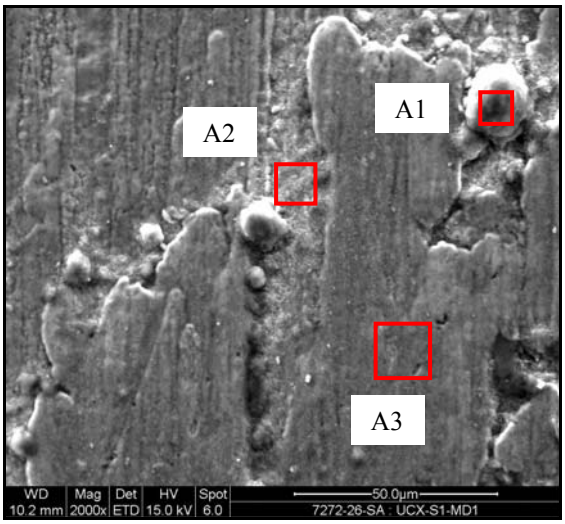

A1

Element	Wt%	At%
C K	48.82	60.40
O K	32.53	30.21
Na K	0.26	0.17
Si K	15.92	8.42
S K	0.29	0.14
Cl K	0.25	0.10
K K	0.14	0.05
Ca K	0.26	0.10
Cr K	0.73	0.21
Fe K	0.41	0.11
Ni K	0.39	0.10
Totals	100.00	

A2

Element	Wt%	At%
C K	18.99	34.39
O K	29.42	39.99
Na K	0.22	0.21
Al K	0.37	0.30
Si K	11.57	8.96
Ca K	0.21	0.11
Cr K	28.37	11.87
Mn K	5.32	2.11
Fe K	0.66	0.26
Ni K	4.87	1.80
Totals	100.00	

A3

Element	Wt%	At%
C K	3.33	7.22
O K	35.39	57.57
Si K	12.17	11.28
Cr K	33.80	16.92
Mn K	6.77	3.21
Fe K	0.94	0.44
Ni K	7.59	3.37
Totals	100.00	

Figure 7.7 A higher magnification image of the alloy surface.

7.5.2 UCX-650ºC-500h

Two layers (A2 and A3) formed on the alloy as a result of increasing the exposure time to 500h (Figure 7.8). Islands, rich with carbon and silica, were also observed to form on the alloy (A1). More than 50 wt% carbon was detected in the outer layer (A2) whilst only 11.8 wt% was found in the inner layer (A3). The decrease in the carbon level was accompanied by a significant increase in the oxide level. A higher magnification image of the inner layer which contained predominantly chromium oxide is shown in Figure 7.9.

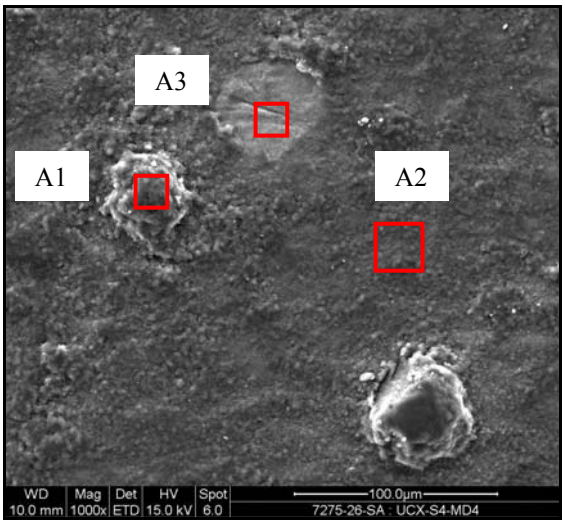

A1

Element	Wt%	At%
C K	59.31	70.97
O K	22.38	20.11
Si K	15.84	8.10
S K	0.41	0.18
Cl K	0.23	0.09
Ca K	0.70	0.25
Cr K	0.44	0.12
Ni K	0.69	0.17
Totals	100.00	

A2

Element	Wt%	At%
C K	52.75	68.57
O K	19.76	19.28
Si K	15.08	8.38
S K	0.30	0.15
Cl K	0.19	0.08
Cr K	10.47	3.14
Mn K	0.47	0.13
Ni K	0.98	0.26
Totals	100.00	

A3

Element	Wt%	At%
C K	11.84	23.15
O K	34.04	49.98
Si K	6.53	5.46
Cr K	44.58	20.14
Mn K	2.26	0.97
Ni K	0.76	0.31
Totals	100.00	

Figure 7.8 UCX surface after 500h at 650ºC.

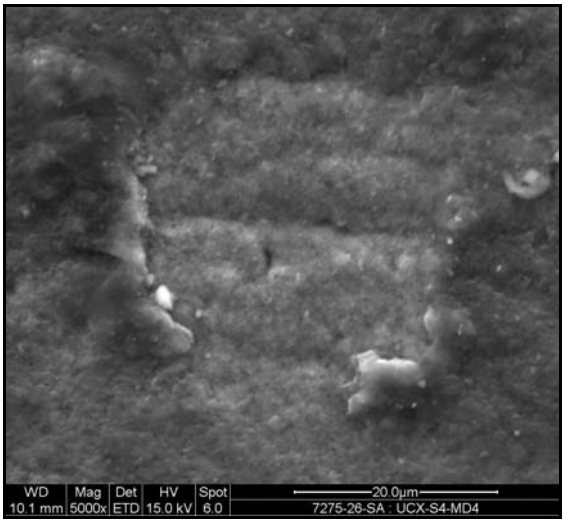

Figure 7.9 A higher magnification image of the inner layer.

7.5.3 UCX-650ºC-1000h

A thick layer formed on the alloy as a consequence of increasing the test time to 1000h (Figure 7.10). The layer (A1) contained a mixture of carbon and oxides of mainly chromium and silicon. Unlike the previous samples (tested for 100h and 500h), the underlying alloy surface was exposed (A2). EDX of that layer showed a low chromium content (27 wt%) that was much lower than that of the base metal (40.4 wt%) suggesting the occurrence of severe chromium depletion due to oxidation.

Pitting was also seen on the alloy surface (Figure 7.11), and more interestingly, the pits appeared to be distributed, in a distinctive manner, along what seemed to be the grain boundaries. The areas near the pits were confirmed to be chromium carbides (Figure 7.12). Figure 7.13 shows a higher magnification image of one of the pits.

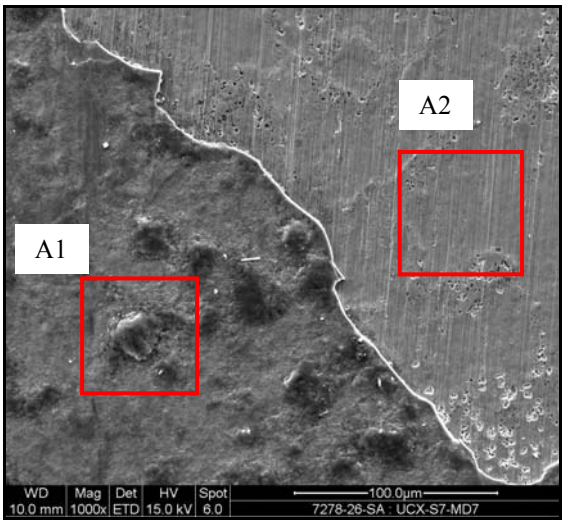

A1

Element	Wt%	At%
C K	30.08	46.64
O K	30.07	35.01
Si K	13.42	8.90
Ca K	0.14	0.07
Cr K	25.05	8.97
Mn K	0.61	0.21
Ni K	0.63	0.20
Totals	100.00	

A2

Element	Wt%	At%
C K	2.86	10.90
O K	3.80	10.88
Si K	3.93	6.42
Cr K	27.05	23.83
Fe K	6.00	4.92
Ni K	54.64	42.63
W M	1.71	0.43
Totals	100.00	

Figure 7.10 The alloy surface after 1000h at 650ºC.

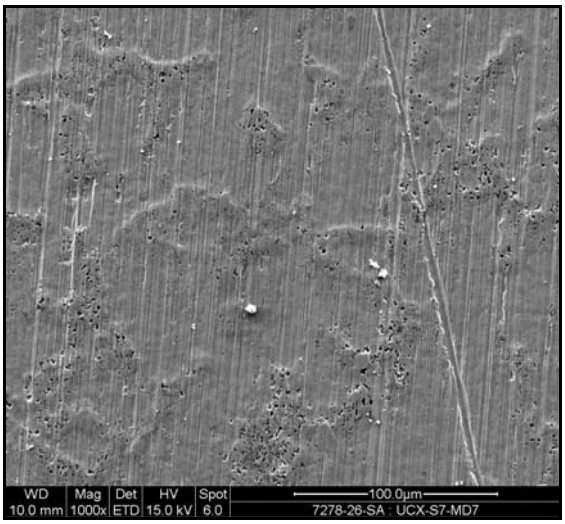

Figure 7.11 Pits observed along the grain boundaries.

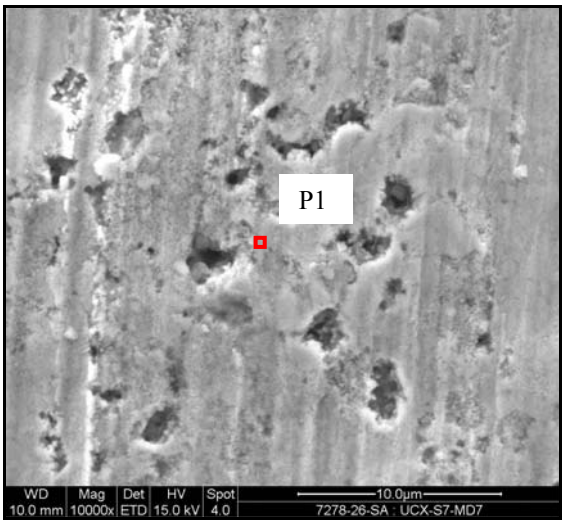

P1

Element	Wt%	At%
C K	4.70	16.49
O K	2.97	7.81
Si K	3.53	5.30
Cr K	71.84	58.22
Ni K	16.96	12.17
Totals	100.00	

Figure 7.12 Areas adjacent to the pits confirmed to be chromium carbides.

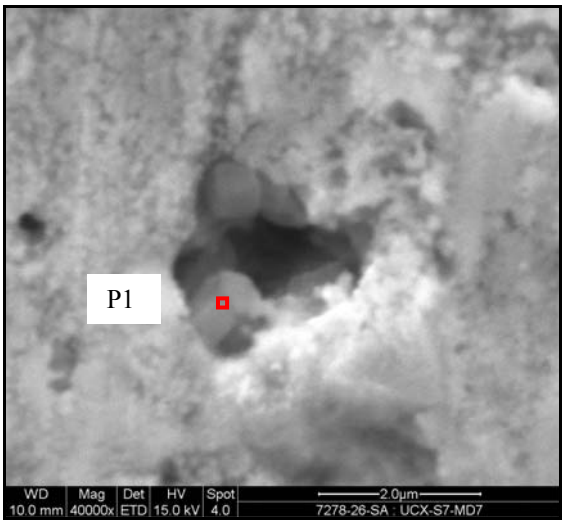

P1

Element	Wt%	At%
C K	17.24	33.37
O K	27.79	40.39
Si K	3.04	2.51
Ca K	12.29	7.13
Cr K	16.48	7.37
Fe K	2.17	0.90
Ni K	21.00	8.32
Totals	100.00	

Figure 7.13 A higher magnification image of a pit.

7.5.4 UCX-750ºC-100h

Exposing the alloy at 750ºC for 100h resulted in the formation of an oxide-rich layer (A1 in Figure 7.14). Carbon at low levels was also detected at this area. Only small areas of the underlying alloy surface were exposed (A2) with no significant pitting noticed at these sites. The chromium percentage at the surface was low compared to the chromium level of the base metal.

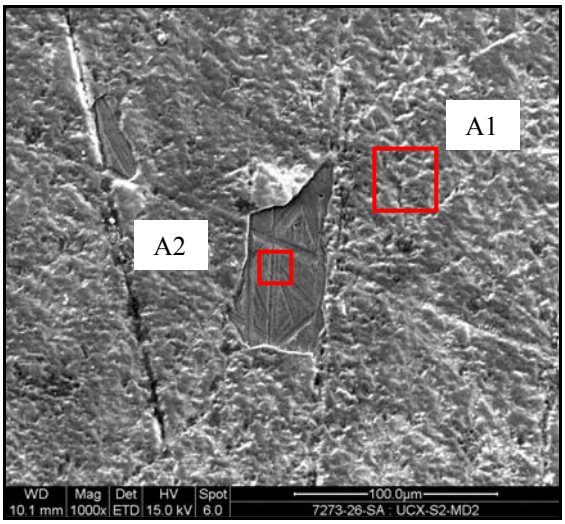

A1

Element	Wt%	At%
C K	6.65	12.91
O K	39.74	57.96
Si K	13.61	11.31
Cr K	35.19	15.79
Mn K	4.04	1.71
Ni K	0.77	0.31
Totals	100.00	

A2

Element	Wt%	At%
C K	4.55	15.52
O K	6.24	15.96
Si K	5.02	7.32
Cr K	25.91	20.40
Fe K	5.28	3.87
Ni K	52.99	36.94
Totals	100.00	

Figure 7.14 The alloy surface after 100h at 750ºC.

7.5.5 UCX-750ºC-500h

The alloy, after exposure at 750ºC for 500h, is shown in Figure 7.15. A layer that contained a mixture of oxides and carbon had formed on the surface (A1). The underlying surface was also analysed (A2).

Compositional variation in the layer was also observed (Figure 7.16). In A1, for example, EDX showed considerably higher levels of chromium and manganese oxides compared to those detected at A2.

A higher magnification image of the bare alloy surface revealed the presence of pitting (Figure 7.17). EDX of the pits content (A1 and A2) showed almost the same composition as that of the near surface (A3). These analyses did not detect any manganese suggesting that all the manganese content at the substrate was consumed during oxidation. The chromium concentration was also found relatively low (28.5 wt%) as some had been consumed during the oxidation process.

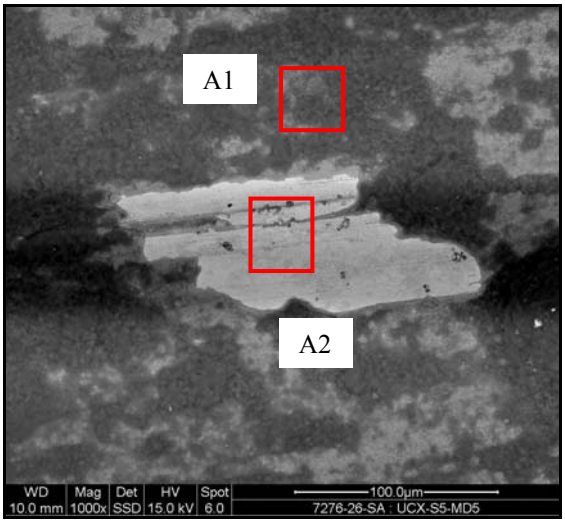

A1

Element	Wt%	At%
C K	27.92	42.21
O K	33.17	37.64
Si K	22.19	14.34
Cr K	14.83	5.18
Mn K	1.90	0.63
Totals	100.00	

A2

Element	Wt%	At%
C K	3.57	12.47
O K	6.53	17.14
Si K	4.86	7.27
Cr K	28.50	23.03
Fe K	5.33	4.01
Ni K	50.05	35.81
W M	1.16	0.27
Totals	100.00	

Figure 7.15 Alloy surface after 500h at 750ºC.

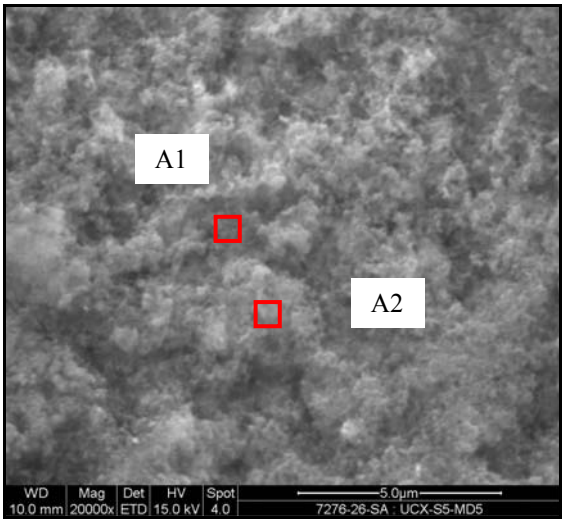

A1

Element	Wt%	At%
C K	17.02	30.48
O K	34.03	45.75
Si K	10.35	7.93
Cr K	33.63	13.91
Mn K	4.25	1.66
Ni K	0.72	0.26
Totals	100.00	

A2

Element	Wt%	At%
C K	19.59	31.90
O K	38.94	47.60
Si K	15.54	10.82
Cr K	23.18	8.72
Mn K	2.29	0.82
Ni K	0.46	0.15
Totals	100.00	

Figure 7.16 Compositional variation across the layer.

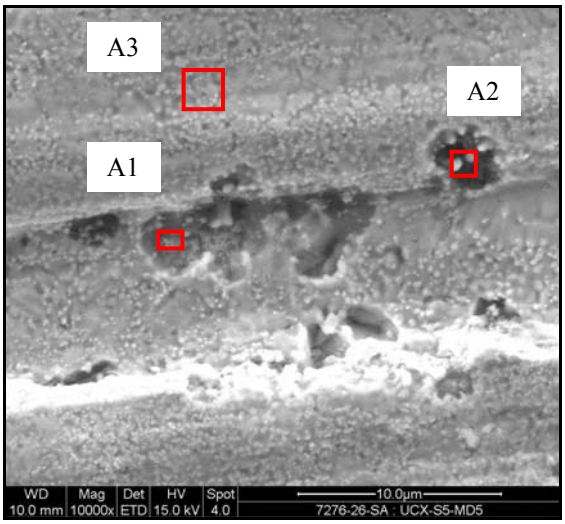

A1

Element	Wt%	At%
C K	1.84	6.37
O K	8.69	22.55
Si K	6.78	10.03
Cr K	25.96	20.73
Fe K	5.27	3.92
Ni K	51.46	36.40
Totals	100.00	

A2

Element	Wt%	At%
C K	1.46	5.72
O K	3.77	11.11
Si K	4.19	7.03
Cr K	32.41	29.37
Fe K	4.87	4.11
Ni K	52.86	42.44
Zr L	0.44	0.23
Totals	100.00	

A3

Element	Wt%	At%
C K	1.58	5.56
O K	8.48	22.48
Al K	0.24	0.38
Si K	6.28	9.48
Cr K	25.06	20.43
Fe K	5.41	4.10
Ni K	51.57	37.24
W M	1.38	0.32
Totals	100.00	

Figure 7.17 Pitting observed on the alloy surface after 500h at 750ºC.

7.5.6 UCX-750ºC-1000h

The layer formed on the alloy (A2) after 1000h at 750ºC was found to contain mainly chromium and silicon oxides in addition to carbon (Figure 7.18). Pitting was also observed on the alloy surface underneath (Figures 7.19 and 7.20). The detection of higher levels of chromium and tungsten at the pit (A1 in Figure 7.20) compared to the area nearby (A2) may imply that the pitting area was originally rich with chromium-containing carbides.

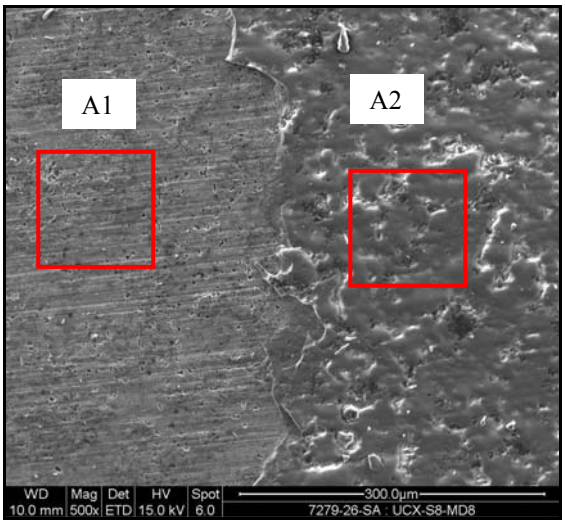

A1

Element	Wt%	At%
C K	2.26	7.70
O K	8.94	22.80
Si K	7.07	10.29
Ti K	0.32	0.27
Cr K	34.67	27.22
Fe K	3.90	2.85
Ni K	40.89	28.43
W M	1.95	0.43
Totals	100.00	

A2

Element	Wt%	At%
C K	19.10	40.05
O K	13.61	21.43
Si K	14.26	12.79
Ca K	0.29	0.18
Cr K	52.75	25.55
Totals	100.0	

Figure 7.18 UCX surface after 1000h at 750°C.

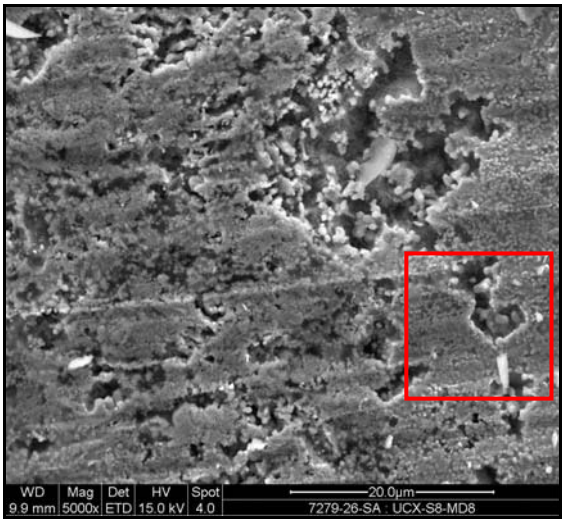

Figure 7.19 A higher magnification image of the pits.

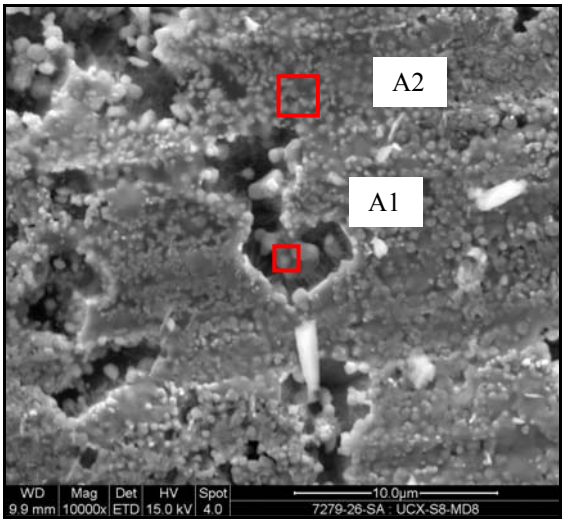

A1

Element	Wt%	At%
C K	1.37	5.37
O K	3.54	10.45
Si K	5.85	9.84
Cr K	40.86	37.11
Fe K	2.04	1.72
Ni K	43.12	34.68
W M	3.22	0.83
Totals	100.00	

A2

Element	Wt%	At%
C K	1.50	4.90
O K	11.87	29.07
Si K	9.46	13.19
Cr K	27.15	20.45
Fe K	4.12	2.89
Ni K	43.39	28.95
W M	2.52	0.54
Totals	100.00	

Figure 7.20 EDX of the pit content and the nearby area.

7.5.7 UCX-850ºC-100h

A part of the layer formed on the alloy after exposure for 100h at 850ºC is shown in Figure 7.21. The analysis of that layer (A1) confirmed that it was composed of chromium and silicon oxides in addition to carbon. A higher magnification micrograph of the layer showed the formation of two phases that had a totally different chemical composition (P1 and P2 in Figure 7.22). One phase (P1) was rich with silica whereas the other (P2) was consisted of chromium oxides. A higher magnification image of the alloy surface is shown in Figure 7.23.

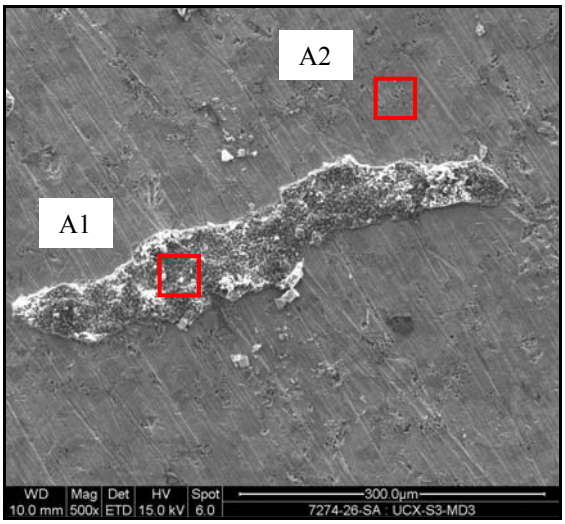

A1

Element	Wt%	At%
C K	9.79	16.70
O K	43.30	55.44
Si K	27.49	20.05
Ca K	1.63	0.83
Cr K	16.28	6.41
Mn K	1.51	0.56
Totals	100.00	

A2

Element	Wt%	At%
C K	4.06	12.17
O K	12.60	28.37
Si K	8.60	11.03
Ca K	0.21	0.19
Cr K	29.78	20.64
Fe K	3.74	2.41
Ni K	41.03	25.18
Totals	100.00	

Figure 7.21 UCX surface after 100h at 850ºC.

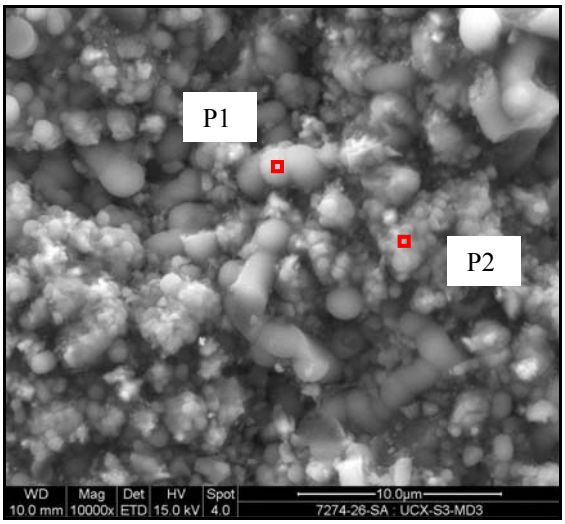

P1

Element	Wt%	At%
C K	7.51	11.47
O K	58.07	66.55
Si K	32.49	21.21
Ca K	0.82	0.38
Cr K	1.11	0.39
Totals	100.00	

P2

Element	Wt%	At%
C K	8.55	17.86
O K	31.77	49.84
Si K	8.78	7.84
Cr K	47.29	22.83
Mn K	2.94	1.34
Ni K	0.67	0.29
Totals	100.00	

Figure 7.22 Two phases observed within the layer.

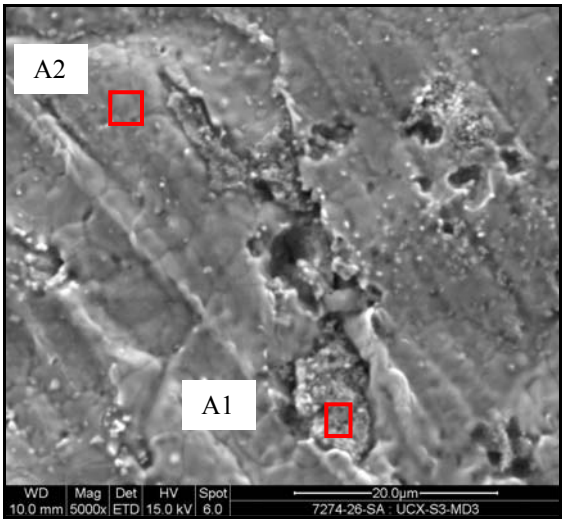

A1

Element	Wt%	At%
C K	8.50	21.65
O K	16.37	31.29
Si K	6.71	7.31
Ca K	0.26	0.20
Cr K	58.93	34.66
Mn K	1.85	1.03
Fe K	0.83	0.46
Ni K	6.54	3.41
Totals	100.00	

A2

Element	Wt%	At%
C K	1.93	8.02
O K	1.40	4.36
Si K	2.57	4.58
Cr K	30.39	29.24
Fe K	5.95	5.33
Ni K	56.43	48.09
W M	1.33	0.36
Totals	100.00	

Figure 7.23 A higher magnification image of the alloy surface.

7.5.8 UCX-850ºC-500h

The exposure for 500h led to the development of a layer (A1) that contained oxides of chromium, silicon, and manganese in addition to appreciable amount of carbon (Figure 7.24). EDX of the alloy bare surface (A2) revealed a reduction in chromium level form 40 wt% (in the bulk metal) to 34.9 wt%. The oxide phases formed on the alloy were further investigated (Figure 7.25). The localised oxide islands (A1) were found to contain high levels of chromium and manganese whereas the other area (A2) contained a higher silica content. Figure 7.26 shows the bare alloy surface which appeared to be pit free.

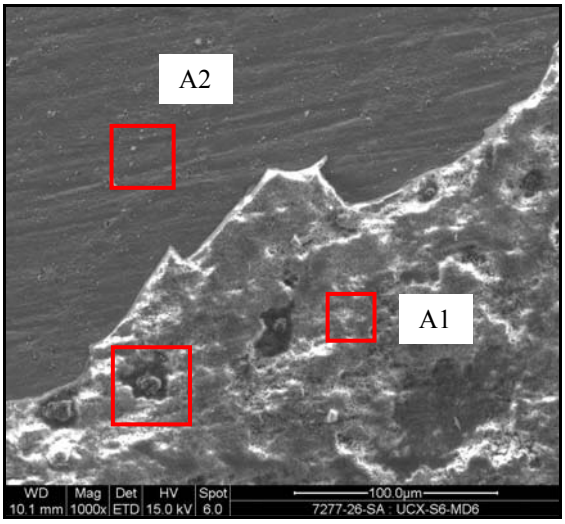

A1

Element	Wt%	At%
C K	10.59	18.99
O K	40.30	54.26
Si K	18.70	14.34
Cr K	22.82	9.45
Mn K	6.84	2.68
Ni K	0.74	0.27
Totals	100.00	

A2

Element	Wt%	At%
C K	1.57	6.49
O K	1.91	5.92
Si K	2.96	5.23
Cr K	34.90	33.30
Fe K	5.19	4.61
Ni K	52.21	44.12
W M	1.26	0.34
Totals	100.00	

Figure 7.24 Alloy surface after 500h at 850ºC.

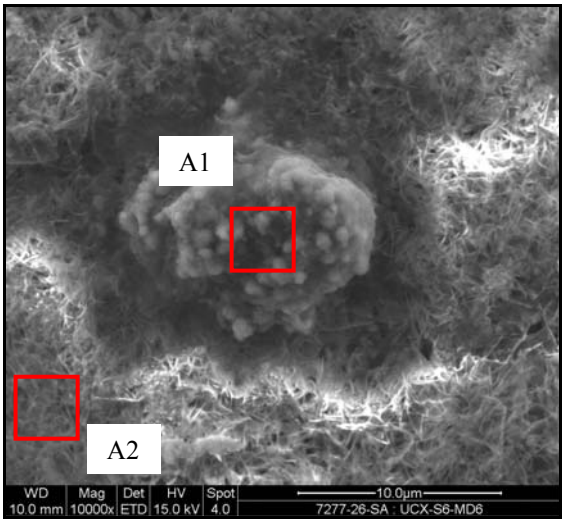

A1

Element	Wt%	At%
C K	15.61	32.49
O K	22.61	35.33
Si K	6.79	6.04
Ca K	0.34	0.21
Cr K	42.61	20.48
Mn K	10.96	4.99
Ni K	1.07	0.46
Totals	100.00	

A2

Element	Wt%	At%
C K	14.85	25.78
O K	38.40	50.03
Si K	16.39	12.16
Cr K	24.44	9.80
Mn K	5.32	2.02
Ni K	0.59	0.21
Totals	100.00	

Figure 7.25 Phases of oxides formed within the layer.

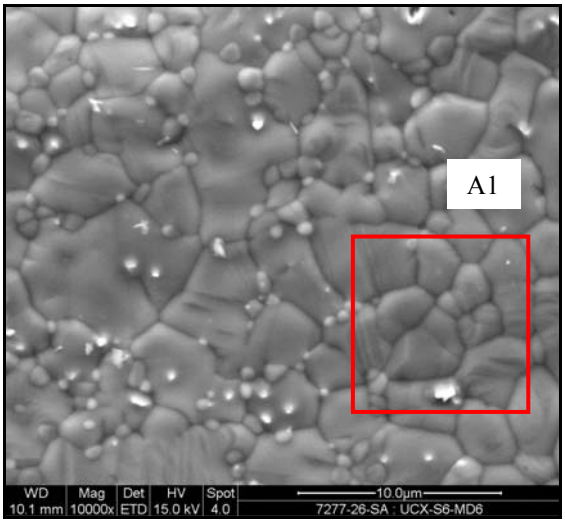

A1

Element	Wt%	At%
C K	1.22	5.19
O K	1.30	4.16
Si K	2.68	4.88
Cr K	31.52	31.02
Fe K	5.90	5.41
Ni K	56.23	49.01
W M	1.15	0.32
Totals	100.00	

Figure 7.26 EDX of the alloy surface.

7.5.9 UCX-850ºC-1000h

Similarly, the layer formed on the alloy after 1000h (A1) was composed of chromium and silicon oxides (Figure 7.27). Minor amounts of manganese and carbon were also detected in the layer. EDX of the bare surface (A2) revealed a low chromium level (31.6 wt%) and no manganese. A further examination of the exposed alloy surface (Figure 7.28) revealed the presence of tiny pits that were confirmed to contain high chromium levels (A1). A higher magnification image of the oxides developed on the alloy is shown in Figure 7.29.

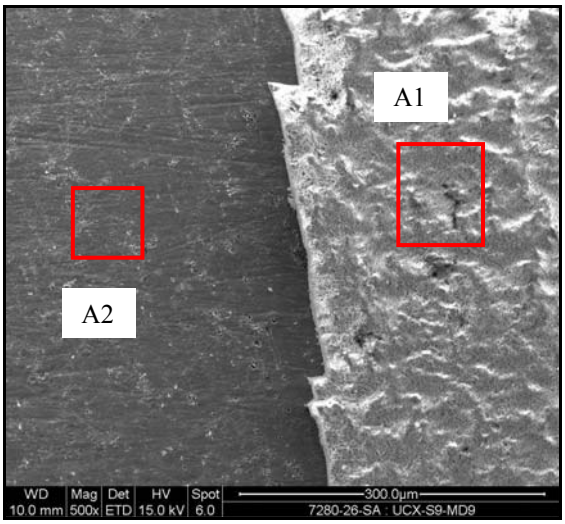

A1

Element	Wt%	At%
C K	3.19	6.08
O K	43.69	62.55
Si K	21.40	17.45
Cr K	29.24	12.88
Mn K	2.49	1.04
Totals	100.00	

A2

Element	Wt%	At%
C K	1.02	4.27
O K	2.36	7.38
Si K	3.05	5.43
Cr K	31.58	30.38
Fe K	5.92	5.30
Ni K	55.13	46.98
W M	0.94	0.26
Totals	100.00	

Figure 7.27 The alloy surface after 1000h at 850ºC.

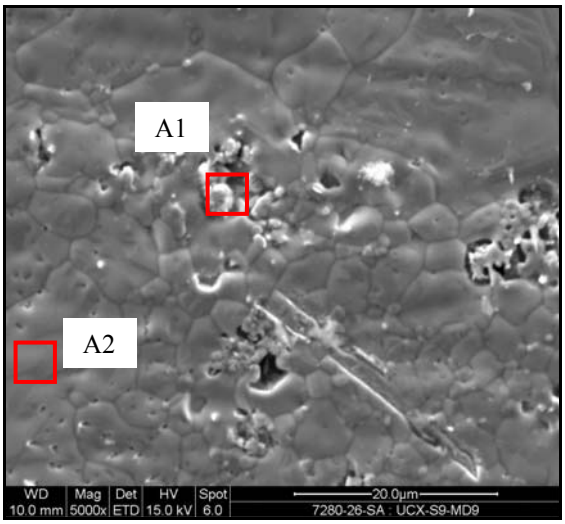

A1

Element	Wt%	At%
C K	3.79	11.95
O K	10.39	24.60
Si K	6.93	9.35
Cr K	44.04	32.08
Mn K	0.74	0.51
Fe K	3.32	2.25
Ni K	29.40	18.97
W M	1.39	0.29
Totals	100.00	

A2

Element	Wt%	At%
C K	0.83	3.59
O K	1.35	4.39
Si K	2.28	4.23
Cr K	30.61	30.68
Fe K	5.92	5.52
Ni K	57.68	51.20
W M	1.33	0.38
Totals	100.00	

Figure 7.28 The alloy bare surface.

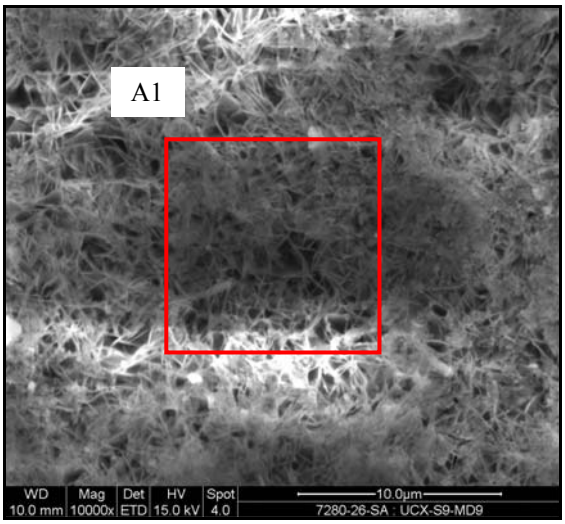

A1

Element	Wt%	At%
O K	44.36	65.76
Si K	22.84	19.29
Cr K	32.79	14.96
Totals	100.00	

Figure 7.29 A higher magnification image of oxides.

7.6 Metallographic Examination

7.6.1 UCX-650ºC-100h

Examining the cross section of the sample exposed at 650ºC for 100h showed that the alloy did not experience significant attack. However, a few isolated pits still could be observed (Figure 7.30), one of which is shown at higher magnification in Figure 7.31. EDX of the layer formed near the pit (i.e. P1) indicated that it was composed mainly of carbon and much lower amounts of chromium, silicon, and manganese oxides. The bottom of the pit (A2) was also analysed and found to contain high levels of carbon. A higher magnification image of the pit bottom is shown in Figure 7.32.

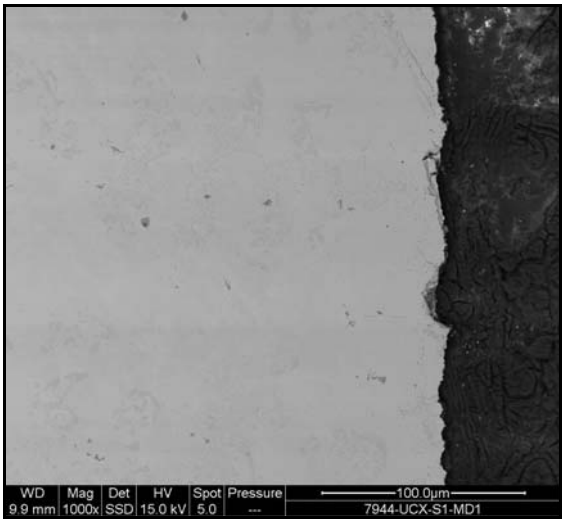

Figure 7.30 UCX cross section after 100h at 650ºC.

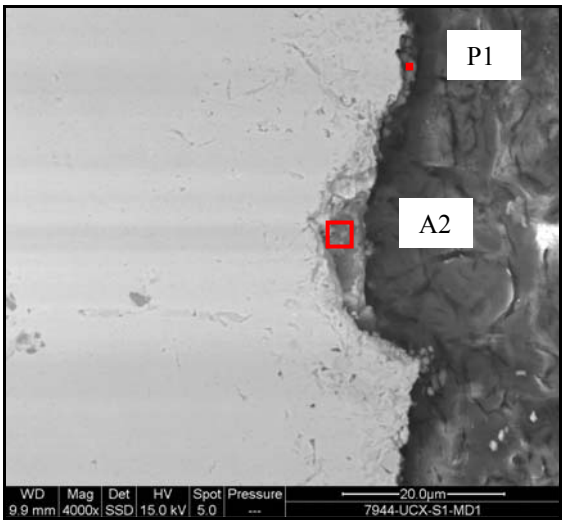

P1

Element	Wt%	At%
C K	63.78	73.25
O K	27.92	24.07
Si K	1.98	0.97
Ca K	0.64	0.22
Cr K	4.79	1.27
Mn K	0.90	0.23
Totals	100.00	

A2

Element	Wt%	At%
C K	33.35	57.54
O K	17.24	22.33
Si K	4.14	3.06
Ca K	0.27	0.14
Cr K	21.37	8.52
Mn K	1.24	0.47
Fe K	2.67	0.99
Ni K	19.71	6.96
Totals	100.00	

Figure 7.31 Pit on the alloy surface.

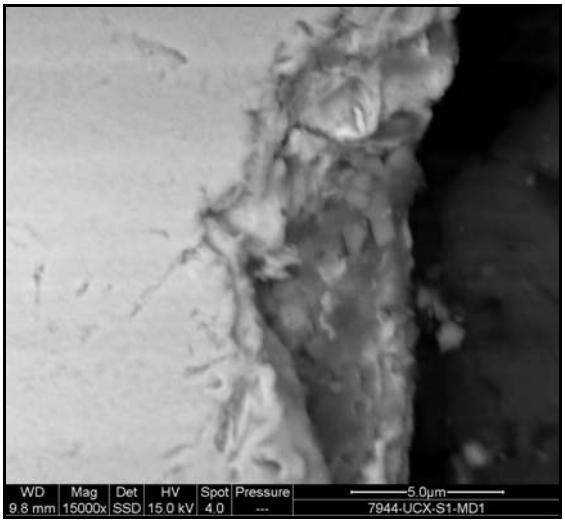

Figure 7.32 A higher magnification image of the pit bottom.

7.6.2 UCX-650ºC-500h

Extending the exposure time to 500h led to a development of a thicker and more continuous layer, (Figure 7.33). No attack was noted on the alloy cross section. The layer which had a maximum thickness of approximately 2µm appeared to be uneven and was very thin at areas. It was found to contain high amounts of chromium oxides (A1 in Figure 7.34). EDX of the substrate (A2) showed severe depletion of chromium and manganese that was probably due to oxidation.

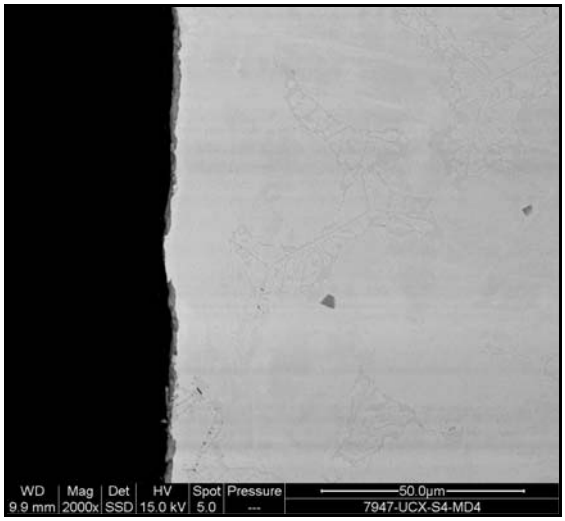

Figure 7.33 UCX cross section after 500h at 650ºC.

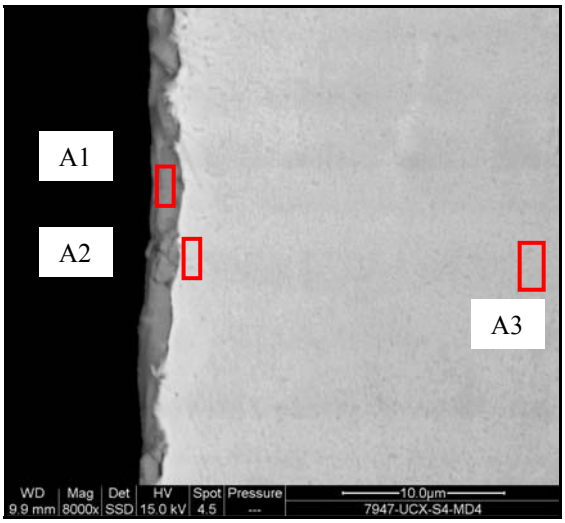

A1

Element	Wt%	At%
C K	5.89	12.35
O K	35.98	56.61
Si K	7.25	6.50
Ca K	0.24	0.15
Cr K	46.95	22.73
Mn K	2.54	1.17
Ni K	1.15	0.49
Totals	100.00	

A2

Element	Wt%	At%
C K	1.63	6.85
O K	1.71	5.39
Si K	2.55	4.57
Ca K	0.25	0.32
Cr K	25.72	24.90
Fe K	6.58	5.93
Ni K	60.32	51.71
W M	1.23	0.34
Totals	100.00	

A3

Element	Wt%	At%
C K	1.45	6.03
O K	1.80	5.62
Si K	2.50	4.44
Cr K	38.02	36.44
Mn K	1.02	0.93
Fe K	5.14	4.59
Ni K	49.16	41.72
W M	0.89	0.24
Totals	100.00	

Figure 7.34 EDX of the layer formed on UCX after 500h at 650ºC.

7.6.3 UCX-650ºC-1000h

A layer with a maximum thickness of ~4µm was observed to have formed on the alloy as a result of exposure at 650ºC for 1000h (Figure 7.35).

No significant pitting appeared to have occurred along the cross section. The different phases formed in the layer were analysed (Figure 7.36). Small, lighter, discontinuous chromium-rich layers were detected at the metal/oxide interface (A1). In addition to carbon, the layer (A2) also contained oxides of chromium, silicon, and manganese. The localised, internal sites (A3) were also found to have high levels of carbon and chromium-based oxides. Compositional variations were also noticed on the layer as the darker area, A4, contained higher amounts of carbon associated with lower levels of chromium. Severe chromium depletion was also observed at the sample substrate (A5).

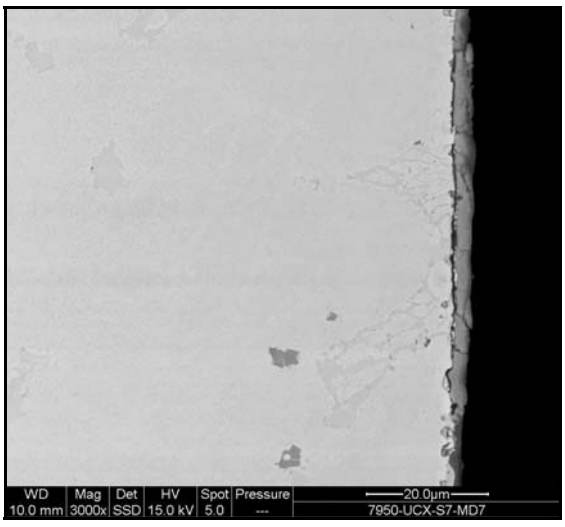

Figure 7.35 Cross section of UCX after 1000h at 650ºC.

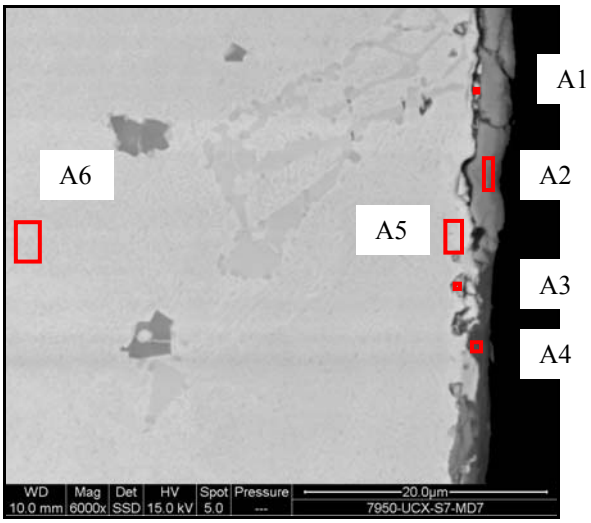

A1

Element	Wt%	At%
C K	1.91	4.96
O K	25.32	49.22
Si K	7.04	7.80
Ca K	0.36	0.28
Ti K	0.34	0.22
Cr K	41.55	24.85
Mn K	5.15	2.92
Fe K	1.70	0.95
Ni K	16.62	8.81
Totals	100.00	

A2

Element	Wt%	At%
C K	21.14	33.56
O K	41.66	49.65
Si K	10.19	6.92
Ca K	0.18	0.09
Cr K	24.70	9.06
Mn K	1.64	0.57
Ni K	0.50	0.16
Totals	100.00	

A3

Element	Wt%	At%
C K	14.90	34.28
O K	16.84	29.08
Si K	4.24	4.17
Ca K	0.42	0.29
Cr K	39.56	21.02
Mn K	1.05	0.53
Fe K	1.96	0.97
Ni K	20.29	9.55
W M	0.74	0.11
Totals	100.00	

A4

Element	Wt%	At%
C K	32.87	45.10
O K	43.61	44.92
Na K	0.27	0.19
Mg K	0.22	0.15
Si K	8.52	5.00
S K	0.09	0.05
Ca K	0.52	0.22
Cr K	12.55	3.98
Mn K	0.29	0.09
Fe K	0.42	0.12
Ni K	0.64	0.18
Totals	100.00	

A5

Element	Wt%	At%
C K	2.98	10.89
O K	5.70	15.64
Si K	3.99	6.23
Ca K	0.26	0.28
Cr K	24.17	20.39
Mn K	0.53	0.43
Fe K	5.95	4.67
Ni K	55.12	41.18
W M	1.29	0.31
Totals	100.00	

A6

Element	Wt%	At%
C K	1.36	5.70
O K	1.80	5.68
Si K	1.89	3.40
Cr K	37.58	36.47
Mn K	0.62	0.57
Fe K	5.45	4.93
Ni K	49.87	42.86
W M	1.43	0.39
Totals	100.00	

Figure 7.36 Phases formed at the reaction front.

7.6.4 UCX-750ºC-100h

A layer, which was relatively uneven, had formed on the alloy as a consequence of exposing the alloy at 750ºC for 100h (Figure 7.37).

No noticeable attack was seen to have taken place across the alloy cross section. The maximum layer thickness was approximately 5µm. EDX of the layer at two areas, A1 and A2 (Figure 7.38), indicated increasing carbon levels in the outer area (A2). Also, high amount of nickel and iron was detected at A1. The oxides formed at both areas were mainly those of chromium and silicon.

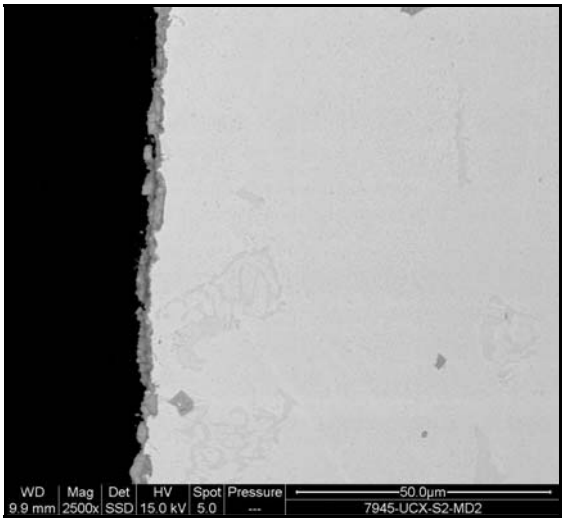

Figure 7.37 UCX cross section after 100h at 750ºC.

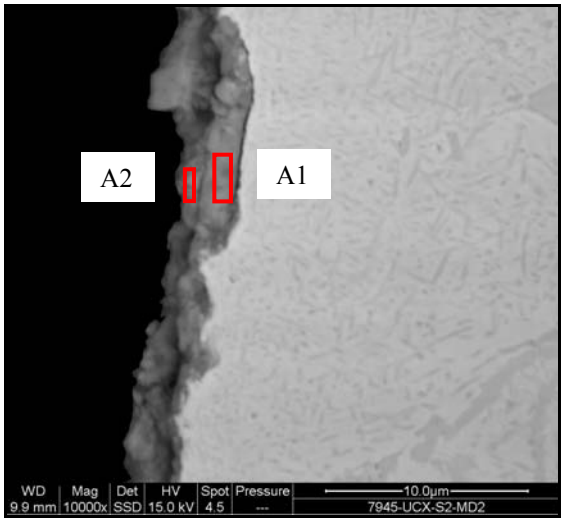

A1

Element	Wt%	At%
C K	2.20	5.27
O K	29.47	52.99
Si K	9.92	10.16
Ca K	1.14	0.82
Ti K	0.20	0.12
Cr K	39.85	22.04
Mn K	3.35	1.75
Fe K	1.69	0.87
Ni K	12.18	5.97
Totals	100.00	

A2

Element	Wt%	At%
C K	11.26	21.90
O K	33.88	49.46
Si K	10.45	8.69
Ca K	0.87	0.51
Cr K	39.23	17.62
Mn K	3.78	1.61
Ni K	0.53	0.21
Totals	100.00	

Figure 7.38 EDX of the layer formed on the alloy.

7.6.5 UCX-750ºC-500h

A micrograph of the alloy cross section is shown in Figure 7.39. A continuous layer, typically 3µm thick, had formed on the alloy. EDX of the scale (A1 and A2) confirmed that it was composed of a mixture of oxides and carbon. At A1, chromium and oxygen were the main contents. However, at A2, a much more carbon was detected.

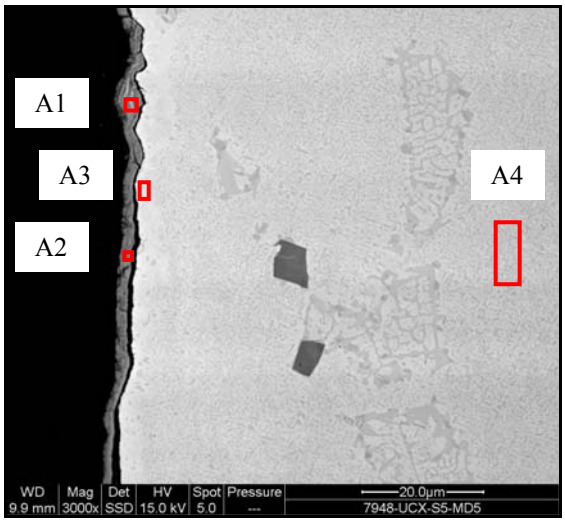

A1

	Wt%	At%
C K	6.47	16.40
O K	20.25	38.54
Si K	4.35	4.72
Ca K	0.26	0.20
Cr K	66.71	39.07
Mn K	1.01	0.56
Fe K	0.35	0.19
Ni K	0.60	0.31
Totals	100.0	

A2

	Wt%	At%
C K	19.00	32.10
O K	38.93	49.39
Si K	6.13	4.43
Ca K	0.69	0.35
Cr K	34.02	13.28
Mn K	1.23	0.45
Totals	100.0	

A3

	Wt%	At%
C K	2.23	7.58
O K	9.92	25.35
Si K	3.88	5.64
Ca K	0.22	0.23
Cr K	34.10	26.81
Mn K	1.37	1.02
Fe K	4.49	3.29
Ni K	42.93	29.89
W M	0.86	0.19
Totals	100.0	

A4

	Wt%	At%
C K	1.60	6.59
O K	1.96	6.06
Si K	2.29	4.04
Cr K	39.19	37.35
Mn K	0.59	0.53
Fe K	4.84	4.30
Ni K	48.32	40.79
W M	1.22	0.33
Totals	100.0	

Figure 7.39 UCX cross section after 500h at 750ºC.

Localised pits, approximately 4µm deep, were also observed in some areas along the alloy's cross section (Figure 7.40). Moreover, the whole area including the pits was covered with a ~2µm layer.

The area in red in Figure 7.40 was magnified to investigate further the pit's content (Figure 7.41). The layer formed at the pit bottom (A1 and A3) was composed of chromium, manganese, and silicon oxides in addition to carbon. The shape and distribution of carbides at the reaction zone appeared to differ from that in the base metal. Coarsened and rounded islands of chromium-based carbides (A5) were observed to precipitate at the substrate. Furthermore, the substrate suffered depletion of chromium and manganese (A6) as a result of their consumption in the oxidation process. It is also worth noting that, despite being a scale-forming element, the percentage of silicon at this area matched that of base metal.

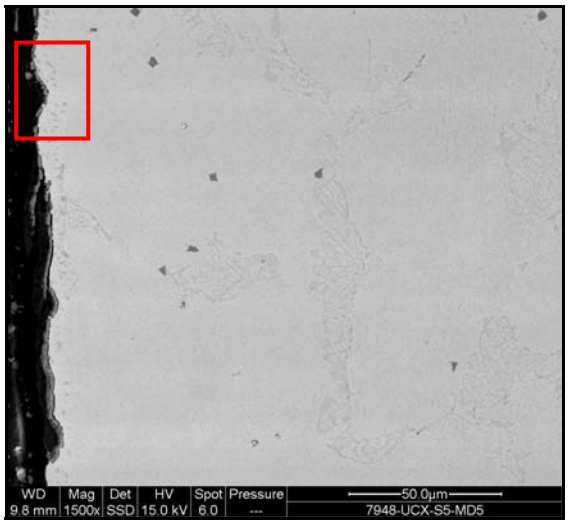

Figure 7.40 Pitting on the alloy surface.

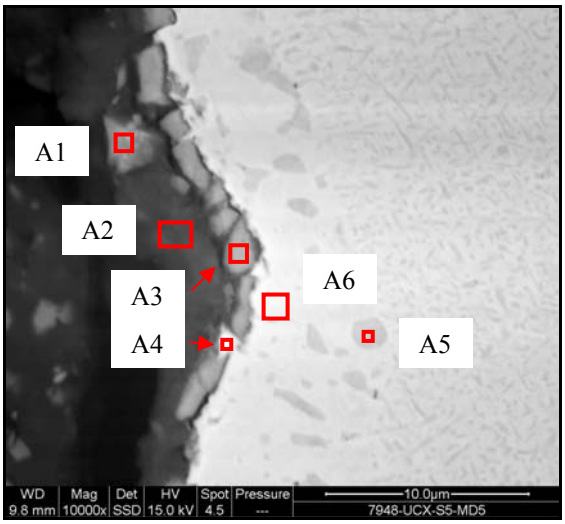

A1

Element	Wt%	At%
C K	9.16	18.45
O K	35.15	53.14
Si K	6.75	5.81
Ca K	0.31	0.19
Ti K	0.66	0.33
Cr K	38.73	18.02
Mn K	9.23	4.06
Totals	100.00	

A2

Element	Wt%	At%
C K	42.85	55.79
O K	35.07	34.28
Na K	0.67	0.46
Si K	8.02	4.47
Ca K	12.43	4.85
Mo L	0.96	0.16
Totals	100.00	

A3

Element	Wt%	At%
C K	6.68	13.74
O K	36.55	56.42
Si K	8.09	7.11
Cr K	34.63	16.45
Mn K	13.07	5.87
Ni K	0.98	0.41
Totals	100.00	

A4

Element	Wt%	At%
C K	11.67	27.69
O K	17.81	31.72
Si K	8.71	8.84
Ca K	0.88	0.63
Cr K	21.96	12.04
Mn K	2.95	1.53
Fe K	3.08	1.57
Ni K	32.94	15.99
Totals	100.00	

A5

Element	Wt%	At%
C K	1.48	5.77
O K	3.65	10.68
Cr K	86.38	77.79
Fe K	1.43	1.20
Ni K	5.10	4.07
W M	1.96	0.50
Totals	100.00	

A6

Element	Wt%	At%
C K	2.07	8.34
O K	2.42	7.31
Si K	2.64	4.54
Cr K	28.88	26.85
Fe K	6.08	5.26
Ni K	57.91	47.69
Totals	100.00	

Figure 7.41 EDX of the pit contents.

7.6.6 UCX-750ºC-1000h

An approximately 8µm thick layer had formed on the alloy after 1000h exposure at 750ºC (Figure 7.42). The layer appeared adherent, continuous and even.

The outer, middle, and inner sections of the layer were analysed (A1, A2, A3 in Figure 7.43). The outer surface, A1, was composed of chromium and silicon oxides in addition to significant amount of carbon. The middle and inner areas, however, contained more oxides and less carbon. The highest manganese level (3.2 wt%) was detected at the inner section. EDX of the substrate revealed a remarkable reduction in manganese and chromium that could be attributed to oxidation.

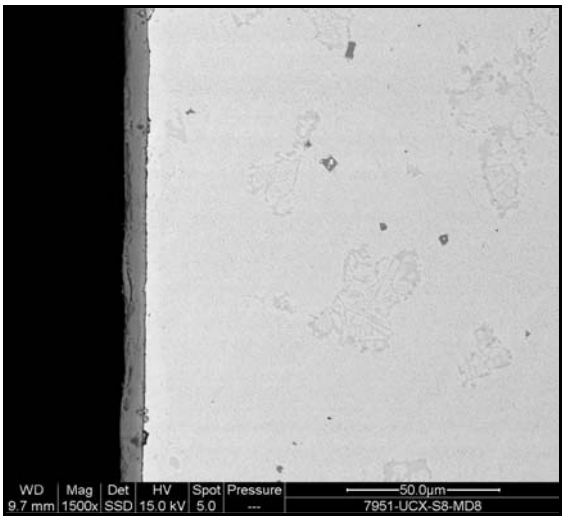

Figure 7.42 UCX cross section after 1000h at 750ºC.

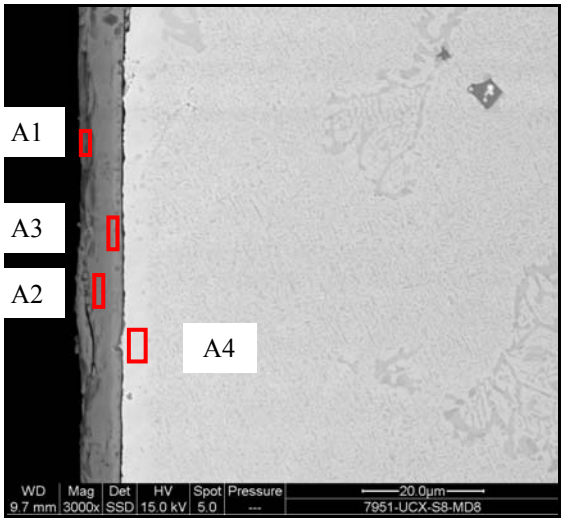

A1

	Wt%	At%
C K	19.10	40.05
O K	13.61	21.43
Si K	14.26	12.79
Ca K	0.29	0.18
Cr K	52.75	25.55
Totals	100.0	

A2

	Wt%	At%
C K	1.18	2.47
O K	40.92	64.22
Si K	13.00	11.62
Ca K	0.16	0.10
Cr K	44.03	21.26
Mn K	0.70	0.32
Totals	100.0	

A3

	Wt%	At%
C K	1.47	3.19
O K	38.94	63.37
Si K	8.69	8.06
Ca K	0.19	0.12
Cr K	46.85	23.46
Mn K	3.18	1.51
Ni K	0.67	0.30
Totals	100.0	

A4

	Wt%	At%
C K	1.68	6.93
O K	2.70	8.36
Si K	2.44	4.30
Cr K	24.07	22.89
Fe K	6.63	5.87
Ni K	60.81	51.22
W M	1.67	0.45
Totals	100.0	

Figure 7.43 EDX of the layer formed on the alloy.

The alloy also seemed to have suffered large pitting damage in distinctive sites along the cross section (Figure 7.44). It appeared that this selective attack occurred in places that were composed mainly of chromium carbides (A3). A mixture of oxides and carbon was also detected at the pit bottom (A4) in the void between the base metal and the carbides. The reaction zone, around the pit (A1 and A5), was depleted in chromium and manganese as a result of the oxidation process. A higher magnification image of the pit is shown in Figure 7.45.

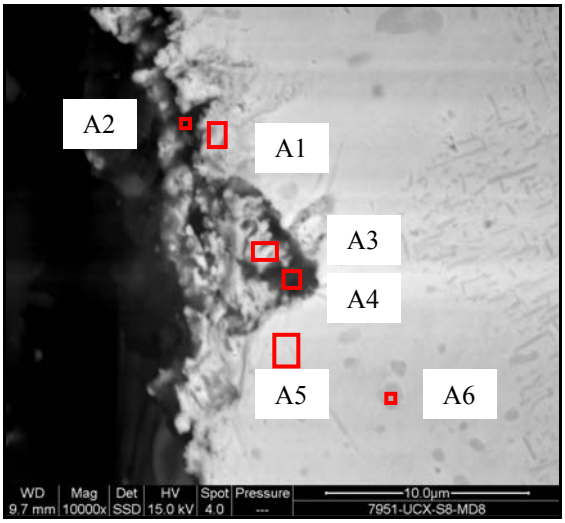

A1

	Wt%	At%
C K	5.41	19.76
O K	2.79	7.65
Si K	2.35	3.67
Cr K	26.49	22.36
Fe K	5.64	4.43
Ni K	55.89	41.79
W M	1.44	0.34
Totals	100.0	

A2

	Wt%	At%
C K	8.49	27.54
O K	2.21	5.37
Si K	3.97	5.51
Ca K	0.71	0.69
Ti K	1.19	0.97
Cr K	52.46	39.30
Fe K	2.37	1.65
Ni K	28.60	18.98
Totals	100.0	

A3

	Wt%	At%
C K	10.77	28.80
O K	9.96	20.00
Si K	5.50	6.30
Ca K	0.19	0.15
Cr K	62.75	38.78
Mn K	0.62	0.36
Fe K	0.86	0.49
Ni K	9.35	5.12
Totals	100.0	

A4

	Wt%	At%
C K	34.12	53.42
O K	23.22	27.29
Si K	14.28	9.56
Cr K	14.82	5.36
Fe K	1.68	0.56
Ni K	11.90	3.81
Totals	100.0	

A5

Element	Wt%	At%
C K	2.23	9.24
O K	1.53	4.75
Si K	2.30	4.08
Cr K	25.54	24.44
Fe K	6.48	5.77
Ni K	60.60	51.36
W M	1.32	0.36
Totals	100.00	

A6

Element	Wt%	At%
C K	2.08	8.06
O K	3.26	9.47
Si K	1.15	1.90
Ca K	0.17	0.19
Cr K	68.81	61.55
Fe K	2.86	2.38
Ni K	20.33	16.11
W M	1.35	0.34
Totals	100.00	

Figure 7.44 Disintegration of carbides on alloy surface.

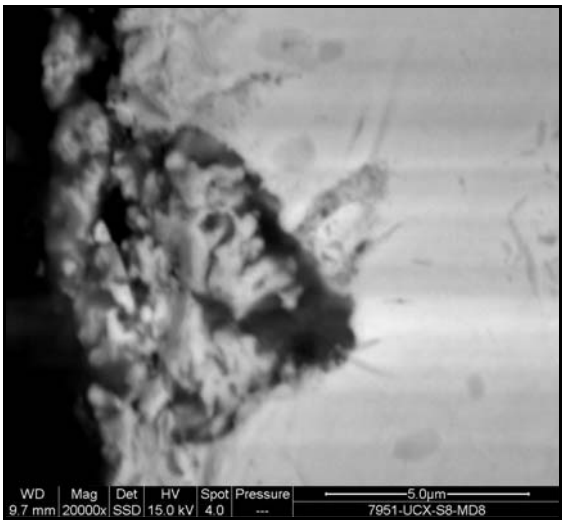

Figure 7.45 A higher magnification image of the pitting area.

7.6.7 UCX-850ºC-100h

Superficial pitting appeared to have occurred on the alloy surface after 100h at 850ºC (Figure 7.46). No layer was observed along the cross section that might be removed during sample cleaning or preparation.

One of the pits was examined further (Figures 7.47) and EDX of the reaction front and pit's content was carried out (Figure 7.48). Considerable amounts of silicon, chromium, and nickel were detected within the carbon deposit at the pit (A4). Also, the particles embedded inside the pit (P3) were found to contain high levels of chromium, iron, and nickel.

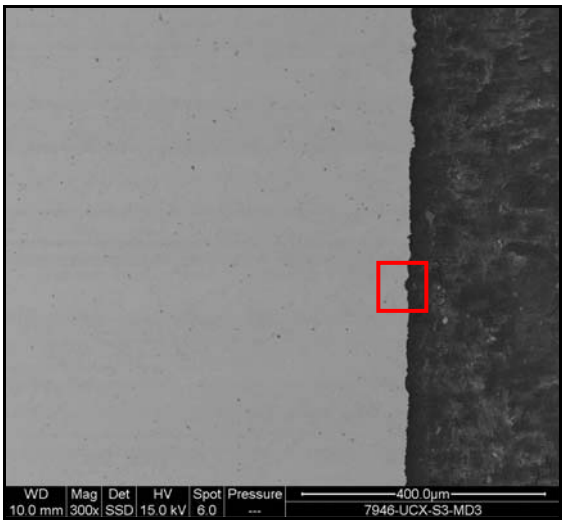

Figure 7.46 UCX cross section after 100h at 850°C.

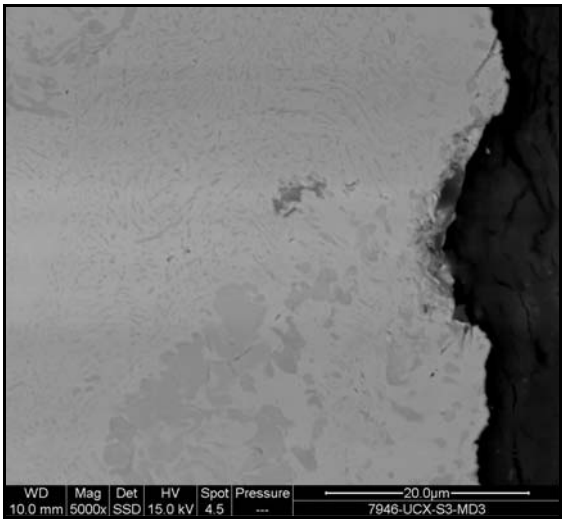

Figure 7.47 A pit formed after 100h at 850°C.

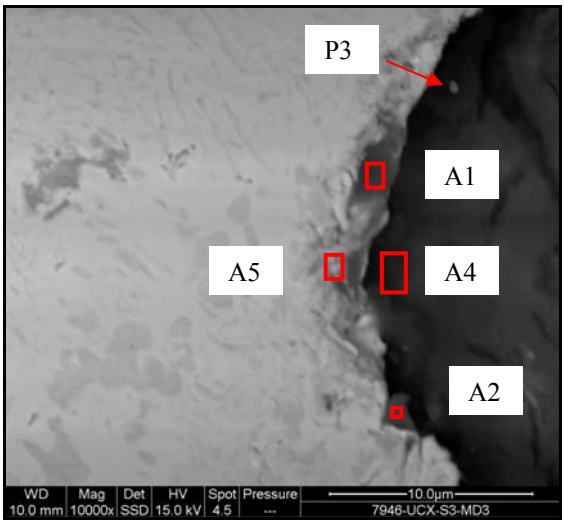

A1

Element	Wt%	At%
C K	54.44	75.66
O K	13.64	14.23
Si K	1.85	1.10
Ca K	0.15	0.06
Cr K	11.28	3.62
Fe K	1.99	0.60
Ni K	16.64	4.73
Totals	100.00	

A2

Element	Wt%	At%
C K	26.70	41.68
O K	34.65	40.61
Na K	0.70	0.57
Al K	1.89	1.31
Si K	10.58	7.07
K K	0.85	0.41
Ca K	0.23	0.11
Cr K	10.19	3.67
Fe K	1.85	0.62
Ni K	12.37	3.95
Totals	100.00	

P3

Element	Wt%	At%
C K	56.73	78.24
O K	11.71	12.13
Si K	0.84	0.50
Ca K	0.31	0.13
Cr K	8.14	2.59
Fe K	9.09	2.70
Ni K	13.17	3.72
Totals	100.00	

A4

Element	Wt%	At%
C K	76.23	84.20
O K	16.27	13.49
Al K	0.16	0.08
Si K	1.70	0.80
Ca K	0.64	0.21
Cr K	2.92	0.75
Ni K	2.08	0.47
Totals	100.00	

A5

Element	Wt%	At%
C K	15.73	41.79
O K	6.47	12.90
Si K	1.02	1.16
Ca K	0.18	0.14
Cr K	44.35	27.22
Fe K	6.24	3.56
Ni K	23.52	12.78
W M	2.51	0.44
Totals	100.00	

Figure 7.48 EDX of the pit's content.

7.6.8 UCX-850ºC-500h

An approximately 5µm thick layer had formed on the alloy as a result of exposure at 850ºC for 500h (Figure 7.49). Two phases were observed within the layer, the internal grey (A2) and external darker grey (A1) layers. The former contained high concentrations of chromium, manganese, and silicon oxides whereas the latter was found to consist of mainly carbon and silica. No pitting was observed along the alloy cross section.

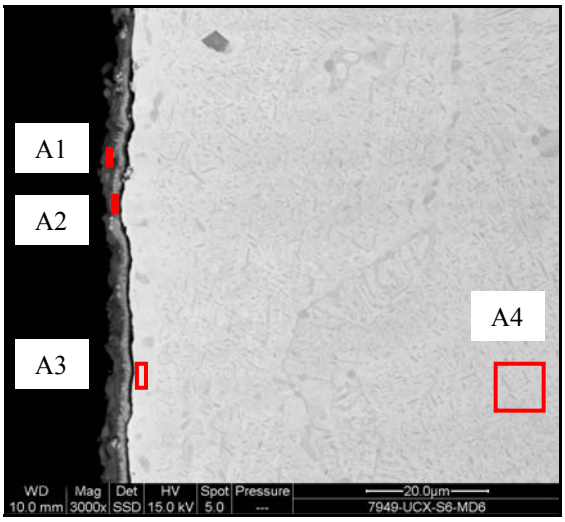

A1		
	Wt%	At%
C K	14.82	22.01
O K	51.47	57.38
Na K	0.15	0.12
Mg K	0.24	0.18
Si K	30.71	19.50
Ca K	0.29	0.13
Cr K	1.18	0.41
Mn K	0.74	0.24
Tl M	0.40	0.03
Totals	100.0	

A2		
	Wt%	At%
C K	4.19	8.47
O K	39.86	60.40
Si K	13.37	11.55
Ca K	0.15	0.09
Ti K	0.68	0.35
Cr K	29.79	13.89
Mn K	11.20	4.94
Ni K	0.75	0.31
Totals	100.0	

A3		
	Wt%	At%
C K	1.89	7.59
O K	2.99	8.99
Si K	2.81	4.81
Ca K	0.21	0.25
Cr K	29.57	27.36
Mn K	0.55	0.48
Fe K	5.60	4.82
Ni K	55.46	45.45
W M	0.91	0.24
Totals	100.0	

A4		
	Wt%	At%
C K	1.47	6.14
O K	1.67	5.26
Si K	2.06	3.70
Cr K	36.81	35.63
Mn K	0.99	0.91
Fe K	5.33	4.80
Ni K	50.42	43.23
W M	1.25	0.34
Totals	100.0	

Figure 7.49 UCX cross section after 500h at 850ºC.

7.6.9 UCX-850ºC-1000h

An adherent, continuous layer with a maximum thickness of ~7μm had developed on the alloy as a consequence of increasing the test time to 1000h (Figure 7.50). The layer was composed mainly of chromium oxides (A1 in Figure 7.51). As observed in almost all samples, the alloy substrate suffered a depletion of chromium and manganese that were consumed at the surface by oxidation. The cross section examination did not reveal any noticeable pitting.

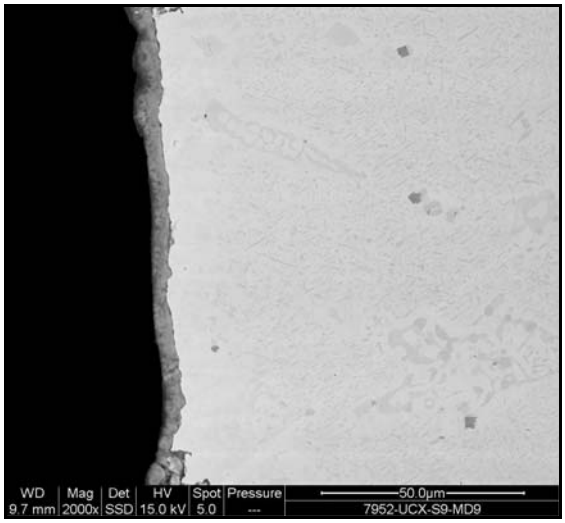

Figure 7.50 UCX cross section after 1000h at 850ºC.

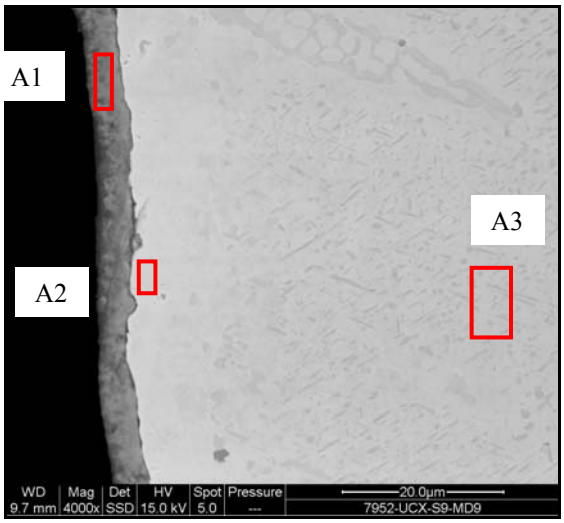

A1			A2			A3		
Element	Wt%	At%	Element	Wt%	At%	Element	Wt%	At%
C K	4.63	9.99	C K	1.44	6.10	C K	1.42	5.91
O K	34.21	55.39	O K	1.75	5.57	O K	1.98	6.19
Si K	9.86	9.10	Si K	2.14	3.87	Si K	1.93	3.44
Ca K	0.28	0.18	Cr K	28.52	27.87	Cr K	38.05	36.56
Cr K	49.30	24.57	Fe K	6.19	5.63	Mn K	0.65	0.59
Mn K	0.62	0.29	Ni K	58.37	50.52	Fe K	5.59	5.00
Ni K	1.09	0.48	W M	1.59	0.44	Ni K	49.43	42.06
						W M	0.96	0.26
Totals	100.00		Totals	100.00		Totals	100.00	

Figure 7.51 EDX of the scale formed on the alloy.

8 METAL DUSTING OF HEAT-RESISTANT ALLOYS: DISCUSSION

8.1 Introduction

The purpose of this chapter is to discuss the results illustrated in previous chapters 5, 6, and 7 and to evaluate and compare the alloys performance in the gas mixture at 650, 750, and 850ºC for 100, 500, and 1000h. The mechanisms by which the attack took place are also suggested.

8.2 Discussion

The highest amount of carbon deposition was observed on the alloys exposed at 650ºC whereas the least was seen after exposure at 850ºC. For samples exposed at 750ºC for 500 and 1000h, carbon deposition was gradually lessening across the rack in agreement with the gas flow direction. Increasing the exposure time also caused more carbon deposition especially at 650 and 750ºC.

The formation of less carbon as a result of the temperature increase may be explained by considering the thermodynamic aspects of the dominant carbon-producing reactions (i.e. the carbon monoxide reduction (1.5) and the Boudouard reaction (1.11)) as well as the temperature profile along the furnace tube at each temperature (Appendix C). For reactions in equilibrium, the equilibrium constants were calculated using the software, HSC Chemistry 6.0 (Figure 8.1). In general, the forward reactions are favourable at low temperatures up to temperatures just below 700ºC. However, carbon deposition was also observed on the alloys at temperatures above 700ºC implying that the reactions were probably not in equilibrium.

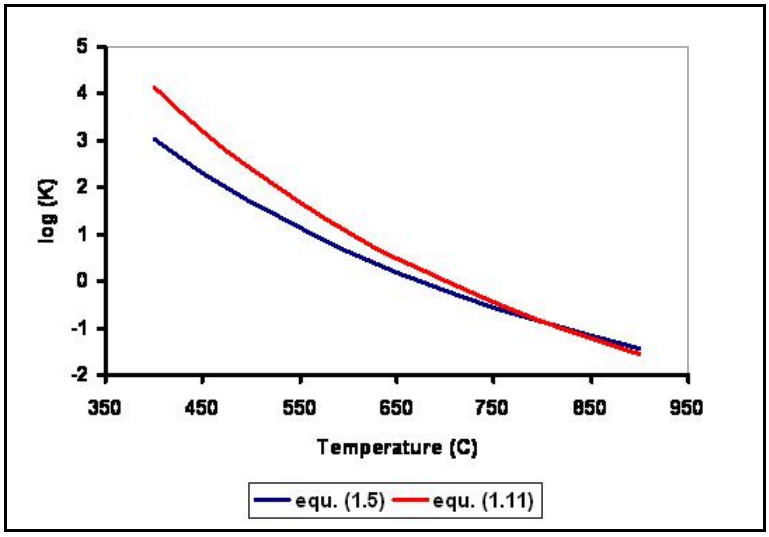

Figure 8.1 **The equilibrium constants of the carbon-producing reactions (1.5) and (1.11) as functions of temperature.**

8.2.1 Carbon Formation

The forward reactions are expected to be favourable from 400ºC (i.e. the reported minimum temperature at which metal dusting occurs [4]) up to 700ºC. The distances between these two temperature regions on the temperature profiles across the furnace tube (shown in Appendix C) were measured at each testing temperature. In view of that, at 650ºC, the forward reactions were favourable from 400ºC until the end of the sample rack since the maximum temperature did not reach 700ºC and that region was around 39cm. At 750 and 850ºC, however, the equilibrium reaction regions were much shorter, ~16cm and 12cm respectively, suggesting that the carbon production might have been proportional to the length of the reaction regions.

The difference in carbon deposition might also be attributed to the difference in temperatures at the rack itself as several researches have suggested that the forward reactions are catalysed by alloying elements such as iron and/or nickel. In that case, gas decomposition might not have taken place before the rack. Therefore, it might be that the gas was heated as it passed through the tube until it reached the rack where it just needed the alloy surface to catalyse the decomposition and release carbon. At 650ºC, the reactions were expected to have readily taken place along the rack whereas, at 750ºC, the gas first arrived at the rack at temperatures where the reactions could have taken place but as the

gas passed through the rack it gained more heat and its temperature would have exceeded 700ºC and hence the reactions were somewhat suppressed which may also explain the gradual change in the carbon deposition on the samples along the rack. At 850ºC, the gas arrived at the rack at temperatures that were considerably higher than 700ºC making the reactions unlikely and leading to the least carbon deposition.

The carbon potential of the two reactions, expressed by equations (1.7) and (1.13), was calculated assuming the partial pressures of carbon dioxide and water to be those given in the gas data sheet (Figure 8.2). It is obvious that the carbon potential of the gas mixture was highest at 650ºC and thus the environment was expected to be the most aggressive. However, the carbon potential was drastically decreased with increasing temperature leading to less aggressive environments.

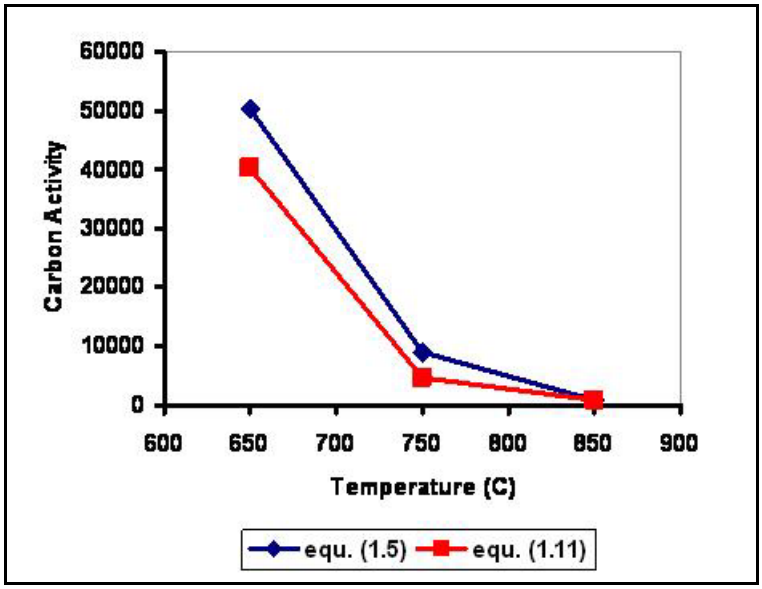

Figure 8.2 **Carbon activity in gas mixture vs. temperature for the reactions (1.5) and (1.11)**

8.2.2 Oxygen Generation

Oxygen in the gas mixture could be produced by two reactions; the water dissociation reaction (1.20), and carbon dioxide dissociation (1.23). Although the system sealing had been ensured before each experiment, the potential of air leakage from the outside could not be ruled out. The equilibrium constants of the oxygen-producing reactions are plotted

as functions of temperature (Figure 8.3). However, some research [21] has suggested that the reaction (1.20) is generally dominant due to its rapid kinetics.

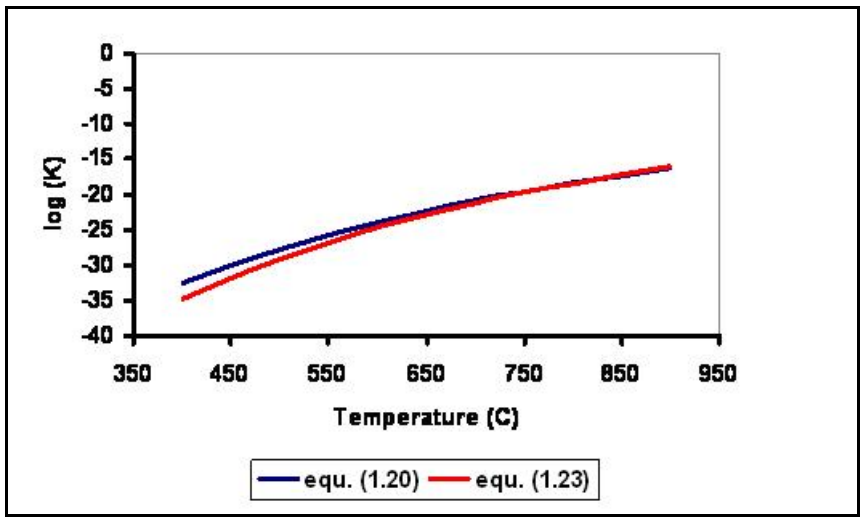

Figure 8.3 **The equilibrium constants of oxygen-producing reactions (1.20) and (1.23) vs. temperature.**

Oxygen partial pressures were also calculated using the water dissociation reaction (1.22) and carbon dioxide dissociation reaction (1.25), Figure 8.4. The oxygen partial pressure in the environment is increased as a result of the temperature increase suggesting oxidation to be more favourable at higher temperatures.

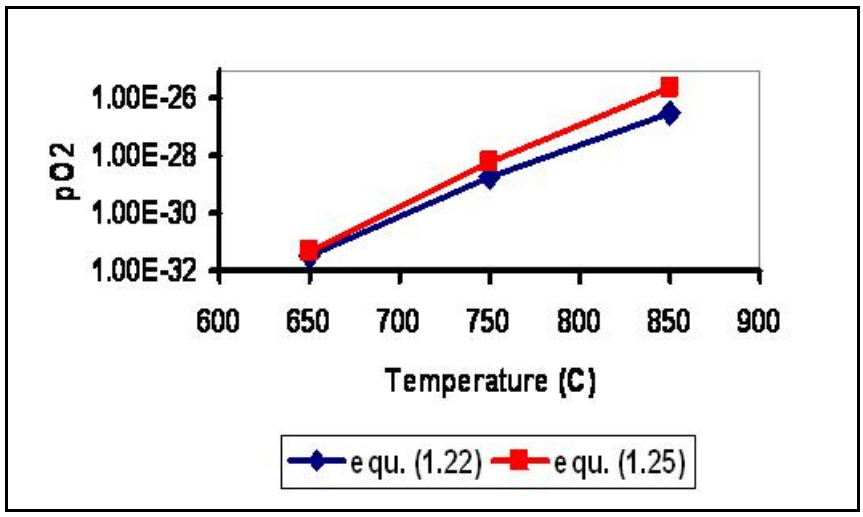

Figure 8.4 **Oxygen partial pressure vs. temperature for the H_2O and CO_2 dissociation reactions.**

8.2.3 Occurrence of Metal Dusting

As explained in the literature review, carbon deposition generally indicates the occurrence of metal dusting as it is caused by metals like iron and nickel [35].

The surface of alloy HP may become magnetic as a result of carburisation or the formation of a chromium-depleted layer (caused by oxidation). This behaviour was observed on the sample exposed at 650ºC for 500h. Figure 8.5 shows the Fe-Cr-Ni diagram where the non-magnetic and ferromagnetic regions are indicated. Due to carburisation, the alloy matrix becomes depleted of chromium, which exhibits antiferromagnetism, rendering the alloy substrate ferromagnetic. The other alloys, however, do not show magnetic transformation even after carburisation or oxidation due to their high chromium contents.

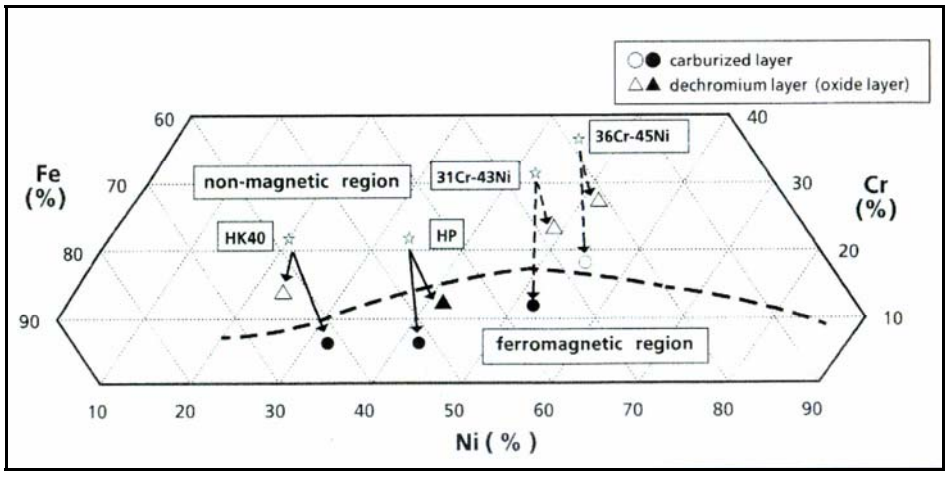

Figure 8.5 **Phase diagram of Fe-Cr-Ni alloys showing the magnetic and non magnetic regions (Source: Kubota Corporation, Japan).**

Weight loss might indicate that the alloy suffered metal dusting, especially for samples exposed at relatively low temperatures (650 and 750ºC) where the spallation or volatilisation of the oxide scales is unlikely. Weight change measurements showed that alloy HP suffered metal dusting after 100 and 500h at 650ºC. Weight loss was also observed on the alloy after 500h at 750ºC. Alloy 35Cr-45Ni showed metal loss after 500h at 650ºC whereas alloy UCX did not show any weight loss at 650 or 750ºC. Weight gain, however, did not prove to be a reliable tool to assess the alloy's condition after exposure to the gas mixture as the surface and metallographic examinations confirmed that some of the samples that showed weight gain also suffered pitting. The weight gain was caused by

carbon deposition and diffusion, oxidation and carburisation despite the presence of pitting.

XRD and EDX of the deposits removed from alloy HP after 100, 500, and 1000h at 650 and 750ºC collectively confirmed the presence of different concentrations of alloying elements such as iron, nickel, chromium and silicon in addition to oxygen in all samples. The alloying elements were also detected in deposits collected from alloy 35Cr-45Ni after 100, 500, and 1000h at 650ºC and 100 and 1000h at 750ºC. The deposit removed from UCX after 500h at 650 and 850ºC also contained alloying elements and oxygen. The presence of elements such as chromium, nickel, iron, silicon in the deposits may be deemed as an evidence of metal dusting. However, some of these elements might have been constituents of oxides that had been removed during sample collection. Indeed, the presence of oxides in the deposits may be due to either metal dusting or spallation.

8.2.4 Performance of HP

8.2.4.1 HP at 650ºC

Investigating the surfaces and cross sections of alloy HP confirmed the onset of metal dusting after 100h exposure at 650ºC. It was obvious that increasing exposure time led to the formation of deeper and larger pits. Some of the pits were also observed to link up to form bigger pits.

EDX of the layer formed on the alloy surface after 100h at 650ºC (Figure 5.13) showed high concentrations of the alloying elements nickel and iron suggesting that the layer was relatively thin such that the interaction volume, caused by the electron beam, penetrated a considerable volume of the base metal. Increasing the exposure time, however, led to denser and thicker layers that contained more carbon and oxides. Nonetheless, the oxide-containing layer formed after 1000h was uneven, discontinuous and mixed with carbon making its protection effectiveness questionable. This observation is supported by other researches which concluded that exposures at relatively low temperatures, < 650ºC, did not lead to quick formation of the protective Cr_2O_3 scale because of the slow diffusion of chromium through the alloy [11].

The pits caused by exposure at 650ºC had initiated at the alloy matrix rather than the primary carbides and also progressed through the matrix suggesting that the carbon diffusion was much easier in the austenitic base metal compared to the carbides which originally contain higher concentrations of carbon. This behaviour contradicts the metal dusting mechanism suggested by Szakalos [17] which involves selective oxidation of the carbides. Indeed, the stability of primary carbides in metal dusting conditions may suggest the possibility of using carbide-rich films at alloy surfaces in order to improve their resistance against metal dusting.

Most of the deposits within the pits contained particles of oxides and alloy that were most probably the result of the disintegration of the alloy due to metal dusting. However, whereas it is possible that the oxides might also have been removed during sample preparation, it is unlikely that alloy particles were removed solely because of that. Instead, it is thought that the alloy particles at the alloy substrate had been weakened as a consequence of exposure to the gas mixture and might ultimately have been separated due to cross sectioning.

The attack appeared to have progressed by a process that involved inward diffusion of carbon followed by growth of very small, hair-like carbon filaments into the reaction front which eventually led to carbon saturation and alloy disintegration that resulted in a fibrous, sponge-like layer of approximately 1μm thickness (e.g. Figures 5.43 and 5.48). The reaction front was covered with numerous micropits that were probably caused by carbon diffusion and subsequent carbon growth into the substrate which in turn induced internal high stresses on the alloy particles and ultimately caused them to disintegrate. The presence of insignificant amounts of oxides at the bottom of the pits suggested that once the attack had started, the oxide scale did not seem to have reformed (assuming it formed before the attack) and that might have allowed the continuous progress of the attack. The carbon deposition and subsequent saturation at the reaction front may have acted as a barrier between the oxygen in the environment and the oxide-forming elements in the alloy. Moreover, carburisation at the reaction zone might have halted the chromium diffusion toward the surface by binding it in the form of chromium carbides.

The stabilities of chromium carbides can be predicted by considering the predominance diagram (Figure 8.6). At equilibrium, carbides will form when the carbon and oxygen activities of the environment are in Cr_3C_2, Cr_7C_3, and $Cr_{23}C_6$ regions. As shown in Figures

8.2 and 8.4, the carbon activity of the gas at 650ºC is very high whilst the oxygen partial pressure is approximately $3x10^{-32}$ suggesting the formation of Cr_3C_2 near the alloy surface.

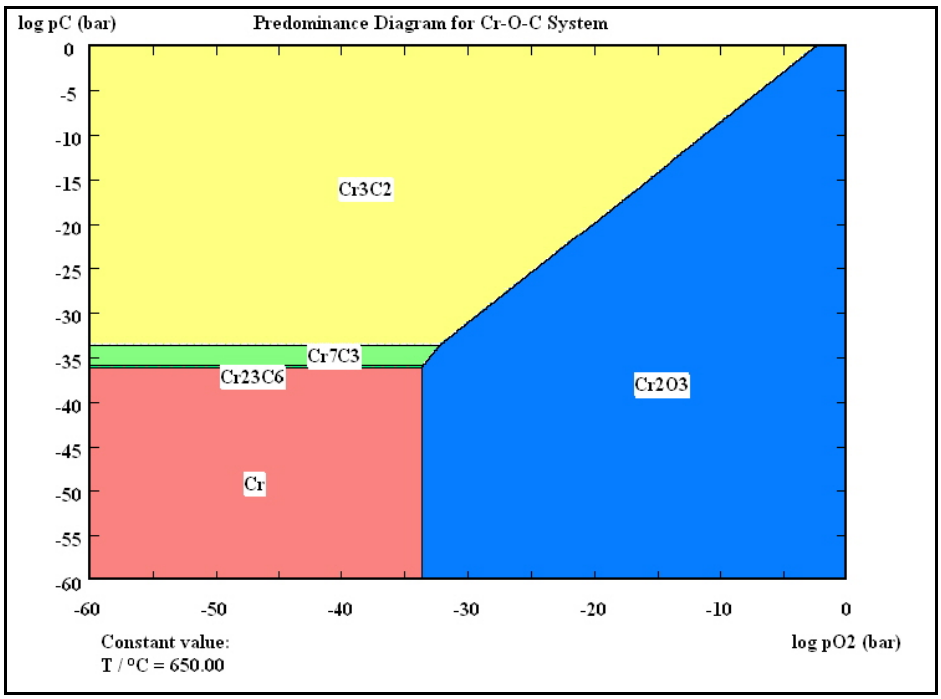

Figure 8.6 Stability diagram of Cr-C-O system at 650ºC (plotted by HSC Chemistry 6.0).

Carburisation was observed in the reaction zones below the pits bottom (e.g. Figure 5.50). Interestingly, some of the carbides observed had a strip-shape, i.e. relatively long films (Figure 5.54). The diffusion of carbon into the alloy and the resultant carbides may lead to a volume increase and create internal stresses on the non-carburised regions in the reaction zone.

8.2.4.2 HP at 750ºC

It was evident that increasing the exposure temperature to 750ºC led to a reduction in carbon deposition which was accompanied by an increase in oxide formation on the alloy. Generally, compared to the 650ºC experiments, the corrosion was relatively less aggressive as fewer pits were observed.

Isolated alloy particles were seen in the pits after 100h and layers of carbon and oxides accumulated around them (e.g. Figure 5.56). Although these particles might have been removed during sample preparation, it seemed that the attack was probably facilitated by the precipitation of some carbide bands (e.g. Figure 5.59) that created internal stresses that caused microcracking leading to carbon diffusion and oxidation-assisted crack propagation.

The corrosion observed after 500h was somewhat different from that seen at 650ºC as a mixture of chromium-based oxides and carbon was detected at the reaction front. Moreover, a relatively uniform, heavily carburised zone, of about 20μm was discovered surrounding the pit (Figure 5.60). Investigation of the reaction front revealed a shark's teeth-like pattern suggesting that the metal wastage process was progressing through the formation of a high number of micropits. The process may have started with carbon diffusion into the reaction zone leading to the formation of a high density of carbides. Then, as the alloy substrate became supersaturated with carbon the reaction front started disintegrating into a ~2μm layer that contained high concentrations of carbon, alloying elements, and oxides. It is worth noting that although the primary carbides seemed more resistant to the attack than the matrix, the carbides produced by carburisation did not appear to retard the corrosion progression which might be attributed to the difference in the morphology, shape, and/or size between the two carbides.

8.2.4.3 HP at 850ºC

The 850ºC samples showed the least attack accompanied by little carbon deposition and the most oxide formation. The alloy reaction zone suffered carburisation after 100h and some of the carbides precipitated in the form of relatively long bands (e.g. Figure 5.64).

A totally different type of attack took place on the alloy after 500h as localised, thick layers containing mainly oxides, alloy particles, and niobium carbides were observed to grow into the alloy (Figures 5.66 and 5.67). The alloy and carbide particles were embedded and surrounded by the oxides, and the reaction zone, just below the attack, was heavily carburised suggesting the combined action of oxidation and carburisation. Interestingly, an outer oxide layer which also contained carbon appeared to form on the top of the localised attack implying that the carbon must have diffused through that layer toward the alloy. It

also appeared that the alloy area adjacent to the oxides was depleted of carbides which might indicate that after carburisation oxidation took place consuming some chromium at the nearby substrate. Collectively, this mechanism led to disintegration of the alloy and caused removal of carbides, oxides, and alloy particles that contained mainly nickel and iron. Although a similar attack was observed on the alloy after 1000h (Figure 5.69), carburisation was not seen at the reaction zone suggesting that the processes were possibly at a different stage. These findings agree with the studies that have strongly suggested that metal dusting is significantly influenced by oxidation where it was observed that simultaneous carburisation and oxidation exposure would lead to damage that appears similar to metal dusting [43]. It has also been suggested that the metal dusting process is controlled by the simultaneous reaction of carbon and oxygen with chromium.

The unusually high concentrations of silicon oxide detected on the alloy were unlikely to have formed due to the silicon content in the alloy. Normally, the alloys tend to form discontinuous silica layers at the substrate/Cr_2O_3 interface in order to improve the integrity of the oxide scale. In the current case, however, the silicon oxides were found in abnormal concentrations on the chromium-rich oxides. More details about the silicon role in oxidation are given in Chapter 4.

The most probable source of silicon oxide was, however, the mullite furnace tube as literature shows that mullite readily corrodes after exposure to strongly reducing environments such as the gas mixture used in this research. These showed that hydrogen can degrade mullite according to the reaction:

$$A1_6Si_2O_{13}(s) + 2H_2\,(g) \rightarrow 3Al_2O_3(s) + 2SiO\,(g) + 2H_2O\,(g) \qquad (8.1)$$

This reaction, which was quickened by increasing the temperature, led to the formation of a porous alumina layer [126]. Also, mullite has reportedly disintegrated as a result of exposure to CO following the reaction [127]:

$$A1_6Si_2O_{13}(s) + 2CO\,(g) \rightarrow 3Al_2O_3(s) + 2SiO\,(g) + 2CO_2\,(g) \qquad (8.2)$$

8.2.5 Performance of 35Cr-45Ni at all Temperatures

Pitting also occurred on this alloy after 650ºC, but to a lesser extent when compared with HP, with an increasing pitting concentration with time. The alloy also formed more oxides although the carbon was still detected in high concentrations. This alloy originally contained a low carbon concentration compared to HP and UCX which might have enhanced its resistance to the attack due to the ability to dissolve more carbon and precipitate more carbide before the onset of the alloy disintegration.

Some of the pits were full of alloy particles separated from the base metal and carburisation was observed in reaction zones (e.g. Figure 6.32). The attack observed on the alloy after 1000h seemed to have involved simultaneous oxidation and carburisation (Figure 6.35). Heavy carburisation was observed in the reaction zone, just below the localised oxidation. A decarburised zone was however noticed in the reaction zone of another localised attack suggesting either a different corrosion mechanism or a different stage of the corrosion process (Figure 6.37). The oxides surrounded chromium-based carbides in the pit and seemed to facilitate their removal from the alloy.

Only a few pits were observed on samples exposed at 750ºC. The mechanism by which the attack took place did not seem to be different from that discussed at 650ºC after 100 and 500h. More oxides formed on the alloy as a result of increasing the temperature to 750ºC.

Slightly different pitting was seen after 100h at 850ºC where, in addition to the oxide layer formed at the pit's bottom, internal islands of oxides grew into the substrate (e.g. Figure 6.48). The corrosion changed as a consequence of increasing the exposure time to 1000h where the alloy exhibited localised oxidation and carburisation (Figure 6.53). The presence of a relatively high concentration of carbides surrounding the attack area and a decarburised region between the carburised and oxidised zones may suggest the occurrence of a simultaneous oxidation and carburisation process.

8.2.6 Performance of UCX at all Temperatures

UCX proved to be the most resistant alloy to metal dusting as it experienced little significant attack at 650ºC apart from tiny pits which formed along the grain boundaries. The alloy formed the most continuous and thickest oxide layers at this temperature although they were still uneven and thin in some areas at shorter times. It seems that as chromium diffusion through the alloy at such low temperature is expected to be slow the alloy with the highest chromium concentration performs the best. The presence of a sufficient chromium concentration at the substrate enabled fast formation of the oxide layers that acted as a barrier between the environment and the alloy. However, the carbon diffusion from environment into the substrates may have also been influenced by the alloy's overall chemical composition and/or the microstructure in addition to the surface condition. As discussed in the literature review, the presence of carbide-forming elements such as chromium, tungsten, and niobium in the alloy increases the incubation period before the onset of metal dusting as they have an affinity for the diffused carbon. Also, alloys with higher nickel concentrations have exhibited less metal dusting because of the resulting slower carbon diffusion into the substrates.

Increasing the temperature to 750ºC led to formation of thicker and more even oxide-containing layers that also contained carbon in varying concentrations. The surfaces of the pits formed on the alloy after 500h were covered with oxide layers implying that the attack possibly took place prior to the development of the oxide scale until the pit's progress was probably interrupted by the scale formation. After 1000h, however, selective attack occurred on sites rich with chromium carbides and was possibly caused by the growth of oxides and diffusion of carbon in regions between the matrix and the carbides that apparently caused disintegration and removal of the carbides (Figure 7.45).

8.2.7 Observations

It is worth noting that the bottom of the pits in all alloys had two main features. Some of the reaction fronts appeared to be active and hence the attack was progressing until the removal of the sample from the furnace. These reaction fronts had a fibrous and filamentous appearance and were rich with alloying elements and carbon. Some pits,

however, appeared to have stopped growing and the reaction fronts were uniform and smooth and covered with carbon/oxide layers. It is suggested that the attack might have started at sites on the alloy surfaces where no protective oxide scales formed but, perhaps as time progressed, more protective oxides developed and hindered the diffusion of carbon into the substrate.

The presence of carbides and/or nitrides in the alloys might have negatively influenced their metal dusting resistance as it was very possible that many of these intermetallic phases happened to be on the alloy surfaces and that might have led to oxide scale disruption which in turn caused more carbon diffusion and eventually more metal dusting. There is a difference in growth rates of the oxide scale on nitrides/carbides and matrix resulting in change in scale thickness. Such a local heterogeneity may also create excessive stress and lead to scale spallation [118].

While the carbide precipitation in the form of dispersed particles in the microstructure is desirable to improve the alloy mechanical properties at high temperatures (Chapter 3), the formation of continuous carbide films has, however, a deleterious effect on the alloy integrity as it provides easy fracture paths and induces an excessive stress build up leading to alloy embrittlement and cracking [128].

9 CONCLUSIONS AND FUTURE WORK

9.1 Conclusions

Considering the results presented in Chapters 5, 6, and 7 and the previous discussion, the following concluding remarks can be made:

1. Increasing the exposure temperature generally caused less carbon deposition and more oxide formation on the alloy surfaces leading to a reduction in the aggressiveness of the attack. Also, increasing the test time resulted in more deposition of carbon at same temperature.
2. Weight loss might indicate the occurrence of metal dusting, especially for samples exposed at the lower temperatures (i.e. 650 and 750ºC). Weight gain, however, did not prove to be a reliable tool to assess the alloy's condition.
3. Deposits collected from the samples contained carbon, metal, oxide, and probably carbide particles which suggests the onset of metal dusting.
4. Alloy HP suffered metal dusting pitting at 650ºC. Deeper and larger pits formed as a result of increasing the time.
    a. The pits initiated and progressed at the matrix rather than the primary carbides.
    b. The attack process appeared to involve inward diffusion of carbon followed by growth of very small carbon filaments at the reaction front which in turn induced internal stresses at the substrate and caused alloy disintegration.
    c. It seemed that the carbon deposition and diffusion in the reaction front posed a barrier between the oxygen in the environment and the oxide-forming elements in the alloy which consequently hindered the formation of a protective oxide scale.
5. Alloy HP also experienced pitting after 750ºC although the attack was less aggressive than that observed at 650ºC.

a. The metal dusting process seemed to have started with carbon diffusion into the reaction zone and formation of a high density of carbides. Then, as the alloy substrate became supersaturated with carbon, the reaction front disintegrated into a layer that contained carbon, alloying elements, and oxides.

6. The least attack observed on alloy HP was after exposure at 850ºC.
    a. Localised, thick layers of oxides surrounding alloy particles and niobium carbides formed on the alloy suggesting the combined action of oxidation and carburisation that resulted in disintegration of the alloy into carbides, oxides, and alloy particles.
7. Pitting occurred on alloy 35Cr-45Ni after 650ºC but to a lesser extent compared to HP.
    a. The mechanism by which the attack took place did not seem to differ from that discussed for HP at 650ºC.
    b. The attack observed on the alloy after 1000h seemed to involve simultaneous oxidation and carburisation.
8. A few pits were observed on 35Cr-45Ni exposed at 750ºC. The mechanism by which the attack took place was similar to that observed on the alloy at 650ºC
9. The least pitting on 35Cr-45Ni was observed at 850ºC.
10. Although it did not show complete immunity, UCX proved to be the most resistant alloy to metal dusting at the test temperatures.
11. Pitting was observed on UCX after 500h at 750ºC.
12. After 1000h, selective attacks were observed where the formation of oxides and diffusion of carbon into regions between the matrix and the chromium-carbides at the surface caused disintegration of the latter.
13. It was evident that increasing the concentration of alloying elements in the alloys resulted in a significant improvement in their performance in metal dusting conditions. The presence of high amount of chromium at the alloy surface (as in UCX) catalysed a quick formation of a protective chromium oxide scale that acted as a barrier between the gas and the alloy. This was important especially at 650ºC

where the chromium diffusion through the alloy is anticipated to have been slow. Furthermore, incorporating high percentage of nickel seemed to have enhanced the alloys' resistance owing to the slow diffusion of carbon in nickel.

14. The increase of nickel and chromium in the alloys was accompanied by a reduction in iron content. Indeed, the presence of high concentration of iron, as in the case of HP, might have resulted in the formation of unstable iron-containing oxides that could be reduced by the gas mixture, thus aggravating the attack. The reduction of the oxides resulted in exposure of the alloy bare surface and subsequently deposition of more carbon that was catalysed by elements like iron.

15. The carbon low content in 35Cr-45Ni might well have had a beneficial effect on its metal dusting behaviour. The alloy would contain a higher level of free carbide-forming elements such as chromium and niobium which would bind with the diffused carbon and as a consequent delay the onset of metal dusting.

16. The addition of other oxide and carbide-forming elements (e.g. Si, W, Nb, and Mn) might have also improved the alloy's performance in metal dusting. Silicon oxide tends to form at the alloy/oxide scale interface and acts as a second defence against carbon diffusion from the gas. Also, the formation of Mn-containing oxide is thought to be beneficial in slowing down the carbon diffusion. Once carbon diffused into the alloy, the presence of carbide formers became important. They bind with carbon to form stable carbides and that would delay the onset of metal dusting and increase the alloy useful life.

17. It was obvious that the presence of niobium and silicon in HP was not enough to exhibit a good resistance to metal dusting. It should be, however, accompanied by the addition of more nickel and chromium at the expense of iron and that was evident in 35Cr-45Ni that showed a better behaviour in the gas mixture. Further addition of nickel and chromium as well as tungsten resulted in the best performance, as in the case of UCX.

18. The carburisation on alloy surfaces led to a volume increase and created internal stresses on the non-carburised areas. Such stress generation might have contributed to the disintegration of the alloys' particles by pressing them out.

19. The formation of continuous carbide films (strips) was observed in reaction zone and that might provide easy fracture paths that may facilitate cracking and removal of alloy particles.
20. Some of the attacks seemed to have possibly taken place before the development of the oxide scale and the pit's progress was then interrupted by the scale formation.

9.2 Future Work

In addition to the current literature, this research has clearly shown the need for further investigation in order to gain a better understanding of metal dusting. The metal dusting processes for iron and nickel-based alloys appeared to be complex and involved interaction of mechanisms such as oxidation and carburisation. Furthermore, the nature of the attack seemed to differ from one exposure temperature to the other and from one alloy to the other.

It is strongly suggested there should be established standardised metal dusting testing and characterisation procedures that cover the best practices accumulated over the years. This will undoubtedly ensure a more accurate evaluation and comparison of the alloys and provide a solid base for investigating the attack mechanism(s). More studies are also necessary to bridge the knowledge gap concerning gas/alloy interaction and to establish thermodynamic and kinetics correlations.

The temperature distribution across the working tube was naturally non uniform with the middle being the hottest and the ends being the coldest which may have influenced the gas decomposition rate and eventually the corrosion process. To overcome this, it is proposed to design a system that has a more uniform temperature distribution, e.g. a modified chamber furnace, which will ensure more accurate and reliable results at a given temperature.

This investigation showed that carbon deposition on the alloys changed according to exposure temperature and increased with time at the given gas composition and flow rate (which was constant). Since it has been proposed that carbon accumulation on the alloy surface is a precursor of metal dusting, it would be interesting to study the effect of altering the carbon monoxide and hydrogen ratio in the gas on the carbon deposition and metal

dusting. It would also be useful to relate the carbon deposition to the gas flow rate at a given temperature.

Primary carbides were found to be more resistant to the attack than the matrix. This may suggest that the alloy metal dusting behaviour is influenced by different distributions and densities of carbides across the microstructure. The carbides role may be understood by testing alloys with the same composition but different microstructure, e.g. fine, coarse, equiaxed, and columnar grains. Furthermore, it would be meaningful to investigate the behaviour of wrought and cast alloys that have similar composition since the cast alloys are know to have inhomogeneous microstructure and suffer segregation of alloying elements.

10 BIBLIOGRAPHY

[1] Jones, Richard T., Kenneth L. Baumert, *Metal Dusting-An Overview of Current Literature*, NACE International, Corrosion 2001, Paper No. 01372.

[2] E. Pippel, J. Woltersdrof and R. Schneider, *Micromechanisms of Metal Dusting on Fe-Base and Ni-Base alloys*, , Materials and Corrosion 49, 309-316 (1998).

[3] R. F. Hochman, *Catastrophic Deterioration of High Temperature Alloys in Carbonaceous Atmospheres*, Georgia Inst. of Technology, Proc.-Electrochem. Soc. (1976), 77-1 (Proc. Symp. Prop High Temp. Alloys, 1976), pp. 715-732.

[4] Baker, Brian A. and Gaylord D. Smith, *Metal Dusting Behaviour of High Temperature Alloys*, NACE International, Corrosion 99, Paper No. 54.

[5] Agarwal, D.C., U. Brill and Jutta Kloewer, *Recent Results on Metal Dusting of Nickel Base Alloys and Some Applications*, NACE International, Corrosion 2001, Houston.

[6] Lai, George Y., *High-Temperature Corrosion of Engineering Alloys*, ASM International, 1997, USA.

[7] Kelly, James, Jason Wilson, and Devin Wachowiak, *Metal Dusting a.k.a Carbon Rot in the Heat Treat Industry, 50 years*, July 2004.

[8] Hrivnak, Ivan, Lubomir Caplovic, Gejza Bakay, and Aurel Bitter, *Metal Dusting of Inlet Tube Made of Alloy 800*, Kovove Mater. 43, 2005, 290-299.

[9] Levi, T.P., N. Briggs, I. Minchington and C.W. Thomas, *A Study of the Relationship Between Metal Dusting and Pressure*, NACE International, Corrosion 2001, Paper No. 01375.

[10] Natesan, K., Z. Zeng, V.A. Maroni, W. K. Soppet, and D. L. Rink, *Metal Dusting Research at Argonne National Laboratory*, Argonne National Laboratory, June 2002, USA.

[11] Grabke, H. J., M. Spiegel, *Occurrence of Metal Dusting-Referring to Failures Cases*, Materials and Corrosion 2003, 54, No. 10, pp. 799-804.

[12] Di Gabriele, F., J. R. Bernstein, M. M. Al-Qhatani, Z. Liu, M. P. Jordan, J. A. Richardson and F. H. Stott, *Study of the Metal Dusting Behaviour of High Temperature Alloys*, Materials and Corrosion, 2003, 54, No. 11.

[13] Robert F. Hochman, *"Metal Dusting" Catastrophic Deterioration of Metals and Alloys in Carbonaceous Gases*, 6th I.C.M.C., Sydney, pp. 1-5, 1975.

[14] Klarstrom, D.L. and S.K. Srivastava, *Selection of High Performance Alloys for High Temperature Corrosion Environments*, NACE International, Corrosion 2005, Paper No. 05421.

[15] Baker, B.A., G.D. Smith, V.W.Hartmann, L.E.Shoemaker, and S.A. McCoy, *Nickel-Base Material Solutions to Metal Dusting*, NACE International, Corrosion 2002, Paper No. 02394.

[16] Mirabal, Edmundo, Carlos Molina, Anelsy Mayorga and Jorge L. Hau, *Fireside Carburisation of Stainless Steel Furnace Tubes*, NACE International, Corrosion 99, Paper No. 80.

[17] Szakalos, Peter, *Mechanisms of Metal Dusting*, Doctoral Thesis, Department of Material Science and Engineering, Division of Corrosion Science, Royal Institute of Technology, Sweden AND Swedish Institute for Metals Research, Sweden, 2004.

[18] Klower, J., H. J. Grabke, E.M. Muller-Lorenz, and D.C. Agarwal, *Metal Dusting and Carburisation Resistance of Nickel Base Alloys*, NACE International, Corrosion 97, Paper No. 139.

[19] Ravestein, M. H., *Metal Dusting in Catalytic Reforming Furnace Tubes*, NACE International, Corrosion 97, Paper No. 496.

[20] Fabiszewski, A.S., W.R. Watkins, J.J.Hoffman, and S.W.Dean, *The Effect of Temperature and Gas Composition on the Metal Dusting Susceptibility of Various Alloys*, NACE International, Corrosion 2000, Paper No. 00532.

[21] Grabke, H. J., *Metal Dusting*, Materials and Corrosion 2003, 54, No. 10.

[22] Nishiyama, Y., N. Otsuka, T. Kudo, and O. Miyahara, *Metal Dusting of Nickel Base Alloys in Simulated Syngas Mixtures*, NACE International, Corrosion 2003, Paper No. 03471.

[23] Dean, Sheldon W., *Calculation of Carbon Activities and Related Values for Project ANL -02/05*, MTI Project 138-00, Dean Corrosion Technology, Inc., 2002.

[24] Baker, Brian A. and Gaylord D. Smith, *Alloy Selection for Environments Which Promote Metal Dusting*, NACE International, Corrosion 2000, Paper No. 00257.

[25] Holland, M.L. and H. J. De Bruyn, *Metal Dusting Failures in Methane Reforming Plant*, Int. J. Pres. Ves. & Piping 66 (1996) 125-133.

[26] Schueler, Robert C., *Metal Dusting*, Hydrocarbon Processing, August 1972.

[27] Grabke, H.J., R. Krajak and J.C. Nava Paz, *On the Mechanism of Catastrophic Carburisation: "Metal Dusting"*, Corrosion Science, Vol. 35, Nos 5-8, pp. 1141-1150, 1993.

[28] Chun, C.M., and T.A. Ramanarayanan, *Metal Dusting Corrosion of Low Chromium Steels*, Oxidation of Metals, Vol. 62, Nos. 112, August 2004.

[29] Schneider, A., J. Zhang, and G. Inden, *Metal Dusting of Binary Fe-Al Alloys in CO-H_2-H_2O Gas Mixtures*, JCSE, Volume 6, Paper H043, 2003.

[30] Collin, R., S. Gunnarson, and D. Thulin, *A Mathematical Model for Predicting Carbon Concentration Profiles of Gas-Carburised Steel*, Journal of The Iron and Steel Institute, October 1972.

[31] Grabke, H.J., *Kinetics of Oxygen Transfer from Dioxide to the surface of Iron*, 928; 1965, Amsterdam, North Holland Publishing Co., Ber der Bunsenges. Fur phys. Chemie, 1967,71,1067.

[32] Grabke, H. J., Ber der Bunsenges. Fur phys. Chemie, 1965, 69,409.

[33] Chun and T. A. Ramanarayanan, *Metal Dusting Corrosion of Austenitic 304 Stainless Steel*, Journal of the Electrochemical Society, 152 (5) B169-B177 (2005).

[34] Steurbaut, C., H. J. Grabke, D. Stobbe, F. R. van Buren, S. J. Korf, and J. Defrancq, *Kinetic Studies of Coke Formation and Removal on HP40 in Cycled Atmospheres at High Temperatures*, Materials and Corrosion 49, 352-359 (1998).

[35] Muller-Lorenz, E.M., H.J. Grabke and M. Zinke, *Metal Dusting Resistance of Welded Nickel Based Alloys,* EUROCORR 2001.

[36] Turkdogan, E. T. and J. R. Vinters, *Catalytic Effect of Iron on Decomposition of Carbon Monoxide: I. Carbon Deposition in H_2-CO Mixtures*, Metallurgical Transactions, volume 5, pp. 11-19, 1974.

[37] Olsson, R. G. and E. T. Turkdogan, *Catalytic Effect of Iron on Decomposition of Carbon Monoxide:II. Effect of Additions of H_2, H_2O, CO_2, SO_2 and H_2S*, Metallurgical Transactions, volume 5, pp. 21-26, 1974.

[38] Tillack, D. J., and J. E. Guthrie, *Wrought and Cast Heat Resistant Stainless Steels and Nickel Alloys for the Refining and Petrochemical Industries*, Nickel Institute Technical Series # 10071.

[39] Baker, B. A., V. W. Hartmann, and S. A. McCoy, *A new Nickel Base Alloy for Resisting Metal Dusting Attack*, Special Metals Corporation, www.specialmetals.com/documents.

[40] Kirchheiner, R., and J. L. Jimenez Solar, *Correlation of Oxidation, Carburisation and Metal Dusting; "Controlling Corrosion by Corrosion"*, NACE International, Corrosion 2001, Paper No. 01374.

[41] Schutze, M., C. Rosado, and F. Dettenwanger, *Protection of Steels against Metal Dusting Attack by Coating*, EUROCORR 2001.

[42] Wei, Q., E. Pippel, J. Woltersdrof and H.J. Grabke, *Microprocesses of Coke Formation in Metal Dusting*, Materials and Corrosion 50, 628-633 (1999).

[43] De Bruyn, Hendrik J., Emil H. Edwin and Stein Brendryen, *Apparent Influence of Steam on Metal Dusting*, NACE International, Corrosion 2001, Paper No. 01383.

[44] Pippel, E., J. Woltersdorf, and H. J. Grabke, *Microprocesses of Metal Dusting on Iron-Nickel Alloys and Their Dependence on Composition*, Materials and Corrosion 2003, 54, No. 10, 747-751. .

[45] Grabke, Hans Jurgen, Else Marie Muller-Lorenz, and Andre Schneider, *Review-Carburisation and Metal Dusting on Iron*, ISIJ International, Vol. 41 (2001), Supplement, pp. S1-S8.

[46] A. Schneider, *Iron Layer Formation during Cementite Decomposition in Carburising Atmospheres*, Corrosion Science 44 (2002) 2353-2365.

[47] Jiang, D. E. and Emily A. Carter, *Effects of Alloying on the Chemistry of CO and H_2S on Fe Surfaces*, J. Phys. Chem. B 2005, 109, 20469-20478.

[48] R. F. Hochman, *Basic Studies of Metal Deterioration ("Metal Dusting") in Carbonaceous Environments at Elevated Temperatures*, Proceedings of the Fourth International Congress on Metallic Corrosion, NACE (1972), pp. 260-263.

[49] Szakálos, P., M Lundberg and R. Pettersson, *The Role of Discontinuous Precipitation in Metal Dusting*, Materials Science Forum Vols. 461-464 (2004) pp 561-570.

[50] Szakálos, P., M Lundberg and R. Pettersson, *Metal Dusting on an Alumina Forming Ni-base Alloy*, Corrosion Science 48 (2006) 1679-1695.

[51] Toh, C.H., P.R. Munroe, and D.J. Young, *Metal Dusting of Fe-Cr and Fe-Ni-Cr Alloys under Cyclic Conditions*, Oxidation of Metals, Vol. 58, Nos. ½, August 2002.

[52] Zeng, Z., and K. Natesan, *Relationship between the Growth of Carbon Nanofilaments and Metal Dusting Corrosion*, Chem. Mater 2005, 17, 3794-3801.

[53] Zhang, J., A. Schneider, and G. Inden, *Characterisation of the Coke formed during Metal Dusting of Iron in CO-H_2-H_2O gas mixtures*, Corrosion Science 45(2003) 1329-1341.

[54] LeFrancois, P. A. and W. B. Hoyt, *Chemical Thermodynamics of High Temperature Reaction in Metal Dusting Corrosion*, Corrosion 19 (1963), pp. 360t-368t.

[55] Hotcman, R. F. and J. H. Burson, *The Fundamentals of Metal Dusting*, III. API Division of Refining Proceedings 46, (1966), pp. 331-334.

[56] H.J. Grabke, *Nickel-Based Alloys in Carbonaceous Gases*, Corrosion-Vol. 56, No.8, 801-808, 2000.

[57] Chun, C. M., J. M. Mumford, and T. A. Ramanarayanan, *Metal Dusting Corrosion of Cobalt*, Journal of the Electrochemical Society, 150 (2) B76-B82 (2003).

[58] Chun, C. M., J. M. Mumford, and T. A. Ramanarayanan, *Mechanism of Metal Dusting Corrosion of Iron*, Journal of the Electrochemical Society, 149 (7) B348-B355 (2002).

[59] Chun, C. M., J. D. Mumford, and T. A. Ramanarayanan, *Carbon Induced Corrosion of Nickel Anode*, Journal of Electrochemical Society, 147 (10) 3680-3686 (2000).

[60] Motin, M.A.A., P.R. Munroe, M.P. Brady and D.J. Young, *Metal Dusting of ferrite Fe-Ge in the absence of cementite*, Scripta Materialia 56 (2007) 281-284.

[61] Zhang, J., A. Schneider and G. Inden, *Metal dusting of iron in CO-H_2-H_2O gas mixtures at 600°C*, Volume 6 Paper 100, JCSE, 2004.

[62] Grabke, H.J., *Carburisation, Carbide Formation, Metal Dusting, Coking*, MTAEC 9, 36(6)297(2002).

[63] Grabke, H. J., and E. M. Muller-Lorenz, *Occurrence and Prevention of Metal Dusting on Stainless Steels*, NACE International, Corrosion 2001, Paper No. 01373.

[64] Maier, Mark, and James F. Norton, *Studies Concerned with the Metal Dusting of Fe-Cr-Ni Materials*, NACE International, Corrosion 99, Paper No. 75.

[65] Toh,Chin Hock, *Metal Dusting on Heat-resistant alloys under Thermal Cyclic Conditions*, A thesis submitted for the degree of doctor of philosophy, University of New South Wales, December 2002, www.library.unsw.edu.au.

[66] De Bruyn, Hendrik J., and Michael L. Holland, *Materials Experience in a Methane Reforming Plant*, NACE International, Corrosion 98, Paper No. 429.

[67] Klarstrom, Dwaine L., Hans J. Grabke, and Larry D. Paul, *The Metal Dusting Behaviour of Several High Temperature Nickel Based Alloys*, NACE International, Corrosion 2001, Paper No. 01379.

[68] Di Gabriele, F., F. H. Stott, J. R. Bernstein and Z. Liu, *Characterisation of Several Nickel Base Alloys in Metal Dusting Environments*, JCSE, Volume 6, Paper H009, 2003.

[69] Agarwal, D. C. and Ulrich Brill, *Performance of Alloy 602CA (UNS N06025) in High Temperature Environment up to 1200℃ (=2200℉)*, NACE International, Corrosion 2000, Paper No. 00521.

[70] Elliott, Peter, *Materials Performance in High Temperature Environments-Making the Choice*, NACE International, Corrosion 2000, Paper No. 00527.

[71] Elliott, Peter, *Choose Materials for High-Temperature Environments*, www.aiche.org/cep, 2001.

[72] Baker, B. A. and G. D. Smith, *Metal Dusting in Laboratory Environment-Alloying Addition Effect*, www.specialmetals.com/documents.

[73] Li, B. and B. Gleeson, *Effects of Minor Elements on the Cyclic Oxidation Behaviour of Commercial Fe-bas 800-Series Alloys*, Oxidation of Metals, Vol. 62, Nos. 112, 2004.

[74] Zhang, Jianqiang and David J. Young, *Effect of copper on metal dusting of austenitic stainless steels*, Corrosion Science 49 (2007) 1450-1467.

[75] Wolf, I, H. J. Grabke, and P. Schmidt, *Carbon Transport Through Oxide Scales on Fe-Cr Alloys*, Oxidation of Metals 29, Nos. ¾, (1988), pp. 289-306.

[76] Jones, Richard T., *An Overview of Metal Dusting, MTI Project 133-99*, Materials Technology Institute, Inc., 2000.

[77] O. Coreno-Alonso, A. Duffus-Scott, C. Zanchez-Cornejo, J. Coreno-Alonso, F. Sanchez-de Jesus, and A. Bolarin-Miro, *On the effect of σ-phase formation during metal dusting*, Materials Chemistry and Physics 84(2004) 20-28.

[78] Brill, U., G. K. Grossmann, and T. Kremser, *Corrosion Behaviour of the Ni-Cr-Si Alloy 45 TM (UNS N 06045) in High Temperature Applications*, NACE International, Corrosion 2001, Paper 01156.

[79] Ramanathan, L.V., *Role of Rare Earth Elements on the High Temperature Oxidation Behaviour of Fe-Cr, Ni-Cr and Ni-Cr-Al Alloys*, Corrosion Science, Vol. 35, Nos5-8, pp. 871-878, 1993.

[80] Yuan, Z. X., Z. S. Yu, P. Tan, and S. H. Song, *Effect of Rare Earths on the Carburisation of Steel*, Materials Science and Engineering A267 (1999) 162-166.

[81] Elliott, P., *A practical Guide to High Temperature Alloys*, Materials and Design, Vol. 12, No. 6, 1991.

[82] Kelly, James, *Metal Dusting in the Heat Treating Industry*, Stainless Steel World Conference, 1999.

[83] Kelly, James, *Metal Dusting Causes HRA Headaches*, Rolled Alloys, Temperance, Mich, http://industrialheating.com.

[84] Grabke, H. J, *Corrosion by Carbonaceous Gases, Carburisation and Metal Dusting, and Methods of Prevention*, Materials at High Temperatures 17(4) 483-487, 2000.

[85] Grabke, H. J., E. M. Muller-Lorenz, S. Strauss, E. Pippel and J. Woltersdorf, *Effects of Grain Size, Cold Working, and Surface Finish on the Metal Dusting Resistance of Steels*, Oxidation of Metals, Vol. 50, Nos. 3/4, 1998.

[86] Palasantzas, G., H. J. Kooij, J. Th. M. DeHosson, *Carbon Induced Metal Dusting of Iron-Nickel-Chromium Alloy Surfaces: A Scanning Auger Microscopy Study*, Applied Surface Science 229 (2004) 190-196.

[87] Smith, P. J., O. Van der Biest, and J. Corish, *The Initial Stages of High-Temperature Corrosion of Fe-Cr-Ni and Cr-Ni Alloys in a Carburizing Atmosphere of Low Oxygen Partial Pressure*, Oxidation of Metals, Vol. 24, Nos. 1/2 , 1985.

[88] Voisey, K. T., Z. Liu, and F.H. Stott, *Inhibition of Metal Dusting of Alloy 800H by Laser Surface Melting*, Applied Surface Science, 2005, www.sciencedirect.com.

[89] Baker, B.A. and G.D Smith, *Metal Dusting of Nickel Containing Alloys*, NACE International, Corrosion 98, Paper No. 445.

[90] Schmid, Bernd, John Charles Walmsley, Oystein Grong, and Rolf Odegard, *Microscale Investigations of the Metal-Dusting Corrosion Mechanism on Mild Steel*, Metallurgical and Materials Transactions A, volume 34A, 2003, 345-354.

[91] Broutin, P., F. Ropital, M.F. Reyniers and G. F. Froment, *Anticoking Coatings for High Temperature Petrochemical Reactors*, Oil & Gas Science and Technology, Vol. 54 (1999), No. 33, pp. 375-385.

[92] Natesan, K., Z. Zeng, W. K. Soppet, and D. L. Rink, *Metal Dusting Behaviour of Coatings*, Argonne National Laboratory, USA, 2002

[93] Voisey, K. T., Z. Liu, and F. H. Stott, *Inhibition of Metal Dusting using Thermal Spray Coatings and Laser Treatment*, Surface and Coating Technology, 2005, www.sciencedirect.com.

[94] Bayer, George T., *Surface Engineered Coatings for Metal Dusting*, NACE International, Corrosion 2001, Paper No. 01387.

[95] Trimm, D. L., *Control of Coking*, Chem. Eng. Proces., 18(1984) 137-148.

[96] Zeng, Z, K. Natesan, abd M. Grimsditch, *Effect of Oxide Scale Compositions on Metal Dusting Corrosion of Fe-Based Alloys*, Corrosion-Vol. 60, No. 7,pp. 632-642, NACE International, July 2004.

[97] Natesan, K. and Z. Zeng, *Metal Dusting Performance of Structural Alloys*, NACE International, Corrosion2005, Paper No. 05409.

[98] Cai, Haiyong, Andrzej Krzywicki, Michael C. Oballa, *Coke Formation in Steam Crackers for Ethylene Production*, Chemical Engineering and Processing 41 (2002) 199-214.

[99] *Coking Behaviour of Cracking Tube Materials for Ethylene Plants*, Sumitomo Metal Industries Ltd., Japan.

[100] *Corrosion (3rd Edition) – Volume 2-Nickel and its Alloys: Carburisation and Attack by Carbon Containing Gases*, 7:126-131, Elsevier, 1994.

[101] Juarez-Islas, J.A., B. Campillo, N. Chaudhary, R. Mendoza, and A. Gonzalez, *High Temperature Corrosion of Austenitic Stainless Steel Coils in A Direct Reduction Plant in Mexico*, NACE International, Corrosion 96, Paper No. 425.

[102] H. J. Grabke, *Metal Dusting of Low- and High- Alloy Steels*, Corrosion –Vol. 51, No. 9, 711-720, 1995.

[103] *Heat Resistant Alloy KHR35C-Hi Si: Alloy Data Sheet*, Kubota Corporation, Japan, 2003.

[104] *Heat Resistant Alloy KHR45 LC: Alloy Data Sheet,* Kubota Corporation, Japan, 2003.

[105] *Heat Resistant Alloy UCX: Alloy Data Sheet*, Kubota Corporation, Japan, 2003.

[106] *Mill Sheet of KHR35C-Hi Si, KHR45 LC, and UCX*, Kubota Corporation, Japan, 2005.

[107] *A Working Party Report on Guidelines for Methods of Testing and Research in High Temperature Corrosion*, European Federation of Corrosion Publications, Number 14, The Institute of Materials, 1995.

[108] Dillinger, L., R. D. Buchheit, J.A. VanEcho, D.B.Roach and A. M. Hall, *Microstructures of Heat-resistant alloys*, Battelle Memorial Institute-Columbus Laboratories, Alloy Casting Institute Division, Steel Founders' Society of America, 1970.

[109] *Metallography and Microstructures*, ASM International Handbook, Volume 9, USA, 2004.

[110] Wu, X. Q., H.M. Jing, Y. G. Zheng, Z. M. Yao, W. Ke and Z. Q. Hu, *The Eutectic Carbides and Creep Rupture Strength of 25Cr20Ni Heat Resistant Steel Tubes Centrifugally Cast with Different Solidification Conditions*, Materials Science and Engineering, A293 (2000) 252-260.

[111] Abada, Ahmad, *Why Do Heat-resistant alloys Fail?* , Steeltech Ltd., Grand Rapids, Mich./Advanced Centrifugals Ltd., Cambridge, Wis.

[112] Raul Alejandro Pedro Ibanez, Gloria Dulce de Almeida Soares, Luiz Henrique de Almeida, and Iain Le May, *"Effect of Si Content on the Microstructure of Modified-HP Austenitic Steels"* Materials Characterisation, 30:243-249(1993).

[113] Knowles, D. M., C. W. Thomas, D. J. Keen, and Q. Z. Chen, *"In service embrittlement of cast 20Cr30Ni1Nb components used in steam reformer applications"* , International Journal of Pressure Vessels and Piping, 81 (2004) 499-506.

[114] *Alloying, Understanding the Basics*, Edited by J. R. Davis, ASM International, USA, 2001.

[115] Rohrig, Klaus, *Castings from Stainless Steels and Nickel Base Alloys*, Consultant to the Nickel Development Institute, Germany.

[116] Stott, F. H., *MSc (Corrosion Science and Engineering) Course: High Temperature Degradation and Protection Module*, 2001-2002, UMIST, Manchester, UK.

[117] Khanna, A. S., *Introduction to High Temperature Oxidation and Corrosion*, ASM International, 2002.

[118] Stott, F. H., *The Protective Action of Oxide Scales in Gaseous Environments at High Temperatures*, Rep. Prog. Phys. 50(1987) 861-913.

[119] Riffard, F., H. Buscail, E. Caudron, R. Cueff, C. Issartel, S. El Messki, and S. Perrier, *Peculiar high temperature corrosion behaviour of AISI 304 stainless steel at 900ºC*, EuroCorr2005, Lisbon, Portugal.

[120] Li, Bintgtao and B. Gleeson, *Effects of Silicon on the Oxidation Behaviour of Commercial Chromia-Forming Alloys*, Nace International, Corrosion 2002, Paper No. 02393.

[121] Li, Bintgtao and B. Gleeson, *Effects of Minor Elements on Cyclic-Oxidastion Behaviour of Commercial Fe-base 800-series Alloys*, Oxidation of Metals, Vol. 62, Nos. 1/2, 2004.

[122] Douglass, D. L. and J. S. Armijo, *The Effect of Silicon and Manganese on the Oxidation Mechanism of Ni-20Cr,* Oxidation of Metals, Vol. 2, No. 2, pp. 207-231, 1970.

[123] Holcomb, Gordon R. and David E. Alman, *The Effect of Manganese Additions on the Reactive Evaporation of Chromium in Ni-Cr Alloys,* Albany Research Center, U.S. Department of Energy, www.osti.gov.

[124] Ramanathan, L. V., *Role of Rare-Earth Elements on High Temperature Oxidation Behaviour of Fe-Cr, Ni-Cr and Ni-Cr-Al Alloys*, Corrosion Science, Vol. 35, Nos. 5-8, pp. 871-878, 1993.

[125] Birks, N. and G. H. Meier, *Introduction to High Temperature Oxidation of Metals*, Edward Arnold Ltd, 1983.

[126] Herbell, Thomas P., David R. Hull, and Anita Garg, *Hot Hydrogen Exposure Degradation of the Strength of Mullite*, NASA, http://gltrs.grc.nasa.gov.

[127] F. A. Costa Oliveira, *High Temperature Corrosion of Ceramic Foam Radiant Gas Burners,* EuroCorr 2005, paper 125, Lisbon.

[128] Wang, Frances and Derek O. Northwood, *The Effect of Carbon Content on the Microstructure of an Experimental Heat-Resistant Steel*, Materials Characterisation, 31:3-10(1993).